UNIVERSITAT POLITÈCNICA DE VALÈNCIA

Departamento de Máquinas y Motores Térmicos

Instituto Universtiario CMT - Motores Térmicos

DOCTORAL THESIS:

"Characterization of Fluid Structure Interaction Mechanisms and its application to the vibroacoustic phenomena"

Presented by: D. PEDRO MANUEL QUINTERO IGEÑO
Supervised by: DR. D. ANTONIO JOSÉ TORREGROSA HUGUET
DR. D. ANTONIO GIL MEGÍAS

in fulfillement of the requisites for the degree of

Doctor of Philosophy

Valencia, June 2019

PhD. Thesis

“Characterization of Fluid Structure Interaction Mechanisms and its application to the vibroacoustic phenomena”

AUTHORS

Presented by: D. PEDRO MANUEL QUINTERO IGEÑO
Supervised by: DR. D. ANTONIO JOSÉ TORREGROSA HUGUET
DR. D. ANTONIO GIL MEGÍAS

DEFENSE COMMITTEE

Chairman: DR. D. JOSÉ MARÍA DESANTES
Secretary: DR. D. PABLO FAJARDO
Member: DR. D. WIM DE ROECK

Valencia, June 2019

Characterization of Fluid Structure Interaction Mechanisms and its application to the vibroacoustic phenomena

Pedro Quintero Igeño

Abstract

Fluid Structure Interaction is a physical problem where two different materials, governed by different set of fundamental equation, are coupled on different ways.

The research on the field of Fluid Structure Interaction experienced a noticeable growth since the beginnings of the XXth century, by means of the field of aeroelasticity. During the development of the aerospace industry in the context of first and second Wolrd War, as the use of lighter (and softer) materials became mandatory for the correct behavior (and cost savings) of the produced aircrafts.

During these past years, the use of use of increasingly lighter construction materials has extended to the rest of fields of the industry. As an example, it could be mentioned the use of solar trackers on the solar energy sector; the use of light materials on civil engineering or the use of plastic for some constructive elements in the context of the automotive field. As a consequence, the accurate prediction of the deformations induced to a fluid flow over a structure and, if needed, the influence of this deformation on the fluid flow itself is becoming of primal importance.

This document intends to provide with a deep review of the computational and experimental reported methodologies already available on the literature and the previous works performed by other researches in order to infer a first approximation to the Fluid Structure Interaction Problem.

It will be observed how an important amount of solving methodologies is available in order to face these problems regarding with the strength of the interaction. However, a general approximation allowing to predict this strength as a function of a set of dimensional number is rarely known. In this sense, a full parametric study will be performed during the development of Chapter 2 showing which of them are of higher importance.

Once the influence of these parameters is determined, a case of special interest will be analyzed: aerovibroacoustics. This, is a particular case of Fluid Structure Interaction where, due to the combination of its non-dimensional parameters, one directional coupling can be supposed for most of the cases. Aerovibroacoustics and vibroacoustics will be analyzed by means of two reference cases, allowing finally to propose a methodology which could be extended for other related problems.

Resumen

La Interacción Fluido Estructura consiste en un problema físico en el que dos materiales, gobernados por conjuntos de ecuaciones distintas, se acoplan de diferentes formas.

La investigación en el campo de la Interacción Fluido Esructura experimentó un importante desarrollo desde principios del siglo XX, de la mano del campo de la aeroelasticdad. Durante el desarrollo de la industria aeroespacial en el contexto de las guerras mundiales, el uso de materiales más ligeros (y flexibles) comenzó a hacerse obligatorio para la obtención de aeronaves con un comportamiento (y costes) aceptable.

A lo largo de los últimos años, el uso de materiales de construcción cada vez más ligeros, se ha extendido al resto de campos de la industria. A modo de ejemplo, podría servir el desarrollo de *trackers* en la producción de energia solar; la utilización de materiales ligeros en ingeniería civil o el desarrollo de elementos constructivos de plástico en la industria del automóvil. Como consecuencia, la predicción con exactitud de las deformaciones inducidas por un fluido y, si aplica, la influencia de estas deformaciones en el propio flujo, ha adquirido una importancia vital.

Este documento intenta porporcionar, en primer lugar, una profunda revisión de los métodos experimentales y computacionales que se han utilizado en este contexto en la bibliografía, así como los análisis en problemas de este tipo realizados por otros investigadores de cara a presentar una primera aproximación a la Interacción Fluido Estructura.

Se verá cómo existe una importante cantidad de herramientas y metodologías aplicables a cualquier tipo de problema y para cualquier combinación de flujos y estructuras. Sin embargo, no existe una aproximación general que, en función de valores de números adimensionales, permita establecer cuáles de ellos son los de mayor importancia en este tipo de problemas. En este sentido, se llevará a cabo un completo análisis paramétrico durante el desarrollo del Capítulo 2 para establecer cuáles de ellos son de mayor importancia.

Una vez se establezca la importancia de estos parámetros, se analizará un caso que es de especial interés en la industria: la aerovibroacústica. Éste es un caso particular de Interacción Fluido Estructura en el que, debido a la combinación de parámetros adimensionales, la interacción se puede considerar como prácticamente unidireccional, permitiendo extender estudios mediante un conste computacional relativamente acotado. La Aerovibroacústica y la vibroacústica se analizarán mediante la presentación de dos casos de referencia, permitiendo proponer una metodología que se podrá extender a otros problemas similares.

Resum

La Interacció Fluid Estructura consisteix en un problema físic en què dos materials, governats per conjunts d'equacions diferents, s'acoblen de diferents formes.

La investigació en el camp de la Interacció Fluid Esructura va experimentar un important desenvolupament des de principis del segle XX, de la mà del camp de la aeroelasticdad. Durant el desenvolupament de la indústria aeroespacial en el context de les guerres mundials, l'ús de materials més lleugers (i flexibles) va començar a fer-se obligatori per a l'obtenció d'aeronaus amb un comportament (i costos) acceptable.

Al llarg dels últims anys, l'ús de materials de construcció cada vegada més lleugers, s'ha estès a la resta de camps de la indústria. A tall d'exemple, podria servir el desenvolupament de textit trackers en la producció d'energia solar; la utilització de materials lleugers en enginyeria civil, el desenvolupament d'elements constructius de plàstic a la indústria de l'automòbil. Com a conseqüència, la predicció amb exactitud de les deformacions induïdes per un fluid i, si escau, la influència d'aquestes deformacions en el propi flux, ha adquirit una importància vital.

Aquest document intenta porporcionar, en primer lloc, una profunda revisió dels mètodes experimentals i computacionals que s'han utilitzat en aquest context en la bibliografia, així com les anàlisis en problemes d'aquest tipus realitzats per altres investigadors de cara a presentar una primera aproximació a la Interacció Fluid Estructura.

Es veurà com, encara que existeix una important quantitat d'eines i metodologies aplicables a qualsevol tipus de problema i per a qualsevol combinació de fluxos i estructures, no hi ha una aproximació general que, en funció de valors de nombres adimensionals, permeti establir quins d'ells són els de major importància en aquest tipus de problemes. En aquest sentit, es durà a terme una completa anàlisi paramètric durant el desenvolupament del Capítol 2 per a establir quins d'ells són de major importància.

Un cop s'estableixi la importància d'aquests paràmetres, s'analitzarà un cas que és d'especial interès en la indústria: la aerovibroacústica. Això és un cas particular d'Interacció Fluid Estructura en què, a causa de la combinació de paràmetres adimensionals, la interacció es pot considerar com pràcticament unidireccional, permetent estendre estudis mitjançant un consti computacional relativament acotat. La Aerovibroacústica i la vibroacústica s'analitzaran mitjançant la presentació de dos casos de referència, permetent proposar una metodologia que es podrà estendre a altres problemes similars.

List of publications

The following papers form the basis of this thesis:

- Torregrosa, A., Gil, A., García-Cuevas, L.M., Quintero, P. Denia, F.D. (2018) Prediction of the transmission loss in a flexible chamber. *Journal of Fluids and Structures*, 82, 134-153 [1].
- Torregrosa, A., Gil, A., Quintero, P., Ammirati, A., Denayer, H., Desmet, W. (2019). Prediction of flow induced vibration of a flat plate located after a bluff wall mounted obstacle. *Journal of Wind Engineering and Industrial Aerodynamics*, 190, 23-39 [2].

Division of work between authors

These publications have been done in collaboration with other researchers, being the author signatures in order of seniority. The respondent performed the experimental measurements, results post-processing and developed the models presented here.

Other publications

The following is a list of other publications in which the author of this thesis has been involved during the researches leading to the present work. Although not directly present in this document, they have provided a deeper insight in the behaviour of the processes of Fluid Structure Interaction.

- Torregrosa, A., Gil, A., Quintero, P., Tiseira, A. (2019) Enhanced design methodology of a low power stall regulated wind turbine. BEMT and MRF-RANS combination and comparison with existing designs. *Journal of Wind Engineering and Industrial Aerodynamics*, 190, 230-244 [3].

Agradecimientos

Es muy difícil comenzar a escribir este apartado, debido a la cantidad de personas que, de un modo u otro han contribuido a la forma final de este documento. Al mismo tiempo, han hecho de mí una persona diferente a la que comenzó la tesis, en septiembre de 2015. Por tanto, los siguientes párrafos fueron escritos por separado para, finalmente, introducirlos aquí de forma aleatoria y evitar así dar más importancia a unos que a otros.

En primer lugar, me gustaría agradecer a los profesores José María Desantes y Francisco Payri, con los que tuve mi primera entrevista , y confiaron en mí para incorporarme a CMT. Gracias por haberme permitido empezar este camino.

Como no, ha sido importantísima la contribución de mis directores de tesis, los profesores Antonio y Tono, que me guiaron durante el proceso y, especialmente durante este último año, consiguieron evitar que divergiera mientras los artículos se encontraban *under review*.

Además de a Antonio (para no salir del despacho) agradecer muchísimo la colaboración de Pau Raga, que siempre ha estado disponible para echarme una mano en este duro mundo del CFD. Y aunque hace ya algún tiempo que está en la industria, a José Pedro, que se dejó robar incontables minutos para ayudarme, incluso en su último año de tesis.

Muchísimas gracias a los tres profesores que llevaron a cabo la evaluación externa del documento: Manuel Gallardo, Wim de Roeck y Gianluca Montenegro. Su contribución a la mejora final del documento queda fuera de toda duda.

Quiero nombrar también a todas las personas maravillosas que conocí durante mi estancia en Leuven, donde fui consciente de la aplicación práctica que se le podía dar a la Interacción Fluido Estructura. Espero dejarme los menos posibles en el tintero, pero me gustaría hacer un listado aquí: Hervé, Luigi, Simon, Viacheslav, Wim, Antonio, Luca, María...

A todos los alumnos cuyos TFG/TFM he tenido el placer de dirigir. En especial a Andrés Cremades, que se ofreció *voluntario* para hacer una primera lectura de la tesis.

Gracias también al resto de compañeros de CMT, en especial a los *aeros*: Andrés (con quien pude dar mi primera clase de teoría, en Cálculo de Aviones), Luismi (con quien siempre puedo tener una discusión, aunque sea de tonterías que el profesor de Aerodinámica II debería saber), Marcos (que me ayudó de

forma extraordinaria con las gestiones necesarias para mi estancia y he compartido algunos momentos de fútbol sala), Pedro (es imposible heredar una asignatura mejor hecha que Aerodinámica II) y Roberto (el infiltrado, con el que también he tenido conversaciones sobre turbulencia y sobre cómo tratar de superar la falta de conocimiento en algunos campos).

A mis amigos, que me acogieron cuando llegué desde el principio, a pesar de lo asocial que puedo ser a veces: Marcos, Morales, Mario(x2), Laura, Julia, Patri, Héctor, Chamaco, Sarah, Pablo. Gracias a todos.

Esto se está alargando más de lo que tenía previsto. No obstante, esta tesis no habría sido posible sin el apoyo de mi tía Toñi y mi prima Araceli, que me han soportado durante estos años (queda lejos ya 2009, cuando me instalé en Massamagrell) y han sido una ayuda vital cuando el mundo se me ha venido encima.

A mis padres y mi hermana. Incluso a 700 km me han apoyado en todo momento, tanto con las decisiones más acertadas que he tomado (ir a Valencia a cursar Ingeniería Aeronáutica, el año que pasé en Albacete y la vuelta a la universidad) como con las que han tenido peores consecuencias. No obstante, todas estas decisiones me han llevado a ser quien soy y volvería a tomar cada una de ellas, por lo que me han aportado y por los buenos momentos que me han brindado.

Me gustaría, por último, recordar a Ismael Gómez, mi primer jefe, que siempre estuvo dispuesto a ayudarme y me brindó la oportunidad de trabajar con él (a pesar de que sabía que terminaría huyendo a la Universidad) y con otra gente maravillosa: Cristina, Fidel, Emilio...

Ha sido un camino extraordinariamente duro, con momentos de inseguridad, ansiedad y miedo cuando los resultados no acompañaban. No obstante, espero que haya dado sus frutos y que este documento pueda servir de ayuda si esta investigación continúa sus andaduras.

Gracias

Contents

List of Figures

List of Tables

CHAPTER 1

Introduction

Contents

Figures

1.1 Introduction

Due to the use of increasingly lighter materials, the interaction between structures and the fluid flow around or inside them is becoming of crucial importance. Moreover, due to the increase of available computational power, the prediction of the phenomena related to Fluid Structure Interaction is becoming an important research topic in numerous engineering application, such as in micro aerial vehicles, transport of fluids in elastic structures, energy harvesting devices, biomedical engineering or bio-inspired systems.

Regarding with the aim and features of the system under study, the problems of Fluid Structure can be classified in four main groups. Note that in some cases the classification of a problem in one group or other can be somehow arbitrary, as sketched on Figure 1.1:

- Vortex Induced Vibrations: In VIV, a fluid flow around a solid object produces a vortex shedding of very defined frequency. As a consequence, this solid body will start vibrating at a similar frequency than this shedding. When the stiffness of the structure is low, both the fluid and the solid fields are dominated by coupling phenomena. Due to the resulting sinusoidal excitation these kind of problems are normally related with fatigue-related failure [4] and/or the emission of tonal noise [5].

- Flow Induced Vibrations: In FIV, a fully turbulent fluid flow produces a non-stationary load whose Fourier transform has important components at a wide range of frequencies. As a result, the structure vibrates in a wide range of frequency with defined peaks on the structural resonances [6]. These vibrations could lead to sound emission in broadband [7].

- Aeroelasticity: Typically, the role of Aeroelasticity is to find the coupled response between a stationary airflow and a structure. One of the main targets of this field is to find zones of FSI unstability which, eventually, could lead to a catastrophic abrupt failure of the structural system. Some of the phenomena aeroelasticity deals with are the appereance of divergence, flutter, buffeting or control reversal phenomena [8]. The main difference which could be found between VIV and Aeroelasticity is that, for the latter, the flow does not have to necessarily be unsteady in order to induce coupling.

- Other important field of investigation on FSI could be identified, as those investigating the effects of fluid flow inside flexible pipes. One important example could be the phenomenon known as water hammer, where an

abrupt change of the conditions of the inner fluid can lead to the appearance of a deformation wave which can lead to the destruction of the pipe system [9].

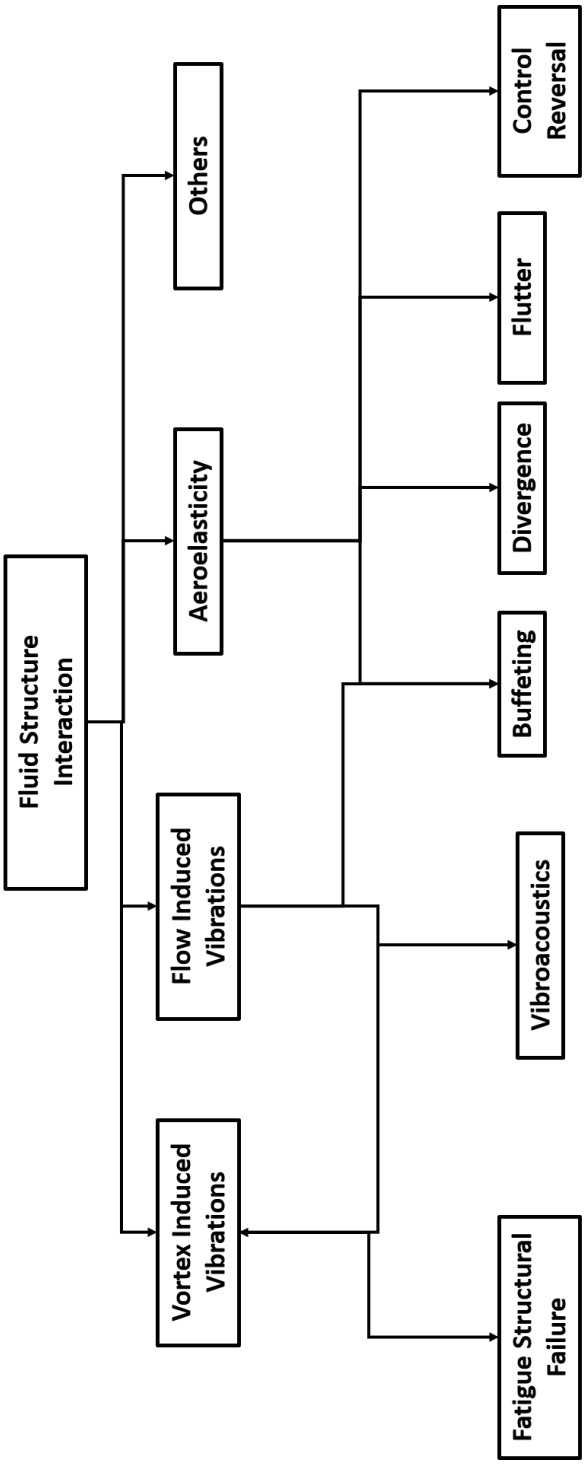

Figure 1.1: Proposal of a classification of the different problems of fluid structure interaction regarding with the research field and applicability

1.2 Motivation and Objectives

As it has been explained, nowadays, FSI is playing a major role. In consequence, it is crucial to understand the phenomenology and problems associated with this kind of problems. As it will be explained later, the methodologies to characterize particular problems of FSI have spectacularly evolved during the past years, both experimental (measurements on Wind Tunnel, Particle Image Velocimetry, Laser Scanner Vibrometry, Digital Image Correlation....) and computational techniques (RANS, URANS, LES, DES, DNS...). Therefore, with the current tools, almost any kind of problem can be faced (being the grade of simplifications only a matter of the available computational resources or the experimental facilities).

However, and probably due to the interdisciplinary characteristics of this field, the problem itself has not been so deeply studied as fluid dynamics or solid structures. Some dimensional analysis have been nevertheless performed in the literature, leading to the conclusion that, besides the usual non-dimensional numbers used at fluid dynamics, the behavior of the problem depends strongly of a non dimensional stiffness parameter, $E/\rho_\infty V_\infty^2$, which can be identified as a form of the Cauchy number applied to FSI problems, and the relative densities between the solid and the fluid, ρ_s/ρ_∞.

In accordance with the knowledge of the author, however, there exist a lack of information on how these numbers can in fact affect the behavior of the coupled system. Although on some case this can be somehow obvious or intuitive (for instance, it can be expected that a low velocity flow around a steel plate of 5mm thickness will not be affected by the own vibrations of the plate) in other cases will not be so.

In fact, it will be of primal interest being able to predict the order of magnitude of the variables at which the bidirectional coupling between solid and fluid arises and quantify its importance in order to select the most proper tools to characterize it.

Therefore, the main aim of the Thesis is performing a recompilation of the most important existing tools in order to model or measure FSI problems and, once it is done, propose a non dimensional methodology in order to have a easy to use guide to predict which kind of coupling is expected and which tool can be used as a first approximation for any kind of problem.

1.3 Structure of the work

In order to achieve the stated objectives, the next structure has been followed:

In Chapter 2 a bibliographic review is preformed. Here, the different existing methods allowing to properly model both the fluid dynamic and solid structures will be explored. Additionally, it will be seen how they can be supposed to be coupled by means of their boundary conditions. The available numerical and experimental methods will also be discussed, and the range of application of each one.

Next, in Chapter 3, a systematic study of how the FSI parameters affect to the interaction itself is explored. Here, a swept of both the non dimensional stiffness and mass will be performed for a simplified case of Vortex Induced Vibrations. Thanks to this, the main zones of coupling will be identified and it will be seen how, regarding with the combination of non dimensional stiffness and masses, the most proper numerical methodology can be chosen for the computation of the problem.

Once this non-dimensional analysis has been performed, Chapter 4 will be proposed as a validation of this study for the computation of some engineering vibroacoustic and aerovibroacosutic problems. First, it will be shown how Chapter 3 developed methodology will allow to have an order of magnitude of the beginning of two way FSI on the transmission of pressure wave inside a flexible silencer and, later it will be observed how the dimensional analysis allows to suppose one way coupling on the simulation of the flow induced vibrations on the simplified underbody of a car

Finally, at Chapter 5, the main conclusions of the current work will be exposed, as well as the indication of possible future lines of investigation in order to improve the capabilities of the presented tools for modeling Fluid Structure Interaction.

1.4 References

[4] G. Barrholm, C. Larsen, and H. Lie. “On fatigue damage accumulation from in-line and cross-flow vortex-induced vibrations on risers”. In: *Journal of Fluids and Structures* 22 (2006), pp. 109–127 (cit. on p. 2).

[5] W. Blaje. *Mechanics of flow-induced sound and vibration, Volume 2*. Ed. by A. press. 2017 (cit. on pp. 2, 38).

[6] M. Pettigrew, C. Taylor, N. Fisher, M. Yetisir, and B. Smith. “Flow-induced vibration: recent findings and open questions”. In: *Nuclear Engineering and Desing* 185 (1998), pp. 249–276 (cit. on p. 2).

[7] Y. Chen. “Flow-induced vibration and noise in tube-bank heat exchangers due to von Karman streets”. In: *Journal of Engineering for Industry* 90 (1968), pp. 134–146 (cit. on p. 2).

[8] H. Dowell E.H. adn Curtiss, R. Schalan, and F. Sisto. *A modern course in aeroelsaticity*. Ed. by T. N. K. a. p. Dordrecht. 1989 (cit. on p. 2).

[9] M. Guidaoui, M. Zhao, D. McInnis, and F. Axworthy. “A review of water hammer theory and practice”. In: *Applied Mechanics Reviews* 58 (2005), pp. 49–76 (cit. on p. 3).

CHAPTER 2

Fundamentals of the Fluid Structure Interaction

Contents

Figures

2.1 Introduction

A moving fluid passing through a structure generates a pressure and shear stress distribution around it that, when the material is sufficiently flexible, can give rise to the appearance of noticeable displacements. As a consequence, these displacement could affect the fluid flow itself, giving rise to a coupled system whose features can be of importance when characterizing an engineering system.

Fluid-structure interaction (FSI) is an interdisciplinary subject of interest to many researchers in the fluid dynamics field. FSI exists in its various forms in both natural systems and man-made objects. The interaction between a tree and wind and groundwater interaction with the soil are typical examples of FSI in nature. FSI for engineered systems occurs in modeling behavior of offshore platforms with the ocean, flights characteristics of aircraft, or the displacement field of dams with reservoirs. Although the nature and the interaction between the solid and fluid within these problems are different, all these problems come under the category of FSI. It is also important to note that the degree of severity in interaction between the solid and fluid varies between different problems. While many cases involve solid deformation as an integral part, there are many situations in which the solid may be considered to move as a rigid body. It is also possible to have one-directional coupling between the fluid and solid under certain circumstances.

Classification in accordance with the nature of the fluid domain

The subject may be divided into two categories, based on the flow physics, as (a) **gas** and (b) **liquid** interaction with solid. While incompressible flow assumption is always made for liquid-solid interaction, both compressible and incompressible flow assumptions are made when a gas interacts with a solid. When the Mach number of the flow is under Ma = 0.30, an incompressible flow assumption is justified for gas-solid interaction. The main application of air-solid interaction is the determination of aerodynamic forces on structures such as aircraft wings. Such study is often referred to as aeroelasticity. Static aeroelasticity involves the study of the interaction between aerodynamic and elastic forces, while dynamic aeroelasticity is the topic that normally investigates the interaction between aerodynamic, elastic and inertial forces. Aerodynamic flutter or aerodynamic divergence are two of the severe consequences of dynamic aerodynamic forces and responsible for destructive effects in aircraft and other structures.

Classification in accordance with the nature of the solid domain

The subject may also be classified based on the nature of the structure interacting with a fluid as (a) **rigid body** and (b) **deforming body** interaction with the fluid. Examples where rigid body interaction may often be used include internal combustion engines, gas and water turbines, ships and offshore platforms. Although the rigid body-fluid interaction problem is simpler to some extent, the dynamics of rigid body motion requires a solution that reflects the fluid forces. Examples of deforming body-fluid interaction include aeroelasticity, a majority of biomedical applications and poroelasticity. Both the rigid body and deforming body interaction with a fluid is often strongly coupled, influencing both fluid and solid forces. Within the deformable body-fluid interaction the nature of the deforming body may vary from very simple linear elastic models in small strain to highly complex nonlinear deformations of inelastic materials. The solid material may also be compressible or nearly incompressible in nature.

Classification in accordance with the numerical tools

In addition to the classification based on the physical nature of the problems, the fluid-structure interaction may also be classified based on the solution procedure employed. These classifications include (a) a **monolithic approach** in which both fluid and solid are treated as one unified system and (b) a **partitioned approach** in which the fluid and solid are treated as two different systems coupled through the interface. A partitioned approach is often preferred in practical engineering applications as this method allows the use of independently developed and tested solvers for fluid and solid. Within the partitioned approach, the coupling between the the fluid and solid may be carried out using a strongly or weakly coupled approach. Although the weakly coupled approach is used in aerodynamic applications, it is seldom used in other areas due to instability issues. Thus, a strongly coupled approach is the one that is preferred by most researches. This obviously leads to various issues of coupling procedures at the interface between the fluid and solid.

Due to the emergence of immersed boundary methods in the last two decades, a further classification based on immersed boundary methods or non-conforming mesh methods may also be used. In an immersed boundary method the structure is assumed to be immersed into the fluid and the forces are transferred between the fluid and solid boundaries. Since only interface forces require transferring, the need for conforming meshes is eliminated in such methods. These methods are useful in complex problems of fluid-structure interaction in which complex mesh regeneration may be difficult to carry out.

Depending on the importance of these displacements and their velocities, the own fluid flow could be affected leading to a physical coupling between the solid and fluid domain and making thus necessary to include the whole system in the analysis in order to obtain a physically meaningful interpretation.

Traditionally, the aircraft industry has been one of the fields leading the investigation on Fluid-Structure Interactions. This is because, in this field, since its early beginning, it has been important using the lightest possible materials. Therefore, the correct prediction of elastic deformation allows predicting which flight conditions will not jeopardize the aircraft [10]. It is generally believed that the catastrophe of Langley's flight in 1903 was caused by an aeroelastic instability, as suggested by Hill [11]. As a result, important aeroelasticity scientific references can be found since the beginning of the XXth century [12].

It can be stated that Fluid-Structure Interactions can be usually visualized as forming a triangle of disciplines: dynamics (which studies the inertial motion of complex bodies and structures under a combination of loads), solid mechanics (which takes into consideration how a structure can be deformed by the action of a loads) and fluid dynamics (which allows to characterize the pressure and shear stress distribution generated by a fluid field around a solid body). The interdisciplinary nature of FSI can be better illustrated by Figure 2.1 ,which is traditionally called as the Collar's triangle and was proposed by Professor A.R. Collar in the 40s [13].

One of the main targets of this chapter is to introduce to the FSI problem through a brief description of the fields sketched in Figure 2.1 and the physical causes which can lead to the multiphysics problem. Section 2.2 and will introduce the physical laws which governs the behavior of the fluid and solid domains and how each of them can be separately analyzed and characterized both by computational or experimental tools.

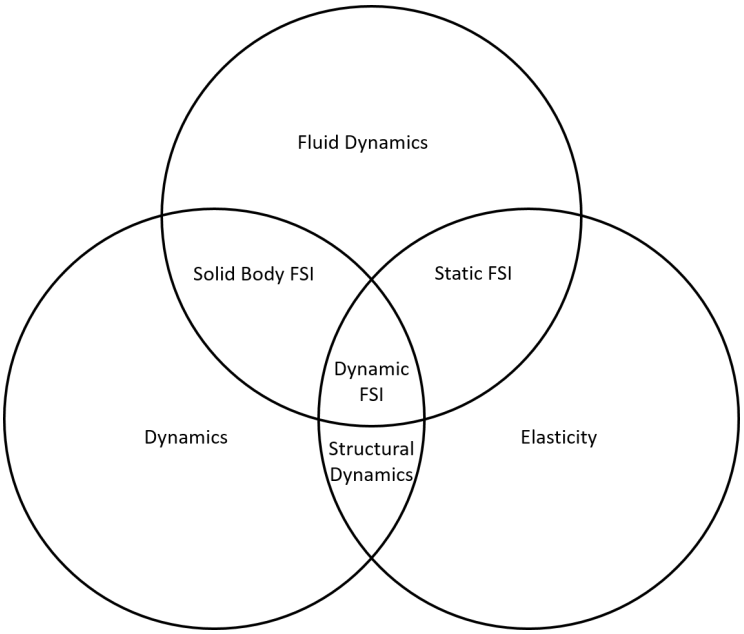

Figure 2.1: Schematic of the field of Fluid-Structure Interaction

Later, in Section 2.3, an analysis of the origin of the coupling between the solid and the fluid domains is carried out, concluding how it arises by the own definition of the boundary conditions. Some considerations of possible strategies to numerically resolve the interaction will be sketched. This will lead to a classification of the different FSI problems solved in the literature regarding with the coupling strength and the most useful tools for their modeling.

In Section 2.5 it will be concluded how, although there exist affordable methodologies to resolve most of the engineering FSI possible problems, they differ in their computational cost by orders of magnitude. Nowadays, the selection of one of the available methodologies is adopted based on the previous experience of the simulation engineer, as the dimensional analysis of the interaction has not been fully explored by previous work.

Therefore, Chapter 3 is dedicated to contribute to the fulfillment of this gap and a proposal of non-dimensional analysis is proposed in order to infer the strength of FSI for the case of a low Reynolds Vortex Induced Vibrations case.

2.2 Numerical Tools

2.2.1 Equations of the fluid flow

When dealing with the resolution of a single phase compressible flow, the Equations governing the flow field can be written, in their conservative form, as [14]:

$$\begin{cases} \dfrac{\partial \rho}{\partial t} + \dfrac{\partial \rho \mathrm{v}_i}{\partial x_i} = 0 \\ \dfrac{\partial \mathrm{v}_i}{\partial t} + \mathrm{v}_j \dfrac{\partial \mathrm{v}_i}{\partial x_j} = -\dfrac{1}{\rho}\dfrac{\partial p}{\partial x_i} + \dfrac{\partial}{\partial x_j}\left(\tau_{ij}\right) + f_i \\ \dfrac{\partial}{\partial t}\left[\rho\left(e + \dfrac{1}{2}\mathrm{v}_i\mathrm{v}_i\right)\right] + \dfrac{\partial}{\partial x_j}\left[\rho\left(e + \dfrac{1}{2}\mathrm{v}_i\mathrm{v}_i\right)\mathrm{v}_j\right] = \dfrac{\partial}{\partial x_j}\left(-p\mathrm{v}_j + \tau_{ji}\mathrm{v}_i + \mathrm{k}\dfrac{\partial}{\partial x_i}T\right) + \rho f_i \mathrm{v}_i + Q \\ e = e(T,p) \quad \rho = \rho(T,p) \end{cases} \tag{2.1}$$

These equations are the equation of mass continuity; the Navier Stokes equations and the energy equation. Their closure can be achieved by using a state equation. Here, the variables which completely identify the fluid flow behaviour can be found to be: ρ is the local fluid density; v_i is the i^{th} component of the velocity vector, $\vec{\mathrm{v}}$; p is the local fluid pressure and τ_{ij} is the ij^{th} component of the stress tensor, τ, which, for the case of a Newtonian flow can be expressed in accordance with Equation 2.2. f_i is the i^{th} component of the mass forces vector, $\vec{f}$; e is defined as the flow local internal energy; k is the thermal conductivity; T is the temperature and Q is the source term of energy, which would allow to model phenomena as chemical reactions and/or heat radiation.

$$\tau_{ij} = \mu\left(\frac{\partial \mathrm{v_i}}{\partial x_j} + \frac{\partial \mathrm{v}_j}{\partial x_i}\right) + \left(\mu_v - \frac{2}{3}\mu\right)\frac{\partial \mathrm{v}_k}{\partial x_k}\delta_{ij} \tag{2.2}$$

where μ is the kinematic viscosity and δ_{ij} is the Kronecker delta. This set of equations can be discretized and resolved by numerical methods, as the finite volume method [15],[16],[17], [18], the finite element method [19], [20], or the finite differences method [21], [22], among others. Other way to resolve the fluid domain which is being used recently are the Lattice Boltzmann Methods, which is a mathematical artifice which emulates the physics of Navier Stokes equations [23], [24]. It is based on the kinetic theory formulation, which relates the molecule motion with the macroscopic properties of the fluid [25]. During the development of the current document, unless explicitly mentioned, the

finite volume method will be the preferred discretization when dealing with the resolution of viscous flows.

Turbulence Modeling

The previous set of equations completely describe any kind of fluid flow and, for cases of low value of the Reynolds number, lying in the laminar range, their resolution can be achieved numerically with relatively low computational cost. However, as the Reynolds number increases the fluid flow becomes irregular, unsteady and chaotic. Moreover, the scale of the turbulent structures becomes smaller, leading to the necessity of meshes of lower size in order to capture them. This affirmation can be reinforced by the observation of Equation 2.3 [14], which relates the Kolmogorov length, η, (the smallest size of the turbulent structures) with a reference length, L_{ref} and the Reynolds number, Re. Note the fast decrease of η with Re.

$$\frac{\eta}{L_{ref}} \sim \mathrm{Re}^{-3/4} \tag{2.3}$$

Even with the increase of the available computational power which has been experienced during the past decades, the direct resolution of the equations (*DNS, Direct Numerical Simulation*) is not computationally achievable for engineering turbulent flows in industrial time scales. Some interesting works with DNS can be found in the literature as, for example Das et al. [26], Hutl et al. [27] or Friedrich et al. [28], who used DNS to characterize the fluid flow on cases of simple geometries for incompressible flows.

In order to achieve a computationally affordable resolution of the fluid flow, some extra assumptions are introduced on the formulation of the fluid flow equations. Regarding with these assumptions three main methodologies are usually used to simplify the equations, namely (a) Reynolds Averaged Navier Stokes (RANS), (b) Large Eddy Simulation (LES) and (c) Detached Eddy Simulation (DES).

- **RANS methodology**: These methods are based on the Reynolds time average: being ϕ a characteristic variable of the Navier-Stokes equation, it is decomposed in a mean value, $\langle\phi\rangle$, and a deviation, ϕ'. When those assumptions are substituted at the conservation equations, it can be observed how an unknown term based on the deviation of the velocity field arises, $\langle-\rho u_i' u_j'\rangle$, which is known as the Reynolds stress tensor. This term makes the averaged system of equations to be unclosed, and, as a

consequence, the Reynolds stress must be modeled in order to solve them. Most of the alternatives to model this stresses are based on the Boussineq Hypothesis [18], which relates them with a turbulent viscosity, μ_t and the turbulent kinetic energy, k.

Different developed models worth to be mentioned at this stage. For instance the *Spalart-Allmaras* solves and additional transport equation for the turbulent kinetic energy, k, in order to obtain the turbulent viscosity [29]; $k-\varepsilon$ model uses another additional equation in order to solve the transport of the turbulent dissipation rate, ε [30] while the $k-\omega$ solves the specific dissipation rate, ω, instead [31]. $k-\omega$ SST acts as an intermediate model between $k-\varepsilon$ and $k-\omega$ [32]. There are other models which establish an extra transport equation for each component of the Reynolds stress tensor. They are the so called Reynolds Stress Models (RSM), but, currently, they are not so widely used due to the comparatively higher computational expense in comparison with the previous ones [33], [34].

- **LES methodology**: LES is an inherently transient technique in which the large scales of the turbulence are directly resolved everywhere in the flow domain, and the small-scale motions are modeled. One justification for the LES technique is that by modeling "less" of the turbulence, and explicitly resolving for more of it, the error in the modeling assumptions is not as consequential. Furthermore, it is hypothesized that the smaller eddies are self-similar and, thus, lend themselves to simpler and more universal models. The downside of the approach is that the computational expense is higher by orders of magnitude than the RANS methodology when the Reynolds number is high. LES equations are derived from Navier Stokes equations by applying a spatial filter. Then, each solution variable, ϕ, is decomposed into a filtered value $\hat{\phi}$ and a subgrid value, ϕ'. When applyting this methodology to the fluid flow equations, similarly as occurred with RANS, a new unknown stress tensor term arises from the effect of the unfiltered values. Normally, in order to resolve this term the Bousineq Hypothesis is again used. The simplest developed model for the subgrid viscosity is the Smagorinski subgrid scale model, which provides a mixing length type formula for this parameter [35]. However it contains certain limitations, especially for the flow near the walls, as the model constant is not completely universal (which would lead to a necessity of DNS resolution at these zones). Other models have been developed which allows to avoid this problem. As an example, it could be mentioned the Dynamic Smagorinsky Subgrid Scale Model [36], [37] or the Wall-Adapting Local-Eddy Viscosity (WALE) Subgrid Scale Model [38].

- **DES methodology**: Detached Eddy Simulation is a hybrid modeling approach that combines features of RANS simulation in some parts of the flow and LES in others. The unsteady RANS equations are applicable to transient situations where the unsteadiness is either imposed, such as by a time-varying boundary condition, or is inherent, such as the vortex shedding in a massively separated flow. In the latter case, transient simulation often yield better results than attempting to use a steady-state approach. However, successful unsteady RANS simulations requires the time scales of the turbulence to be disparate from the mean-flow unsteadiness. Furthermore, the limitations of the turbulence model may preclude good unsteady results. In this context, DES turbulence models are set up so that boundary layers and irrotational flow regions are solved using a base unsteady RANS closure model. However, the turbulence model is intrinsically modified so that, if the grid is fine engough, it will emulate a basic LES subgrid scale model in detached flow regions [39]. Then, DES model can be combined with any of the previously mentioned RANS models. Regarding with how the transition between the RANS and LES zone is made, multiple variants of the scheme can be found, as the Delayed Detached Eddy Simulation (DDES) [40] and the Improved Delayed Detached Eddy Simulation (IDDES) [41].

2.2.2 Equations of the deformable solid

Making use of the equations of mass and momentum conservation, Equation 2.4 for the displacement field of a deformable solid body can be derived [42]:

$$\rho \frac{\partial^2}{\partial t^2} u_i = \frac{\partial}{\partial x_j} \sigma_{ij} + b_i \tag{2.4}$$

Here, ρ represents the density of the solid body; u_i represents the displacement of the solid body along the i direction; b_i is the i^{th} component of any volume forces present and σ_{ij} are the components of the stress tensor, which can be related to the strain tensor, $\varepsilon_{kl} = \frac{1}{2}\left(\frac{\partial u_k}{\partial x_l} + \frac{\partial u_l}{\partial x_k}\right)$, by means of Equation 2.5:

$$\sigma_{ij} = c_{ijkl} \varepsilon_{kl} \tag{2.5}$$

where c_{ijkl} are constants which allows to express the relationship between the strain and stresses for any kind of load condition. However, it is usual to suppose that, when the solid is istropic and the stress is low enough, the

relationship expressed by Equation 2.5 can be further developed and the value of the constants can be expressed as in accordance with Equation 2.6 [43]:

$$\begin{aligned} c_{iiii} = \alpha = E \cdot \frac{\nu - 1}{2(\nu+1)\left(\nu - \frac{1}{2}\right)} \\ c_{iijj} = c_{jjii} = \beta = -E \cdot \frac{\nu}{2(\nu+1)\left(\nu - \frac{1}{2}\right)} \\ c_{ijij} = c_{jiji} = \chi = E \cdot \frac{1}{2(\nu+1)} \end{aligned} \tag{2.6}$$

where E is the solid body Young's modulus and ν is the Poisson's ratio. Note how, once these relationships have been established, Equation 2.4 can be expressed in vectorial form as a function of only the displacement field:

$$\frac{\partial^2}{\partial t^2} \begin{Bmatrix} u_x \\ u_y \\ u_z \end{Bmatrix} = [Q] \begin{Bmatrix} u_x \\ u_y \\ u_z \end{Bmatrix} \tag{2.7}$$

here, Q is a differential operator that, for the case of an isotropic linear elastic solid, can be calculated by using Equation 2.8:

$$[Q] = \begin{bmatrix} \alpha \frac{\partial^2}{\partial x^2} + \frac{\chi}{2}\left(\frac{\partial^2}{\partial y^2} + \frac{\partial^2}{\partial z^2}\right) & \left(\beta + \frac{\chi}{2}\right)\frac{\partial^2}{\partial x \partial y} & \left(\beta + \frac{\chi}{2}\right)\frac{\partial^2}{\partial x \partial z} \\ \left(\beta + \frac{\chi}{2}\right)\frac{\partial^2}{\partial x \partial y} & \alpha \frac{\partial^2}{\partial y^2} + \frac{\chi}{2}\left(\frac{\partial^2}{\partial x^2} + \frac{\partial^2}{\partial z^2}\right) & \left(\beta + \frac{\chi}{2}\right)\frac{\partial^2}{\partial y \partial z} \\ \left(\beta + \frac{\chi}{2}\right)\frac{\partial^2}{\partial x \partial z} & \left(\beta + \frac{\chi}{2}\right)\frac{\partial^2}{\partial y \partial z} & \alpha \frac{\partial^2}{\partial z^2} + \frac{\chi}{2}\left(\frac{\partial^2}{\partial x^2} + \frac{\partial^2}{\partial y^2}\right) \end{bmatrix} \tag{2.8}$$

2.2.3 Coupling of the Fluid and Structural Domains

Once the governing equations of both the fluid and solid domain have been presented, it is possible to introduce how they can be coupled in order to resolve the Fluid Structure Interaction problem. As an example, Figure 2.2 shows a sketch of an arbitrary fluid structure interaction case. Here, Ω_{fluid} represents the fluid domain, where the set of Equations 2.1 applies and Ω_{solid} is the solid domain, governed by the set of Equations 2.4. Three different types of surfaces can be identified in the system. Different sets of boundary conditions will be applied in order to obtain the solution of the coupled system:

- Γ_{fluid} is a surface in contact only with the fluid flow, where the usual boundary conditions of Navier-Stokes equations can be applied.
- Γ_{solid} is a surface where the displacement field of the solid domain is known by means of a prescribed displacement (displacement boundary condition) or by its derivatives (solid stress boundary condition).
- Γ_{FSI} is a surface where the fluid domain and the solid domain are in direct contact, here both the boundary conditions of the fluid flow and the solid domain must be applied simultaneously, as will be later explained, and is the region where the coupling between domains arises.

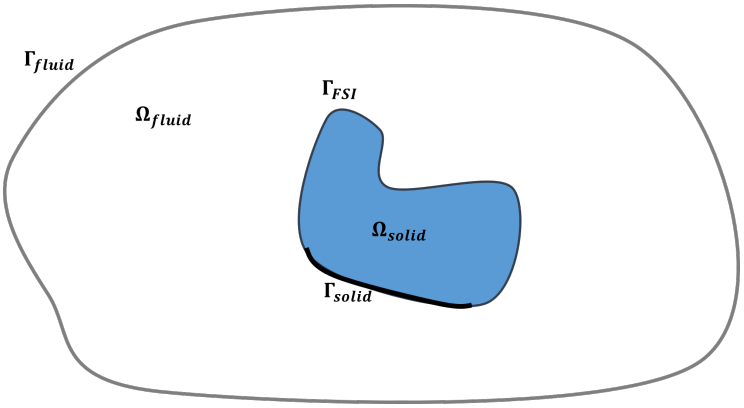

Figure 2.2: Sketch of a general problem of Fluid Structure Interaction. Identification of the surfaces where boundary conditions can be applied separately for fluid and solid Γ_{fluid}, Γ_{solid} and the surface of contact Γ_{FSI}

At the surface Γ_{FSI} the movement of the solid body leads to the appearance of a wall velocity. In this region the non-slip boundary of condition states that

the velocity of a point of the wall at the solid domain must be the same than the velocity of the same point at the fluid domain (for inviscid flows this condition is transformed and only the wall normal velocity should be computed), as sketched by Equation 2.9:

$$v_i = \frac{\partial u_i}{\partial t} \quad \text{on} \quad \Gamma_{FSI} \tag{2.9}$$

In the same way, at the solid part of the interface, some boundary conditions should be applied on the derivatives of the displacement field. If the structure was located in void, or in a fluid in rest, it is well known that the value of the stresses at the interface must be zero in order to ensure the equilibrium of the surface. When dealing with a Fluid-Structure coupled problem, this condition must be changed, as the fluid is know applying both normal and shear stresses at the wall and hence, in order to ensure stress continuity, they should be the same of the solid stresses at the solid part. This is stated by Equation 2.10:

$$p\delta_{ij}n_j + \tau_{ij}n_j = c_{ijkl}\frac{1}{2}\left(\frac{\partial u_k}{\partial x_l} + \frac{\partial u_l}{\partial x_k}\right) \tag{2.10}$$

This equation implies that the fluid pressure and shear stress (mainly the first, normally) will act as a load over the solid system. This load will produce the appearance of a displacement field which, in fact, will affect the fluid domain through the non-slip boundary condition (Equation 2.9).

2.3 Coupling Methodologies

During the past years, an important amount of effort has been focused on the development of numerical methodologies allowing to compute the coupling between a solid and a fluid domains. In this section these methodologies will be analyzed in depth and some important applications taken from the literature will be explored. These methodologies are summarized below:

- **Monolithic methods**: in these methods only one solver is used in order to resolve the interaction. It is a very stable methodology which allows to use large values of the time step minimizing the numerical instabilities. The drawback of this method is that it needs the development of *ad hoc* software and it is characterized by a need of high computational requirements, both in the amount of required RAM memory and the elapsed time by iteration.
- **Segregated methods**: In these methods, already defined solvers are used separately for the solid and fluid domains. They can be splited as follows:
  - **Explicit coupling**: The coupling between solid and fluid domains is performed in only one inner iteration. As a consequence, the residuals at the interface can be high which, eventually, can be a cause of numerical instabilities. When the fluid and structure are tightly coupled and the density of both materials is similar, the needed time step must be very small in order to ensure that the numerical scheme is stable. A typical application of this kind of methodology is the prediction of the aerodynamic pre and flutter characteristics, as can be observed at Figure 2.3 where the velocity and displacement fields are shown at four arbitrary time steps for the case of the pre stall flutter of a medium aspect ratio flat plate.
  - **Implicit coupling**: The coupling between solid and fluid domains is performed by means of using inner iterations. As a consequence, the residuals at the interface can be minimized and it is a methodology which ensures stability with large time steps. A typical application of this kind of methodology is the prediction of the aerodynamic flutter and post flutter characteristics, as can be observed at Figure 2.4 where the velocity and displacement fields are shown at four arbitrary time steps for the case of the post stall flutter of a medium aspect ratio flat plate.
  - **One way coupling**: This is the simplest approach. It is supposed that only one of the domains affect the others and viceversa. De-

spite its simplicity, as it will be later explained, this method allows to obtain accurate solutions for a wide range of engineering applications, specially with those related with flow induced vibrations and vibroacoustics. Moreover, as fluid flow and structure are only coupled in one direction, resolving the fluid flow one time allows obtaining the structural results for a wide range of materials and/or solid geometries.

During the next pages, a more detailed description of these methods is provided, at the same time that interesting research applications of each of them are referred.

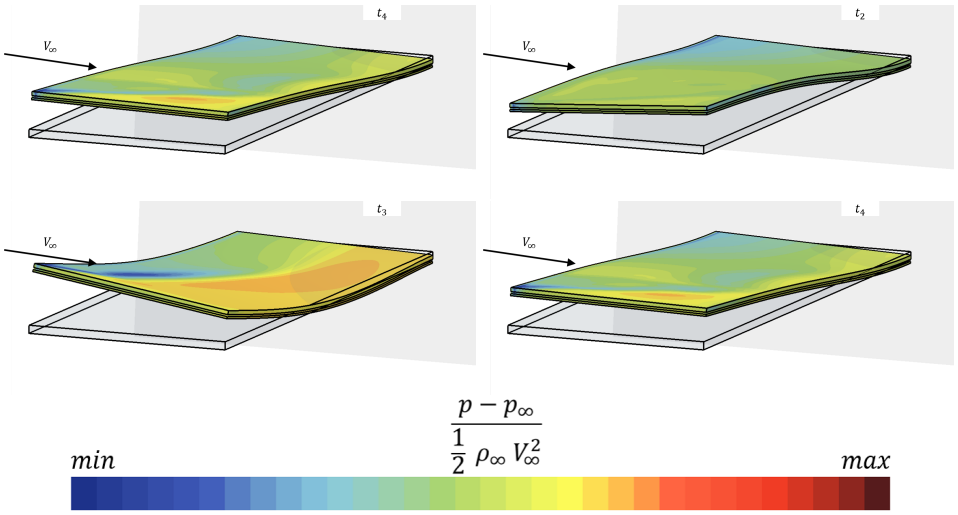

Figure 2.3: Example of application of an explicit segregated approach. Pressure field over the deformed structure of a coupled system consisting of air flow around a clamped 3D flat plate of aspect ratio, $AR = 4.4$ and chord, $c = 0.10$m. The plate is subjected to a fluid flow with velocity $V_\infty = 20\text{m s}^{-1}$, which correspond to pre stall flutter conditions

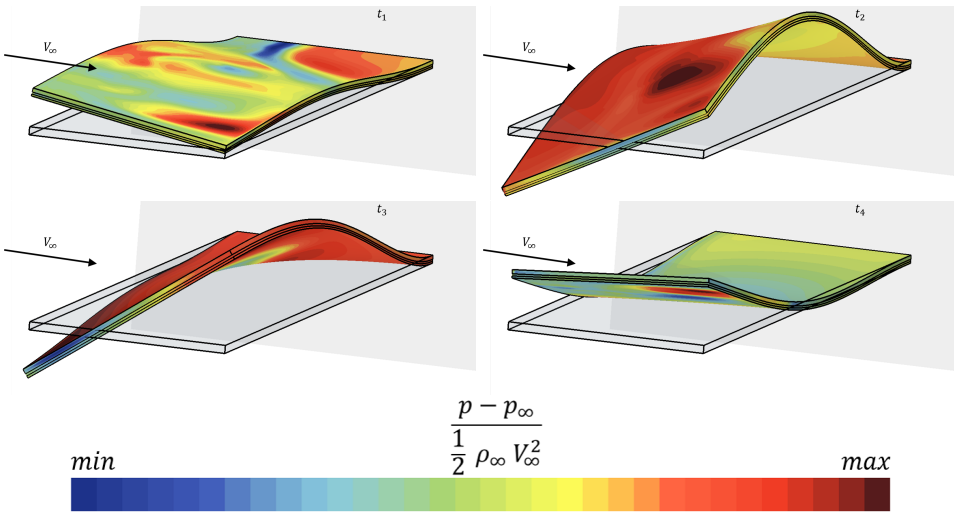

Figure 2.4: Example of application of an implicit segregated approach. Pressure field over the deformed structure of a coupled system consisting of air flow around a clamped 3D flat plate of aspect ratio, $AR = 4.4$, and chord, $c = 0.10$m. The plate is subjected to a fluid flow with velocity $V_\infty = 25\text{m s}^{-1}$, which correspond to post stall flutter conditions

2.3.1 Monotithic Approach

When the structural and fluid flow are discretized with similar techniques, it will always be possible to find a system of equations which allows to simultaneously solve for both fields for each time step. In particular, the whole complex interaction problem can be summarized by the equation:

$$\vec{R}(\vec{W}) = \vec{0} \tag{2.11}$$

where $\vec{W} \in \mathbb{R}^N$, being N the number of unknowns. It is therefore possible to solve previous equation by implementing a Newton-Raphson method, as sketched in Figure 2.5. In accordance with the work of Michler et al. [44] or Brummelen et al. [45], using a monolithic scheme, maintenance of the conservation properties at the interface is possible, which guarantees unconditional stability. Thus, with this approach, the admissible time-step size appears to be limited only by the required accuracy, and stability conditions are achieved for higher values of time-step than those used by a similar segregated solver. The robustness of the monolithic approach comes with the expense of more computationally demanding algebraic systems to be solved ([46],[47]) and cannot take advantage of software modularity to the same extent as segregated solvers.

The alleged increase of computational cost of the monolithic approach against the segregated one [48] is generally attributed to the fact that in a segregated scheme smaller and better conditioned subsystems are solved instead of one overall problem [49]. It is also believed to be "difficult to devise efficient global preconditioners and to maintain state-of-the-art schemes in each solver" [50] when a monolithic solver is used.

However, and due to its robustness, the monolithic approach is often used as the optimum tool for the resolution of very tight coupled fluid-solid systems, although it is normally unsuited for large-scale problems.

This approach has been extensively used on application of fluid flow around biological systems. For example, see the works of Takizawa et al. [51], where the coupling between fluid flow and insects wings is computationally studied. Hwang et al. [52] developed a monolithic code of FSI and tested its capabilities with very tight coupled systems, as the deformation of a rubber gate. Their results are shown as an example at Figure 2.6.

This same approach is usually adopted when studying the blood fluid flow inside veins under conditions of aneurythms or aortic stenosis, as can be observed from the works of Loon [53], Wu et al. [54] or Leng et al. [55].

Nevertheless, for lower coupling levels this strategy is marginally used.

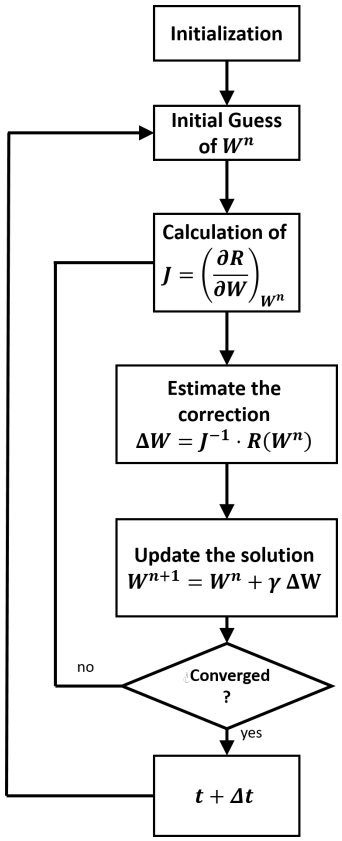

Figure 2.5: Schematic of the Newton Raphson algorithm applied to a Monolitic approach of a FSI problem

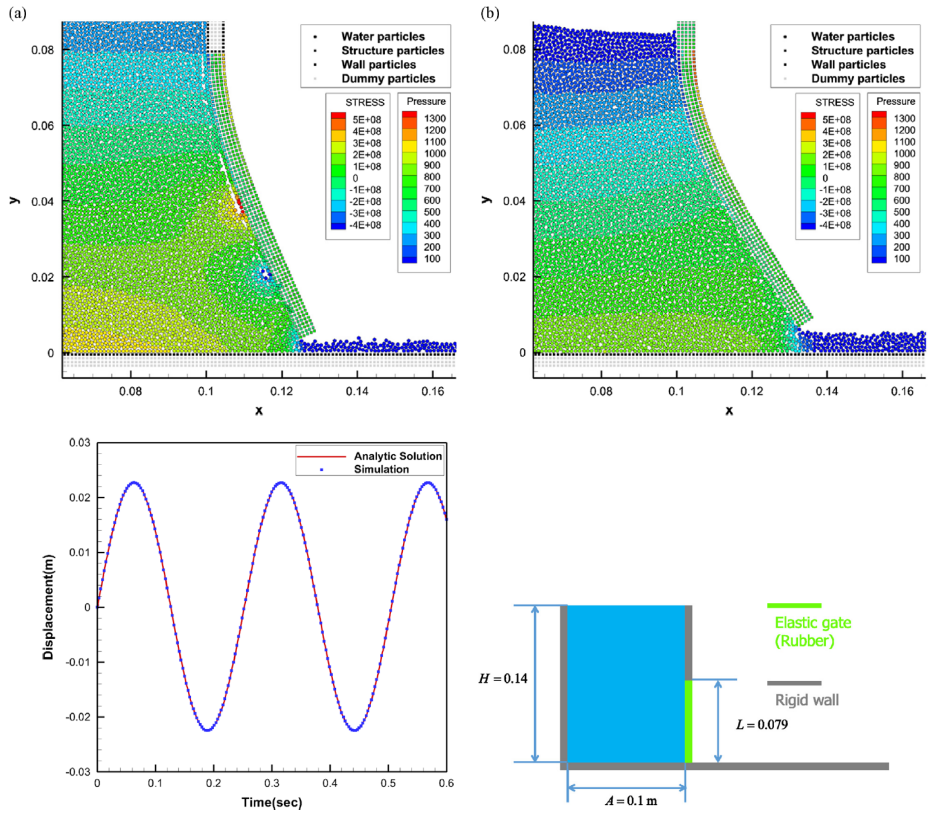

Figure 2.6: Example of the application of a monolithical approach for the computation of the deformation of a flexible gate under the action of a fluid flow induced pressure. Image taken from [52]

2.3.2 Segregated Approach

In a segregated approach, the resolution of the fluid domain and the solid domain are carried out by different solvers. The coupling between them is done through the dynamic and kinematic conditions at the interface [56]. When the fluid and solid solvers are separately available, the interaction between the different physical domains may be carried out via Dirichlet-Neumann coupling. To understand such a coupling lets assume that the discrete form of fluid equation and fully discrete form of solid equation are given respectively by Equations 2.12.

$$\mathbf{K^f} \cdot \vec{\mathrm{v}}^f = \vec{F}^f \qquad \mathbf{K^s} \cdot \vec{u}^s = \vec{F}^s \tag{2.12}$$

To strongly couple the two equations, start the iteration with the initial solutions of solid and fluid variables and solve the fluid equation to determine the fluid forces at the interface. This is followed by solution of the solid equation to determine the displacements within the solid domain; calculation of fluid velocity at the interface from the interface displacements and determination of new mesh position. Now, check whether or not the interface displacements converged. If not, the interface velocity values are used to solve the flow equation again. Continue this iteration between fluid, solid and mesh until interface displacements are converged. The interface displacements are often converged quickly using relaxation methods.

Figure 2.9 will show a scheme were the work flow of a segregated methodology is sketched for a generic case. This Figure can be interpreted as follows:

- At the beginning of a time step, both the fluid and solid fields are completely determined. However, it is supposed that they are not in equilibrium and, in consequence, variations on them are expected.
- The fluid flow solver is invoked at this stage in order to simulate how the fluid flow should behave at the next time step, given the interface positions and velocities.
- As a consequence, the solid domain must be resolved in order to compute the expected displacements under the previous updated conditions.
- If the expected displacements are high enough, a mesh morphing strategy has to be followed in order to update the fluid domain.

- Now, in an iterative manner, the fluid domain is solved again for the new interface displacements and velocities untill the displacement field remains unchanged between iterations.
- Once the fluid and solid domain are converged, the loop breaks and a new time step can be calculated.

Regarding on how the coupling methodology is carried out, it is possible to follow an explicit (loosely) or an implicit (strongly) coupled methodology.

Explicit Coupling

Roughly speaking, a **explicit (or loosely)** methodology is performed when the coupling is performed in a unique or very few iterations per time step [57],[58], as will be sketched in Figure 2.10, aiding to understand the low computational cost of this methodology.

Under these circumstances, if the time step is not low enough, boundary conditions of continuity of displacement and stresses are not fully satisfied. As a consequence, this approach does not ensure an exact balance of energy at the interface. These energy losses have been found to produce numerical instabilities, specially for incompressible flow, under circumstances of (a) very high structural displacements; (b) for a given geometry, as soon as the density of the structure is lower than a certain threshold or (c) for a given structure density, as soon as the length of the domain is greater than a certain threshold [59].

Sometimes, the numerical instabilities can be avoided by using sufficiently small time steps, although, at some circumstances this condition leads to inadmissible computational costs ([60], [61], [62], [63]). Theoretical explanations have been reported by Causin et al. [59] (see also Figueroa et al. [64]). Here, they proved how, for a given stiffness, an explicit segregated strategy leads to instabilities when Equation 2.13 is complied:

$$\frac{\rho_s \, \epsilon}{\rho_f \lambda_{add}} < 1 \tag{2.13}$$

where ρ^s and ρ^f are the solid and fluid densities, respectively. ϵ is related to the thickness of the structure and λ_{add} represents an added mass characteristic length, which increases with the length of the domain (it is the largest eigenvalue of the so-called added-mass interface operator) and only slightly depends on the time step size.

Explicit coupling has been successfully applied to multiple engineering problems and stabilization techniques can be performed in order to ensure its applicability even when high displacements are computed. For instance, Guidoboni et al. [65] used a loosely coupling strategy in order to simulate fluid flow inside a deformable duct for low Reynolds number, although presented problems when applying to tight coupled three dimensional systems.

The field where explicit coupling has been most widely applied is aeroelasticity where, normally, only the prediction of the beginning of FSI instabilities is needed to be modeled. In this sense, it is worth to mention the works of Piperno et al. [66] or Fourestey et al. [67], where they modeled aeroelastic phenomena on representative 2D bridge sections; Piperno et al. [68] designed an explicit coupling procedure to model aeroelastic phenomena on complete 3D wings. In the work of Farhat et al. [69], they proposed an explicit tool which could even be used on aeroelastic applications with very tight interaction. Figure 2.7, taken from [69], shows the application of an explicit method for the computation of the displacement of a wing geometry. The left image shows the wing tip vertical displacement while the right image shows how the energy conservation is violated at the interface, which is related with the difficult stabilization of this kind of methodologies.

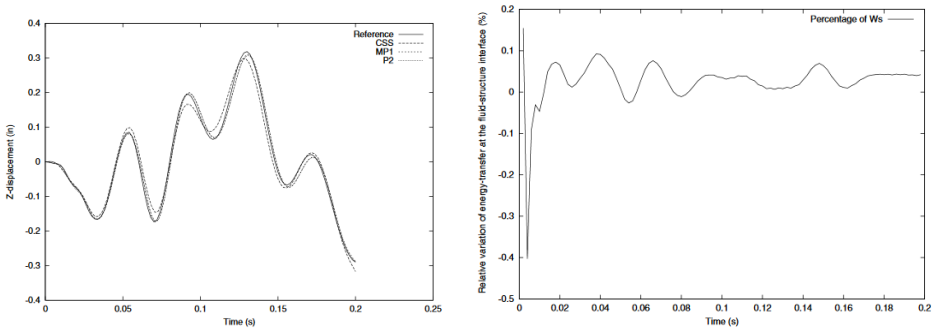

Figure 2.7: Example of application of an improved explicit coupling methodology to an aeroelastic cantilivered wing. Tip displacement (left) and interface energy violation (right) as a function of time. Figure taken from [69]

Implicit Coupling

In an **implicit (or strongly)** coupling scheme, the process sketched at Figure 2.9 is followed with no simplifications, and the solid and fluid domains are all iteratively solved for each time step until convergence is achieved at the interface. However, a large number of different options to couple the fluid and structure exist, as can be seen from [70], [71], [72], [73], [74], [75], [76], [77] or [78]. These schemes have been, for years, the unique way of circumventing the numerical instabilities associated with explicit methods. Somehow, this explains why the development of efficient methods for the resolution of the coupled non-linear systems arising in implicit coupling has been a very active field of research. These algorithms have been proven to be energetically stable (see [61], [79], [80]).

Due to its stability capabilities, implicit coupling can be chosen when predicting phenomena where strong non-linear interactions between fluid and solid appear, as, for example, for predicting aeroelastic post-flutter phenomena [81], [82].

Implicit techniques have been successfully applied for the resolution of problems where the coupling between the solid and the fluid domain is high. For instance, Formaggia et al. [83] computationally studied the transmission of pressure waves inside very flexible pipes. The same problem has been boarded by Gerbeau et al. [63]. Habchi et al. [84] proposed a new partitioned implicit strategy and proved its capability for the modeling of a flexible lid-driven cavity and flexible splitters.

Tezduyar et al. [85] or Takizawa et al. [86] applied segregated implicit coupling for the prediction of fluid flow around parachutes under different situations. Rebouillat et al. [87] have shown implicit segregated coupling as a good approach to model sloshing when the walls of the container are supposed to be flexible. The approach has also been applied to problems of complex geometries. For instance, Bazilevs et al. [88], [89] or Hsu et al. [90] showed how implicit fluid structure interaction methodologies can be used in order to predict the behavior of a complex system such as a wind turbine of composite blades under high wind velocities. Figure 2.8 shows a summary of one of their most important results. Guner et al. [91] recently developed a numerical methodology to predict flutter behavior using a reduced order modal decomposition for the modeling of the structural part. Similar results can be found at Jonsson et al. [92], but using a simpler potential model for the fluid flow.

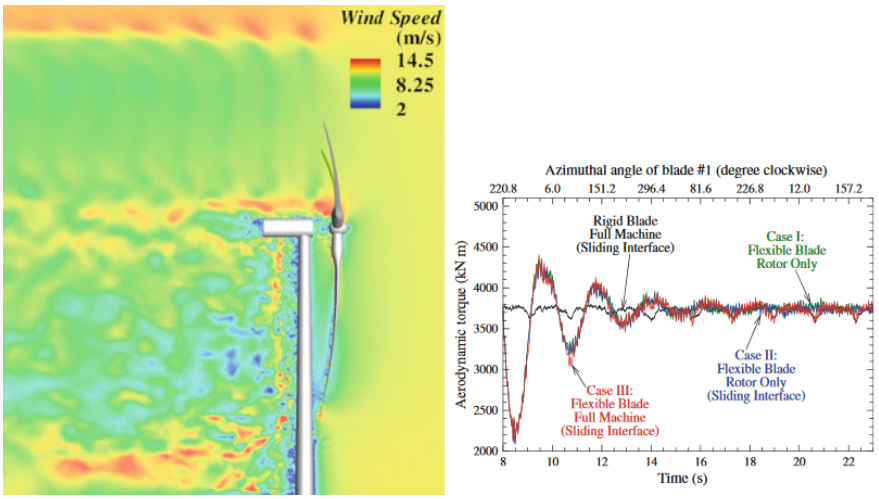

Figure 2.8: Example of computation using an implicit methodology the fluid flow over a flexible wind turbine under very high wind conditions. Contours of fluid velocity (left) and evolution of blade torque, compared with rigid computations (right). Figure taken from [90]

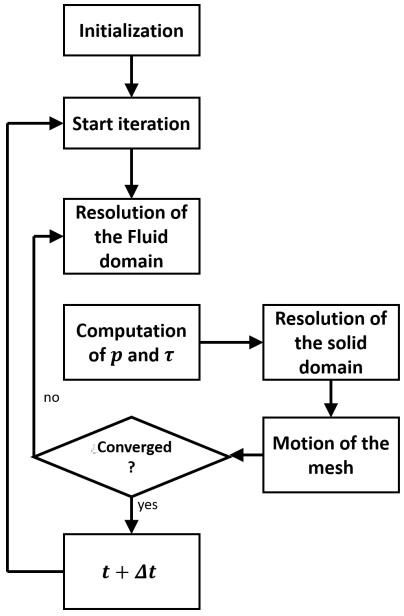

Figure 2.9: Schematic of a segregated methodology for the resolution of the Fluid Structure Interaction problem

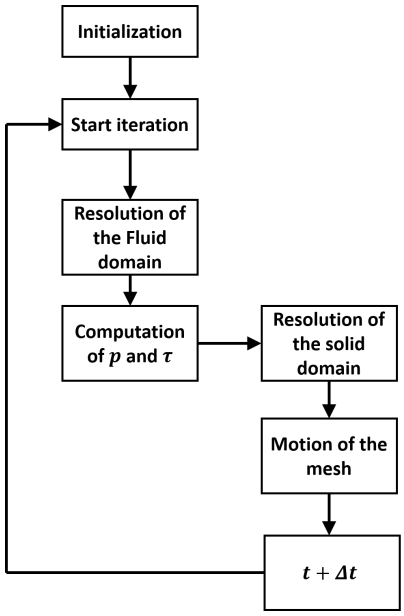

Figure 2.10: Schematic of a segregated explicit methodology for the resolution of the Fluid Structure Interaction problem

One way fluid structure interaction

Although not considered by all the authors as a case of Fluid Structure Interaction, the one way model of FSI is of crucial importance for analyzing a wide range of engineering applications. In this case, the flow excites a structure, but the generated displacements of the second do not significantly affect to the behavior of the fluid flow. One way coupling is also often found to act on the other direction: if the elastic forces are much higher than those associated with the pressure and wall shear stress distribution, the structure displacements can be supposed to be given and fluid flow should not be used in order to compute them.

Understanding one way fluid structure interaction is of primal interest in order to correctly model engineering problems and to ensure this assumption is made only when it is applicable.

An important amount of examples where this methodology is successfully employed can be found in the literature. Beginning with the case where the fluid flow induces one way displacements over a structure, it should be mentioned the work of Shyang et al. [93] where they performed URANS simulations in order to obtain the non-stationary pressure field over the blades of a centrifugal impeller and used them as a boundary condition in order to compute their vibrational response. Jiang et al. [94] used a similar approach, solving the fluid using Scale Resolivng Simulations in order to obtain the vibrational behavior of a full-scale turbomachinery machine and posteriorly used those vibrations in order to compute the response in terms of radiated noise from the system. The work was later expanded by Hayashi et al. [95], who explored the effects of accounting for damping in a simplified version of the previous work. Although some empirical models have been tried to be developed in order to compute the induced vibration by turbulent flows (see [96], [97], [98]), they normally only allows to compute for the effect of the contribution of isotropic turbulence and, when large anisotropic scales of the fluid motion are of interest, the correct unsteady resolution of fluid flow equations becomes mandatory.

As it can be deduced from the references, one way fluid structure interaction plays an important role for the modeling of both fluid induced vibrations and radiated noise. In nearly all problems of flow-generated noise, the energy source for sound production is some form of flow unsteadiness. This unsteadiness needs not always to be turbulent, or random, as there are numerous cases of tonal sounds that involve sinusoidal disturbances in the fluid. Most other cases of flow-induced vibration, at low velocity (or Mach number) especially, involve a restricted region of turbulence that is either free of solid boundaries or in contact with a body. Figure 2.11, which has been reconstructed from the work

of Blaje [5] illustrates one example, showing how, between the parameters of noise generation from a lifting surface passing through unsteady flow, the flow induced vibration, with characteristic wave length, λ_s plays an important role and should be had into account.

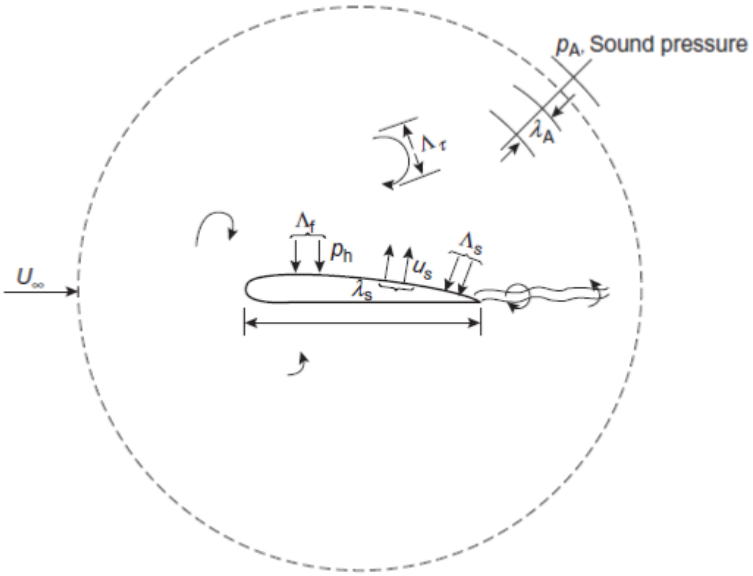

Figure 2.11: Illustration of a body subjected to a disturbed flow of scale Λ_r; body vibration, u_s of wave length Λ_s resulting from surface pressure p_h of length scale Λ_f. Figure reconstructed from Blaje [5]

On the other hand of one way fluid structure interactions it should be mentioned the cases where the rigid body movement and/or deformation of the structure is completely defined by external forces different from the fluid exerted ones or is completely described as an external boundary condition. Obviously, when only a rigid body motion is imposed the equations of the elastic body do not have to be resolved. In consequence, although some examples of this kind of systems are going to be shown next, they will not be deeply explored during the development of this document.

In this last context, one of the most widely used examples of these flows can be found at the resolution of the unsteady flow inside the cylinder of an internal combustion engine. In this kind of systems, normally, the motion of the cylinder is prescribed using the cinematic of the mechanisms when the engine works under conditions of constant rotational speed. Multiple examples of this can be found at the literature. As some interesting cases, it should be mentioned the

works of Broatch et al. [99] or Robert et al. [100].

2.3.3 Mesh motion methodologies

As it was stated during the previous sections, when computationally solving a problem of fluid structure interaction, if the strength of the interaction is high enough to provide bi-directional coupling, it is necessary to perform an updating of the mesh for each time step (explicit coupling) or each coupling iteration (implicit coupling). Often, the solid domain is treated using a Lagrangian form of mesh movement and the fluid domain is subjected to the so-called arbitrary Lagrangian-Eulerian (ALE) method. In an ALE formulation, the mesh is allowed to move independently of the material points. This independent motion of the mesh to maintain mesh quality in general is not necessarily always straight forward.

It is very common to use topology-preserving mesh moving algorithms in fluid-structure interaction applications. Although a deep description of these methodologies is out of scope of the present document, it is necessary to provide with a brief description of some of the most used methods. As an example of mesh motion methodologies, it could be named the spring analogy; the Delaunay graph method; the obtainment of the grid method as a solution of partial differential equations or the Laplacian smoothing.

Spring analogy

In this method, the edges connecting two nodes are assumed to be connected by a spring that maintains equilibrium. To find the position of node a, the total force between node a and nodes connected to its must be zero to maintain equilibrium. Each edge b connected to a is assigned a spring constant.

With this assumptions, it is common practice to use a Gauss-Seidel method to solve a global equilibrium equation, as Equation 2.14 in order to obtain the displacement of the nodes:

$$\mathbf{K_s} \cdot \vec{\delta} = \vec{0} \tag{2.14}$$

where $\vec{\delta}$ is the displacement of the nodes of the grid. The previous equation must be solved with known values of the displacements along the moving boundaries. The linear spring analogy has no control over the angle between edges. For keeping the angles between edges under control, the method needs to be modified by incorporating the torsional effects as well to the total force. More information about this mesh morphing methodology can be found at Burg [101] or Farhat et al. [102].

Delaunay graph method

This method follows a one-to-one mapping between the nodes and a background element. The method starts with generation of a background mesh followed by allocation of the nodes of a finite element mesh to the background elements. A finite element node should only belong to one background element. As the structure moves within a fluid, the background mesh is moved with the structural movement. This is followed by the mapping of the nodes to the new position of the background element by means of simple finite element interpolation using barycentric area coordinates. Thus, the new position of a point within a background mesh may be written in terms of area coordinates as follows:

$$\vec{x}_a = \sum_{b=1}^{3} L_b \vec{x}_b \tag{2.15}$$

where L_b is the barycentric area coordinate of the background mesh, calculated based on the original position of the node and the new position of the background element. For linear triangular elements, this can simply be replaced with the shape functions. Although simple and robust for a problem with fairly uniform movement, certain difficulties are faced by the method if element nodes are shared between two background elements. For instance, if two adjacent background elements are moving at much different rates, the element shared by these may be stretched or compressed excessively to create entanglement. Information about this method could be found at Liu et al. [103]. Boer et al. [104] proposed an improvement to this scheme in order to preserve mesh orthogonality near the deforming boundary, Radial Basis Functions, with some modifications, were shown by Gagliardi et al. [105] to provide acceptable computationally efficient results even for problems with a big amount of elements.

Radial Basis Functions

With this methodology, a system of radial functions is used to produce a solution for mesh movement-morphing from a list of source points and their displacements [106], [104]. This approach is valid for both surface shape changes and volume mesh smoothing.

Radial basis were born as an interpolation tool for scattered data and consist of a very powerful tool because they are able to interpolate everywhere in the space a function defined at discrete points giving the exact value at original points. The behaviour of the function between points depends on the kind of basis adopted. The radial function can be fully or compactly supported, in any case a polynomial corrector is added to guarantee compatibility for rigid modes.

An interpolator, s is introduced in order to have an approximating smooth function in the same space. At a location $\vec{x}$ its value is:

$$s(\vec{x}) = \sum_{i=1}^{N} \gamma_i \varphi \left(|\vec{x} - \vec{x_{k_i}}| \right) \tag{2.16}$$

where φ is the so-called radial function, namely defined a scalar function of the Euclidean distance between source and target points. γ_i are weights of the radial basis. A complete description of this method can be found at Lee et al. [107].

Solution to partial differential equations

It has been shown how, although expensive, moving a mesh by solving an equilibrium equation appears to be robust and valid for most of the engineering fluid structure interaction problems [78]. The most general form of equation used in moving a mesh is an equation of elasticity. This is logical with displacement boundary conditions prescribed on the boundaries of a domain. The discrete form of the elasticity equation may be written as

$$\iiint_{\Omega_t} \mathbf{B}^T \mathbf{D} \mathbf{B} (\vec{\delta}^{n+1} - \vec{\delta}^{n}) d\Omega = \vec{F} \tag{2.17}$$

where $\mathbf{B}$ is the matrix that contains the derivatives of shape functions, $\mathbf{D}$ is the elasticity matrix, $\vec{\delta}$ is the vector of displacements within the fluid domain and $\mathbf{F}$ contains the prescribed displacements on the solid surface. Additional information of this technique could be found at [108], [109] or [110].

Laplacian smoothing

Laplacian smoothing is a very simple method which can be used for small displacements. In this method the coordinate of a node is taken equal to the average of the coordinates surrounding that node. This method works well if the displacement is much smaller than the element size. Often this method, combined with a more general method provides better quality elements. On its own this method is unsuitable for boundary layer meshes and very fine meshes close to solid surfaces. See the works of Vollmer et al. [111], Nealen et al. [112] or Zhou et al. [113].

2.4 Experimental Methodologies for Fluid Structure Interaction

In order to perform an experimental characterization of the fluid structure interaction, the usual approach is to use a combination of the well established methodologies of the experimental fluid mechanics and experimental solid strucutres. In this sense, the present document tries to show some of the most interesting techniques used for each one of this fields. Note how a complete listing of all the available techniques of measurements would be much more extense and, therefore, it is out of the scope of this text. In this sense, an important ammount of work has been performed in order, mainly, to validate the existing numerical or analytical interactoin models and algorithms. For instance, in the work of Hessenthaler et al. [114] they provide an easy-to-setup FSI test case that addresses the need for rigorous testing of FSI algorithms and modeling frameworks focused on biomedical engineering applications with flow being in the laminar regime.

2.4.1 Experimental Methodologies for Fluid Dynamics

Experimental Characterization on Wind Tunnel

In the field of aeroelasticity, wind tunnel is one of the most widely used experimental facilities to characterize the fluid structure interactions of structures which normally work under high wind speed conditions. A wind tunnel consists of a tubular passage with the object under test mounted in the middle. Air is made to move past the object usually by means of a fan system. The test object is instrumented with suitable sensors to measure aerodynamic forces, pressure distribution, displacements or strains. Multiple variants of wind tunnel can be found, but they all can be briefly described by means of the previous sentences.

The earliest wind tunnels were invented towards the end of the 19th century, in the early days of aeronautic research, when many attempted to develop successful heavier-than-air flying machines. The wind tunnel was envisioned as a means of reversing the usual paradigm: instead of the air standing still and an object moving at speed through it, the same effect would be obtained if the object stood still and the air moved at speed past it. In that way a stationary observer could study the flying object in action, and could measure the aerodynamic forces and displacements being imposed on it.

One of the most difficult problems which arise when facing experimental characterization of aeroelastic problems is given by the scalability of the problem. Later, it will be shown how any incompressible-flow fluid structure interaction case can be characterized, given a geometry, by the Reynolds number, $\mathrm{Re} = \rho_\infty V_\infty L_{ref}/\mu_\infty$; a non dimensional stiffness parameter, $\mathrm{K} = E/\left(\frac{1}{2}\,\rho_\infty V_\infty^2\right)$, which expresses the relative importance of elastic and inertial forces and a non dimensional mass parameter, $\mathrm{M} = \rho_s/\rho_f$, which expresses the relative inertia between the solid and fluid materials.

While the influence of the Reynolds number can be explored by the case of a perfectly stiff body simply by performing a continuous swept of the wind tunnel velocity, for the case of a flexible object this swept is less straight-forward, as the fluid velocity also affects (and even more significantly) to the value of the non dimensional stiffness parameter. This has made that some researchers incorrectly associate Reynolds number to be the dominant effect on the Vortex Induced galloping on infinite cylinders, misunderstanding the more important factor, the non-dimensional stiffness, as will be later shown.

Fortunately, it is well known that if the Reynolds number is high enough and/or the body under study is characterized for containing abrupt hard edges, the dependence with this parameter becomes of second order and a parametric swept of the velocity would correspond to a swept of the non-dimensional stiffness parameter.

Some examples of aeroelastic and flow induced vibration experiments can be found in the literature. For instance, Xie et al. [115] studied a 1:4.5 scale model of a train catenary in wind tunnel and characterized its coupled vibrational response for different values of wind speed and tension.Bdeiwi et al. [116] proposed a numerical validation of the pre instability structural deformation of an aircraft model my measurements on the NASA CRM transonic wind tunnel. Figure 2.12 shows an example of the mounting of the aircraft model for this reference (left) and the measured aerodynamic lift coefficient comparing a rigid and a flexible model (right).

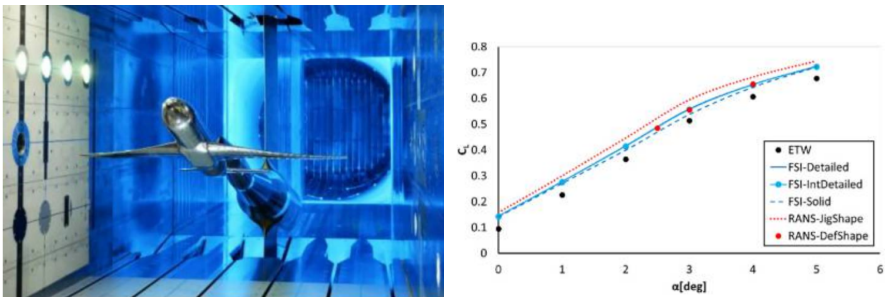

Figure 2.12: Example of application of wind tunnel measurements for the characterization of the aeroelastic features of an aircraft model. Image taken from [116]

Particle Image Velocimetry

Particle image velocimetry (PIV) has been used since the mid-1980s to obtain high spatial resolution two-dimensional velocity field in macroscopic flows. The experimental procedure is relatively simple to understand. A flow is made visible

by seeding it with particles. The particles are photographed at two different times. The images are sectioned into many smaller regions called interrogation regions. The motion of the group of particles within each interrogation region is determined using a statistical technique called a cross-correlation.

A typical PIV apparatus consist of a camera, a strobe or laser with an optical arrangement to limit the physical region illuminated, a synchronizer to act as an external trigger for control of the camera and laser, the seeding particles and the fluid under investigation. A fiber optic cable or liquid light guide may connect the laser to the lens setup. PIV software is used to post-process the optical images.

Due to its own formulation, PIV is not a well suited tool in order to study the structural deformations of a fully coupled FSI problem. Nevertheless, this limitation can be overcome by using PIV in combination with other structural tools.

Multiple examples can be found in the literature of the PIV technique applied to problems of Fluid Structure Interaction in a wide range of fields. For instance, Panciroli et al. [117] used this technique in order to characterize the fluid flow generated by the impact of a flexible solid body over a initially stationary water tank, using different materials for the solid body.

Dey et al. [118] used PIV applied to the case of a fluid flow of high viscosity fluid flowing around a three dimensional flexible cylinder for different values of the incoming velocity. Figure 2.13 reproduces their results as an example of the capabilities of this kind experimental of tool.

Other interesting study can be found at Zhang et al. [119]. Here they show how PIV can be used in combination with Digital Image Correlation (DIC) in order to fully characterize the fluid flow around a flexible valve plate.

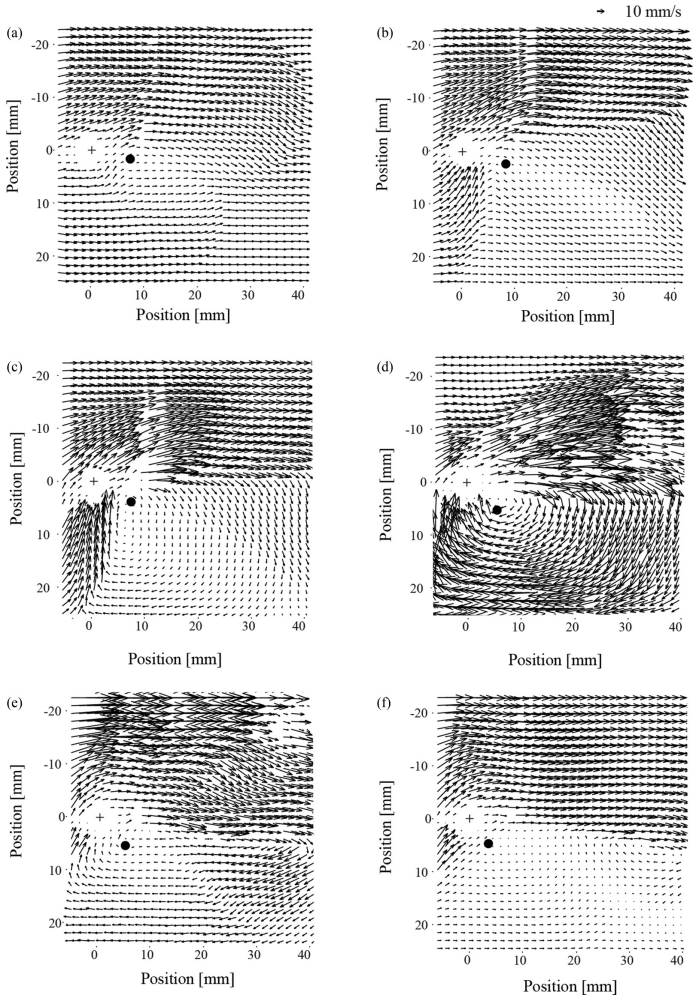

Figure 2.13: Example of application of PIV for the characterization of the fluid flow around a flexible cylinder. Image taken from [118]

2.4.2 Experimental Methodologies for Structural Dynamics

Laser Scanning Vibrometry

The scanning laser vibrometer (LSV) or laser Doppler vbrometer (LDV) was introduced during the 1980s. It is an instrument which allows fast non-contact measurements of vibrations.

The operating principle is based on the Doppler effect, which occurs when light is back-scattered from a vibrating surface. Both velocity and displacement can be determined by analyzing the optical signals in different ways. A scanning laser vibrometer integrates computer-controlled X,Y scanning mirrors and a video camera inside an optical head. The laser is scanned point-by-point over the test object's surface to provide a large number of very high spatial resolution measurements. This sequentially measured vibration data can be used to calculate and visualize animated deflection shapes in the relevant frequency bands from frequency domain analysis. Alternatively, data can be acquired in the time domain to, for example, generate animations showing wave propagation across structures [120]. In contrast to contact measuring methods the test object is unaffected by the vibration measuring process.

Some examples worth to be mentioned from the literature. For instance, Zhang et al. [121] used this technique in order to characterize the interaction between a fluid flowing inside flexible tubes. It was also used by Garafolo et al. [122] in order to study the vibrational response of a flat plate under flutter conditions with different temperatures.

Figure 2.14 (up) shows an example of the mounting of a Laser Vibrometer for the wall vibration characterization of a flexible plastic made silencer under conditions of constant velocity inflow and the typical vibration pattern which can be computed at the walls (bottom).

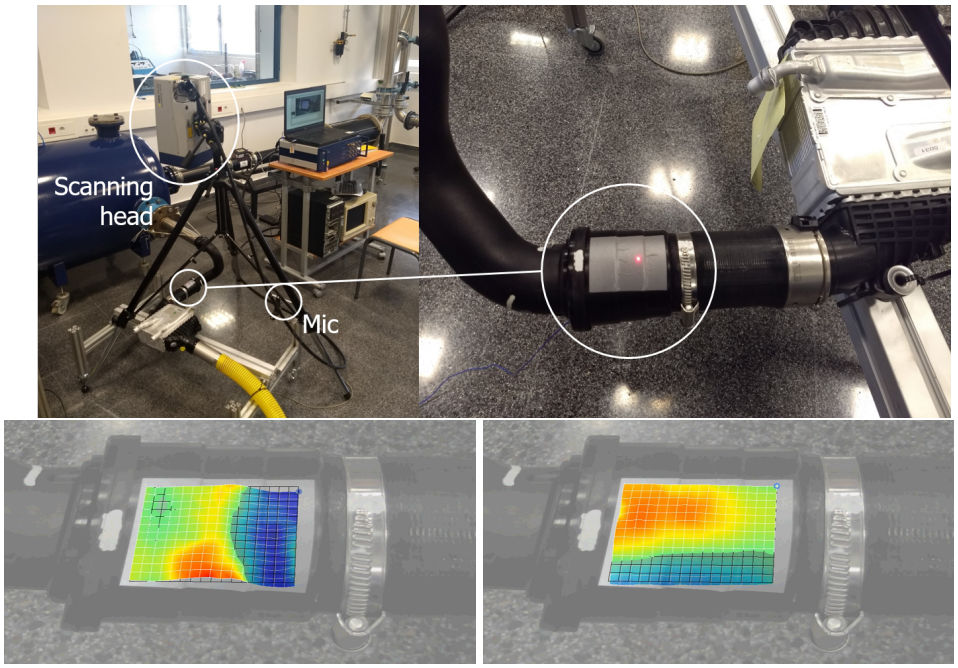

Figure 2.14: Example of application of Laser Vibrometry for the characterization of the vibrational response of a plastic made silencer. Mounting (top) and displacement response for two different frequencies (bottom)

Digital image correlation

Digital image correlation (DIC) is an optical method that employs tracking and image registration techniques for accurate 2D and 3D measurements of changes in images. This method is often used to measure full-field displacement and strains, and it is widely applied in many areas of science and engineering, with new applications being constantly found. Compared to strain gages and extensometers, the amount of information gathered about the fine details of deformation during mechanical tests is increased due to the ability to provide both local and average data using digital image correlation.

The concept of using cross-correlation to measure shifts in datasets has been known for a long time, and it has been applied to digital images since at least the early 1970s.

DIC has been proven to be very effective at mapping deformation in macroscopic mechanical testing, where the application of specular markers or surfaces finishes from machining and polishing provide the needed contrast to correlate images well.

Some examples can be found of the use of this technique (in conjunction with others) in order to characterize the FSI. For instance, D.R. et al. [123] presented an application of DIC which, in conjunction with the use of pressure-sensitive paint allowed to study the behavior of a flexible panel subjected to a supersonic flow.

Wood et al. [124] used DIC and PIV in order to develop a wind tunnel model of an air-inflated membrane structure which can be considered to be a correct simplification of some modern thin wall structures varying the incoming fluid velocity. Both the internal pressure and Reynolds number were varied in this study.

Also related with DIC it should to be mentioned the recent application made by Sousa et al. [125], where they measured the fluid induced displacements of a rotating RC helicopter blade under the dynamic loading from a rotation of 680 rpm.

Figure 2.15 shows a typical example of the application of this technique for the identification of both the flexural and torsional behavior of a cantilevered plate subjected to an almost steady free stream fluid flow. The identification of characteristic points of the plate allows to compute both the time response of the vertical displacement and the changes on angle of attack of the tip section.

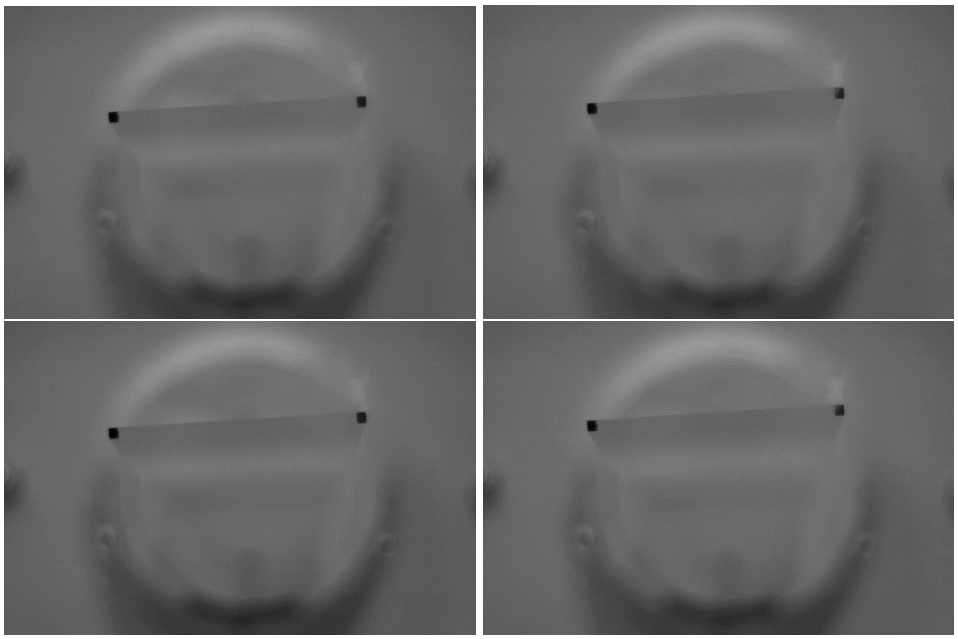

Figure 2.15: Example of application of Digital Image Correlation for the identification of the pre flutter response of a elastic cantilevered polymeric plate at 25m s^{-1}

2.5 Summary and conclusions

At the beginning of this chapter a very brief introduction of the fluid structure interaction has been given, while some of the main physical classification and engineering applications are introduced, depending, mainly, on the strength of the fluid structure interaction and/or the behavior of the solid body.

Subsequently, in order to illustrate the rise of the fluid structure interaction and with the aim of presenting the main tools which are normally used for this type of problems, the numerical approachs commonly used in the literature are presented.

In this context, the general equations of the fluid flow are introduced, as well as the equations of the deformable solid. Note how they are presented in their complete form and ,thus, simplifications and assumptions will be allowed to be taken depending on the problem of study, as will be shown in later chapters (for instance, neglecting the influence of viscosity on problems of wave transmission; modeling turbulence in order to avoid the need of performing DNS; simplifying the solid body equations in order to obtain the simpler and easier to resolve Kirchoff-Love plate equations...).

Once the general equations of both domains are introduced it is shown how the coupling between them arises from the own definition of the boundary conditions of each domain: On one hand, the fluid non-slip boundary condition ensures that any displacement computed on the solid part would change the frontier of the own fluid domain. On the other hand, the boundary condition of continuity of stresses makes that the fluid pressure and stresses are transmitted as a load to the solid domain and, in fact, are responsible of its displacements.

Consequently, it was shown how, during the past years, the computational strategies to numerically resolve the coupled problem have been spectacularly developed and, in fact, nowadays almost any kind of problem can be computed (in theory), regardless with the strength of the interaction. The two main strategies to computationally resolve the coupled problem are then presented: The monolithic and the segregated approachs.

The monolithic approach is characterized by the use of one only solver for the discretization of both domains, and can be used to accurately compute any kind of interaction, but with the drawback of an increased computational cost.

The segregated approach, on the other hand, allows to use already defined solvers for the fluid flow and for the solid deformation. The coupling between the domains is performed by an additional step which involves the boundary

conditions of each physics. Among these methods three main strategies can be numbered:

- The so-called explicit coupling was one of the first methods to be developed, with this approximation, the coupling between the domains is performed in a unique iteration. This methodology is characterized by a low computational cost, although it can only be applied to problems where the tight between fluid and solid is medium or low.
- The implicit coupling was later developed in order to overcome the stability issues of the explicit strategy when the deformations are high or the density of fluid and solid are similar. With this methodology, the coupling is performed by means of an additional loop which iteratively invokes both boundary conditions in order to very accurately couple them.
- Despite its simplicity, the one way coupling strategy should not be missprized, as a wide range of engineering applications can be found to lie in this case. Here, it is suppose that one of the domains affect to the response of the other but the reverse coupling is not appearing, i.e., only one of the boundary conditions is used in order to solve the problem.

Therefore, it has been seen how it can be considered how, with the available tools, most of the engineering important problems can now be accurately modeled or measured. However, from the development of this chapter a reader will notice how the interaction itself has not been widely studied. In fact, during the whole development of the chapter the words *strength of the interaction* have been intensively used (as are also used in the literature) but no additional information has been provided about how to compute this *strength*.

Additionally, the dimensional analysis of these kind of problems has not been fully analyzed and, in fact, in some situations the system is not correctly characterized, as some of this features are attributed to a non-dimensional parameter which should not be the dominant number of the coupled problem. For instance, it is usual that some researchers attributes the beginning of important structural coupling to the effects of the Reynolds number. However, and as shown later, they sometimes depreciate the effect of the non-dimensional stiffness of the problem, $E/(\frac{1}{2}\ \rho_\infty V_\infty^2)$, which, in most of the cases, results to be the dominant parameter of the coupled problem.

2.6 References

[5] W. Blaje. *Mechanics of flow-induced sound and vibration, Volume 2*. Ed. by A. press. 2017 (cit. on pp. 2, 38).

[10] I. E. Garrick and H. Wilmer. "Historical Development of Aircraft Flutter". In: *Journal of Aircraft* 18 (1981), pp. 897–912 (cit. on p. 15).

[11] G. Hill. "Advances in aircraft structural design". In: *Third Anglo-American Aeronautical Conference* (1951) (cit. on p. 15).

[12] G. Brewer. "The Collapse of Monoplane Wings". In: *Flight* 5 (1913), p. 33 (cit. on p. 15).

[13] A. Collar. "The First Fifty Years of Aeroelasticity". In: *Aerospace* 5 (1978), pp. 12–20 (cit. on p. 15).

[14] S. Pope. *Turbulent Flows*. Ed. by C. U. Press. Cambridge University Press, 2009 (cit. on pp. 17, 18, 76, 169, 170, 179).

[15] H. Hirsch. "Numerical computation of internal and external flows. Volume 1, Fundamentals of numerical discretization". In: *John Wiley and Sons* (1988) (cit. on p. 17).

[16] H. Hirsch. "Numerical computation of internal and external flows. Volume 2, Computational methods for inviscid and viscous flows". In: *John Wiley and Sons* (1988) (cit. on p. 17).

[17] P. V.S. "Numerical heat transfer and fluid flow". In: *Hemisphere Publishing* (1980) (cit. on p. 17).

[18] H. Versteeg and W. Malalasekera. "An introduction to Computational Fluid Dynamics". In: *LongMan Scientific and Technical* (1995) (cit. on pp. 17, 19).

[19] K. D. and J. Hamamalainen. "Finite Element Methods for Computational Fluid Dynamics". In: *Siam Computational Science and Engineering* (2014) (cit. on p. 17).

[20] O. Zienkiewicz, R. Taylor, and P. Nithiarasu. "The Finite Element Method for Fluid Dynamics". In: *Butterworth-Heinemann* (2014) (cit. on pp. 17, 130, 131).

[21] C. Shu. "High-order finite difference and finite volume WENO schemes and discontinuous Galerkin methods for CFD". In: *International Journal of Computational Fluid Dynamics* 17 (2003), pp. 107–118 (cit. on p. 17).

[22] J. Boris, M. Fritts, R. Madala, B. McDonald, N. Winsor, and S. Zalesak. *Finite-difference techniques for vectorized fluid dynamics calculations*. Springer Science and Business Media, 2012 (cit. on p. 17).

[23] J. Galache. “Study of the flow field through the wall of diesel particulate filter using Lattice Boltzmann methods”. In: *Doctoral dissertation. Universitat Politecnica de Valencia* (2017) (cit. on p. 17).

[24] A. Gil, J. Galache, C. Godenschwager, and U. Rude. “Optimum configuration ofor accurate simulations of chaotic porous media with Lattice Boltzmann Methods considering boundary conditions, lattice spacing and domain size”. In: *Computers and Mathematics with Applications* 73 (2017), pp. 2515–2528 (cit. on p. 17).

[25] S. Chen and G. Doolen. “Lattice Boltzmann Method for Fluid Flows”. In: *Annual Review of Fluid Mechanics* 30 (1998), pp. 329–364 (cit. on p. 17).

[26] A. Das and J. Mathew. “Direct numerical simulation of turbulent spots”. In: *Computers and Fluids* 30 (2001), pp. 553–541 (cit. on p. 18).

[27] T. Hutl and R. Friedrich. “Direct numerical simulation of turbulent flows in curved and helitically coiled pipes”. In: *Computers and Fluids* 30 (2001), pp. 591–605 (cit. on p. 18).

[28] R. Friedrich, T. Hutl, M. Manhart, and C. Wagner. “Direct numerical simulation of incompressible turbulent flows”. In: *Computers and Fluids* 30 (2001), pp. 555–579 (cit. on p. 18).

[29] P. Spalart and S. Allmaras. “A one-equation turbulence model for aerodynamic flows”. In: *30 th aerospace science meeting and exhibit* (1992), p. 439 (cit. on p. 19).

[30] W. Rodi. “Turbulence models for environmental problems”. In: *Von Karman Inst. for Fluid Dynamics: Prediction Methods for Turbulent Flows* (1979) (cit. on p. 19).

[31] F. Menter. “Influence of freestream values on k-omega turbulence model predictions”. In: *AIAA journal* 30 (1992), pp. 1657–1659 (cit. on p. 19).

[32] F. Menter. “Zonal two-equation $k-\omega$ turbulence model for aerodynamic flows”. In: *AIAA, Orlando, Florida* 93 (1986), pp. 93–2906 (cit. on pp. 19, 169).

[33] F. Lien and M. Leschziner. “Assessment of turbulence-transport models including non-linear RNG eddy-viscosity formulation and second-moment closure for flow over a backward-facing step”. In: *Computers and Fluids* 23 (1994), pp. 983–1004 (cit. on p. 19).

[34] F. Sarkar and L. Balakrishnan. “Application of a Reynolds-stress turbulence model to the compressible shear layer”. In: *ICASE Report 90-18, NASA CR 182002* (1990) (cit. on p. 19).

[35] J. Smagorinsky. “General Circulation Experiments with the Primitive Equations: Part I, The Basic Experiment”. In: *Monthly Weather Review* 91 (1963), pp. 99–164 (cit. on pp. 19, 166).

[36] M. Germano, U. Piomelli, P. Moin, and W. Cabot. “A Dynamic Subgrid-Scale Eddy Viscosity Model”. In: *Physics of Fluids* 3 (1991), pp. 1760–1765 (cit. on p. 19).

[37] D. Lilly. “A proposed modification of the Germano subgrid-scale closure method”. In: *Physics of Fluids* 4 (1992), pp. 663–635 (cit. on p. 19).

[38] F. Nicoud and F. Ducros. “Subgrid-Scale Stress Modelling Based on the Square of the Velocity Gradient Tensor”. In: *Flow, Turbulence and Combustion* 62 (1999), pp. 183–200 (cit. on pp. 19, 166, 179).

[39] P. Spalart, W. Jou, M. Strelets, and S. Allmaras. “Comments on the feasibility of LES for wings, and on a hybrid RANS/LES approach”. In: *1st AFOSR Int. Conf. on DNS/LES Aug, 4-8. In: Advances in DNS/LES* (1997) (cit. on p. 20).

[40] M. Shur, P. Spalart, M. Strelets, and A. Travin. “A hybrid RANS-LES approach with delayed.DES and wall-modelled LES capabilities”. In: *International Journal of Heat and Fluid Flow* 29 (2008), pp. 1638–1649 (cit. on p. 20).

[41] P. Spalart. “Detached-eddy simulation”. In: *Annual Review of fluid mechanics* 41 (2009), pp. 181–202 (cit. on p. 20).

[42] O. Zienkiewicz and R. Taylor. *The Finite Element Method for Solid and Structural Mechanics*. Ed. by E. Butterworth-Heinemann. Oxford, 2006 (cit. on pp. 20, 74).

[43] O. Zienkiewicz, R. Taylor, and J. Zhu. *The Finite Element Method: Its Basics and Fundamentals*. Ed. by E. Butterworth-Heinemann. Oxford, 2005 (cit. on pp. 21, 74).

[44] C. Michler, S. Hulshoff, E. H. van Brummelen, and R. Borst. “A monolithic approach to Fluid-Structure Interaction”. In: *Computers and fluids* 33 (2004), pp. 839–848 (cit. on p. 27).

[45] E. van Brummelen, S. Hulshoff, and R. Borst. “Energy conservation under incompatibility for fluid-structure interaction problems”. In: *Proceedings of the Fifth World Congress on Computational Mechanics, Vienna University of Technology* (2002) (cit. on p. 27).

[46] A. Lozovskiy, M. Olshanskii, and Y. Vassilevski. “Analysis and assessment of a monolithic FSI finite element method”. In: *Computers and Fluids* (2019) (cit. on p. 27).

[47] M. Heil, A. Hazel, and J. Boyle. “Solvers for large-displacement fluid-structure interaction problems: segregated versus monolithic approaches”. In: *Computational Mechanics* (2008) (cit. on p. 27).

[48] E. Krause, Y. Shokin, M. Resch, and N. Shokin. “Computational Science and High Performance Computing II”. In: *Proceedings of the 2nd Russian-German Advance Workshop, Sttugart, Germany* (2005) (cit. on p. 27).

[49] C. Forster, W. Wall, and E. Ramm. “Artificial mass instabilities in sequential staggered coupling of nonllinear structures and incompressible viscous flows”. In: *Computational Methods Applied to Mechanical Engineering* 196 (2007), pp. 1278–1293 (cit. on p. 27).

[50] M. Fernandez, J. Gerbeau, and C. Grandmont. “A projection semi-implicit scheme for the coupling of an elastic structure with an incompressible fluid”. In: *International Journal of Numerical Methods in Engineering* 69 (2007), pp. 794–821 (cit. on p. 27).

[51] K. Takizawa, B. Henicke, A. Puntel, N. Kostov, and T. Tezduyar. “Computer modeling techniques for flapping-wing aerodynamics of a locust”. In: *Computers and Fluids* 85 (2013), pp. 125–134 (cit. on p. 27).

[52] S. Hwang, A. Khayyer, H. Gotoh, and J. Park. “Development of a fully Lagrangian MPS-based coupled method for simulation of fluid-structure interaction problems”. In: *Journal of Fluids and Structures* 50 (2014), pp. 497–511 (cit. on pp. 27, 29).

[53] R. Loon. “Towards computational modelling of aortic stenosis”. In: *International Jounral for Numerical Methods in Biomedical Engineering* 26 (2010), pp. 405–420 (cit. on p. 27).

[54] Y. Wu and X. Cai. “A fully implicit domain decomposition based ALE framework for three-dimensional fluid-structure interaction with applicatoin in blood flow computation”. In: *Journal of Computational Physics* 258 (2014), pp. 524–537 (cit. on p. 27).

[55] W. Leng, C. Zhang, P. Sun, B. Gao, and J. Xu. “Numerical simulation of an immersed rotating structure in fluid for hemodynamic applcations”. In: *Journal of Computational Science* 30 (2019), pp. 79–89 (cit. on p. 27).

[56] M. Fernandez. “Coupling schemes for incompresible fluid-structure interaction: implicit, semi-implicit and explicit”. In: *SeMA Journal* 55 (2011), pp. 59–108 (cit. on p. 30).

[57] J. Banks, W. Henshaw, and D. Schwendeman. “An analysis of a new stable partitioned algorithm for FSI problems. Part I: Incompressible flow and elastic solids”. In: *Journal of Computational Physics* 269 (2014), pp. 108–137 (cit. on p. 32).

[58] J. Banks, W. Henshaw, and D. Schwendeman. “An analysis of a new stable partitioned algorithm for FSI problems. Part II: Incompressible flow and structural shells”. In: *Journal of Computational Physics* 268 (2014), pp. 399–416 (cit. on p. 32).

[59] P. Causin, J. Gerbeau, and F. Nobile. “Added-mass effect in the design of partitioned algorithms for fluid-structure problems”. In: *Computational Methods Applied to Mechanical Engineering* 194 (2005), pp. 4506–4527 (cit. on p. 32).

[60] D. Mok, W. Wall, and E. Ramm. “Partitioned analysis approach for the transient, coupled response of viscouse fluids and flexible structures”. In: *Proceedings of the European Conference on Computational Mechanics* (1999) (cit. on p. 32).

[61] P. Tallec and J. Moure. “Fluid Structure Interaction with large structural displacements”. In: *Computational Methods applied to Mechanical Engineering* 190 (2001), pp. 3039–3067 (cit. on pp. 32, 34, 79).

[62] S. Rugngy and K. Bathe. “On finite element analysis of fluid flows coupled with structural interaction”. In: *Computational Modeling Engineering Science* 2 (2001), pp. 195–212 (cit. on p. 32).

[63] J. Gerbeau and M. Vidrascu. “A quasi-Newton algorithm based on a reduced model for fluid-structure interactions problems in blood flows”. In: *Mathematical Modeling Numerical Analysis* 37 (2003), pp. 631–648 (cit. on pp. 32, 34).

[64] C. Figueroa, I. Vignon-Clementel, K. Jansen, T. Highes, and C. Taylor. “A coupled momentum method for modeling blood flow in three-dimesnional deformable arteries”. In: *Computational Methods Applied to Mechanical Engineering* 195 (2006), pp. 5685–5706 (cit. on p. 32).

[65] G. Guidoboni, R. Glowinski, N. Cavallini, and S. Canic. “Stable loosely-coupled-type algorithm for fluid-structure interaction in blood flow”. In: *Journal of Computational Physics* 228 (2009), pp. 6916–6937 (cit. on p. 33).

[66] S. Piperno and P. Bournet. “Numerical simulations of wind effects on flexible civil engineering structures”. In: *Revue Europeenne des Elements Finis* 8 (1999), pp. 659–687 (cit. on p. 33).

[67] G. Fourestey and S. Piperno. “A second-order time-accurate ALE Lagrange-Galerkin method applied to wind engineering and control of brige profiles”. In: *Computer methods in applied mechanics and engineering* 193 (2004), pp. 4117–4137 (cit. on p. 33).

[68] S. Piperno and C. Farhat. “Design of efficient partitioned procedures for the transient solution of aeroelastic problems”. In: *Revue Europeenne des Elements Finis* 9 (2000), pp. 655–680 (cit. on p. 33).

[69] C. Farhat, K. van der Zee, and P. Geuzaine. “Provably second-order time-accurate loosely-coupled solution algorithms for transient nonlinear computational aeroelasticity”. In: *Computer Methods in Applied Mechanics and Engineering* 195 (2006), pp. 1973–2001. DOI: 10.1016/j.cma.2004.11.031 (cit. on pp. 33, 69).

[70] J. Degroote, K. Bathe, and J. Vierendeels. “Performance of a new partitioned procedure versus a monolithic procedure in fluid-structure interaction”. In: *Computational Structures* 87 (2009), pp. 793–801 (cit. on p. 34).

[71] U. Kuttler, M. Gee, C. Forster, and W. Comeford. “Coupling strategies for biomedical fluid-structure interaction problems”. In: *International Journal of Numerical Methods in Biomedical Engineering* 26 (2010), pp. 305–321 (cit. on p. 34).

[72] W. Dettmer and D. Peric. “A computational framework for fluid-structure interaction: finite element formulation and applications”. In: *Computational methods applied to mechanical engineering* 195 (2006), pp. 5754–5779 (cit. on p. 34).

[73] T. Tezduyar and S. Sathe. “Modelling of fluid-structure interaction with the space-time finite elements: solution techniques”. In: *International Journal of Numerical Methods in Fluids* 54 (2007), pp. 855–900 (cit. on p. 34).

[74] W. Wall, S. Genkinger, and E. Ramm. “A strong coupling partitioned approach for fluid-structure interaction with free surfaces”. In: *Computational Fluids* 36 (2007), pp. 169–183 (cit. on p. 34).

[75] U. Kuttler and W. Wall. “Fixed-point fluid-structure interaction solvers with dynamic relaxation”. In: *Computational Mechanics* 43 (2008), pp. 61–72 (cit. on p. 34).

[76] T. Kloppel, A. Popp, U. Kuttler, and W. Wall. “Fluid-structure interaction for non-conforming interfaces based on a dual mortar formulation”. In: *Computational Nethods for applied mechanical engineering* 200 (2011), pp. 3111–3126 (cit. on p. 34).

[77] D. Sternel, M. Schafer, M. Heck, and S. Yigit. “Efficiency and accuracy of fluid-structure interaction simulations using an implicit partitioned approach”. In: *Computational Mechanics* 43 (2008), pp. 103–113 (cit. on p. 34).

[78] Y. Bazilevs, K. Takizawa, and T. Tezduyar. “Computational Fluid-Structure Interactions Mehtods and Applications”. In: *Wiley* (2013) (cit. on pp. 34, 41).

[79] P. L. Tallec and P. Hauret. “Energy conservation in fluid structure interactions”. In: *Computational Mehtods for scientific computing. Variational problems and applications* (2003) (cit. on p. 34).

[80] M. Fernandez, J. Gerbeau, and C. Grandmont. “A proyection algorithm for fluid-structure interaction problems with strong added-mass effect”. In: *Comptes Rendus Mathematique* 342 (2006), pp. 279–284 (cit. on p. 34).

[81] H. Matthies and J. Steindorf. “Partitioned but strongly coupled iteration schemes for nonlinear fluid-structure interaction”. In: *Computers and Structures* 80 (2002), pp. 1991–1999 (cit. on p. 34).

[82] H. Matthies, R. Niekamp, and J. Steindorf. “Algorithms for strong coupling procedures”. In: *Computational Methods Applied to Mechanical Engineering* 195 (2006), pp. 2028–2049 (cit. on p. 34).

[83] L. Formaggia, J. Gerbeau, F. Nobile, and A. Quarteroni. “On the coupling of 3D and 1D Navier-Stokes equations for flow problems in compliant vessels”. In: *Computational Methods Applied to Mechanical Engineering* 191 (2001), pp. 561–582 (cit. on p. 34).

[84] C. Habchi, S. Russeil, D. Bougeard, J. Harion, T. Lemenand, A. Ghanem, D. Valle, and H. Peerhossaini. “Partitioned solver for strongly coupled fluid-structure interaction”. In: *Computers and Fluids* 71 (2013), pp. 306–319 (cit. on p. 34).

[85] T. Tezduyar, S. Sathe, M. Shcwaab, J. Pausewank, J. Cristopher, and J. Crabtree. “Fluid-Structure Interaction modeling of a ringsail parachutes”. In: *Computational Mechanics* 43 (2008), pp. 133–142 (cit. on p. 34).

[86] K. Takizawa, S. Wright, C. Moorman, and E. Tezduyar. “Fluid-Structure Interaction modeling of parachite clusters”. In: *International Journal for Numerical Methods in Fluids* 65 (2011), pp. 286–307 (cit. on p. 34).

[87] S. Rebouillat and D. Liksonov. “Fluid-Structure Interaction in partially filled liquid containers: A comparative review of numerical approaches”. In: *Computers and Fluids* 39 (2010), pp. 739–746 (cit. on p. 34).

[88] Y. Bazilevs, M. Hsu, J. Kiendl, R. Wuchner, and K. Bletzinger. “3D Simulation of wind turbine rotors at full scale. Part II: Fluid-Structure interaction modeling with composite blades”. In: *International Journal for numerical methods in fluids* 65 (2011), pp. 236–253 (cit. on p. 34).

[89] Y. Bazilevs, M. Hsu, I. Akkerman, S. Wright, K. Takizawa, B. Henicke, T. Spelman, and T. Tezduyar. “3D Simulation of wind turbine rotors at full scale. Part I: Geometry modeling and aerodynamics”. In: *International Journal for numerical methods in fluids* 65 (2011), pp. 207–235 (cit. on p. 34).

[90] M. Hsu and Y. Bazilevs. “Fluid-structure interaction modeling of wind turbines: simulating the full machine”. In: *Computational Mechanics* 50 (2012), pp. 821–833 (cit. on pp. 34, 35).

[91] H. Guner, D. Thomas, G. Dimitriadis, and V. Terrapon. “Unsteady aerodynamic modeling methodology based on dynamic mode interpolation for transonic flutter calculations”. In: *Journal of Fluids and Structures* 84 (2019), pp. 218–232 (cit. on p. 34).

[92] E. Jonsson, C. Mader, G. Kennedy, and J. Martins. “Computational Modeling of Flutter Constraint for High-Fidelity Aeroestructural Optimization”. In: *AIAA Scitech 2019 Forum* (2019), p. 2354 (cit. on p. 34).

[93] L. Shyang, C. Ning, Y. Peng, W. Dazhuan, and A. Jerome. “Cyclostationary approach to detect flow-induced effects on vibration signals from centrifugal pumps”. In: *Mechanical Systems and Signal Processing* 114 (2019), pp. 275–289 (cit. on p. 37).

[94] Y. Jiang, S. Yoshimura, R. Imai, H. Katsura, T. Yoshida, and C. Kato. “Quantitative evaluation of flow-induced structural vibration and noise in turbomachinery by full-scale wakly coupled simulation”. In: *Journal of Fluids and Structures* 23 (2007), pp. 531–544 (cit. on p. 37).

[95] I. Hayashi and S. Kaneko. “Pressure pulations in piping system excited by a centrifugal turbomachinery taking the damping characteristics into consideration”. In: *Journal of Fluids and Structures* 45 (2014), pp. 216–234 (cit. on p. 37).

[96] S. Finnveden, F. Birgesson, U. Ross, and T. Kremer. “A model of wall pressure correlation for prediction of turbulence-induced vibration”. In: *Journal of Fluids and Structures* 70 (2005), pp. 1127–1143 (cit. on p. 37).

[97] D. Chase. “Modelling the wavevector-frequency spectrum of turbulent boundary layer wall-pressure”. In: *Journal of Sound and Vibration* 70 (1980), pp. 125–147 (cit. on p. 37).

[98] B. Liu. “Noise radiation of aircraft panels subjected to boundary layer pressure fluctuations”. In: *Journal of Sound and Vibration* 314 (2008), pp. 693–711 (cit. on p. 37).

[99] A. Broatch, P. Olmeda, X. Margot, and J. Gomez-Soriano. “Numerical simulations for evaluating the impact of advanced coatings on H2 additivated gasoline lean combustion in a turbocharged spark-ignited engine”. In: *Applied Thermal Engineering* 148 (2019), pp. 674–683 (cit. on p. 39).

[100] A. Robert, S. Richard, O. Colin, I. Martinez, and I. Francqueville. “LES prediction and analysis of knocking combustion in a spark ignition engine”. In: *Combustion Flame* 162 (2015), pp. 2788–2807 (cit. on p. 39).

[101] C. Burg. “A robust unstructured grid movement strategy using three-dimensional torsional springs”. In: *34th AIAA Fluid Dynamics Conference and Exhibit* 84 (2004), p. 2529 (cit. on p. 39).

[102] C. Farhat, C. Degand, B. Koobus, and M. Losoinne. “Torsional springs for two dimensional dynamics unstructured fluid meshes”. In: *Computational Methods Applied to Mechanica Engineering* (1998), pp. 231–245 (cit. on p. 39).

[103] X. Liu, N. Qin, and H. Xia. “Fast dynamic grid deformation based on Delaunay graph mapping”. In: *Journal of Computational Physics* 211 (2006), pp. 405–423 (cit. on p. 40).

[104] M. Boer A. Schoot and H. Bikil. “Mesh deformation based on radial basis function interpolation”. In: *Computers and Structures* 85 (2007), pp. 784–795 (cit. on p. 40).

[105] F. Gagliardi and K. Giannakoglou. “A two-step radial basis function-based CFD mesh displacement tool”. In: *Advances in Engineering Software* 128 (2019), pp. 86–97 (cit. on p. 40).

[106] S. Jakobsson and O. Amoignon. “Mesh deformation using radial basis functions for gradient-based aerodynamic shape optimization”. In: *Computers and Fluids* 36 (2007), pp. 1119–1136 (cit. on p. 40).

[107] S. Lee, G. Wolberg, and S. Shin. “Scattered Data Interpolation with Multilevel B-Splines”. In: *IEEE Transactions on Visualization and Computer Graphics* 3 (1997), pp. 228–244 (cit. on pp. 41, 79).

[108] T. Tezduyar, M. Behr, S. Mittal, and A. Johnson. “Computation of unsteady incompressible flows with the finite element methods space time formulations, iterative strategies and massively parallel implementations”. In: *New Methods in Transient Analysis* 246 (1992), pp. 7–24 (cit. on p. 41).

[109] T. Tezduyar, M. Behr, S. Mittal, and A. Johnson. “Parallel finite-element computation of 3D flows”. In: *Computer* 26 (1993), pp. 27–36 (cit. on p. 41).

[110] A. Johnson and T. Tezduyar. “Mesh update strategies in parallel finite element computations of flow problems with moving boundaries and interfaces”. In: *Computer Merhods in Applied Mechanics and Engineering* 119 (1994), pp. 73–94 (cit. on p. 41).

[111] J. Vollmer, R. Mencl, and H. Mueller. “Improved Laplacian smoothing of noisy surface meshes”. In: *Computer graphics forum* 18 (1999), pp. 131–138 (cit. on p. 41).

[112] A. Nealen, T. Igarashi, and O. Sorkine. “Laplacian mesh optimization”. In: *Proceedings of the 4th international conference on Computer graphics and interactive techniques in Australasia and Southeast Asia* (2006), pp. 381–389 (cit. on p. 41).

[113] K. Zhou, J. Huang, J. Snyder, X. Liu, H. Bao, B. Guo, and H. Shum. “Large mesh deformation using the volumetric graph laplacian”. In: *ACM transactions on graphics* 24 (2005), pp. 496–503 (cit. on p. 41).

[114] A. Hessenthaler, N. Gaddum, O. Holub, R. Sinkus, O. Rohrle, and D. Nordsletten. “Experiment for validation of fluid-structure interaction models and algorithms”. In: *International journal for numerical methods in biomedical engineering* 33 (2017), e2848 (cit. on p. 42).

[115] Q. Xie and X. Zhi. “Wind tunnel test of an aeroelastic model of a catenary system for high-speed railway in China”. In: *Journal of Wind Engineering and Industrial Aerodynamics* 184 (2019), pp. 23–33 (cit. on p. 44).

[116] H. Bdeiwi, A. Ciarella, A. Peace, and M. Hahn. “Model structure effect on static aeroelastic deformation of the NASA CRM”. In: *International Jounral of Numerical Methods for Heat and Fluid Flo* 184 (2019), pp. 23–33 (cit. on p. 44).

[117] R. Panciroli and M. Porfiri. “Analysis of hydroelastic slamming through particle image velocimetry”. In: *Journal of Sound and Vibration* 347 (2015), pp. 63–78 (cit. on p. 45).

[118] A. Dey, Y. Modarres-Sadeghi, and J. Rothstein. “Viscoelastic fluid-structure interactions between a flexible cylinder and wormlike micelle solution”. In: *Physical Review Fluids* 3 (2018), p. 063301 (cit. on pp. 45, 46).

[119] P. Zhang, S. Peterson, and M. Porfiri. “Combined particle image velocimetry/digital image correlation for load estimation”. In: *Experimental Thermal and Fluid Science* 100 (2019), pp. 207–221 (cit. on p. 45).

[120] M. Palacz. “Spectral Methods for Modelling of Wave Propagation in Structures in Terms of Damage Detection. A review”. In: *Applied Sciences* 8 (2018), p. 1124 (cit. on p. 47).

[121] X. Zhang, M. Fatemi, R. Kinnick, and J. Greenleaf. “Noncontact ultrasound stimulated optical vibrometry study of coupled vibration of arterial tubes in fluids”. In: *Journal of the Acoustic Society of America* 118 (2003), pp. 1249–1257 (cit. on p. 47).

[122] N. Garafolo and G. McHugh. “Mitigation of flutter vibration using embedded shape memory alloys”. In: *Journal of Fluids and Structures* 76 (2018), pp. 495–605 (cit. on p. 47).

[123] O. D.R., B. Rice, S. Peltier, J. Staines, S. Claucherty, and C. Combs. “Simultaneous Stereo Digital Image Correlation and Pressure-Sensitive Paint Measurements of a Compliant Panel in a Mach 2 Wind Tunnel”. In: *AIAA Fluid Dynamics Conference* (2018), p. 3869 (cit. on p. 49).

[124] J. Wood, M. Breuer, and G. De Nayer. “Experimental studies on the instantaneous fluid-structure interaction of an air-inflated flexible membrane in turbulent flow”. In: *Journal of Fluids and Structures* 80 (2018), pp. 405–440 (cit. on p. 49).

[125] P. Sousa, J. Barros, O. Tavares, and P. Moreira. “Digital image correlation diplacement measurement of a rotating RC helicopter blade”. In: *Engineering Failure Analysis* 90 (2018), pp. 371–379 (cit. on p. 49).

CHAPTER 3

Non-Dimensional characterization of Fluid Structure Interaction

Contents

Figures

3.1 Introduction

During the developement of the previous chapter, the main equations governing the Fluid Structure Interaction were presented, and the analysis of the main contributions on the field was performed. It was seen how a moving fluid passing through a structure generates a pressure distribution around it that, when the material is flexible enough, can give rise to the appearance of noticeable displacements. These displacements can, in turn, influence the flow field, resulting in a coupling process between the fluid and the structure, which is normally referred to as Fluid-Structure Interaction (FSI).

Due to the use of increasingly lighter materials and to the increase of computational power availability, the prediction of phenomena related to FSI is becoming an important research topic in numerous engineering applications, such as in micro aerial vehicles, transport of fluids in elastic structures, energy harvesting devices, biomedical engineering or bio-inspired systems.

Thanks to the development of efficient numerical algorithms, some investigations have been performed in the past years in the context of a wide range of applications. Subhash et al. [126] studied the influence of FSI on the sloshing phenomenon in a closed vessel assuming inner potential flow; Eisinger et al. [127] performed numerical simulations in order to predict the onset of the fluid-elastic vibration in an array of tubes excited by a stationary flow; Young [128] used numerical simulations to compare the differences in behavior between a perfectly rigid and a flexible marine propeller, arriving to the conclusion that FSI can be important for large values of the advance ratio, or Gramola [129], who studied the effect of the inclusion of a fluid-deformable bump to control the location of shocks in supersonic supercritical airfoils.

It is apparent that, for the previous works to be possible, important efforts have been devoted to the development of suitable tools able to account for any kind of fluid-structure interaction through the solution of the wholly coupled problem. In this sense, Hubner et al. [130] or Hron et al. [131] developed a monolithic method that can be used for solving strongly coupled problems, but providing a disperse matrix due to the large difference in stiffness between the fluid and the solid. The partitioned approach allows the use of two different solvers for the fluid and the solid domains, being therefore necessary to perform the coupling through inner iterations (strong coupling, see Hermann et al. [132]) or at each time step (loose coupling, see Farhat et al. [69]). For more information, reader is refer to Chapter 2 of the current document, where those methods where more deeply explained.

When facing a problem of Fluid Structure Interaction, it is crucial to dispose

of suitable criteria allowing to determine the strength of the interaction and, consequently, to select the best method to characterize the domain in terms of both accuracy and computational effort. In accordance with the author' s knowledge, such a study has not been properly carried out. In this sense, it is worth to mention the work performed by Wenyong et al. [133]. In this paper, the authors performed an interesting wind tunnel parametric study to predict the onset of the galloping phenomena for the case of a spring supported cylinder. They varied the incoming flow velocity (and, as a consequence, the Reynolds number) and came to the conclusion that, above a critical Reynolds, the galloping phenomenon appears. However, in accordance with the present work, this conclusion can only be partially assumed as they also varied the value of the non-dimensional stiffness parameter which, in fact, will be seen to be the dominant parameter for this kind of predictions. Therefore, the main aim of this chapter is to identify a set of non-dimensional parameters whose order of magnitude may allow to determine the strength of the interaction and the assumptions allowable in each problem considered.

With this purpose, the benchmark problem proposed by Turek et al. [134] is analyzed, varying both the stiffness parameter $\left(K = E/(\frac{1}{2}\rho_\infty V_\infty^2)\right)$, which can be considered to be a form of the Cauchy number (Ca) for analyzing FSI systems. Additionally, the influence of the mass ratio parameter $\left(M = \rho_s/\rho_\infty\right)$ will be analyzed. This problem basically consists of a flexible plate excited by the unsteady laminar flow induced by a two-dimensional (infinite) cylinder located upstream and it is normally used in order to test calculation codes [135].

Some additional work on this benchmark case or similar ones has already been reported. Tang et al. [136] proposed an analytic model to study the flutter instability for the case of a cantilever flexible plate immersed in a constant velocity field with a Reynolds number sufficiently high to neglect the effects of fluid viscosity, concluding that the flutter instability was achieved for a certain value of the non-dimensional stiffness $\left(E/(\rho_\infty V_\infty^2)\right)$. However, this solution cannot be directly applied in cases where the flow field cannot be solved analytically.

More recently, Purohit et al. [137] studied a similar problem in order to characterize the displacement response of a plate, and presented a way of computing the radiated noise due to both the fluid flow and the plate motion. They analyzed the evolution of both the fluid field and the solid when the Young modulus and flow velocity were varied. However, as will be shown later, the number of points studied was too small to allow for the characterization of the whole range of possible FSI phenomena. Finally, similar conclusions can be extracted from the work of Wang et al. [138], who studied numerically the influence of both the position and the stiffness of the plate on the fluid structure

interaction domain. As in the previously mentioned work, however, the selection of only 5 values of the non-dimensional stiffness led to somehow incomplete results, masking the most important phenomena that can be found in this case.

To conclude, another important related reference can be found in Abdi et al. [139]. In this work, they perform a parametric study on the influence of the position of some flexible splitter plates, which are strongly deformed by a laminar flow detached after an infinite cylinder, although they do not identify which kind of Fluid Structure Interaction appears in this case.

The work presented in this chapter tries to complement these previous efforts with a detailed analysis of the Fluid Structure Interaction phenomena appearing in this workbench problem, and to provide a generalizable method to predict the interaction strength and thus, the most adequate tool, based on a parametric study of the most important dimensionless numbers governing these problems.

With this aim, the structure of this Chapter can be sketched as follows: In section 4.3.1, the simple case under study will be presented, as well as the dimensions of the fluid domain which, for reasons of validation, will be the same as those used by the work of Turek et al. [134]. Later, the equations governing the behavior of the coupled system will be introduced and non-dimensionalized, showing which parameters are important for computing a FSI problem.

After that, in section 3.3, the methodology of resolution is validated against the literature data and the complete analysis of the influence of non dimensional stiffness, mass ratio parameter and Reynolds number is carried out.

Finally, in section 3.4, the problem is solved, for the lowest Reynolds number, using one way interaction; segregated explicit approach (with two different values of the time step) and segregated implicit approach. This will allow the construction of the interaction map, presented in section 3.5 which is expected to not be highly influenced by the Reynolds number of the problem.

3.2 Problem Description

Figure 3.1 shows a sketch of the geometry used, which is similar to the one described by Turek et al. [134]. The domain consists of a narrow channel in which a laminar velocity inflow is imposed. In the channel, a rigid two-dimensional circular cylinder is placed, downstream of which a flexible cantilever beam is located. The cylinder diameter is taken to be $D = 0.1\,\mathrm{m}$. Distances upstream and downstream are $L_u = 2D$ and $L_d = 20D$, while the width of the channel is set to $H = 4D$. The length of the plate is $L = 3.5D$, with a thickness $h = 0.2D$.

The origin of the coordinate system is located at the center of the cylinder. The inlet velocity is defined using a parabolic profile, in order to simulate a fully developed laminar flow, as shown in Equation 3.1:

$$V_{inlet}\left(\frac{y}{D}\right) = \frac{3}{2}V_\infty\left[1-\left(\frac{y}{D}\frac{2D}{H}\right)^2\right] \tag{3.1}$$

where V_∞ is the mean inlet velocity which, unless otherwise specified, will be used as the reference value. The flow is assumed to be incompressible, with density $\rho_\infty = 1000\ \mathrm{kg\,m^{-3}}$ and viscosity $\mu = 1\ \mathrm{Pa\,s}$. The deformable plate was assumed to be made of an isotropic linear-elastic material, defined by its Poisson ratio, $\nu = 0.4$; Young Modulus, E and density, ρ_s. In this work, the system response was analyzed as a function of stiffness and density. Thus, the stiffness parameter was varied within the range $2E/\rho_\infty V_\infty^2 \in [2.8\cdot 10^3 - 1.5\cdot 10^7]$ whereas the mass parameter was maintained is varied in the range $\rho_s/\rho_\infty \in [1-1000]$.

In order to compare with the results found in the literature, the Reynolds number was kept constant, with a value $Re = \rho_\infty V_\infty D/\mu = 200$, leading to a value of the free stream mean velocity of $V_\infty = 2\ \mathrm{m\,s^{-1}}$.

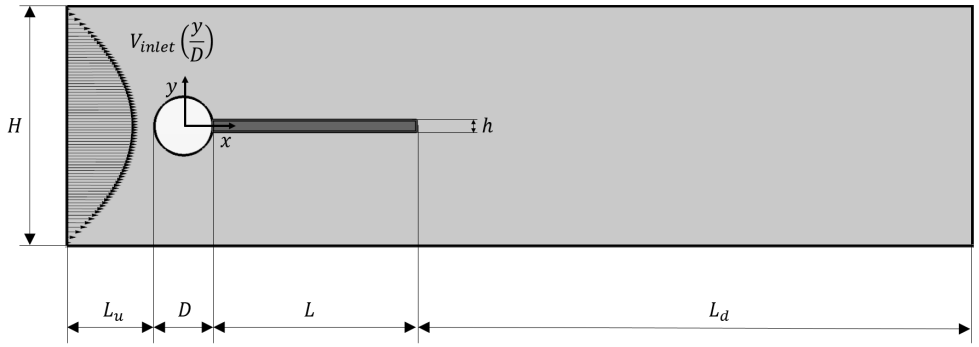

Figure 3.1: Sketch (not to scale) of the case

It is well known that, under these circumstances, a vortex shedding is generated by the rigid cylinder, as can be observed in the works of Kiyoung et al. [140], Unal et al. [141], [142] or Hwang et al. [143], among others. This vortex shedding is responsible of the appearance of fluctuating forces, which excite the structure leading to an unsteady deformation pattern. Depending on the structural properties of the deformable body, those displacements could even affect the flow pattern itself, leading to a fully coupled solution, completely different from the uncoupled solution (Galdi et al. [144]).

In this work, the influence of the body stiffness and mass are analyzed. In particular, special interest was put on the flow patterns, the magnitude and frequency of the forces acting over the whole body and the magnitude and frequency of the displacement of a point located at the tip of the flexible plate.

3.3 Non-Dimensionalization of the equations

3.3.1 Solid body structural model

Making use of the equations of mass and momentum conservation, Equation 3.2 for the displacement field of a deformable solid body can be derived [42]:

$$\rho \frac{\partial^2}{\partial t^2} u_i = \frac{\partial}{\partial x_j} \sigma_{ij} + b_i \tag{3.2}$$

Here, u_i represents the displacement of the solid body along the i direction; b_i is the i-th component of any volume forces present and σ_{ij} are the components of the stress tensor, which can be related to the strain tensor, $\varepsilon_{kl} = 0.5\left(\frac{\partial u_k}{\partial x_l} + \frac{\partial u_l}{\partial x_k}\right)$, by means of Equation 3.3:

$$\sigma_{ij} = c_{ijkl}\varepsilon_{kl} = E c^*_{ijkl}\varepsilon_{kl} \tag{3.3}$$

where E is a characteristic Young Modulus and c^*_{ijkl} are non dimensional constants which, for the case of an isotropic solid with low stress values are given by Equation 3.4 [43]:

$$\begin{aligned} c^*_{iiii} &= \alpha^* = \frac{\nu - 1}{2(\nu+1)\left(\nu - \frac{1}{2}\right)} \\ c^*_{iijj} = c^*_{jjii} &= \beta^* = -\frac{\nu}{2(\nu+1)\left(\nu - \frac{1}{2}\right)} \\ c^*_{ijij} = c^*_{jiji} &= \chi^* = \frac{1}{2(\nu+1)} \end{aligned} \tag{3.4}$$

With these assumptions, Equation 3.2 can be rearranged in vector form in order to render the equation in dimensionless form in accordance with the flow variables as follows:

$$\frac{\rho}{\rho_\infty} \frac{\partial^2}{\partial t^{*2}} \begin{Bmatrix} u^*_x \\ u^*_y \\ u^*_z \end{Bmatrix} = \frac{E}{\frac{1}{2}\rho_\infty V^2_\infty} \frac{1}{2} [Q^*] \begin{Bmatrix} u^*_x \\ u^*_y \\ u^*_z \end{Bmatrix} \tag{3.5}$$

Here, $u^*_i = u_i / L_{ref}$ is the i^{th} component of the displacement, non-dimensionalized using a flow-related reference value, L_{ref}; $t^* = tV_\infty / L_{ref}$ is a characteristic time

of the flow and Q^* is a non-dimensional differential operator that, for the case of an isotropic linear elastic solid, can be calculated by using Equation 3.6:

$$[Q^*] = \begin{bmatrix} \alpha^* \frac{\partial^2}{\partial x^{*2}} + \frac{\chi^*}{2}\left(\frac{\partial^2}{\partial y^{*2}} + \frac{\partial^2}{\partial z^{*2}}\right) & \left(\beta^* + \frac{\chi^*}{2}\right)\frac{\partial^2}{\partial x^* \partial y^*} & \left(\beta^* + \frac{\chi^*}{2}\right)\frac{\partial^2}{\partial x^* \partial z^*} \\ \left(\beta^* + \frac{\chi^*}{2}\right)\frac{\partial^2}{\partial x^* \partial y^*} & \alpha^* \frac{\partial^2}{\partial y^{*2}} + \frac{\chi^*}{2}\left(\frac{\partial^2}{\partial x^{*2}} + \frac{\partial^2}{\partial z^{*2}}\right) & \left(\beta^* + \frac{\chi^*}{2}\right)\frac{\partial^2}{\partial y^* \partial z^*} \\ \left(\beta^* + \frac{\chi^*}{2}\right)\frac{\partial^2}{\partial x^* \partial z^*} & \left(\beta^* + \frac{\chi^*}{2}\right)\frac{\partial^2}{\partial y^* \partial z^*} & \alpha^* \frac{\partial^2}{\partial z^{*2}} + \frac{\chi^*}{2}\left(\frac{\partial^2}{\partial x^{*2}} + \frac{\partial^2}{\partial y^{*2}}\right) \end{bmatrix} \tag{3.6}$$

Thus, for a given fluid excitation and Poisson ratio, Equation 3.5 is dependent of the values of a non-dimensional stiffness parameter, $K = \frac{E}{\frac{1}{2}\rho_\infty V_\infty^2}$, which represents the relative importance of the elastic and fluid forces, and the non-dimensional mass parameter, $M = \frac{\rho}{\rho_\infty}$, which represents the relative importance of the solid and fluid inertia. In order to solve the solid domain, Equations 3.2 are discretized using the Finite Element Method (FEM) via the commercial software $STAR-CCM+$ and written in accordance with Equation 3.7:

$$\mathscr{M}\frac{\partial^2}{\partial t^2}\mathbf{u} + \mathscr{K}\mathbf{u} = \mathbf{f} \tag{3.7}$$

where $\mathscr{M}$ and $\mathscr{K}$ are the mass and stiffness matrices, respectively, and $\mathbf{f}$ represents the nodal forces. Those parameters are influenced by both the material and the shape of the solid body. During the development of this investigation, very low values of stiffness were expected and, thus, very high displacements were obtained. As a consequence of this, $\mathscr{K}$ is not expected to be constant during the whole time history. Thus, this matrix need to be updated. A Newton-Raphson methodology was used with this aim, in a similar way as in the works of Haisler et al. [145] or Wood et al. [146], resulting in a structurally non-linear behavior when the displacements are sufficiently large. With the aim of confirming the necessity of such an update, the results shown below were also compared with those obtained without updating the matrices.

Finally, the solid beam is discretised using a structured mesh with mid-size nodes with a constant size of $0.045D$, resulting in a solid mesh of 400 cells. As an example, Figure 3.2 shows the computational solid mesh used in an arbitrary deformed configuration (top) and in the original non-deformed configuration (bottom). Notice how, as displacements can be of the order of the characteristic fluid length, D, the updating of the matrices will be necessary for low stiffness cases.

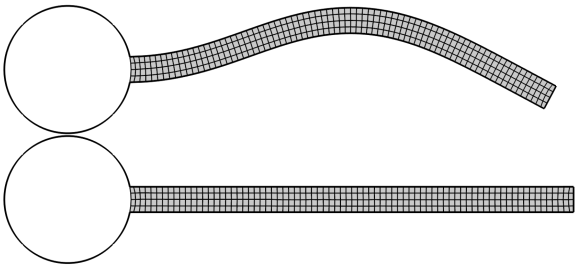

Figure 3.2: Sketch of the solid mesh for a deformed (up) and undeformed (down) configuration

3.3.2 Navier-Stokes Equations

The flow is governed by the Navier-Stokes equations, which express the laws of mass and momentum conservation, and are shown next for an incompressible flow [14].

$$\begin{cases} \dfrac{\partial \mathrm{v}_i}{\partial x_i} = 0 \\ \dfrac{\partial \mathrm{v}_i}{\partial t} + \mathrm{v}_j \dfrac{\partial \mathrm{v}_i}{\partial x_j} = -\dfrac{1}{\rho}\dfrac{\partial p}{\partial x_i} + \dfrac{\partial}{\partial x_j}\left(\tau_{ij}\right) \end{cases} \tag{3.8}$$

where v_i represents the component in the i^{th} direction of the velocity field; p represents the pressure field and τ_{ij} are the components of the fluid shear stress tensor. Due to the low Reynolds number used for the current case (Re = 200), these equations can be solved without introducing any turbulence model with a relatively coarse mesh; additionally, 2D flow can be assumed, as inferred from the works of Humphrey et al. [147], Sahu et al. [148] or Smith et al. [149].

In a similar way as it was done with the solid stress equations, the Navier -Stokes equations can also be non-dimensionalised in order to obtain:

$$\begin{cases} \dfrac{\partial \mathrm{v}_i^*}{\partial x_i^*} = 0 \\ \dfrac{\partial \mathrm{v}_i^*}{\partial t^*} + \dfrac{\partial}{\partial x_i^*}\left(\mathrm{v}_j^* \mathrm{v}_j^*\right) = -\dfrac{1}{2}\dfrac{\partial}{x_i^*} p^* + \dfrac{1}{\mathrm{Re}}\dfrac{\partial}{\partial x_j^*}\left(\dfrac{\partial \mathrm{v}_i^*}{\partial x_j^*} + \dfrac{\partial \mathrm{v}_j^*}{\partial x_i^*}\right) \end{cases} \tag{3.9}$$

Here, $\mathrm{v}_i^* = \mathrm{v}_i / V_\infty$ is the i^{th} component of the velocity vector non-dimensionalised with a reference fluid velocity, V_∞, and $p^* = \frac{p}{\frac{1}{2}\rho_\infty V_\infty^2}$ is the static pressure, non-

dimensionalised by a reference dynamic pressure. These equations were discretised and solved using the commercial software *STAR-CCM+*. When discretising the equations it has to be noted that, as the solid body is expected to move, the contribution of the mesh movement has to be included in the equations. This can be carried out by the inclusion of a source term, in a similar way as done in the works of Yu et al. [150], Gao et al. [151] or Demirdzic et al. [152]. More often, and it is the methodology followed in this work, the inclusion of these displacements and velocities on the resolution fluid flow is performed by the use of an Arbitrary Lagrangian Eulerian (ALE) formulation, [153].

In order to discretize the fluid domain, a polygonal mesh is used. The mesh is set to a size of $7.5 \times 10^{-3} D$ at the wall; a near-field refinement zone with a size of $5 \times 10^{-2} D$ near the body and with a size of $7.5 \cdot 10^{-2} D$ at the wake. In order to ensure time-step and grid size independence, as it will be shown later, the maximum admissible size is set to $2.5 \cdot 10^{-1} D$ for the whole domain. These sizes result in an unstructured mesh of $N = 50000$ cells. About the time step, Δt, it is chosen so that $\Delta t V_\infty / D = 0.02$, which ensured a maximum value of the Courant–Friedrichs–Lewy (CFL) number below 0.50 for the whole fluid domain.Figure 3.3 shows a sketch of the fluid mesh for the undeformed configuration.

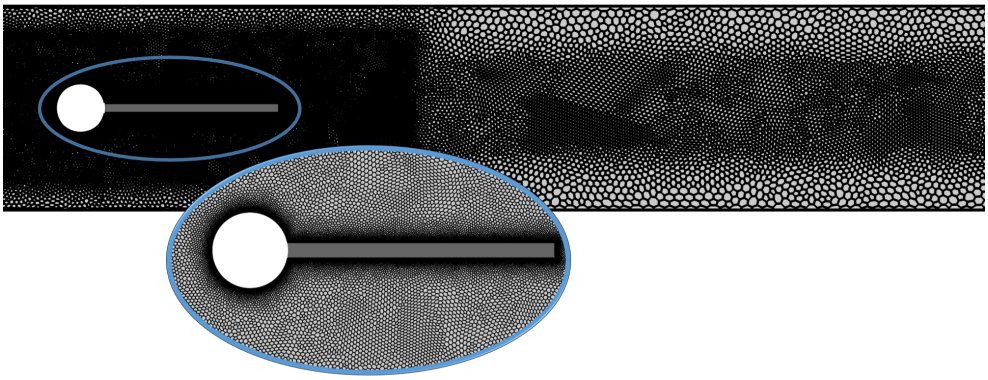

Figure 3.3: Sketch of the fluid mesh for the undeformed configuration

In order to initialize the fluid-structure interaction case, the perfectly rigid case is solved first. The fluid flow over the undeformed configuration is solved with an unsteady methodology until a statistically stationary vortex shedding solution was obtained. As an example, Figure 3.4 shows the contours of non dimensional vorticity $\frac{\omega D}{V_\infty}$ for this initial case at four arbitrary time steps. The Strouhal number for the vertical force was found to be St = 0.107.

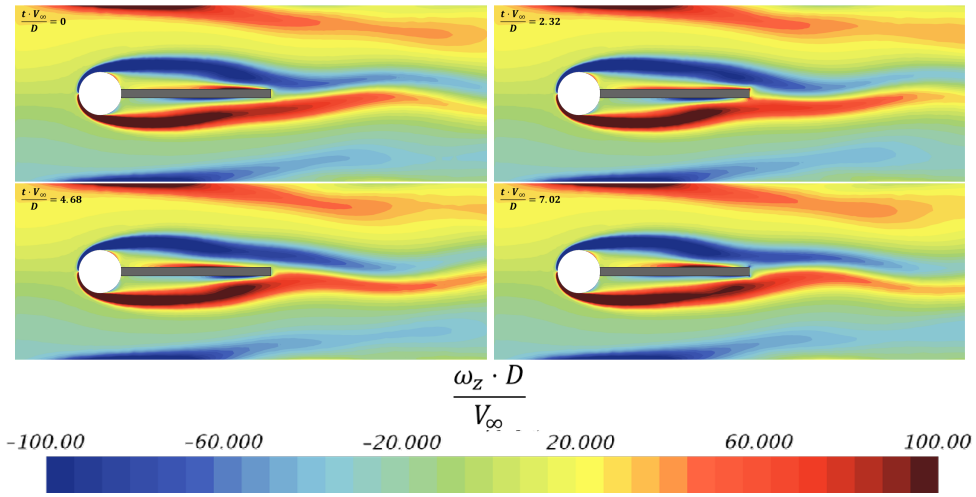

Figure 3.4: Contours of vorticity for the initial rigid state

3.3.3 Coupling of the physical domains

The movement of the solid body leads to the appearance of a wall velocity and a change of the form of the fluid domain, as can be deduced from the works of Tallec et al. [61], Souli et al. [153] or Heil [154]. Thus, the fluid mesh must be changed in accordance with the calculated solid displacements using a morphing algorithm redistributing the wall displacements over the mesh vertices. The morpher generates an interpolation field for the region and translate the mesh vertices to their new positions. More information about the morpher and the interpolation process can be found at Lee et al. [107] and reader could also refer to Chapter 2 of this document. As an example, Figure 3.5 shows the deformed fluid and solid meshes for an arbitrary value of the wall displacements. As very high mesh displacements are expected, the deformed configuration is always computed from the original form, in order to ensure the method is capable to predict periodic response and that the mesh quality is no jeopardized during the whole calculation.

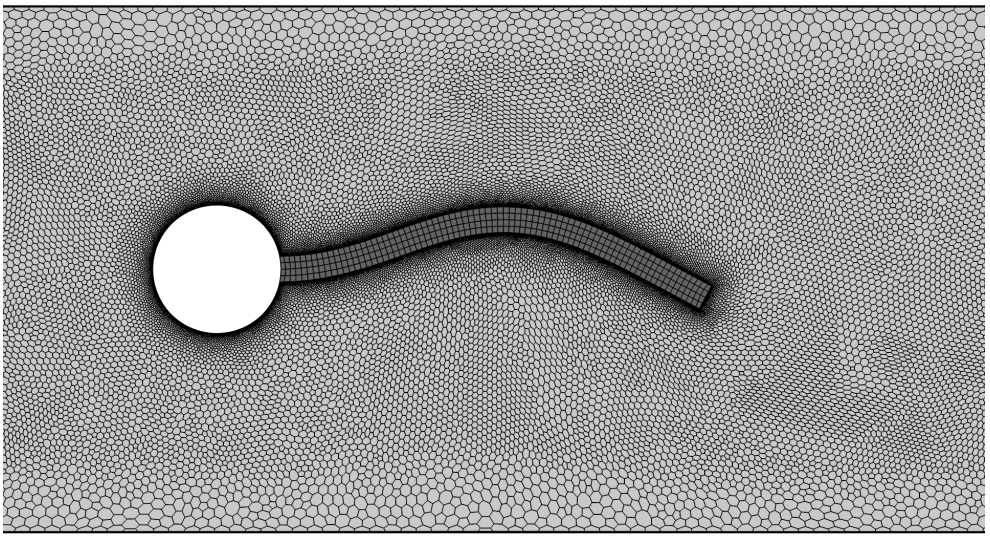

Figure 3.5: Sketch of the fluid and solid meshes for an arbitrary deformation

The fluid pressure and tangential stresses act over the solid domain surface by means of the stress compatibility boundary condition, which is shown at Equation 3.10:

$$p\delta_{ij}n_j + \tau_{ij}n_j = c_{ijkl}\frac{1}{2}\left(\frac{\partial u_k}{\partial x_l} + \frac{\partial u_l}{\partial x_k}\right)n_j \tag{3.10}$$

Where δ_{ij} represents the Kronecker delta and n_j is the j^{th} of the normal vector of the wall where the boundary condition is applied at. These Equations could be non-dimensionalized in order to obtain:

$$\frac{1}{K}\cdot\left(p^*\delta_{ij}+2\frac{1}{Re}\tau^*_{ij}\right)n_j = c^*_{ijkl}\frac{1}{2}\left(\frac{\partial u^*_k}{\partial x^*_l}+\frac{\partial u^*_l}{\partial x^*_k}\right)n_j \tag{3.11}$$

Where it can be deduced how, as expected, for a given Reynolds number and geometry, the strength of the interaction will be highly affected by the value of the stiffness parameter, $K = E/(\frac{1}{2}\rho_\infty V_\infty^2)$, representing the relative importance between the elastic and the fluid forces and the solid to fluid density ratio, $M = \frac{\rho_s}{\rho_\infty}$, which represent the inertial ratio between the moving solid and the displaced fluid. In fact, it can be observed how the whole incompressible fluid-structure domain can be expressed as follows:

$$f\left(\frac{\mathbf{u}}{L_{ref}},\frac{\mathbf{v}}{V_\infty},\frac{p}{\frac{1}{2}\rho_\infty V_\infty^2},\mathrm{Re},\frac{E}{\frac{1}{2}\rho_\infty V_\infty^2},\frac{\rho}{\rho_f}\right)=0 \tag{3.12}$$

The interaction problem is faced by appliying four different strategies, in order to be able to reach a general conclusion for the importance of each non dimensional number on the determination of the most suited tool. These strategies are briefly summarized below:

- First, an implicit segregated methodology is performed, with a total of 30 coupling steps. Due to the expected high value of the displacements, the morphed mesh is computed from the rigid configuration, in order to ensure that the quality of the grid is maintained, even when displacement is high. At this stage, an additional distinction is made between using a linear and a non-linear structural model.
- Additionally, the problem is faced using a one way coupling methodology, in order to specify for which range of the problem parameters this approximation is accurate enough.
- In order to generate an interaction map, indicating the most suitable strategy for each combination of parameters, the case will be also analyzed using an explicit coupling with a time step of $\Delta t V_\infty/D = 0.02$ showing the zones at which this strategy can provide converged solutions.
- Finally, the problem is solved with an explicit segregated methodology of very low time step $\Delta t V_\infty/D = 0.002$.

During the next section, special care will be taken with how the stiffness parameter, K, affects the coupled response and the force of the interaction; later, the influence of the mass parameter will be taken into account and finally, it will be shown how the influence of the Reynolds number is of second order for computing the importance of the coupling and, therefore, for selecting the most proper simulation method.

3.4 Results

3.4.1 Validation of the methodology

In order to validate the numerical methodology described above, a case with $K = 2800$ and $M = 1$ was analyzed in detail and the results were compared with those of Turek et al. [134] paying special attention to the value of the fluctuating lift and drag forces and to the horizontal and vertical tip displacement. Once the pressure and shear stress distribution were calculated around the body, they can be integrated and non-dimensionalized in order to obtain the total force coefficients, as indicated by Equation 3.13:

$$\begin{Bmatrix} C_D \\ C_L \end{Bmatrix} = \frac{2}{\rho_\infty V_\infty^2 D} \oiint_\Gamma (-p\mathbf{I} + \tau)\, \vec{n}\ \mathrm{d}S \tag{3.13}$$

where Γ represents a closed surface comprising both the rigid and the flexible parts of the obstacle and $\mathbf{I}$ is the identity matrix. The value of these forces is shown in Figure 3.6, where good agreement is observed between the two predictions, both in the level and the frequency of the oscillations. The lift force oscillates with a frequency given by $\mathrm{St}_{C_L} = 0.137$ between $C_{L_{min}} = -0.78$ and $C_{L_{max}} = 0.78$ whereas the drag force oscillates with a frequency such that $\mathrm{St}_{C_D} = 2 \cdot \mathrm{St}_{C_L} = 0.274$ between $C_{D_{min}} = 2.16$ and $C_{D_{max}} = 2.39$. Points A, B, C and D simply represent some characteristic time instants of the cycle and are indicated as they will facilitate the interpretation of Figure 3.8.

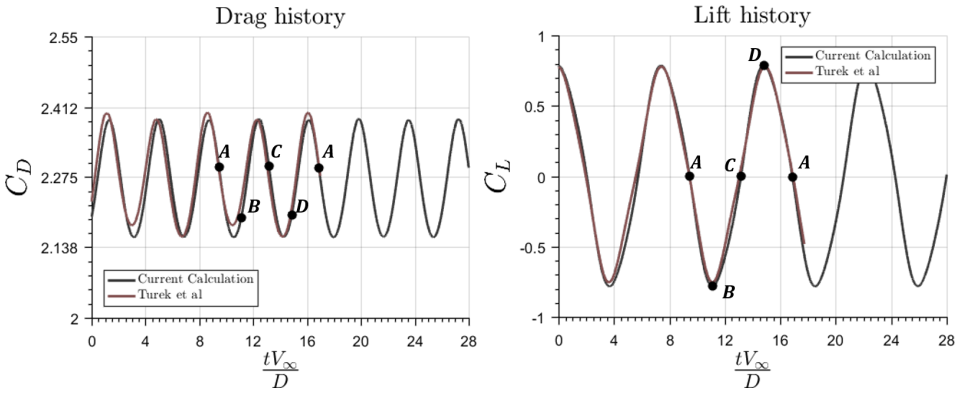

Figure 3.6: Drag (left) and Lift (right) coefficients, comparison with the literature

Similarly, the horizontal and vertical tip displacements are shown in Figure 3.7, where again good agreement between the current calculation and the data

extracted from the literature is observed. It is important to notice that, due to the non-linearity of the system, the forces and their respective displacements are not in phase. In fact, a phase shift of $\phi_{C_L,u_y} = 115$ deg can be observed between the lift coefficient and the vertical displacement while the phase shift between the drag coefficient and the horizontal displacement is $\phi_{C_D,u_x} = 146°$.

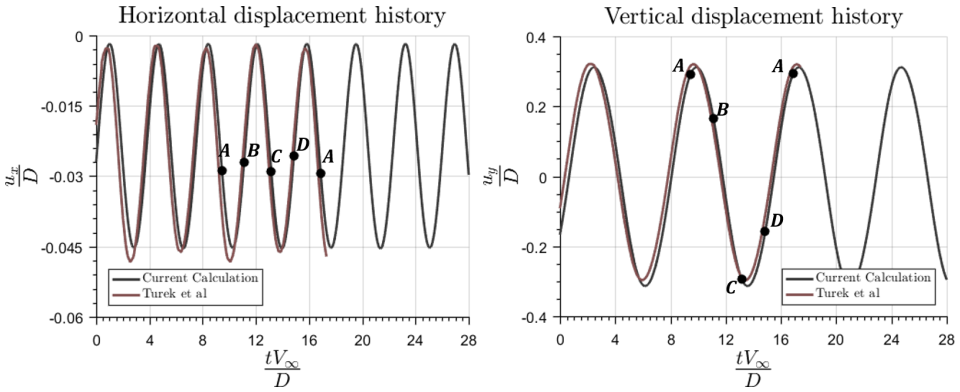

Figure 3.7: Horizontal (left) and vertical (right) displacement coefficients, comparison with the literature

Figure 3.8 shows four flow states corresponding to a full lift period of the problem, whereas in Figure 3.9 the limit cycle of the lift coefficient vs the vertical displacement and the drag coefficient vs the horizontal displacement are shown, and the points corresponding to the states indicated in Figure 3.8 are highlighted. These figures in conjunction provide an intuitive explanation of the phenomena governing the fully-coupled Vortex-Induced Vibration present in this problem, as follows:

- Point (A): three different mechanisms can be identified for the generation of lift at this stage, their joint contribution resulting in a zero net vertical force: (1) due to the Coanda effect, the splitter tends to deflect the flow in such a way that a negative contribution to the lift force is generated; (2) the splitter experiences a (small) displacement with a net positive velocity in the y direction, giving rise to fluid forces opposing this movement, and generating a negative contribution to the lift force, and (3) the vortex which was previously shed at the bottom side of the plate would produce itself a positive lift force. The contribution of the three mechanism produces, as a result, a null net value of the lift coefficient.
- Point (B): the elastic forces tend to return the structure to its equilibrium state, decreasing the value of the vertical displacement. At the same time,

a new vortex has been just shed at the upper part of the domain. As a consequence, at this stage negative lift generation by mechanisms (1) and (3) is maximized and this variable reaches its minimum value.

- Points (C) and (D): these are specular states from (A) and (B), respectively, and thus exactly the same explanation can be given for both of them, just changing the sign of the contribution of the different mechanisms.

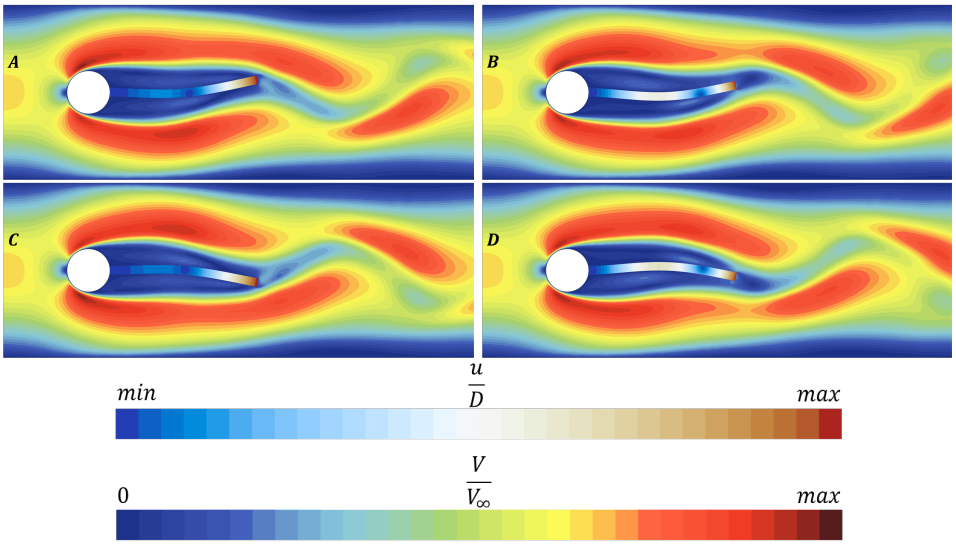

Figure 3.8: Evolution of the vortex shedding during a half period. Velocity and displacement contours. The colormap should be interpreted in a qualitative manner

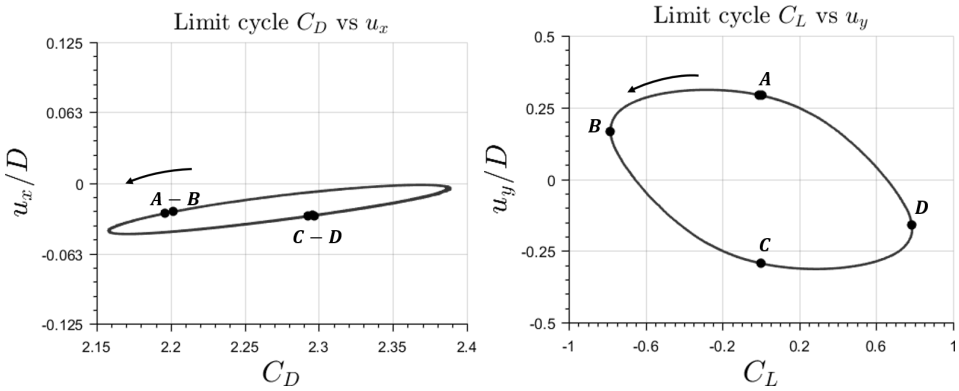

Figure 3.9: Representative limit cycles of the problem

Despite the excellent agreement between the computed response and the results extracted from the literature, it is interesting to perform a study of how the grid size would influence the response. In this sense, Figure 3.10 shows the temporal evolution of the lift and drag coefficients and the displacements for different meshes: Mesh 0 correspond to a coarse grid with a number of cells for the fluid domain of $N_0 = 10^4$; Mesh 1 is a computational mesh with $N_1 = 2.5 \cdot 10^4$; Mesh 2 corresponds to the mesh sketched during Section 3.3, with $N_2 = 5 \cdot 10^4$. Finally, the finest mesh, Mesh 4, is conformed by $N_3 = 1 \cdot 10^5$ elements. Figure 3.10 shows the evolution of the force coefficients and tip displacements for each of the listed meshes. Note how, when $N > N_2$ the response does not substantially changes with the chosen discretization. Therefore, as it is computationally affordable and safer, the third mesh, with $N = 5 \cdot 10^4$ elements will be chosen for the rest of the chapter.

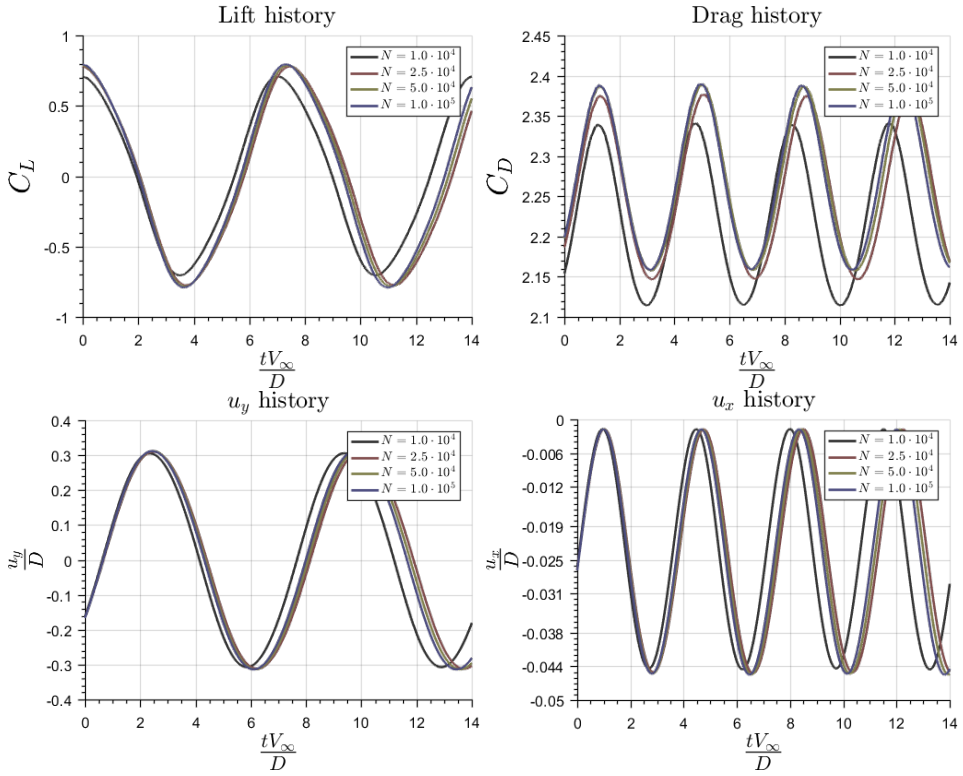

Figure 3.10: Grid independence study, evolution of the lift, drag and tip displacement for different grid resolutions

3.4.2 Parametric study for a low mass ratio

One of the main objectives of this chapter is to provide a good understanding of the mechanisms governing the Fluid Structure Interaction of a simple structure for a wide range of operation parameters. In order to do so, a large number of different working conditions were simulated, using a more dense distribution for those zones which exhibit high gradients of the variables of interest, in order to obtain interpretable global results and to ensure that all the relevant states are properly considered. In order to infer the most adequate structural model for each K value, in this section, each working point was calculated using different assumptions, as follows: (a) 1-way coupling when the displacement of the structure has a negligible influence over the fluid field; (b) 2-way coupling with linear displacements (the mass and stiffness matrices of the structure are assumed to be constant during the whole simulated history) and (c) 2-way coupling with recalculation of the stiffness matrix of the structure for each time step (and thus introducing non linear terms in the structural model).

Figure 3.11 (left) shows the value of the maximum lift coefficient for $M = \rho_0/\rho_\infty = 1$, as a function of the non dimensional stiffness parameter, K. Notice that well differentiated regions can be identified in the maximum lift coefficient as the relative stiffness is decreased. The average drag coefficient remains almost constant, and, for reasons of brevity is not shown in this document. Figure 3.11 (right) shows the dominant Strouhal number of the lift coefficient and, indeed, the same regions as in the left plot can be identified. For all the cases studied, the dominant frequency of the drag coefficient results to be twice the frequency corresponding to the lift coefficient.

Figure 3.12 (left) shows the evolution of the maximum vertical displacement experienced by the structure tip. The behavior is qualitatively similar to that observed for the lift coefficient except that, for very low values of the stiffness, the vertical displacement was found to have a negative slope ($\mathrm{d}u_y/\mathrm{d}K) < 0$, contrary to the slope shown by the lift coefficient ($\mathrm{d}C_L/\mathrm{d}K) > 0$, meaning that, for low values of the non dimensional stiffness, decreasing of this parameter leads to an increase of the vertical displacement and a decrease of the computed vertical force.

Figure 3.12 (right) shows the tip averaged horizontal displacement, and it is observed that it is not noticeable until the stiffness decreases below a certain threshold value. For relatively softer materials the absolute value of u_x increases abruptly. Additionally, this Figure shows the computed vacuum eigenfrequency of the structure.

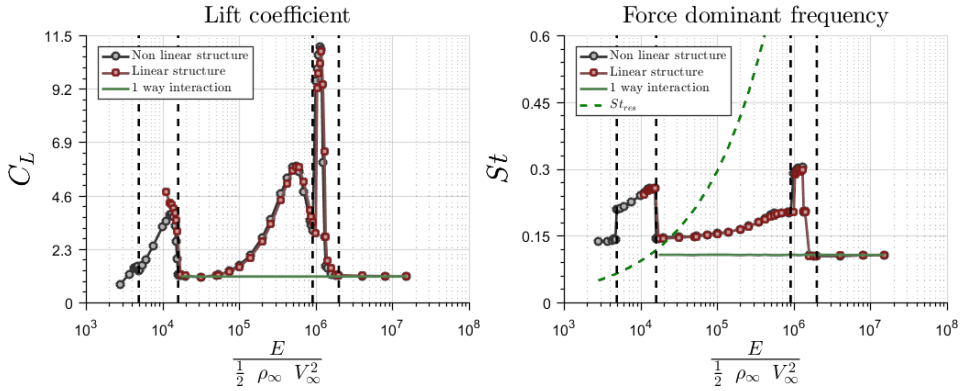

Figure 3.11: Maximum lift coefficient and averaged drag (left) and frequency of the lift force (right) for $M = 1$

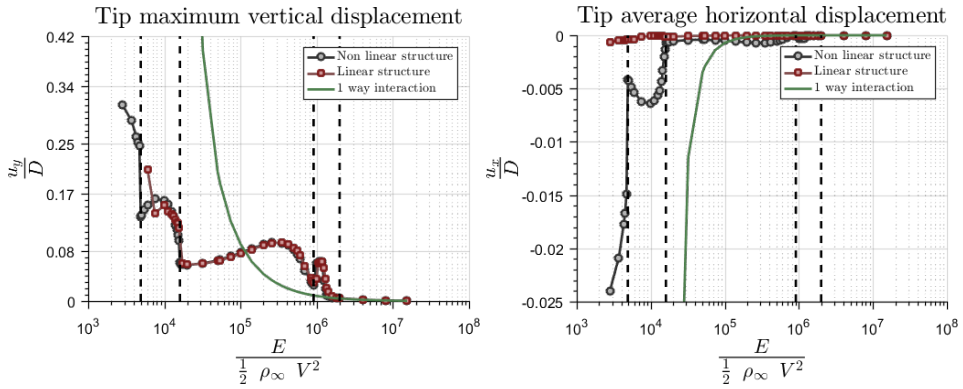

Figure 3.12: Maximum lift coefficient and averaged drag (left) and frequency of the lift force (right) for $M = 1$

As it has been explained, Figure 3.11 and Figure 3.12 show up to five clearly differentiated regions, which are neatly distinguished both by the force and the coupling mechanism between the structure and the fluid flow. These regions can be defined as follows. For an easier interpretation of the excited structural modes, please refer to the following sections:

- Region I. $K \in [2 \times 10^6 - \infty]$. A 1-way interaction region where the response of the structure is completely dominated by the flow and no feedback occurs. The Strouhal number corresponds to that of the rigid case, as for the maximum lift coefficient, which remains constant. The maximum value of the vertical tip displacement is inversely proportional to the stiffness parameter. The first mode is the dominant structural mode.

- Region II. $K \in [9.1 \times 10^5 - 2 \times 10^6]$. A flutter-like region, where the fluid flow injects energy into the structure with a very low value of dissipation. As a consequence, the displacement abruptly increases up to a value of approximately $u_y/D \approx 0.06$. For stiffness values below this range, the frequency of the displacement is not that of the rigid case anymore, but instead is controlled by the non-linear coupling between flow and structure, thus leading to a zone controlled by a lock-in phenomenon. This coupling produces a narrow, abrupt peak in the lift coefficient, which reaches values higher than 10. The structure can still be considered geometrically linear, but the coupling cannot. The first mode is the dominant structural mode.

- Region III. $K \in [1.6 \times 10^4 - 9.1 \times 10^5]$. A post- flutter region, where both the force coefficient and the displacement return to a soft-like behavior. The displacement reaches a maximum of $u_{y_{max}}/D \approx 0.09$ for $K \approx 2.6 \times 10^5$ while the same can be observed for the lift coefficient at $C_{L_{max}} \approx 5.85$ for $K \approx 5.5 \times 10^5$. The structure can still be considered geometrically linear and any modes other than the first structural mode are excited.

- Region IV. $K \in [4900 - 1.6 \times 10^4]$. This new region is characterized by the onset of the excitation of the second structural mode. Notice how the assumption of linear structure allows to obtain accurate results for the lift coefficient, the vertical displacement and the frequency of the forces for a wide range of K in this region. However, this region delimits the range of stiffness in which the structural behavior should be considered as non-linear. Notice also that at the lower limit of this region the frequency of the perfectly rigid case is virtually the same as the first eigenfrequency of the isolated structure.

- Region V. $K \in [0 - 4900]$. In this region the lift coefficient tends to values lower than those found in the 1-way coupling region. The low value of the

stiffness leads to deformations which are of the same order of magnitude as the body characteristic length, so that the linear structural model is not valid anymore. This region is characterized by a very high increment of the tip horizontal displacement. The second solid eigenfrequency starts to be important for the solid movement.

In parallel to the well differentiated regions previously discussed, important behavior differences can be also observed in the displacement field. Figure 3.13 shows the limit cycle followed by the tip displacement. Figure 3.13 (left) shows the tip displacement for non dimensional stiffness corresponding to Regions I, II and III. The trajectory follows a quasi-parabolic path. Figure 3.13 (right) shows the same parameter but corresponding to regions III, IV and V. Regions I, II, III and III, IV, V are shown in different plots in order to facilitate the interpretation of the results. Notice that, as the horizontal displacement becomes significant, a hysteresis phenomenon can be observed, and the tip reaches the 8-like path that has been extensively reported in the literature (see, for instance, Bhardwaj et al. [155], Nayer et al. [156], Wang et al. [138], Gedikli et al. [157] or Sarpkaya [158]). For a better understanding, two different graphics with different scales had to be used in this explanation. The displacement corresponding to Region III is shown both in the left and right plots for comparison.

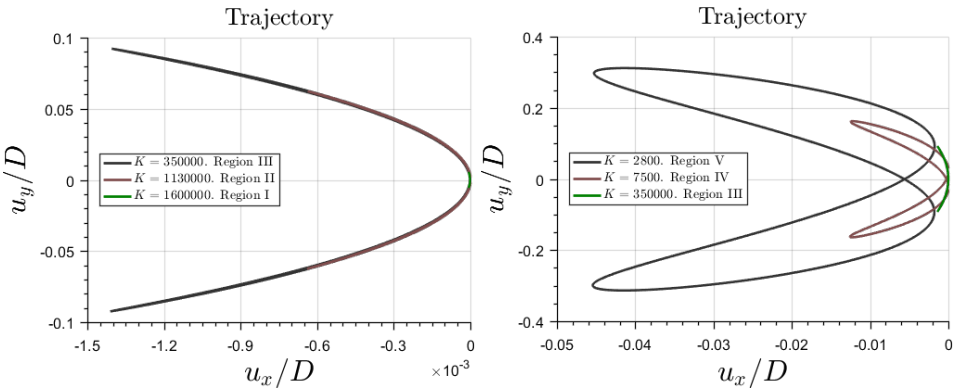

Figure 3.13: Tip trajectory for stiffness belonging to Regions I, II and III (left) and III, IV and V (right)

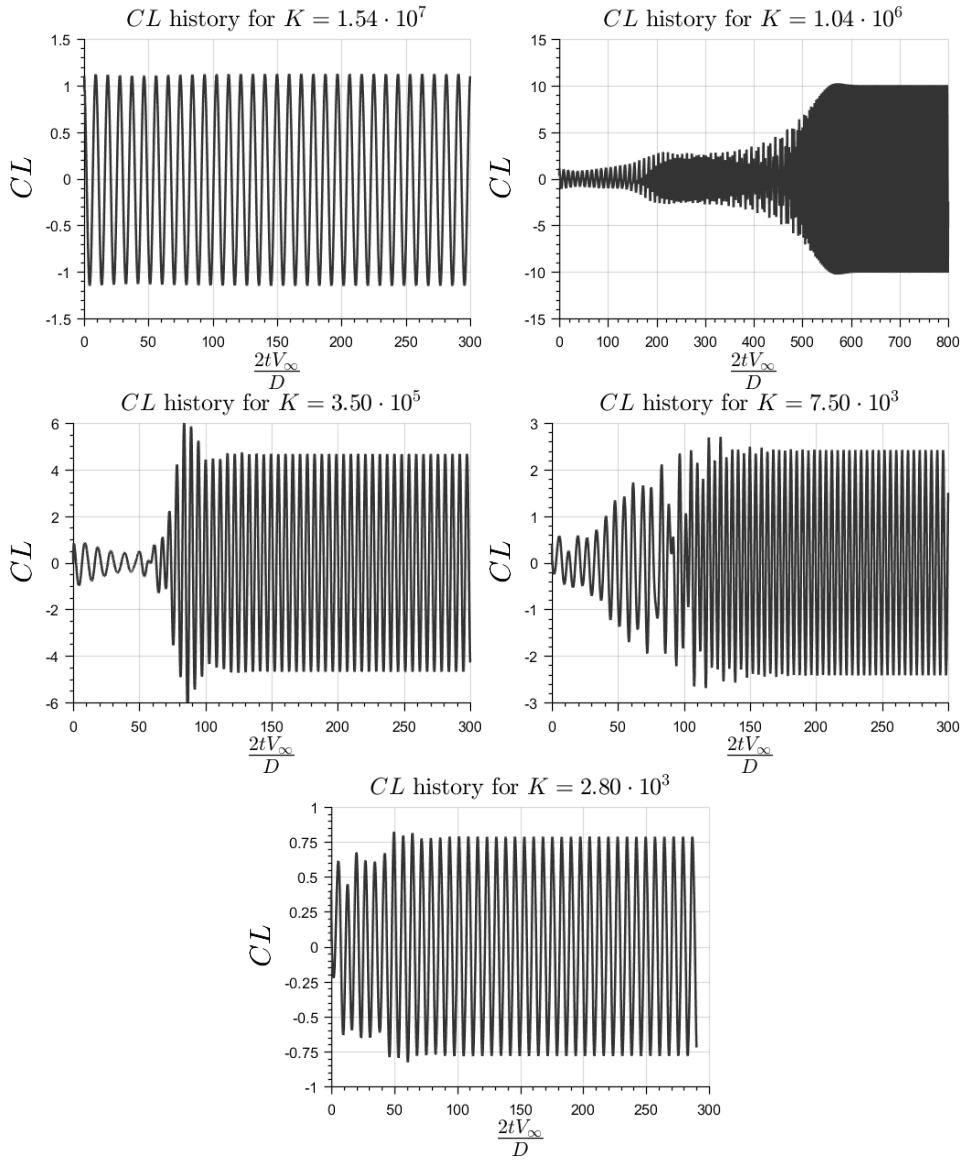

Figure 3.14: Lift coefficient transient evolution for stiffness belonging to Regions I, II, III, IV and V

Figure 3.14 shows the time history of the vertical force coefficient values for K corresponding to each of the regions identified. Due to the numerical setup descried in Section 4.3.2, the value of the lift coefficient at $t = 0$ is the same in all the cases. It can be observed that, except for the case $K = 1.04 \cdot 10^6$, all the responses reach a statistically stationary state for $2tV_\infty/D > 200$. Additionally,

for the case with $K = 1.54 \cdot 10^6$ a statistically stationary C_L history can be considered since the start of the simulation, due to the quasi-1-way coupling.

In the case with $K = 1.04 \cdot 10^6$, corresponding to Region II, a completely different time response was obtained. For $2tV_\infty/D < 150$ the response appears to be the same as that calculated for the perfectly rigid case, consistently with the fact that Region II is characterized by a flutter-like instability. However, the fluid-structure interaction leads to a slow system destabilization which converges to a limit cycle oscillation for $2tV_\infty/D > 600$, characterized by an abrupt increment of the Strouhal number and by very high values of the force coefficient. Due to the long characteristic time of this behavior, the computational effort is higher in this region, simply due to the need of increasing the simulation time. This result agrees well with those reported by Huang [159] or Tang et al. [160]-[161].

This fact can be easily observed in Figure 3.15, where four plots representing the whole history of this case are shown in order to better understand the phenomenon, that can be described as follows:

- $\mathbf{2tV_\infty/D = 0 \in [0, 200]}$ the system behavior is characterized by a low value of the oscillating lift coefficient with a dominating frequency of St ≈ 0.104. At the end of this period, the unstable behavior starts to be noticeable: The lift coefficient starts to increase and a new frequency appears at St ≈ 0.305.
- $\mathbf{2tV_\infty/D = 0 \in [200, 400]}$ the coupled domain exhibits a bounded value of C_L between -3 and 3. However, no isolated dominating frequency exists.
- $\mathbf{2tV_\infty/D = 0 \in [400, 600]}$ during this period only the frequency corresponding to St ≈ 0.305 survives. The lift coefficient starts to increase until reaching values of $CL \approx 10$.
- $\mathbf{2tV_\infty/D > 600}$ the fluid-structure coupled response is completely stabilized. Only one dominating frequency is found and the lift coefficient oscillates stably with a high amplitude.

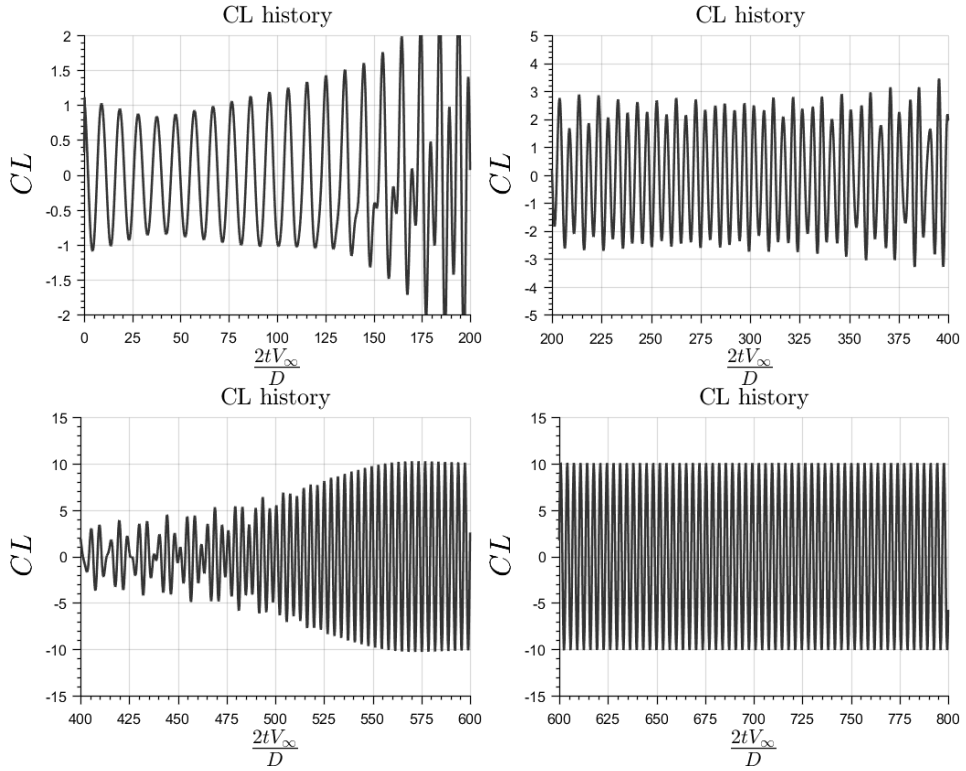

Figure 3.15: Lift coefficient transient evolution for stiffness belonging to Region II.

3.4.3 Parametric study for different values of the mass ratio

Once the behavior of the FSI system for a low value of the mass ratio parameter has been extensively analyzed it is important to introduce how these results will be affected by ρ_s/ρ_∞. In order to do these, the previous methodology was reproduced for a wide number of the non dimensional mass. However, for reasons of brevity, only three different mass ratios is shown in this subsection. Additionally, as will be sketched at section 3.5, the solution using an explicit and a one-way methodologies was obtained. Next results are those corresponding to the implicit method.

For instance Figure 3.16 (left) shows the evolution of the lift coefficient for three different values of the non dimensional mass parameter as a function of $E/(\frac{1}{2}\rho_\infty V_\infty^2)$. Note how, for the three sketched cases, the evolution into a 2 way coupled system appears in a form of a flutter-like instability, similarly as it was previously discussed. However, a new trend can be observed here: As the mass ratio becomes larger, the instability region appears for higher levels of the non-dimensional stiffness. Although this fact has been already observed for the case of the appearance of flutter of wings and airfoils, it has not been observed on more generic cases, with degrees of freedoms in multiple directions.

Additionally, observe how, for the case of medium mass ratio, exactly the same regions sketched in the previous section can be observed while, for the case with $M = 100$ regions IV and V are not shown. This is due to the following: as it will be later checked, for very low values of stiffness the higher mass cases tend to show much higher values of the displacements. In consequence, it was supposed that, when the displacement exceeds certain threshold, the linear behavior of the Young's modulus would not hold anymore and, in consequence, the data under these circumstances was not taken into consideration during this work.

The behavior of the non dimensional dominant frequency of the lift coefficient (note that, similarly as before it is the same than the vertical deformation frequency and half the drag coefficient frequency) shows similar qualitative trends for the three shown values of the non dimensional mass. However, as similar to the lift coefficient, the beginning of the lock-in phenomenon (at which the system frequency is dominated by the fluid structural coupling) is observed for higher values of stiffness when the non dimensional mass is increased. However, note how the increment on the value of the non dimensional frequency between the one way and two way coupling zones is reduced as the mass ratio grows: while for the case of $M = 10$ the frequency is increased by a factor of approximately 2.80 this increment is reduced to a factor of 1.90 for the case with $M = 100$. This tend is in agreement with the expected decrease on the frequency sketched by the relationship between the resonance frequency and stiffness and mass ratio which can be written, in non dimensional form, as $\mathrm{St}_{res} = C_i \sqrt{K/M}$.

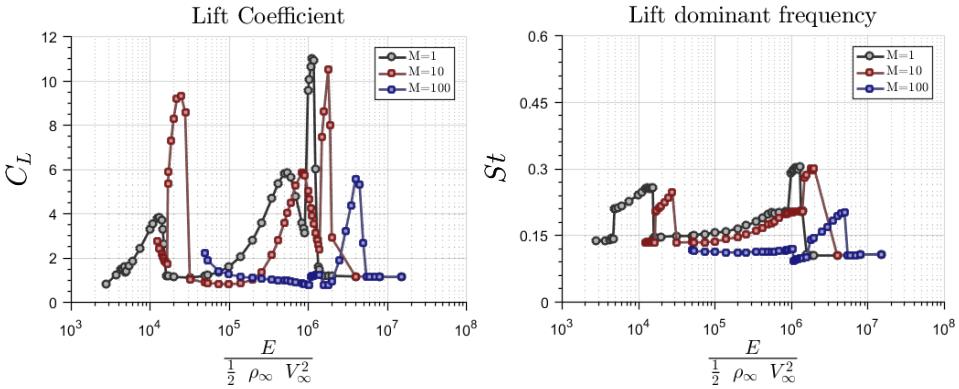

Figure 3.16: Maximum lift coefficient (left) and lift dominant frequency (right) as a function of the non dimensional stiffness for low ($M = 1$), medium ($M = 10$) and high ($M = 100$) mass ratio

Figure 3.17 shows the evolution of the computed maximum tip vertical displacement (left) and the average tip horizontal displacement (right) as a function of the non dimensional stiffness for the same three different values of the non dimensional mass. Note how, for the higher dimensional mass, the maximum vertical displacement is obtained for higher values of the non dimensional stiffness. Furthermore, an interesting conclusion can be extracted from this picture: regardless the value of M, the maximum vertical displacement observed in the so-called region II is practically the same, with value $u_y/D \approx 0.093$, so it could be concluded that this parameter should be a function only of the geometry and Reynolds number.

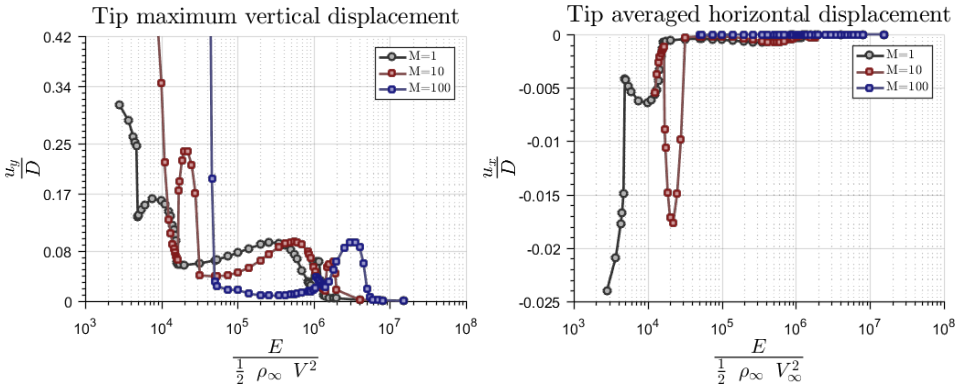

Figure 3.17: Maximum vertical displacement (left) and average horizontal displacement (right) as a function of the non dimensional stiffness for low ($M = 1$), medium ($M = 10$) and high ($M = 100$) mass ratios

The effects of the coupling between the fluid and solid domains can also be observed at Figures 3.18, 3.19 and 3.20, where the velocity and displacement fields are shown for different values of the stiffness for the mass ratio of $M = 100$, $M = 10$ and $M = 1$, respectively. The first subfigure is always the stiffness value which corresponds to the case of almost one way coupling. Note how, in all the cases, the stiffness corresponding to the beginning of the flutter instability is characterized by a tight coupling between the two fields although the computed displacement is still in the linear range. The abrupt increment on the Strouhal number can be observed in all the cases due to the small separation between the downstream convected vortical structures. It should also be noted how, for very low values of the stiffness, the second structural mode can be easily identified from the observation of the displacement field. The displacement field can be more easily observed at Figures 3.21, 3.22 and 3.23, which show the vertical displacement of the mean line for different values of the non dimensional stiffness and mass.

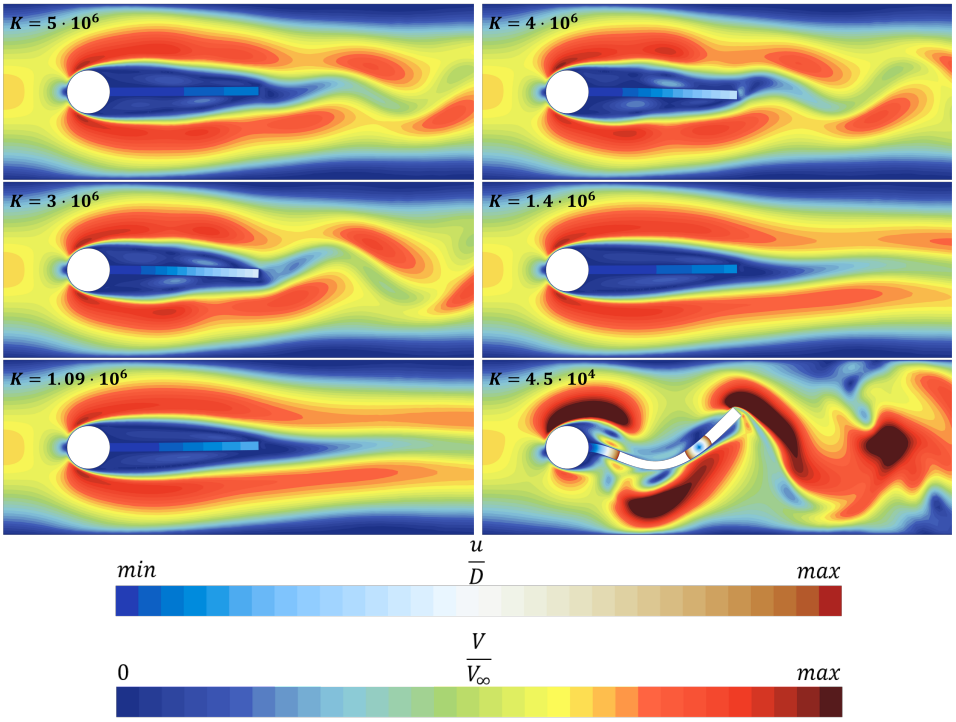

Figure 3.18: Velocity and deformation fields at an arbitrary time step for the case with $M = 100$ and different values of stiffness

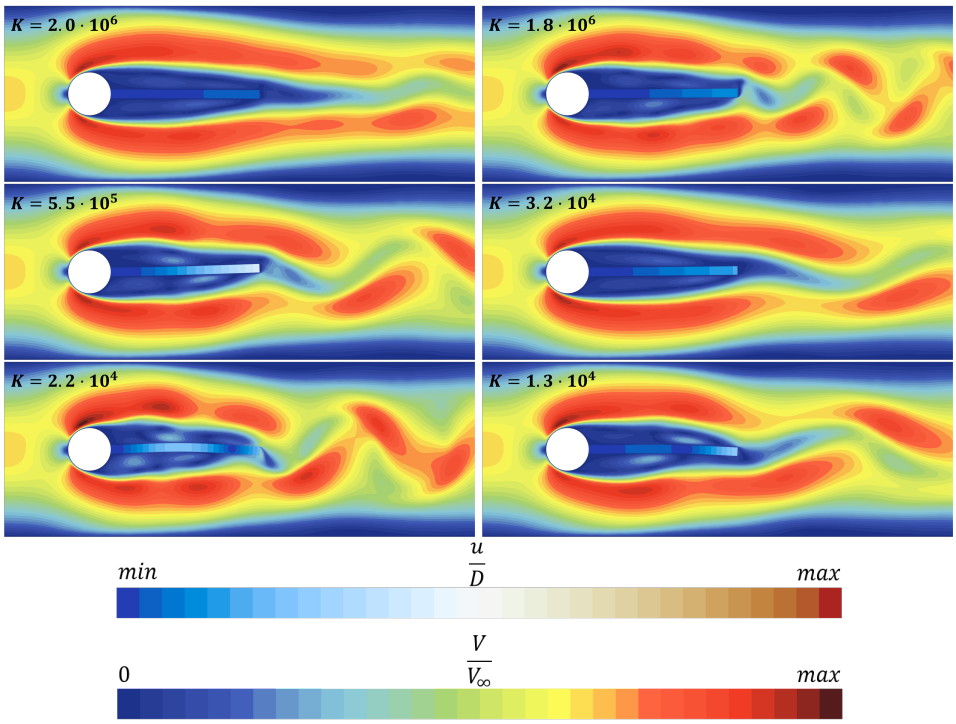

Figure 3.19: Velocity and deformation fields at an arbitrary time step for the case with $M = 10$ and different values of stiffness

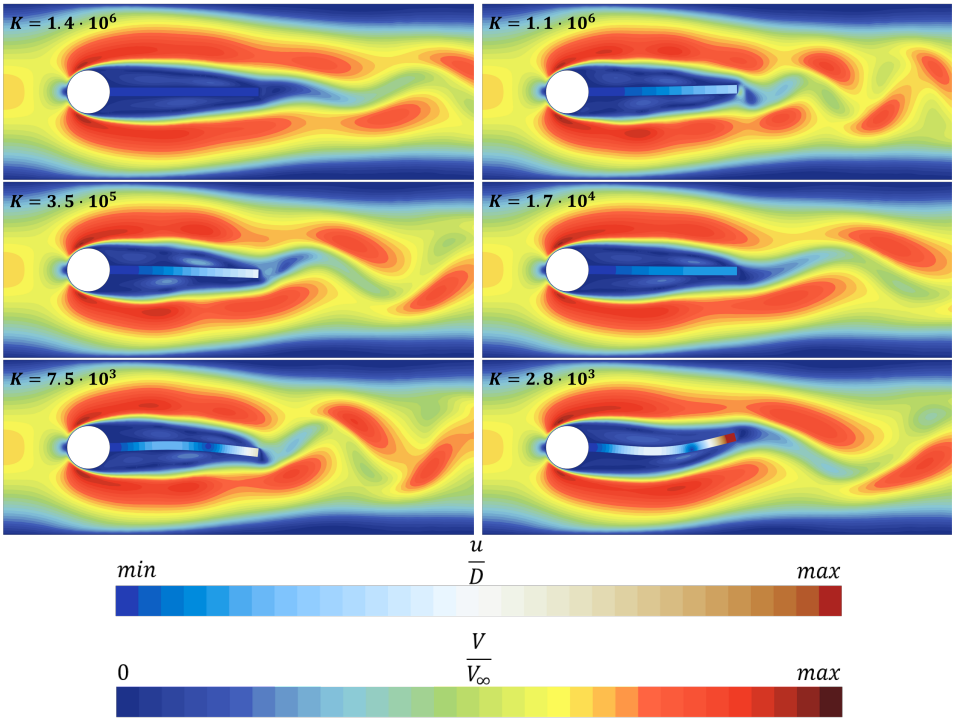

Figure 3.20: Velocity and deformation fields at an arbitrary time step for the case with $M = 1$ and different values of stiffness

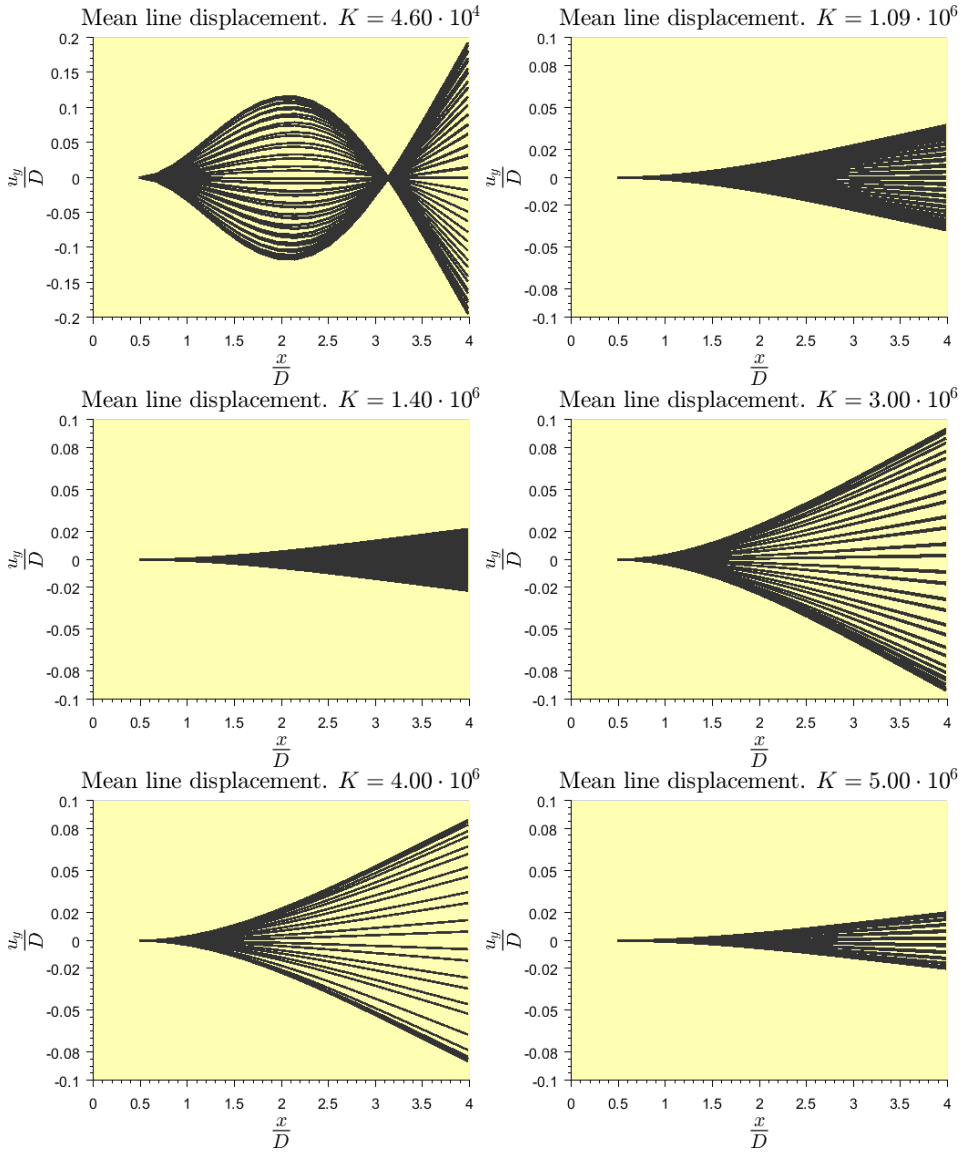

Figure 3.21: Evolution of the mean line vertical displacement as a function of K for various time steps for the case with $M = 100$

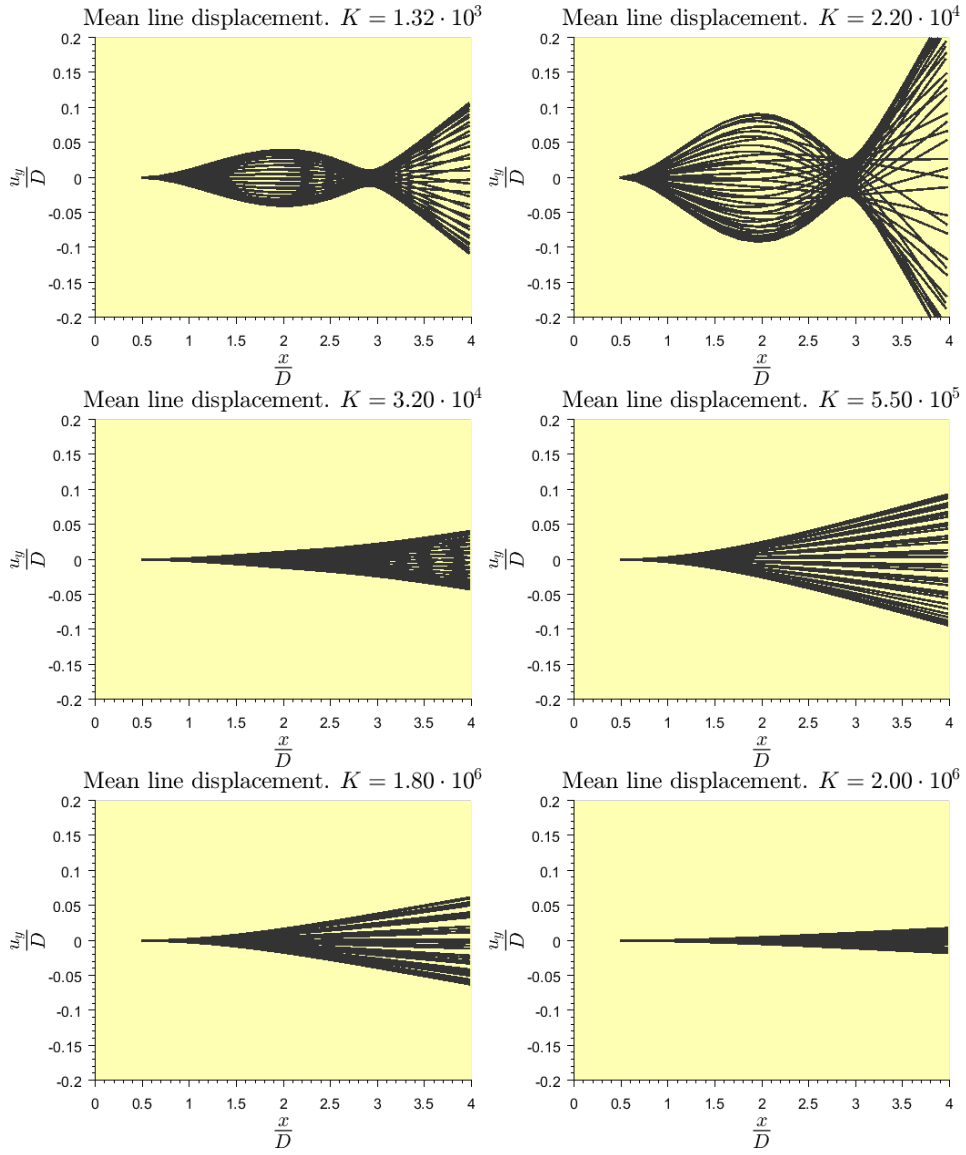

Figure 3.22: Evolution of the mean line vertical displacement as a function of K for various time steps for the case with $M = 10$

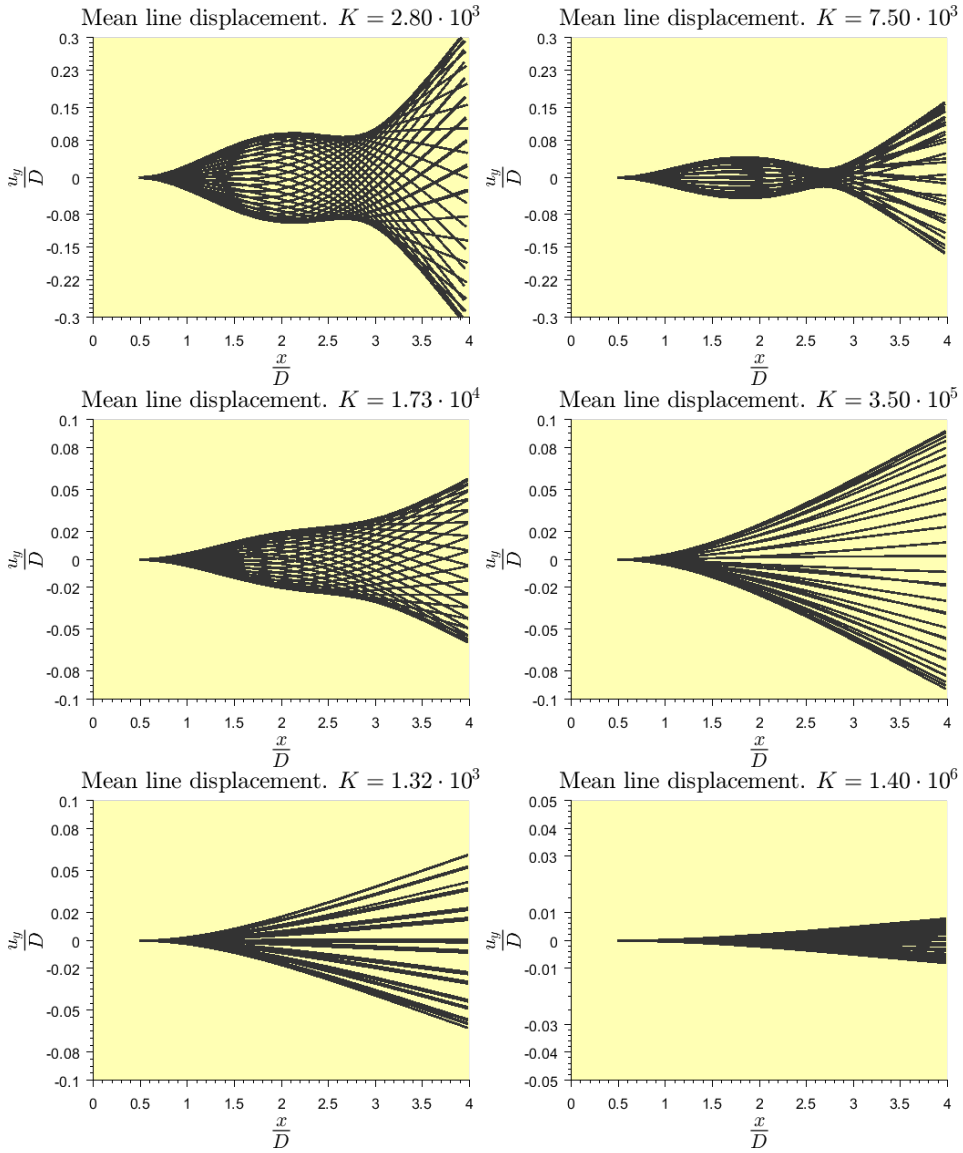

Figure 3.23: Evolution of the mean line vertical displacement as a function of K for various time steps for the case with $M = 1$

3.4.4 Influence of the Reynolds Number on the coupling

During the previous sections, the influence of both the non-dimensional stiffness and the solid to fluid density ratio was analyzed in terms of the kind of coupling. It was observed how, when the density ratio tends towards high values, the first fluid structure instabilities rise for higher values of the stiffness. Additionally, it was observed how the qualitative trends with the stiffness parameter were maintained independently of the mass ratio.

It could be argued that, during the generation of the previous results, the influence of the Reynolds number was not taken into account, as this parameter was maintained constant and equal to Re = 200 during all the simulations. As a consequence, the main aim of this section will be to analyze the role played by this parameter on the coupled system.

Therefore, Figure 3.24 represents the evolution of the maximum value of the lift coefficient and its predominant frequency for the case of low density ratio, $\rho_s/\rho_\infty = 1$ for three different values of the Reynolds number. Re is kept in the laminar range, in order to ensure that the explained methodology is still valid.

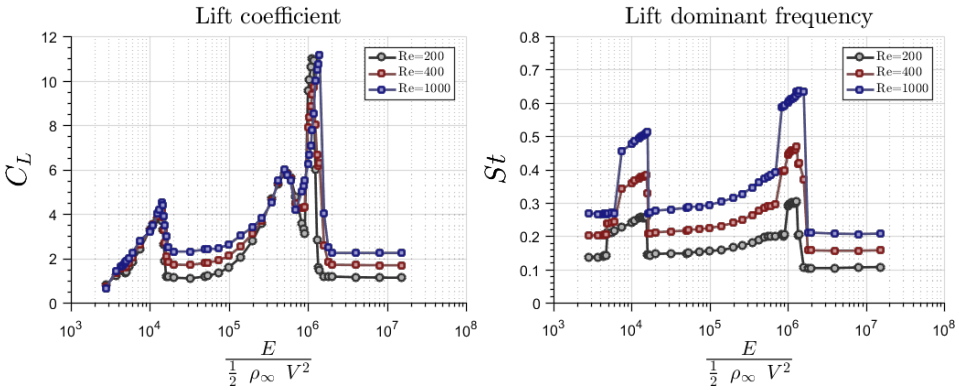

Figure 3.24: Maximum lift coefficient (left) and lift dominant frequency (right) as a function of the Reynolds number for a low value of the mass ratio, $\rho^* = 1$

Observe how, although the value of the coefficient is slightly varied between curves, the beginning of each zone is still rising for approximately the same value of the non dimensional stiffness, indicating how Reynolds number is not the predominant parameter when identifying the coupling strength in a Fluid Structure Interaction system.

It could be argued that the current study was performed only for values

of the Reynolds number lying in the laminar range and, therefore, the results would not be extrapolable to cases where the flow is turbulent. However, the next reasoning could be given:

The possible influence of the Reynolds number on an FSI system could be due to (a) the actuation on the stress tensor which can be observed at Equation 3.11 and (b) how the own fluid flow is affected by this parameter by means of the equation of momentum sketched at Equation 3.5.

It could also be argued that only laminar flows have been analyzed during this dissertation. However, the results could be extrapolated for the case of high Reynolds turbulent flows. From inspection of coupling sources (a) and (b) explained in the previous paragraph, it can be observed, and it is well known that, when the Reynolds number tends to high values, the corresponding terms on the equations becomes less important leading to the conclusion of that, for fluid flows of sufficiently high Reynolds number, the influence of this parameter becomes of second order. As a consequence, the laminar regime of a fluid, as it is defined by a low value of the Reynolds number, is highly influenced by this parameter. If, even at this circumstances of high Reynolds influence on the fluid flow, the Reynolds number is not of importance for the strength of the coupling, it could be expected that the parameter will be even less important for turbulent flows.

Additionally, Figure 3.25 can be referred in order to infer the influence of the Reynolds number on the tip plate maximum vertical displacement (left) and its averaged tip horizontal displacement (right). Show how, even with the already mentioned influence of the Reynolds number on the value of the fluid forces, the same qualitative behavior is observed for the structural response. The increase with Reynolds of the predicted maximum vertical displacement agrees well with the own increase of both the predicted lift coefficient and the dominant lift frequency.

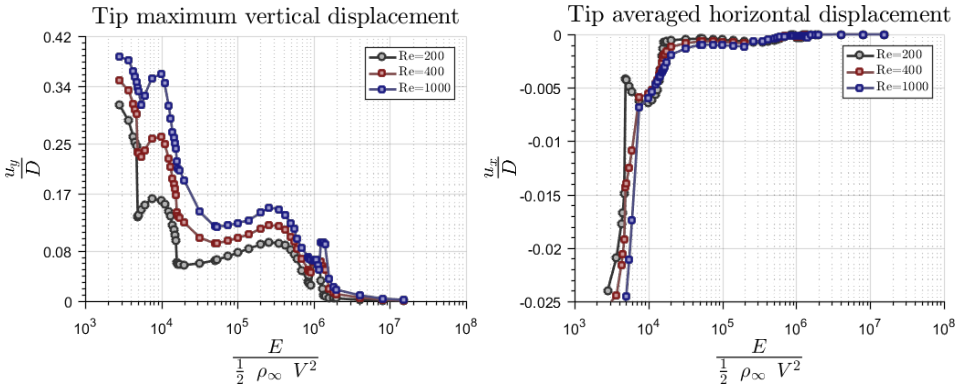

Figure 3.25: Maximum tip vertical displacement (left) and average horizontal tip displacement as a function of the Reynolds number for a low value of the mass ratio, $\rho^* = 1$

3.5 Interaction strength map

In the previous paragraphs, the behavior of the FSI system for different values of the non-dimensional stiffness and mass have been extensively studied. As a consequence, it was observed how different interaction zones with important differences on the vibration pattern and the forces acting over the structure were found.

Once this study has been performed, it is necessary to analyze under which circumstances each of the segregated solvers which were listed during Chapter 2 can be used. This leads to the construction of Figure 3.26, where, depending on the combination of non dimensional mass and stiffness it can be deduced the available computational tool which allows one to obtain an accurate solution of the FSI system:

- The **one-way coupling** zone can be found at the right part of the interaction map. This zone was defined as that where the differences between the fully coupled and one way methodologies were below 2 %.
- The **Explicit coupling** zone was defined as that zone which was possible to be studied using an explicit methodology with a time step $\Delta t\ V_\infty / D = 0.02$, corresponding to a CFL number below 1 for the whole computational domain.
- The **Transition** zone was defined as the combination of mass and stiffness which can be calculated using an explicit methodology but with a time step reduced from the one specified in the previous point. Using this time step or higher resulted in a numerically unstable zone. This area was constructed as follows: The time step was fixed to $\Delta t\ V_\infty / D = 0.002$, corresponding to a CFL number below 0.1 for the whole computational domain. Using higher values of the time step in this area would possibly lead to a numerically unstable set up.
- The **Implicit coupling** zone could not be calculated by any of the three previous methodologies. As a consequence, this zone is necessary to be analyzed by using implicit coupling. All the calculations in this area were carried out using the already mentioned time step of $\Delta t\ V_\infty / D = 0.02$.

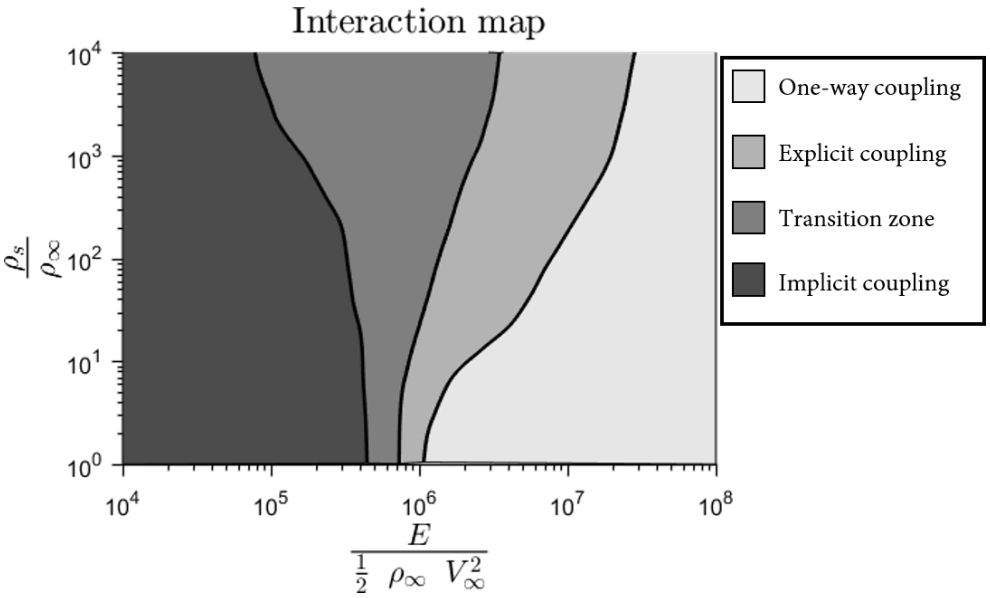

Figure 3.26: Identification of the interaction strength and solver strategy as a function of the stiffness and mass parameters. Darker colors imply stronger coupling and, therefore, necessitiy of more computationally demanding strategies

Note how Figure 3.26 is partially arbitrary, as depends on the choice of the admissible discrepancy between One-way coupling and Two way coupling (for the construction of the rightest zone) and the definition of the minimum admissible time step (for the construction of the transition zone). However, it was found how changing these parameters did not introduce significant differences on the resulting map.

From this result some general trends can be extracted which lately could be applied to engineering cases where the geometry and/or the fluid flow could be much more complex than those shown during this chapter:

- The value of the non dimensional stiffness below at which one way coupling can be performed decreases when increasing the relative mass between the fluid and solid materials. This can be attributed to the increase of the importance of the solid inertia: once a heavy solid acquires an appreciable velocity, the fluid energy dissipation becomes of second order. Similar results have been found at the analysis of wing flutter.
- When the relative mass of the solid with respect the fluid decreases, the interaction map shows how the band at which explicit coupling can be

successfully carried out becomes narrower. This result is in accordance with the already mentioned characteristic of the explicit solver, which becomes unstable for low values of the density ratio.

The former map can be used as a qualitative tool in order to establish which kind of coupling it could be expected to appear at similar problems, where a multiple degree of freedoms deformable solid is excited by a transient fluid flow. The map could even be more useful if next assumption is made. Assuming that aerodynamic forces should weakly depend on the thickness of the plate, it could be argued that the system stiffness should increase with the third power of the thickness and the mass parameter should linearly depend with this parameter. As a consequence, the map could be made even more universal only by multiplying by $\left(\frac{h}{L_{ref}}\right)^3$ the x axis and by $\left(\frac{h}{L_{ref}}\right)$ the y axis.

3.6 Summary and conclusions

During the developement of this chapter, a detailed parametric study performed has allowed taking into account all the possible states of the fluid-structure system, thus providing a comprehensive framework in which the results of the studies of Tang et al. [136], Purohit et al. [137] and Wang et al. [138] can be analyzed in the proper context.

A numerical methodology for the resolution of both an unsteady fluid field and a solid field has been presented, as well as different methodologies for simulating the FSI for different coupling strengths.

A non dimensional analysis has been performed and the main parameters contributing to the Fluid Structure Interaction have been identified.

A complete numerical parametric study on the influence of the non- dimensional stiffness parameter, K has been performed for the case of a flexible plate subject to a non-stationary vortex shedding flow, covering the whole range of possible FSI couplings. The results have been analyzed in terms of the non-stationary tip deflections and the forces acting on the body.

Five different coupling regions have been found to exist depending of the value of K. For region I, it was found that one-way interaction can be assumed. This region is followed by region II, characterized by an abrupt change of flow and solid displacement features, and region III where the post-instability behavior was analyzed. It was found that a linear description of the structure was valid for simulating stiffness values corresponding to regions I, II and III. For lower values of non dimensional stiffness the system behavior corresponds to region IV, where the second structural mode begins to be excited. This region is followed by region V, characterized by large values of the displacement and lower values of the lift force. Regions IV and V should be modeled taking into account geometric non-linearities in the calculation of the stiffness and mass matrices of the structure.

Later, a full discussion of the influence of the non dimensional mass ratio over the response and coupling level of the system has been analyzed. In particular it has been observed how, as a general way, as the solid system becomes heavier with respect the fluid flow, the zone of fully coupling appears for more stiff properties of the solid material. Moreover, when the solid becomes heavier, the transition between region IV and V is characterized by an abrupt increment of the displacement which would make that the assumption of linear relationship between stress and strain would become invalid.

Finally, it has been shown how, depending on the combined value of the non dimensional stiffness, K, and mass, M, the strength of the FSI interaction is varied and, in consequence, the optimum tool for obtaining accurate results with the lower possible computational cost changes in accordance with this parameter. In particular, as it could be somehow obvious, when the elastic forces are much higher than the fluid forces (high values of K) the system can be studied by only using a one-way approach. The end of this *one-way* zone will be determined by the value of the non dimensional mass. As a general rule of the thumb: the higher the value of M the higher the value of K at which coupling effects becomes of importance.

Once this *one-way* interaction zone is passed, the coupling between solid and fluid becomes of importance and, in consequence, it is necessary to use fully coupled tools. In particular, it was found how explicit methodologies could be used for this zone and they could be stabilized using a sufficiently low numerical time step.

It was also found how the stiffness range at which explicit numerical tools are capable of accurately predicting the coupled fluid depends also on the value of ρ_s/ρ_∞. Note how, as this parameter becomes lower, the stiffness range at which this can be done becomes narrower, which agrees with the already mentioned instability of explicit methods.

Therefore, as a final conclusion, it has been observed how the parameters which dominate the FSI coupling are the called non-dimensional stiffness, $E/(\frac{1}{2}\rho_\infty V_\infty^2)$, and the non-dimensional mass, ρ_s/ρ_∞. The effect of the Reynolds number, $\mathrm{Re} = \rho_\infty V_\infty L_{ref}/\mu$ on the determination of this phenomena, is expected to be of second order. During the development of Chapter 4, an application of these methods will be made for two different cases of industrial flows:

- First, it will be shown how, similarly as done here, these parameters also apply for the case of the propagation of pressure waves inside a flexible expansion chamber silencer.
- Then, these parameters will serve to identify and characterize a one way coupling system which tries to represent the fully turbulent vibrational phenomena appearing at the underbody of a moving car

3.7 References

[14] S. Pope. *Turbulent Flows*. Ed. by C. U. Press. Cambridge University Press, 2009 (cit. on pp. 17, 18, 76, 169, 170, 179).

[42] O. Zienkiewicz and R. Taylor. *The Finite Element Method for Solid and Structural Mechanics*. Ed. by E. Butterworth-Heinemann. Oxford, 2006 (cit. on pp. 20, 74).

[43] O. Zienkiewicz, R. Taylor, and J. Zhu. *The Finite Element Method: Its Basics and Fundamentals*. Ed. by E. Butterworth-Heinemann. Oxford, 2005 (cit. on pp. 21, 74).

[61] P. Tallec and J. Moure. "Fluid Structure Interaction with large structural displacements". In: *Computational Methods applied to Mechanical Engineering* 190 (2001), pp. 3039–3067 (cit. on pp. 32, 34, 79).

[69] C. Farhat, K. van der Zee, and P. Geuzaine. "Provably second-order time-accurate loosely-coupled solution algorithms for transient nonlinear computational aeroelasticity". In: *Computer Methods in Applied Mechanics and Engineering* 195 (2006), pp. 1973–2001. DOI: 10.1016/j.cma.2004.11.031 (cit. on pp. 33, 69).

[107] S. Lee, G. Wolberg, and S. Shin. "Scattered Data Interpolation with Multilevel B-Splines". In: *IEEE Transactions on Visualization and Computer Graphics* 3 (1997), pp. 228–244 (cit. on pp. 41, 79).

[126] S. Subhash and S. K. Bhattacharyya. "Finite Element analysis of fluid-structure interaction effect on liquid retaining structures due to sloshing". In: *Computers and Structures* 6 (1996), pp. 1165–1176. DOI: 10.1016/0045-7949(95)00271-5 (cit. on p. 69).

[127] F. Eisinger, M. Rao, D. Steininger, and K. Haslinger. "Numerical Simulation of Cross-Flow-Induced Fluidelastic Vibration of Tube Arrays and Comparison with experimental Results". In: *Journal of Pressure Vessel Technology* 117 (1995), pp. 31–39. DOI: 10.1115/1.2842087 (cit. on p. 69).

[128] Y. Young. "Fluid-structure interaction analysis of flexible composite marine propellers". In: *Journal of Fluids and Structures* 24 (2008), pp. 799–818. DOI: 10.1016/j.jfluidstructs.2007.12.010 (cit. on p. 69).

[129] M. Gramola. "Experimental FSI study of adaptative shock control bumps". In: *Journal of Fluids and Structures* 81 (2018), pp. 361–377. DOI: 10.1016/j.jfluidstructs.2018.05.005 (cit. on p. 69).

[130] B. Hubner, E. walhorn, and D. Dinkler. “A monolithic approach to fluid-structure interaction using space-time finite elements”. In: *Computer methods in applied mechanics and engineering* 193 (2004), pp. 23–26. DOI: 10.1016/j.cma.2004.01.024 (cit. on p. 69).

[131] J. Hron and S. Turek. “A monolithic FEM/multigrid solver for an ALE formulation of fluid-structure interaction with application in biomechanics”. In: *Fluid-Structure Interaction* 53 (2006), pp. 146–170 (cit. on p. 69).

[132] G. Hermann and J. Steindorf. “Partitioned strong coupling algorithms for fluid-structure interaction”. In: *Computers and Structures* 81 (2003), pp. 805–812. DOI: 10.1016/S0045-7949(02)00409-1 (cit. on p. 69).

[133] M. Wenyong, L. Qingkuan, and M. Matsumoto. “Excitation of the large-amplitude vibrations of a circular cylinder under normal wind conditions in the critical Reynolds number range”. In: *Journal of Fluids and Structures* 84 (2019), pp. 318–328 (cit. on p. 70).

[134] S. Turek and J. Hron. “Proposal for Numerical Benchmarking of Fluid-Structure Interaction between an Elastic Object and Laminar Incompressible Flow”. In: *Fluid-Structure Interaction. Lecture Notes in Computational Science and Engineering*. Ed. by H. Springer Berlin. Vol. 53. 2006, pp. 371–385 (cit. on pp. 70–72, 82).

[135] A. Nassar, B. Rogers, A. Revell, and P. Stansby. “Flexible slender body fluid interaction: Vector-based discrete element method with Eulerian smoothed particle hydrodynamics”. In: *Computers and Fluids* 179 (2019), pp. 563–578 (cit. on p. 70).

[136] L. Tang, M. Paidoussis, and J. Jiang. “Cantilivered flexible plates in axial flow: Energy transfer and the concept of flutter-mull”. In: *Journal of Sound and Vibration* 326 (2009), pp. 263–276. DOI: 10.1016/j.jsv.2009.04.041 (cit. on pp. 70, 108).

[137] A. Purohit, A. Darpe, and S. Singh. “Influence of flow velocity and flexural rigidity on the flow induced vibration and acoustic characteristics of a flexible plate”. In: *Journal of Vibration and Control* 24 (2016), pp. 2284–2300. DOI: 10.1177/1077546316685227 (cit. on pp. 70, 108).

[138] H. Wang, Q. Zhai, and J. Zhang. “Numerical study of flow-induced vibration of a flexible plate behind a circular cylinder”. In: *Ocean Engineering* 163 (2018), pp. 419–430. DOI: 10.1016/j.oceaneng.2018.06.004 (cit. on pp. 70, 89, 108).

[139] R. Abdi, N. Rezazadeh, and M. Abdi. “Investigation of passive oscillations of flexible splitter plates attached to a circular cylinder”. In: *Journal of Fluids and Structures* 84 (2019), pp. 302–317 (cit. on p. 71).

[140] K. Kiyoung and C. Haecheon. "Control of laminar vortex shedding behind a circular cylinder using splitter plates". In: *Physics of Fluids* 8 (1996), pp. 479–486. DOI: 10.1063/1.868801 (cit. on p. 73).

[141] M. Unal and D. Rockwell. "On vortex formation from a cylinder. Part 1. The initial instability". In: *Journal of Fluid Mechanics* 190 (1988), pp. 491–512. DOI: 10.1017/S0022112088001429 (cit. on p. 73).

[142] M. Unal and D. Rockwell. "On vortex formation from a cylinder. Part 2. Control by splitter-plate interference". In: *Journal of Fluid Mechanics* 190 (1987), pp. 513–529. DOI: 10.1017/S0022112088001430 (cit. on p. 73).

[143] J. Hwang, K. Yang, and S. Sun. "Reduction of flow-induced forces on a circular cylinder using a detached splitter plate". In: *Physics of Fluids* 15 (2003), pp. 2433–2436. DOI: 10.1063/1.1583733 (cit. on p. 73).

[144] G. P. Galdi and R. Rannacher. *Fundamental Trends in Fluid-Structure Interaction*. Ed. by G. P. Galdi. World Scientific, 2010. DOI: 10.1142/7675 (cit. on p. 73).

[145] W. Haisler, J. Stricklin, and J. Key. "Displacement incrementation in non-linear structural analysis by the self-correcting method". In: *International Journal for Numerical Methods in Engineering* 11 (1977), pp. 3–10 (cit. on p. 75).

[146] R. D. Wood and O. C. Zienkiewicz. "Geometrically nonlinear finite element analysis of beams, frames, arches and axisymmetric shells". In: *Computers and Structures* 7 (1977), pp. 725–735 (cit. on p. 75).

[147] A. C. Humphrey, C. A. Schuler, and D. Webster. "Unsteady laminar flow between a pair of disks corotating in a fixed cylindrical enclosure". In: *Physics of Fluids* 7 (1995), pp. 1225–1240 (cit. on p. 76).

[148] A. K. Sahu, Chhabra, R. P., and V. Eswaran. "Two-dimensional unsteady laminar flow of a power law fluid across a square cylinder". In: *Journal of Non-Newtonian Fluid Mechanics* 160 (2009), pp. 157–167 (cit. on p. 76).

[149] R. Smith and W. Shyy. "Computation of unsteady laminar flow over a flexible two-dimensional membrane wing". In: *Physics of Fluids* 7 (1995), pp. 2175–2184 (cit. on p. 76).

[150] Y. Yu and Y. Li. "Reynolds-Averaged Navier-Stokes simulation of the heave performance of a two-body floating-point absorber wave energy system". In: *Computers and Fluids* 73 (2013), pp. 104–114 (cit. on p. 77).

[151] X. Gao, P. Chen, and L. Tang. "Deforming mesh for computational aeroelasticity using a nonlinear elastic boundary element method". In: *AIAA Journal* 40 (2002), pp. 1512–1517 (cit. on p. 77).

[152] I. Demirdzic and M. Peric. “Space conservation law in finite volume calculations of fluid flow”. In: *International Journal for numerical methods in fluids* 8 (1988), pp. 1037–1050 (cit. on p. 77).

[153] M. Souli, A. Ouahsine, and L. Lewin. “ALE formulation for fluid-structure interaction problems”. In: *Computer methods in applied mechanics and engineering* 190 (2000), pp. 659–675 (cit. on pp. 77, 79).

[154] M. Heil. “An efficient solver for the fully coupled solution of large-displacement fluid-structure interaction problems”. In: *Computer methods in applied mechanics and engineering* 193 (2004), pp. 1–23 (cit. on p. 79).

[155] R. Bhardwaj and R. Mittal. “Benchmarking a coupled immersed-boundary-finite-element solver for large-scale flow-induced deformation”. In: *AIAA Journal* 50 (2012), pp. 1638–1642 (cit. on p. 89).

[156] G. Nayer, A. Kalmbach, M. Breuer, S. Sicklinger, and R. Wuchner. “Flow past a cylinder with a flexible splitter plate: A Complementary experimental-numerical investigation and a new FSI test case (FSI-PfS-1a)”. In: *Computers and Fluids* 99 (2014), pp. 18–43 (cit. on p. 89).

[157] E. Gedikli, D. Chelidze, and J. M. Dahl. “Observed mode shape effects on the vortex-induced vibration of bending dominated flexible cylinders simply supported at both ends”. In: *Journal of Fluids and Structures* 81 (2018), pp. 399–417 (cit. on p. 89).

[158] T. Sarpkaya. “A critical review of the intrinsic nature of vortex-induced vibrations”. In: *Journal of Fluids and Structures* 19 (2004), pp. 389–447 (cit. on p. 89).

[159] L. Huang. “Flutter of cantilevered plates in axial flow”. In: *Journal of Fluids and Structures* 9 (1995), pp. 127–147 (cit. on p. 91).

[160] L. Tang and M. Paidoussis. “On the instability and the post-critical behaivour of two-dimensional cantilevered plates in axial flow”. In: *Journal of Sound and Vibration* 305 (2007), pp. 97–115 (cit. on p. 91).

[161] L. Tang and M. Paidoussiss. “The coupled dynamics of two cantilevered flexible plates in axial flow”. In: *Journal of Sound and Vibration* 323 (2009), pp. 790–801 (cit. on p. 91).

CHAPTER 4

Fluid Structure Interaction applied to vibroacoustics

Contents

Figures

4.1 Introduction

During the development of Chapter 2 the main available computational and experimental methods for the characterization of fluid structure interaction cases were studied. It was shown how, although the available tools have experienced an important development during the past years, the phenomenology inside those phenomena has not been fully explored.

As a consequence, Chapter 3 introduced a fully non dimensional analysis where it was proved how the strength of the fluid structure interaction and, therefore, the optimum computational methodology for the resolution of the coupling physics is mainly a function of two different non dimensional parameters, concluding how the relative importance between the elastic and fluid forces plays an important role when establishing the strength of the interaction between the fluid and solid domains. It was also observed how, although the coupled field can be dependent of the Reynolds number, Re, it does not significantly affects to the strength of the interaction and, therefore, its effects can be safely ignored in the process of selecting the proper tool for optimal computations.

In fact, an important amount of engineering-like cases would lie inside the so-called Region I of the results presented during the previous Chapter. Those, are characterized by relatively low displacements and, therefore, the use of one way interaction models should be enough to completely describe all the phenomena appearing in the system.

Given that, during the current Chapter, a special case of Fluid Structure Interaction, which has become a crucial topic of research during the past years, are analyzed: FSI applied to vibro-acoustic cases.

Vibrating structures can acoustically excite a surrounding fluid flow and, consequently, pressure waves will be generated due to this motion. If the vibrational motion is low (as usual) the excitation can only be appreciated on the fluid acoustic field and can be neglected its action over the hydrodynamic flow, which can be analyzed independently.

A special field of virboacoustic can be found in the field of aero-vibro-acoustics, which can be defined as the transmission of pressure waves through a structure when the exterior source is specifically an aerodynamic or hydrodynamic environement [162]. The characterization of an aero-vibro-acoustic field can be performed using a three steps methodology:

- First, the exterior flow surrounding the structure is independently simulated.
- If the fields are one way coupled, the vibrational response of the structure can be considered on a second step, using the fluid flow variables as boundary conditions for the structural response.
- The vibrational response is used as a boundary condition for a harmonic acoustic analysis.

During last years, interest on the simulation of aero-vibro-acoustics has been growing, as can be observed from the observation of the works of Gloerfelt et al. [163], Lecoq et al. [164] or Amailland et al. [165].

This chapter is therefore used to introduce the methodology applied to the complete characterization of a vibroacoustic and an aero-vibro acoustic case. For the first case, the transmission of pressure waves inside a flexible silencer is analyzed. For the second, the vibrations and radiated noise of a turbulence excited structure are deeply studied.

During the next subsections, a brief introduction for each of these problems is provided, taken into consideration how they have been focused in the literature. Later, Section 4.2 develops a complete example of the vibroacoustics inside a pressure wave excited flexible expansion chamber. Section 4.3 contains an analysis of a typical case of aerovibroacoustics, computing the noise radiated inside a closed chamber by an exterior turbulent flow exiting a flexible plate.

4.1.1 Fluid Structure Interaction applied to vibroacoustics

Following paragraphs serve as an introduction to an example problem of vibroacoustic: the influence of the use of platic light elements for the construction of acoustic elements, such a silencer. The importance of correctly analyzing this kind of FSI problem will be analyzed and, during during following sections it could be inferred how the same conclusions which were analyzed during Chapter 3 are still valid, even for a problem whose features are highly different.

Reduction of noise emissions is currently an important area of interest because of its practical importance. A document of the *World Health Organization for the European Union* [166] showed that near 40% of citizens of the EU experience road noise of about 55 dB(A). A 30% of European population experiences road noise over 55 dB(A) during night.

Recent regulations focus their application on an effective reduction of noise [167]. In order to comply with regulation without jeopardizing engine performance, various noise control methods have been developed. These kind of control methods can be categorized as passive or active systems [168].

Active noise techniques allow obtaining a very high reduction of observer perceived noise. However, this kind of control is associated with some issues of cost and reliability. Currently, their application on the transport industries is not approachable. For instance, Linus et al. [169] demonstrated that the performance of active-noise cancelling headphones is dependent on the noise environment. Under some circumstances, they showed how its performance could be unacceptable. In the automotive field it is necessary for a control mechanism to be useful over the whole range of operation making the use of this kind of devices currently unreachable.

Due to these limitations, passive noise control is, nowadays, the principal engineering solution. A general categorization of passive elements can be split as dissipative or reflective. Dissipative noise control allows a high noise reduction. For example, Hwang et al. [170] showed how using dissipative viscoelastic materials allows an effective noise control. However, porous absorption materials lose acoustic performance at low frequencies. When the frequency is low, the thickness of a porous absorber is less than one quarter of the acoustic wavelength and absorption becomes inappreciable [171].

For reactive noise abatement techniques, part of the sound wave is reflected towards the source, or back and forth among the elements. Some examples of these elements are: expansion chambers, Helmholtz resonators, Herschel Quinke tubes, etc. These elements allow dealing with low frequency noise [172].

Traditionally, reactive elements have been extensively considered as infinitely rigid, i.e. wall displacement and/or velocity is supposed to be negligible from the fluid behavior point of view. This is effectively true in most of the current applications in the automotive industry. However, very low density-low rigidity materials are becoming of interest. As an example it could be useful to refer to the works of Aydemir and Ebrinç [172], Nunes et al. [173] and Hu et al. [174].

Some flexible components have been proposed in the field of passive sound attenuation. For example, Huang [175] analyzed a drumlike silencer, which is a strongly coupled fluid-structure component. It was shown how the coupling of the structural eigenfrequencies with the flow leads to a kind of "storage" of kinetic energy, yielding to an increase of the Transmission Loss (TL) through the main duct.

Some approximations have been made in this context for some academic problems. For example, Fan et al. [176] used numerical methods to compute the fluid-structure interaction of a flexible panel immersed in a fluid flow; Lawrie [177], Ramamoorthy et al. [178] and Ko [179] analytically approached the behavior of canonical cases. Gautier et al. [180] performed measurements on the vibroacoustic phenomena appearing on a flexible rubber tube. Practical geometries have been studied less extensively, but some references could be cited: Venkatesham et al. [181] developed an analytical prediction for the radiated sound from a rectangular flexible expansion chamber; Wang et al. [182] studied the radiated sound from a rectangular cavity through an elastic panel.

Nevertheless, there exists an important lack of information about the influence of structural phenomena on the transmission properties, being of vital importance the quantification of the transmission loss and/or transfer matrix coefficients. For example, Munjal et al. [183] analytically showed how transmission loss should increase when decreasing the rigidity of the wall material. Cummings [184] developed a theoretical model describing acoustic attenuation in a flexible walled duct passing through a reverberant space.

Due to the mentioned lack of information, during this Chapter, numerical modelling will be applied to a typical circular-section expansion chamber. This geometry is characterized via the component acoustic transfer matrix [171] for the rigid case and for various flexible materials.

The expansion chamber under consideration consists of a cylindrical geometry with only one flexible wall. The reason of selecting this kind of geometry is mainly due to its simplicity and, thus, to the possibility of inferring gen-

eral behaviors for more complex geometries. As it will be shown later, due to the inherently stiffness of this geometry, the material must have a very low Young modulus in order to show fully coupled fluid structure interactions under acoustic loads. The main aim of this section is to prove how, when structural modes are excited, it is necessary to consider couplings and to provide appropriate methodologies to predict the behavior of the acoustic element under these circumstances. Additionally, it will be observed how, as previously predicted in Chapter 3, the relationship between elastic and fluid forces determine the strength of the interaction and how, for usual construction materials, it can be supposed to be one directional.

4.1.2 Flow Induced Vibrations applied to aerovibroacoustics

The previous described case tried to face a problem where the unsteadiness of the flow was imposed by the definition of the boundary conditions. However, for a wide range of engineering applications this is not the case. For example, in a case of aerovibroacoustic, the transient nature of the fluid flow arises by the self-induced turbulence of the fluid flow, even with almost stationary boundary conditions. This special case requires the use of scale resolving flow simulations, and is illustrated in the next section by means of a representative example: the generation of underbody noise in a one way coupled system.

During the past decades, because of the increase use of lightweight materials for the construction of components in direct contact with a moving fluid, the accurate prediction of flow-structure interactions (FSI) has become a topic of primal interest. Aerospace industry has traditionally been one of the main drivers for research. For instance, it is well known that a wing subjected to certain values of the flow velocity can experience inadmissible static deformations (divergence, see Hilderbrand et al. [185]) or periodic time-increasing oscillations (flutter, see Bisplinghoff et al. [186] or Jeong et al. [187]) which can lead to mechanical static or fatigue failures.

In this sense, a large number of important engineering problems are related with the flow around bluff bodies. Therefore, the accurate prediction of FSI phenomena over the own body or the vibration of structures located at its wake is of major interest. A specific mention could be given to the work of Schewe et al. [188], who used wind tunnel measurements in order to predict the loads acting over a bluff bridge deck cross section; Augier et al. [189] performed a tight coupled simulation of the FSI phenomena appearing at yacht sails subjected to a turbulent flow. More recently, Zhang et al. [190] performed Detached Eddy Simulations (DES) in order to predict the broadband frequency content of the displacements generated at a high building excited by a turbulent fluid flow supposing one way coupling. This work was later expanded by Ricci et al. [191], solving the flow with Large Eddy Simulations (LES).

In the automotive industry, due to the significantly lower working velocities compared with those expected on aircraft applications, these phenomena less often lead to a tight-high displacement fluid structure interaction (FSI). However, understanding and being able to predict FSI is of growing interest. It is well known that NVH (noise, vibration and harshness) is becoming a crucial topic of study for automotive manufacturers. Because of stricter regulations and increasing customer expectations, a major mechanism for the generation of undesired aerodynamic noise inside the cabin is the excitation of the structure by the turbulent flow around the vehicle. This fact, in combination with the

development of increasingly silent engines, explains the increasing interest on FSI also in automotive applications.

One of the first investigations in this field was carried out by Davies [192] who studied the excitation of a flat plate under a turbulent boundary layer (TBL) using modal analysis. Later, increased efforts have been directed to obtain a correct prediction of this phenomenon as, for instance, in the works of Graham [193], Howe [194] or Frampton [195]. However, their assumptions are of difficult application when the flow is dominated by a highly non-isotropic turbulence, as is the case for the flow downstream of a wall-mounted obstacle, where the large structures containing the energy of the flow should be accounted for, and therefore modeled.

A particularly interesting example can be found in the vibrations appearing under the body of a moving car. In fact, the turbulent unsteady flow generates a fluctuating pressure which acts on the floor of the vehicle. This fluctuating pressure induces vibrations on the floor, which are responsible for radiating noise to the interior of the cabin. Related with this, some interesting studies can be found in the literature. For instance, Springer et al. [196] numerically studied a simplified version of the problem: a fluid flow passes over a wall-mounted obstacle which generates a turbulent wake, and the unsteady pressure fluctuations excite a thin flat plate which starts to vibrate. However, in their work they did not provide experimental data about the plate vibrations; they over predicted the reattachment length over 50 % and a small number of structural modes were excited which, in principle, disagrees with experiments [197].

Mueller et al. [197] investigated both the structural vibration and acoustic behavior of flat plates for different materials and sizes exposed to different excitations. They showed how, for the case were the flow becomes turbulent, most of the natural modes of vibration of the plate are excited which, as could be expected, corresponds to a peak in the Sound Pressure Level spectrum for the corresponding natural frequencies. Schafer et al. [198] investigated the same simplified geometry as [196], using a very thin flat plate of 40 μm, and assuming two-way fluid structure coupling, obtaining accurate results for the flow field, compared with the experiments. However, the prediction of the induced vibration agreed only qualitatively with the experiments. The main factor underlying the deviations between numerical and experimental results could be the low plate stiffness, which leads to large displacements, which are difficult to predict by using a linear structural model. Furthermore, a plate with a such small value of structural stiffness, cannot be considered as representative for most of the cases related with NVH.

The information presented in this Chapter intends to complement the works of [198] and [196]. A similar simplified geometry was considered, where a steel plate of 0.5 mm thickness is located immediately downstream of the obstacle. Both the fluid domain and the structural vibration are numerically modelled, making use of different numerical models, and the results are compared with experiments. It is shown that a one-way interaction model provides accurate results for both the turbulent fluid flow and the flow-induced vibrations of the plate. The mechanisms exciting each vibration mode is analyzed in detail. The capabilities of different turbulence models, such as the Large Eddy Simulation (LES) or the, computationally less demanding, Reynolds Averaged Navier Stokes (RANS) are explored and their applicability to predict the flow field and the plate deformation is assessed.

It will be shown how, as expected after the dimensional analysis of Chapter 3, a one-way interaction model can provide accurate results for both the turbulent fluid flow and the flat plate flow-induced vibrations. The mechanism exciting each vibration mode will be analyzed. Capabilities of mean flow turbulence models, as Reynolds Averaged Navier Stokes (RANS) will be explored and it will be shown that they can provide acceptable values for the time averaged values of the plate deformation, even when some important assumptions are introduced in the computation of the fluid flow. The adopted methodology can be summarized as following. First, the flow field is computed by using LES and RANS for different grid refinement and compared with the available experimental data; at the same time, the structural model of the plate was validated by comparing computational and experimental eigenfrequencies and eigenvectors. When both the flow and structural model are validated, they are coupled using a one-way methodology by mapping the CFD pressure solution onto the FEM structural mesh. Finally, the flow induced vibrations are calculated using this structural model and analyzed, comparing the response at different frequencies with the previously computed eigenfrequencies. Figure 4.1 shows a schematic overview of this workflow for the determination of the vibrational response. in order to ease the interpretation of the chapter.

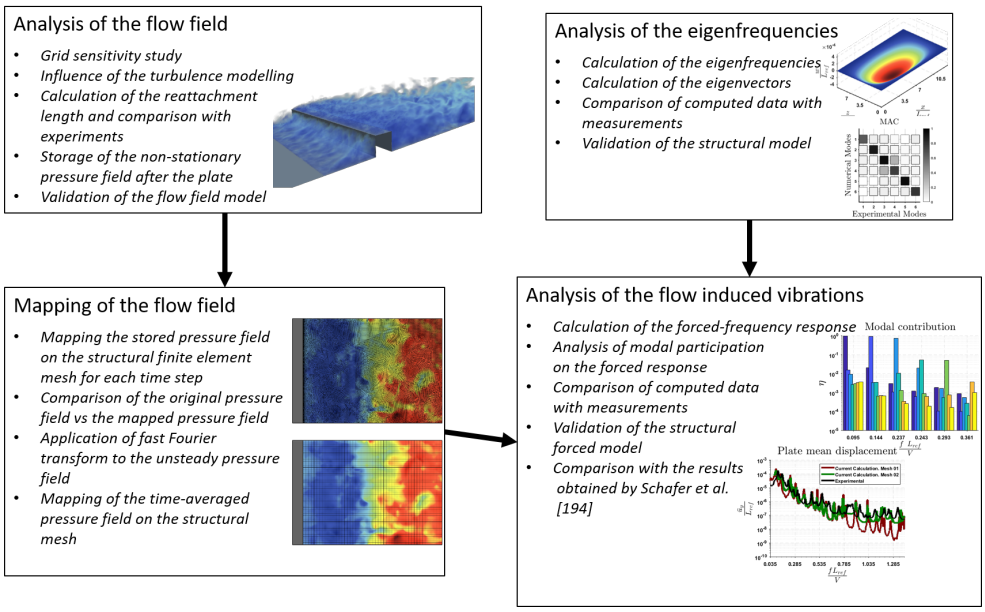

Figure 4.1: Diagram of the working flow for the computation of Flow Induced Vibrations

Once the structural model has been validated, the unsteady wall velocity can be used as a boundary condition for calculating the acoustic pressure field inside the cabin.

4.2 Application to vibroacoustics. Prediction of the Transmission Loss in a Flexible Chamber

4.2.1 Acoustic Theoretical Background

For the solution of this problem, two different zones must be considered: A fluid zone, where sound waves propagate, and a solid zone, which experiences deformations and accelerations as a response to flow characteristics. In order to study the transmission characteristics with flexible walls, a fully coupled case is studied, i.e. as a consequence of wave propagation the solid walls will experience an unsteady deformation which in turn will also have an effect on the unsteady flow field [199]. In this section, the governing equations for each region, which can be derived from the general equations presented in Chapter 3, are summarized.

Solid continua equations

General equations The equations governing the fluid flow and structural solid displacement are essentially the same as those presented in the work of Zienkiewicz et al. [20]. The unsteady governing equations for the solid media can be written in vector form as follows:

$$\rho \frac{\partial^2 \vec{w}}{\partial^2 t} = \nabla \cdot \boldsymbol{\sigma} - \vec{b} \tag{4.1}$$

Here, $\vec{w}$ is the vector representing the displacement field of the solid body, measured from an inertial reference frame; $\vec{b}$ represents the volume forces (as gravity or dissipation); ρ is the material density and $\boldsymbol{\sigma}$ is the Cauchy stress tensor [200], which complies with:

$$\boldsymbol{\sigma} = \boldsymbol{\sigma}^T \tag{4.2}$$

The closure of the solid displacement equation can be obtained by means of the, so-called, strain-stress relationships. If the solid strains is defined as:

$$\varepsilon_{ij} = \frac{1}{2}\left(\frac{\partial w_i}{\partial x_j} + \frac{\partial w_j}{\partial x_i}\right) \tag{4.3}$$

The strain-stress equation allows to obtain a relationship between strain and stress for a given material. For instance, in the case of a linear-homogeneous solid material:

$$\sigma_{ij} = \lambda\ \delta_{ij}\ \varepsilon_{ij} + 2\ \mu\ \varepsilon_{ij} \tag{4.4}$$

where δ_{ij} is the Kronecker delta and λ and μ are the first and second Lamé parameters, respectively. They are usually expressed as a function of the Young modulus, E , and Poisson ratio, ν, as follows:

$$\lambda = \frac{E\ \nu}{(1+\nu)\ (1-2\nu)} \qquad \mu = \frac{E}{2\ (1+\nu)} \tag{4.5}$$

Once the equations are closed and suitable boundary and initial conditions are prescribed, the resulting linear problem can be efficiently solved using the Finite Element Method (FEM) [20].

Free vibration equations The set of discrete equations describing the solid structural domain can be obtained by means of the FEM [20] and is written simply as:

$$[M]\{\ddot{w}\} + [C]\{\dot{w}\} + [K]\{w\} = \{f^{ext}\} \tag{4.6}$$

where $[M]$ is the mass matrix, $[C]$ is the damping matrix, $[K]$ is the stiffness matrix, $\{f^{ext}\}$ is the vector of nodal forces and $\{w\}$ is the vector of nodal displacements.

The free vibration problem consists in solving the following problem (with $\{w\} = \{W\}\ e^{j\omega t}$):

$$-\omega^2[M]\{W\} + j\omega[C]\{W\} + [K]\{W\} = 0 \tag{4.7}$$

The values of ω that satisfy the previous equation are the so-called eigenfrequencies. Any excitation with this frequency can lead to very high values in the displacement. As it will be seen later, eigenfrequencies must be computed because of their great importance when analyzing fluid-structure interaction (FSI) harmonic acoustic problems.

Fluid motion equations

General equations In this study, the propagation of a velocity/pressure pulse through a fluid domain has been modelled. The most straight-forward derivation of the equations governing this system is based on applying the equation of state in conjunction with the mass, momentum and energy equations [201], which are given by the following expressions:

$$\begin{cases} p = \rho\, R\, T \\ \frac{\partial \rho}{\partial t} + \nabla \cdot (\rho \vec{v}) = 0 \\ \rho \left(\frac{\partial \vec{v}}{\partial t} + \vec{u} \cdot \nabla \vec{v} \right) = \nabla \cdot \boldsymbol{\tau} + \rho \vec{f}_m \\ \rho \left(\frac{\partial h}{\partial t} + \vec{v} \cdot \nabla h \right) = \frac{\partial p}{\partial t} + \vec{v} \cdot \nabla p + \nabla (k \nabla T) + \phi_v + Q \\ \mathrm{d}h = c_p\, \mathrm{d}T \end{cases} \tag{4.8}$$

Euler Equations For the propagation of low to moderate wave amplitudes the flow can be considered to behave as non-viscous ($\mu \approx 0$) and heat-transfer dissipative effects can also be neglected ($k \approx 0$). Also, body forces and heat generation will be neglected (see [202] and [203]).

After considering those assumptions, the Euler equations are obtained. These are given by:

$$\begin{cases} p = \rho\, R\, T \\ \frac{\partial \rho}{\partial t} + \nabla \cdot (\rho \vec{v}) = 0 \\ \frac{\partial \vec{u}}{\partial t} + \vec{v} \nabla \vec{v} = -\frac{\nabla p}{\rho} \\ \rho \left(\frac{\partial h}{\partial t} + \vec{u} \cdot \nabla h \right) = \frac{\partial p}{\partial t} + \vec{v} \cdot \nabla p \\ \mathrm{d}h = c_p\, \mathrm{d}T \end{cases} \tag{4.9}$$

For the FSI-coupled case, a morphing mesh scheme is adopted and the wall-velocity inviscid boundary condition can be expressed simply by:

$$\left(\vec{u}_{fluid} \cdot \vec{n} \right)_{wall} = \vec{u}_{wall} \cdot \vec{n} \tag{4.10}$$

The previous equation simply states that fluid and solid must have the same normal velocity components at the interface.

Wave equation In the context of wave motion, it is usual to assume that the flow characteristics can be determined as an unperturbed component and a perturbation, as follows:

$$\begin{aligned} \rho_T(\vec{x},t) &= \rho_0(\vec{x},t) + \rho(\vec{x},t) \\ p_T(\vec{x},t) &= p_0(\vec{x},t) + p(\vec{x},t) \\ \vec{u}_T(\vec{x},t) &= \vec{u}_0(\vec{x},t) + \vec{u}(\vec{x},t) \end{aligned} \tag{4.11}$$

where $\frac{\rho}{\rho_0} \ll 1$; $\frac{p}{p_0} \ll 1$ and $\frac{|\vec{u}|}{|\vec{u}|_0} \ll 1$. Under these circumstances, the Euler equations can be linearized. Also, it is possible to consider the flow to be isentropic, allowing one to define a relation between pressure and density derivatives, as:

$$\left(\frac{\partial p}{\partial \rho}\right)_s = \left(\frac{\partial p}{\partial \rho}\right) = a_0^2 \tag{4.12}$$

Where a_0 is the unperturbed sound velocity in the flow. Finally, for the case of no mean flow, the formulation can be further simplified, and a single equation for the perturbation (acoustic) pressure is obtained:

$$\nabla^2 p - \frac{1}{a_0^2}\frac{\partial^2 p}{\partial^2 t} = 0 \tag{4.13}$$

allowing also to obtain the acoustic velocity, which is related to pressure derivatives as follows:

$$\frac{\partial \vec{u}}{\partial t} = -\frac{1}{\rho_0}\nabla p \tag{4.14}$$

Helmholtz equation Assuming harmonic dependence with time of the acoustics variables (*i.e.* $p = Pe^{j\omega t}$ and $u = Ue^{j\omega t}$), it is possible to obtain the Helmholtz equation, which can be written as [171]:

$$\nabla^2 P + \frac{\omega^2}{a_0^2} P = 0 \rightarrow \nabla^2 P + k_0^2\, P = 0 \tag{4.15}$$

and the corresponding relationship between pressure and velocity:

$$\vec{U} = \frac{j}{\omega\ \rho_0}\ \nabla P \tag{4.16}$$

Eq.(4.15) can be numerically solved by means of a linear FEM [204]. For the solution of the domain sketched in section 4.2.2, the commercial package *COMSOL* was used [205].

4.2.2 Problem Description

The main aim of this study is to characterize a flexible-wall expansion chamber using time-domain CFD methods, and to compare the results with a frequency domain FEM solution for the case of no mean flow. A similar problem was already studied by Broatch et al. [206] for the case of mufflers with rigid walls.

Due to the geometrical characteristics of the fluid domain, the plane wave condition, $\frac{f\ R}{a_0} \ll 0.29$ is sufficiently adequate for the range of frequencies of interest, i.e. $0 < \frac{f\ R}{a_0} < 0.13$. Nevertheless, in order to be able to predict possible non-planar wave effects while avoiding the use of a too large domain, only one quarter of a tube was simulated, assuming periodicity in the angular coordinate.

As it will be checked later, the results for this simple case can be considered as practically axisymmetric. Thus, the simulation of a quarter of a pipe is considered to be representative enough for representing the whole 3D fluid-structure interactions.

Fig. 4.2 shows an sketch of the geometry to be studied and characterized. The radius of the expansion chamber is $R = 0.03$ m. The solid wall is supposed to be clamped at the beginning and ending of the expansion chamber. Table 4.1 shows the other dimensions.

In the simulation, the inlet is fed by a known velocity profile. The outlet section of the tube is extruded a distance $L_{diss} = 10\ R$ and at its end a dissipative boundary condition is applied in order to simulate an anechoic termination. The time evolution of the inlet velocity profile is given by:

$$\frac{v(t)}{v_{max}} = \begin{cases} \frac{1}{2}\left(1 - \cos\left(\frac{2\ \pi\ t}{T_{impulse}}\right)\right) & t \le T_{impulse} \\ 0 & t > T_{impulse} \end{cases} \tag{4.17}$$

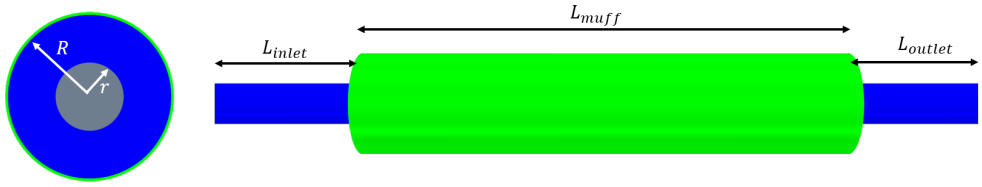

Figure 4.2: Sketch of the geometry

Table 4.1: Geometry dimensions

Variable		Value
Chamber radius	R	0.03 m
Inlet/Outlet radius	r	$R/2.4$
Inlet length	L_{inlet}	$10\,R/3$
Outlet length	L_{outlet}	$10\,R/3$
Chamber length	L_{muff}	$10\,R$
Dissipation length	L_{diss}	$10\,R$

Due to the non-linearity of the convective term and the isentropic state relationship in Euler equations, high values of the velocity or pressure at boundary conditions could lead to a non-linear response. For the current case, simulations are performed for excitations up to 10 m/s, where this influence began to be slightly noted at high frequencies. Thus, a low velocity excitation of $v_{max} = 0.01$ m/s was chosen. This value is high enough to not provide numerical inaccuracies and ensures that the response can be considered to be totally linear for the whole spectra.

The non-dimensional pulse duration is given by $\frac{T\ a_0}{L_{muff}} = 0.3473$ in such a way that the signal frequency content is high enough to resolve up to the desired frequency.

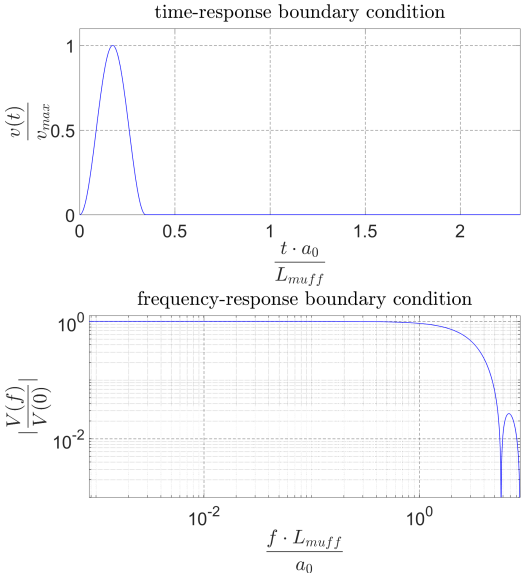

Figure 4.3: Time and frequency response of the inlet velocity profile

Figs. 4.3a and 4.3b show the time and frequency evolution of the inlet velocity profile. It should be noticed that the cut-off frequency at the boundary condition $\frac{f_{cut}\, L_{muff}}{a_0} \approx 4.75$ is sufficiently high for the current requirements.

During next sections, first, acoustic transmission through the rigid expansion chamber are being calculated by means of a time-domain CFD simulation, by a FEM wave equation solution and by an analytical calculation. Furthermore, additional numerical calculations are performed for the case of a flexible expansion chamber, with wall thickness $\frac{\delta}{R} = \frac{1}{15}$ and different Young modulus, E, and solid density, ρ.

Liu et al. [207] demonstrated for a similar domain that the acoustic properties of the flexible muffler are determined by the non-dimensional parameters listed below, which, as can be observed can be directly derived from the already non dimensional numbers sketched during the previous Chapter:

$$L^*_{muff} = \frac{L_{muff}}{R} \qquad t^* = \frac{a_0 \cdot t}{L_{muff}} \qquad f^* = \frac{f \cdot L_{muff}}{a_0}$$
$$p^* = \frac{p}{\rho_0 a_0^2} \qquad D^* = \frac{E\ \delta^3}{12(1-\nu^2)R^3\ \rho_0\ a_0^2} \qquad m^* = \frac{\rho_s\ \delta}{\rho_0\ R} \tag{4.18}$$

During the development of this work a high mass pipe is assumed. Thus

the mass parameter is assumed to be constant and equal to $m^* = 56.6$. This allows for the direct examination of the dependency on stiffness.

4.2.3 Numerical and analytical methods

The case of a simple non-deformable expansion chamber has been extensively studied in the literature: Broatch et al. [206] studied expansion and reversing chamber mufflers by using a time-domain CFD method; Barbieri et al. [208] applied the Finite Element Method to study a similar problem. A number of references can also be found which address the problem analytically (see [171]).

References [206] and [208] allow to conclude that, for the case of linear duct acoustics when the presence of a mean flow is not important, frequency domain FEM provides quite similar results while its computational cost is significantly lower as the time domain does not need to be resolved, being possible to model only the required frequencies.

For CFD calculations the whole "residence-time" of the wave inside the domain of interest must be solved in order to obtain an admissible frequency response. Thus, it is intended here to provide a check of the validity of the current methods for later comparison in the flexible case.

Analytical formulation

For the analytical plane wave approach of the model, it can be split into five parts, as shown in Fig. 4.4:

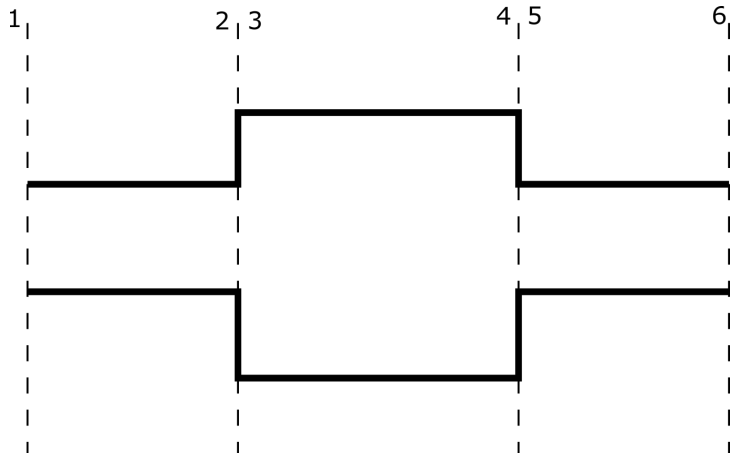

Figure 4.4: Simplified sketch of the geometry

Analytically, each component of the expansion chamber elements can be modelled as an acoustic transfer matrix, which relates the acoustic velocity and pressure at the inlet section with those at the outlet. For an arbitrary acoustic element it can be stated [171]:

$$\begin{Bmatrix} p_{in} \\ u_{in} \end{Bmatrix} = [A] \begin{Bmatrix} p_{out} \\ u_{out} \end{Bmatrix} = \begin{bmatrix} A_{11} & A_{12} \\ A_{21} & A_{22} \end{bmatrix} \begin{Bmatrix} p_{out} \\ u_{out} \end{Bmatrix} \tag{4.19}$$

It follows that, for a linear element consisting of n subelements whose transfer matrices are known one can write [171]:

$$[A] = [A_1]\,[A_2] \cdots [A_n] \tag{4.20}$$

where $[A_i]$ is the transfer matrix of the i sub-element. The transfer matrix of each one has been extensively analyzed in bibliography [171].

Once the acoustic matrix of a system is known it is possible to predict the its acoustical behavior under any harmonic excitation. On the other hand, it is also possible to predict an important acoustic characteristic of the system as follows:

On the other hand, it is also possible to predict the transmission loss (TL) of the system. This parameter represents the quantity of sound power which leaves the acoustic element, related to the incident power provided that the outlet is anechoic [171]. It is usually expressed in dB, and can be deduced from the elements of the transfer matrix:

$$\begin{aligned} TL &= 10\,\log_{10}\left(\frac{W_{out}}{W_{in}}\right) \\ TL &= 20\,\log_{10}\left[\sqrt{\frac{S_{out}}{S_{in}}}\,\frac{\left|A_{11}+A_{12}\cdot\frac{S_{in}}{\rho_0 a_0 S_{out}}+A_{21}\rho_0 a_0\frac{S_{in}}{S_{out}}+A_{22}\left(\frac{S_{in}}{S_{out}}\right)^2\right|}{2}\right] \end{aligned} \tag{4.21}$$

Where S_{out} represents the outlet section of the element and S_{in} is the inlet section. When $S_{out} = S_{in}$ it can be stated:

$$TL = 20\,\log_{10}\left(\frac{|p_{out}|^+}{|p_{in}|^+}\right) \tag{4.22}$$

$|p_{out}|^+$ and $|p_{in}|^+$ being the progressive pressure wave component at outlet and inlet, respectively.

Numerical calculation of the transfer matrix As it was shown in the previous section, the transfer matrix is composed by 4 coefficients. Thus, in order to determine it from a numerical computation two cases have to be calculated. Once the frequency content of the acoustic pressure and velocity is known, the value of the matrix components, for a particular frequency f can be evaluated as follows:

$$\begin{bmatrix} A_{11}(f) \\ A_{12}(f) \\ A_{21}(f) \\ A_{22}(f) \end{bmatrix} = \begin{bmatrix} (P_{out}(f))_{Case\ A} & (V_{out}(f))_{Case\ A} & 0 & 0 \\ 0 & 0 & (P_{out}(f))_{Case\ A} & (V_{out}(f))_{Case\ A} \\ (P_{out}(f))_{Case\ B} & (V_{out}(f))_{Case\ B} & 0 & 0 \\ 0 & 0 & (P_{out}(f))_{Case\ B} & (V_{out}(f))_{Case\ B} \end{bmatrix}^{-1} \begin{bmatrix} (P_{in}(f))_{Case\ A}) \\ (V_{in}(f))_{Case\ A}) \\ (P_{in}(f))_{Case\ B}) \\ (V_{in}(f))_{Case\ B}) \end{bmatrix} \tag{4.23}$$

The previous equation can be resolved only when the boundary conditions of cases A and B are linearly independent in the frequency domain.

Time domain CFD Model

In section 4.2.1 the Euler equations were introduced. In order to solve them, a general-purpose commercial software, *STARCCM+*, has been used.

The fluid considered was air. For the working conditions (i.e. $p_0 = 101325$ Pa and $T_0 = 300$ K), this fluid behaves as a perfect gas characterized by a gas constant $R = 287.02$ J kg^{-1}K^{-1}, an adiabatic index $\gamma = 1.4$, an unperturbed sound velocity $a_0 = 347.28$ m s^{-1} and unperturbed density $\rho_0 = 1.177$ kg m^{-3}.

The selection of a mesh size of the fluid volume-domain must be a compromise between the maximum desired frequency resolved (in this case $\frac{f\,L_{muff}}{a_0} = 1.30$) and a correct discretization of the circular pipe-domain. In this case this size was taken to be $\frac{R}{\Delta x} = 24$.

About the selection of the time-step, as wave propagation is the phenomenon of interest, a low acoustic Courant number (CFL) must be set, based on the wave-speed velocity. In this case, it was taken as $CFL = \frac{a_0\ \Delta t}{\Delta x} < 1 \rightarrow \frac{a_0\ \Delta t}{\Delta x} = 1.2 \cdot 10^{-3}$.

A visualization of the fluid mesh is shown in Fig. 4.5a. The coupled solid problem (4.1) was also solved by using the commercial software *STARCCM+*. Therefore, a FEM mesh was created to model the solid domain.

Limitations of the time domain solver used during this work lead to the use of second order 3D solid elements in order to model the solid domain,

making the solution of the structural problem more CPU consuming than if shell elements are used. Nevertheless, as the number of elements of the flexible wall is much lower that for the fluid domain, this element selection will not become a bottleneck. Thus, the solution of a thin walled solid with 3D elements requires at least three elements across the thickness [209]. Therefore, the surface was modeled by using second order hexahedral elements of side $\frac{R}{\Delta x} = 10$. Fig. 4.5b shows a representation of the solid mesh. It should be noted that, as already mentioned, the use of shell elements could improve the computational effort with negligible effects in the accuracy of the results.

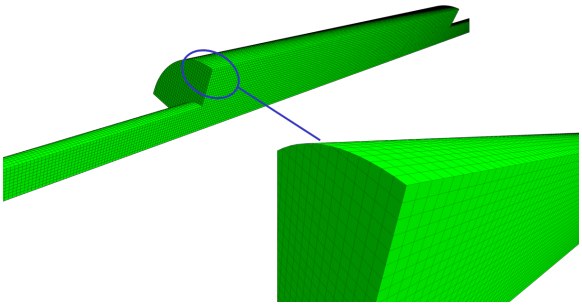

(a) Finite Volume mesh

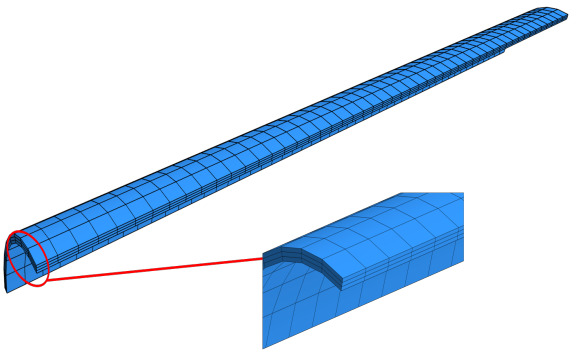

(b) Finite Element mesh

Figure 4.5: *STARCCM+* mesh visualisation

Description of cases for the numerical determination of the transfer matrix coefficients using CFD As previously shown, in order to get the values of the transfer matrix coefficients, resolution of variables for two different cases must be performed. These cases are hereinafter referred to as “Case A” and “Case B”. Description of each case is given below.

Case A For the first case the inlet velocity history is assumed to be known as shown in Equation (4.17). The outlet of the pipe is set to be anechoic, so that no pressure reflections are found in this boundary.

Case B For the second case the inlet velocity history is supposed to be known as shown in Equation (4.17) until the velocity pulse is introduced into the domain. Once the pulse is introduced, this boundary condition is set to be anechoic, so that no pressure reflections occur in the inlet.

The outlet boundary condition is set to be a rigid wall, so at this section the velocity history is supposed to be known and equal to $v_{out}(t) = 0$.

Frequency domain FEM Model

In section 4.2.1, the Helmholtz Equation was introduced. In order to solve it, the general-purpose commercial software *COMSOL* is used. Compromise between geometry and frequency mesh size requirements can be achieved by using a uniform mesh size which could be excessive from the frequency point of view, but adapts well to the geometry [210].

Compared with the CFD model, and due to the linearity of the solved equation, the mesh requirements are significantly lower for the FEM case. Thus, for this case mesh size was taken to be $\frac{R}{\Delta x} = 6$ for the whole domain, using quadratic elements. Fig. 4.6 shows a representation of the FEM mesh. As a disadvantage it can be cited that only linear effects are computed.

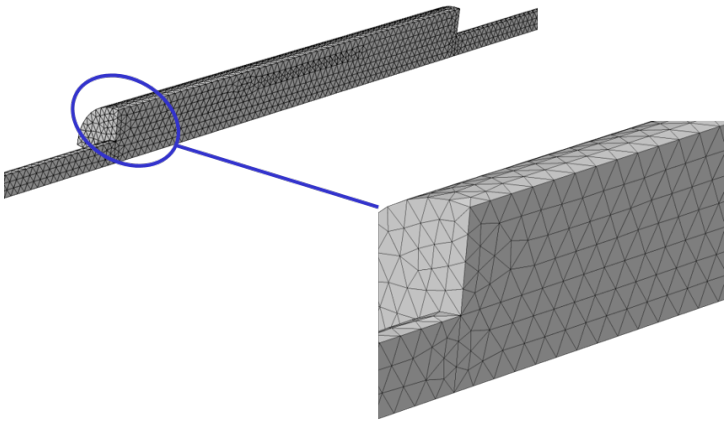

Figure 4.6: *COMSOL* Fluid domain mesh

The solid domain is modelled using a zero-thickness shell approximation, which allows lower CPU time consumption with no significant loss of accuracy, as it was mentioned before. This kind of model allows to account for the whole thickness in the case of thin walls by only using one surface element.

Description of cases for the numerical determination of the transfer matrix coefficients using FEM As previously shown, in order to get the value of the transfer matrix coefficients, solution of variables for two different cases must be performed. Again, these cases are hereinafter referred to as "Case A" and "Case B". Description of each case is given below.

Case A For the first case the inlet pressure is supposed to be harmonic, evolving in accordance with:

$$p_{in}(t) = P_{in}\, e^{j\omega t} \qquad P_{in} = 1\,\text{Pa} \tag{4.24}$$

The outlet face is assumed to be anechoic. Thus, the acoustic impedance is known, with value:

$$Z_{out} = Z_0 = \rho_0\, a_0 \tag{4.25}$$

It should be recalled that, due to the linearity of the Helmholtz equation, the selection of the inlet pressure is completely arbitrary, because it will have no influence on the quantification of the acoustic element features.

Case B Case B uses the same inlet conditions as does Case A. The outlet section is again assumed to behave as a rigid wall. Thus, the acoustic normal velocity is known, with value:

$$v_{out} = 0 \tag{4.26}$$

4.2.4 Results for the rigid expansion chamber

CFD time domain results

When the maximum inlet velocity is set to $v_{max} = 0.01$ ms^{-1}, the maximum value of the inlet pressure pulse can be found to be $p_{max} = 4.081$ Pa. For a correct time domain CFD simulation, the calculation must be run until the whole inlet pulse leaves the domain through the non-reflecting boundary conditions. For the present case all the simulations were performed until a final time of $\frac{t\ a_0}{L_{muff}} = 100$. This value ensures that all the energy supplied at the inlet leaves the domain.

In order to obtain the transmission characteristics of the system it is necessary to perform a computation of both pressure and velocity at the inlet and the outlet for each case studied (Case A and Case B). These values are shown in Fig. 4.7.

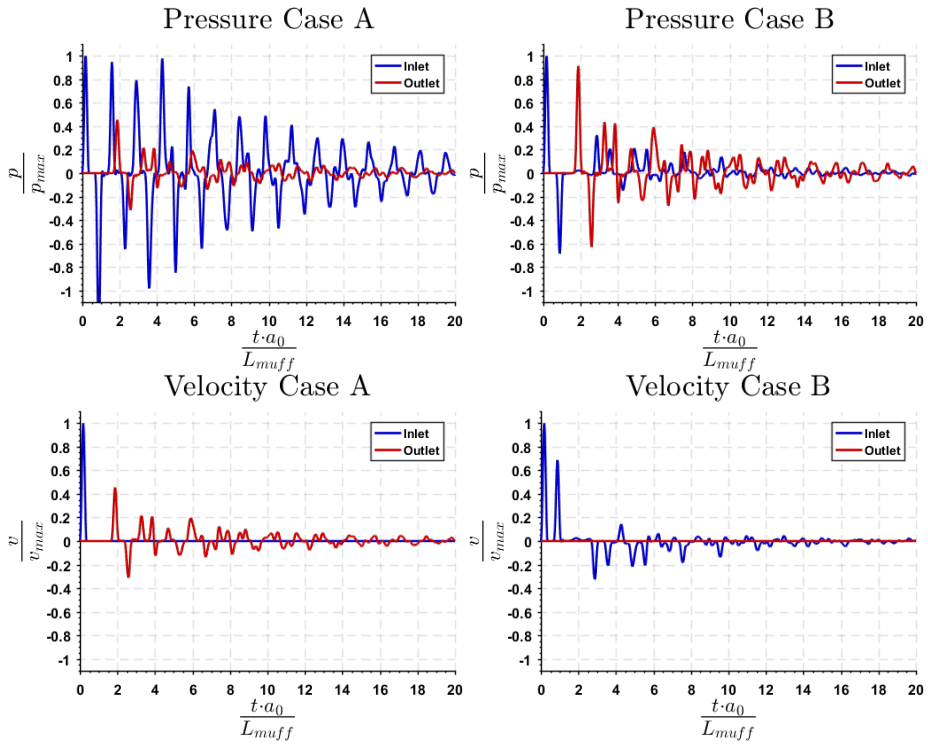

Figure 4.7: Time evolution of the pressure and velocity at domain boundaries

In order to obtain the frequency characteristics of the expansion chamber, a Discrete Fourier Transform must be applied to the boundary data. It is thus supposed that a function $x(t)$ can be approximated by a Fourier Series, as indicated by the following expression:

$$X_k = \sum_{n=0}^{N-1} x_n \, e^{-j \, \frac{2 \cdot \pi \cdot k \cdot n}{N}} \tag{4.27}$$

where x_n is the pressure at sampling time n, N is the number of samples and X_k is the frequency response for the k^{th} frequency. Applying this concept to the computed time signals the frequency response for each of the cases are obtained. These are shown in Fig. 4.8. Sampling time is taken to be $T_s = 1.2 \cdot 10^{-3} \Delta x / a_0$:

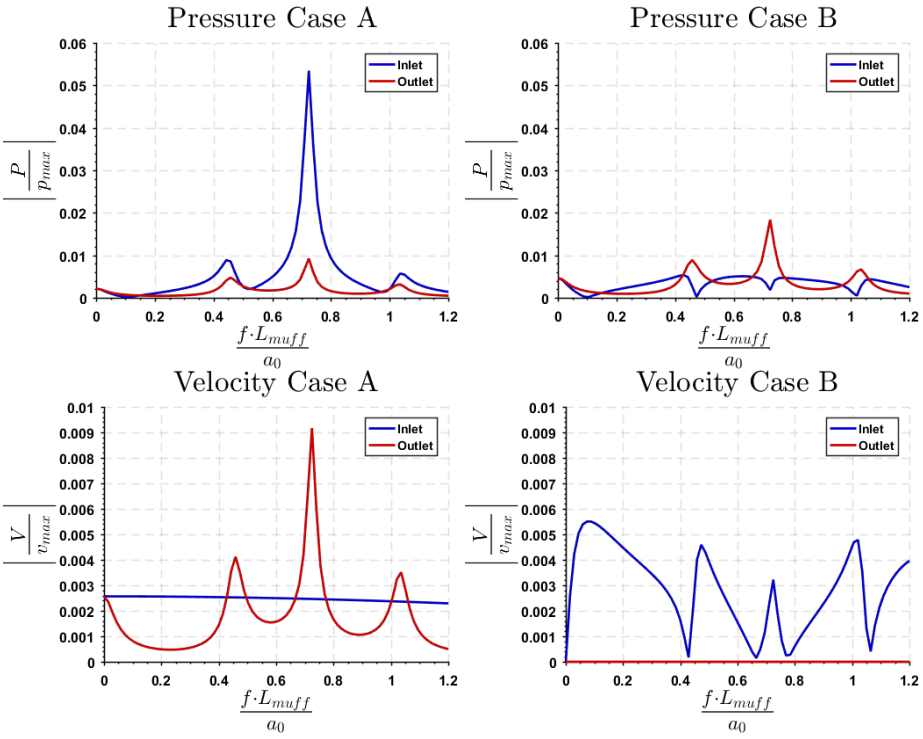

Figure 4.8: Frequency response of pressure and velocity at domain boundaries

It should be noticed that, as expected, the frequency response of the velocity at the inlet for case A is the same as that shown in Fig. 4.3 but it differs for Case B. The reason of this discrepancy is that, for Case B, the inlet boundary

condition is assumed to be anechoic, so that the velocity components must be calculated and, for $t > T_{impulse}$, Equation (4.17) is not valid anymore.

FEM frequency domain results

The Helmholtz equation is solved by means of FEM in the frequency domain, which leads to a significant decrease of the computational cost, compared with the CFD time domain method.

Fig. 4.9 shows the Sound Pressure Level (SPL) in the domain, for different excitation frequencies. SPL is defined as:

$$SPL(f) = 20\ \log_{10}\left(\frac{|P(f)|}{P_{ref}}\right) \qquad P_{ref} = 20\ \mu\text{Pa} \tag{4.28}$$

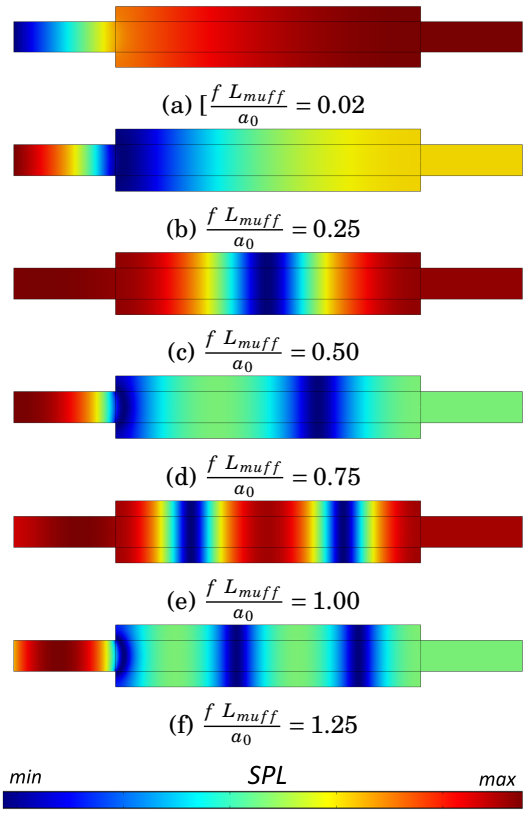

(g) Qualitative color map

Figure 4.9: SPL under different excitation frequencies

It can be noted from Fig. 4.9 that, for the frequencies $\frac{f\,L_{muff}}{a_0} = 0.25$, $\frac{f\,L_{muff}}{a_0} = 0.75$ and $\frac{f\,L_{muff}}{a_0} = 1.25$ the SPL at the outlet is much lower than the SPL at the inlet. As it will be shown later, this corresponds to the frequencies of maximum attenuation. For the frequencies $\frac{f\,L_{muff}}{a_0} = 0.50$ and $\frac{f\,L_{muff}}{a_0} = 1.00$ the muffler enters into a resonance mode and no attenuation on the SPL is found. For higher frequencies 3D effects are easier to be observed at the sudden area change.

Characterisation of the rigid muffler features

In this section the values of the transfer matrix will be obtained and compared using the methods presented in previous paragraphs.

The transfer matrix components are shown in Fig. 4.10

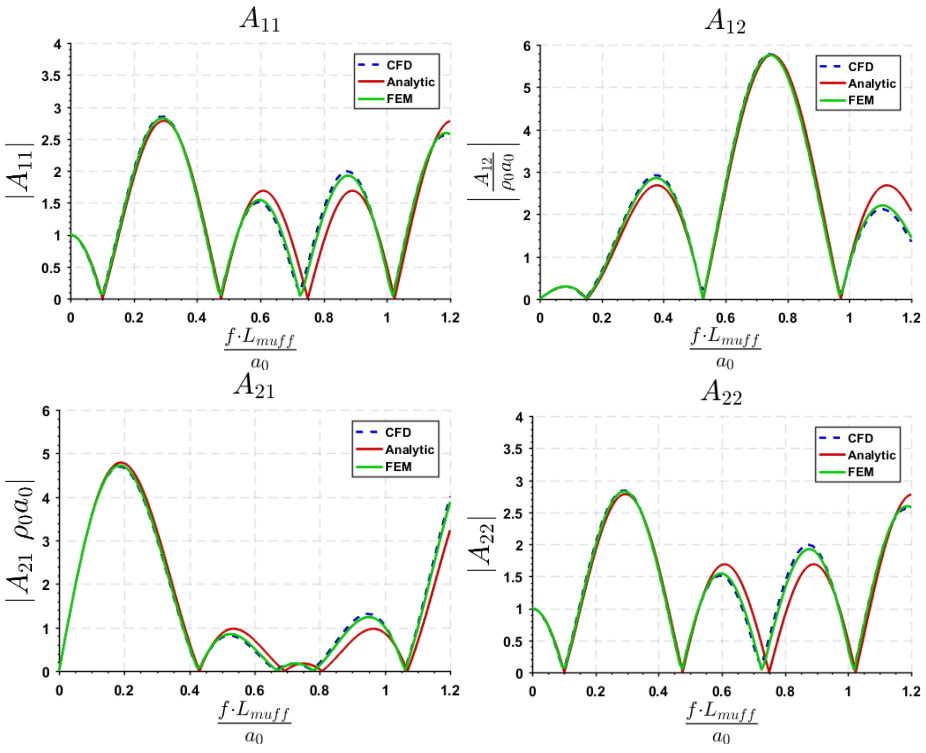

Figure 4.10: Transfer matrix coefficients

All the previously explained methods coincide very well for low frequencies. Some discrepancies appear when quantifying values at higher frequencies.

Nevertheless, this is mainly due to the onset of 3D effects, which are not taken into account by the analytical method. It will be later shown how those 3D issues barely affect the global characteristics of the system, such as Transmission Loss (and Insertion Loss, Velocity Ratio, etc.).

The Transmission Loss is shown, for each of the methods used, in Fig. 4.11. Notice how the analytical and the Finite Element method are perfectly coincident for the whole frequency range. At high frequencies the CFD study predicts a slightly higher value of the Transmission Loss. This could be primarily due to non-linear effects, which are taken into account in this method but are not in the analytical and FEM approximations.

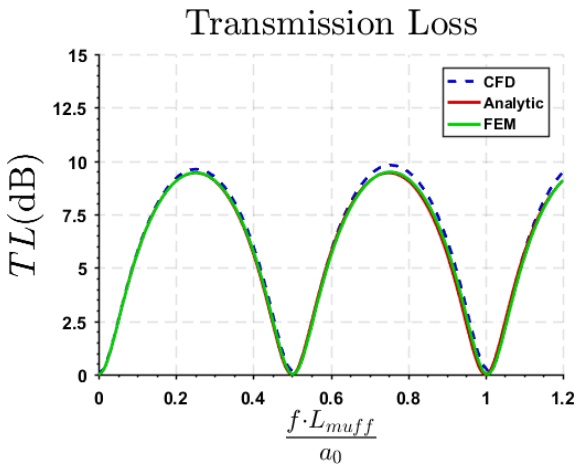

Figure 4.11: Transmission Loss as a function of frequency

These results show a nearly perfect agreement between predictions from a frequency domain FEM and from a time domain CFD calculation. This can be taken as a demonstration of the validity of both methods for this kind of problems. The following sections make use of these validated methods for the prediction of the particular features associated with a flexible expansion chamber.

4.2.5 Results for the flexible expansion chamber

Flexible wall eigenfrequencies

When analyzing the interaction between the acoustic field and the surrounding flexible wall, the excitation of the structural modes is of primal interest. It is thus necessary to perform an uncoupled analysis of those values.

Table 4.2 shows the first six eigenfrequencies of the **quarter pipe**, for the case of wall thickness $\delta = 0.002$ m, wall density $\rho_{wall} = 1000$ kg m^{-3} and Poisson ratio $\nu = 0.33$, and for various values of the Young modulus. These frequencies were calculated using the commercial software *COMSOL Multiphysics* for the isolated structure. As will be shown later apparition of axisymmetric modal shapes occur for higher values of frequency.

Table 4.2: Quarter pipe eigenfrequencies

	fL_{muff}/a_0			
Mode	$E = 0.1$ GPa	$E = 0.5$ GPa	$E = 1$ GPa	$E = 30$ GPa
1	0.103	0.230	0.326	1.784
2	0.178	0.398	0.563	3.084
3	0.286	0.640	0.905	4.956
4	0.409	0.913	1.292	7.076
5	0.426	0.952	1.347	7.376
6	0.436	0.976	1.380	7.558

Fig. 4.12 shows the structural modal shape corresponding to each eigenfrequency calculated using *COMSOL*. Red colors correspond to maximum absolute values of the displacement while blue colors correspond to duct nodal lines.

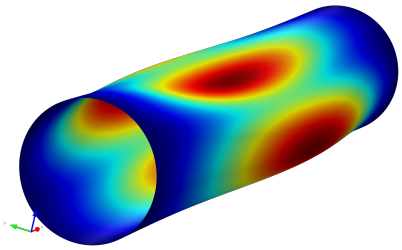

(a) [Modal shape 1

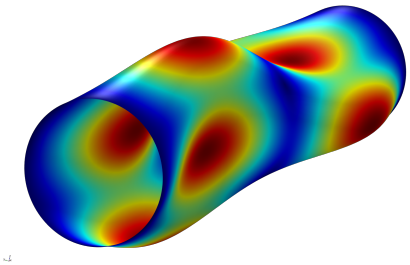

(b) Modal shape 2

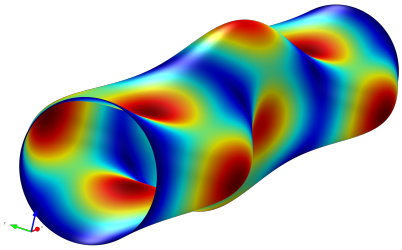

(c) Modal shape 3

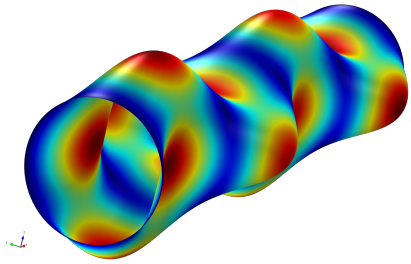

(d) Modal shape 4

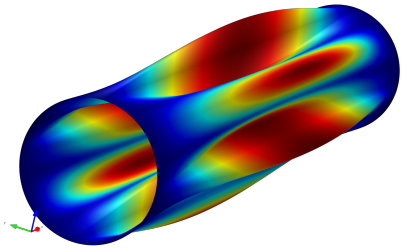

(e) Modal shape 5

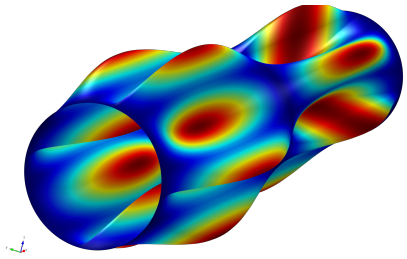

(f) Modal shape 6

Figure 4.12: Structural mode shapes

4.2.6 CFD time domain results

As the inlet tube is perfectly rigid, the maximum value of velocity and pressure during the pulse injection is exactly the same as in section 4.2.4. The inclusion of the FSI interaction leads to a significant increment of the computational cost. Thus, as the Transmission Loss is the most significant parameter when evaluating the performance of an acoustic element, only Case A is considered in this section. For the present case, all simulations are performed until a final time of $\frac{t\ a_0}{L_{muff}} = 100$.

Fig. 4.13 and Fig. 4.14 show the time evolution of the pressure field for different time steps for case A (anechoic outlet), assuming the expansion chamber as flexible.

For illustration purposes, a parametric study of the influence of the Young modulus was performed. Fig. 4.13 shows the results for the case with $E = 30$ GPa (pure tin) and Fig. 4.14 shows results for the case with $E = 1$ GPa (polypropylene). The deformation field of the thin wall is also shown. Notice that the color-scale is shown in a qualitative manner in order to obtain interpretable representation.

- **Fig. 4.13-4.14 a**: The whole velocity-pressure pulse has been introduced into the domain. Because the pulse has not arrived to the expansion zone, reflections or deformations do not appear yet.
- **Fig. 4.13-4.14 b**: The pulse reaches the inlet of the expansion chamber. The pressure is affected exactly by the same phenomena which were explained in section 4.2.4. An axisymmetric deformation field can be observed both in the $E = 30$ GPa and $E = 1$ GPa being higher in the second case, as expected.
- **Fig. 4.13-4.14 c**: The reflected pulse reaches the inlet. The boundary condition $v(t) = 0$ behaves as a rigid wall, so it is reflected again towards the expansion chamber again. In the case $E = 30$ GPa the deformation-pulse propagates together with the pressure pulse in the expansion chamber. In the case $E = 1$ GPa it can be noticed how the low material stiffness leads to an additional wave.
- **Fig. 4.13-4.14 d**: The primary pulse reaches the outlet of the expansion chamber, and here a new partial reflection and transmission are found. The deformation pulse is also reflected. Note the high qualitative difference between the $E = 30$ GPa and $E = 1$ GPa. In the second case it can be seen that the number of axisymmetric waves appearing is significantly higher.

- **Fig. 4.13-4.14 e**: The primary pulse reaches the outlet domain section. Due to the non-reflective boundary condition the outlet behaves as an anechoic termination. The pressure and deformation pulses continue travelling inside the expansion chamber, mutually interacting.

- **Fig. 4.13-4.14 f**: The primary pulse reaches again the inlet of the expansion chamber. Some part of the pulse is reflected towards the outlet, and some other passes through to the inlet of the domain.

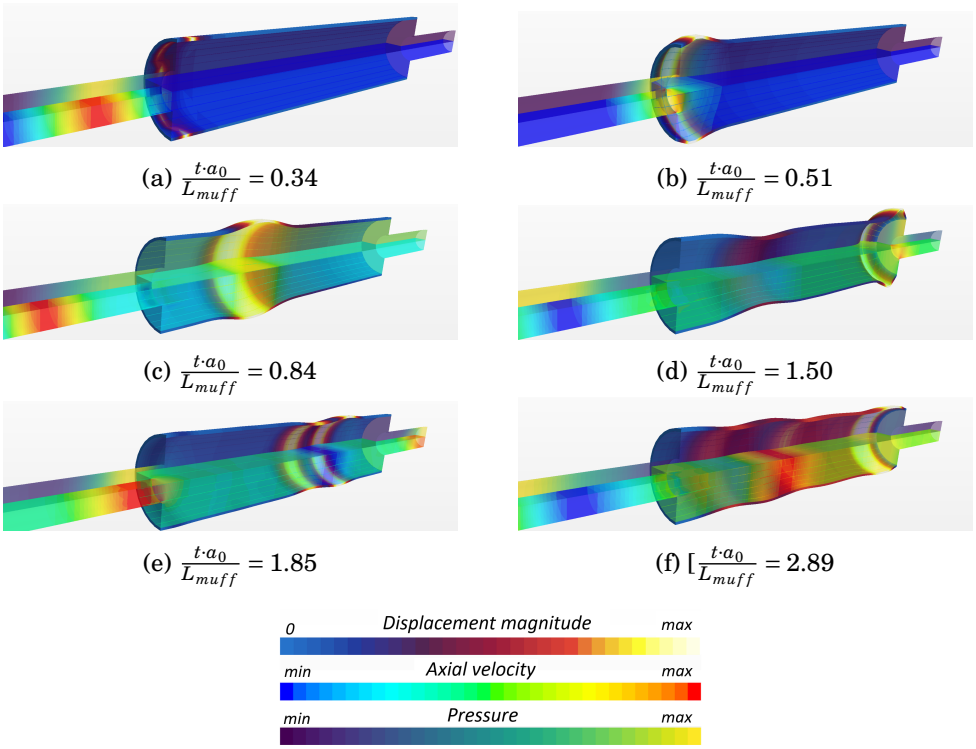

(a) $\frac{t \cdot a_0}{L_{muff}} = 0.34$ (b) $\frac{t \cdot a_0}{L_{muff}} = 0.51$

(c) $\frac{t \cdot a_0}{L_{muff}} = 0.84$ (d) $\frac{t \cdot a_0}{L_{muff}} = 1.50$

(e) $\frac{t \cdot a_0}{L_{muff}} = 1.85$ (f) [$\frac{t \cdot a_0}{L_{muff}} = 2.89$

(g) Qualitative color map

Figure 4.13: Time evolution of the pressure and velocity pulse for different time instants and $E = 30$ GPa

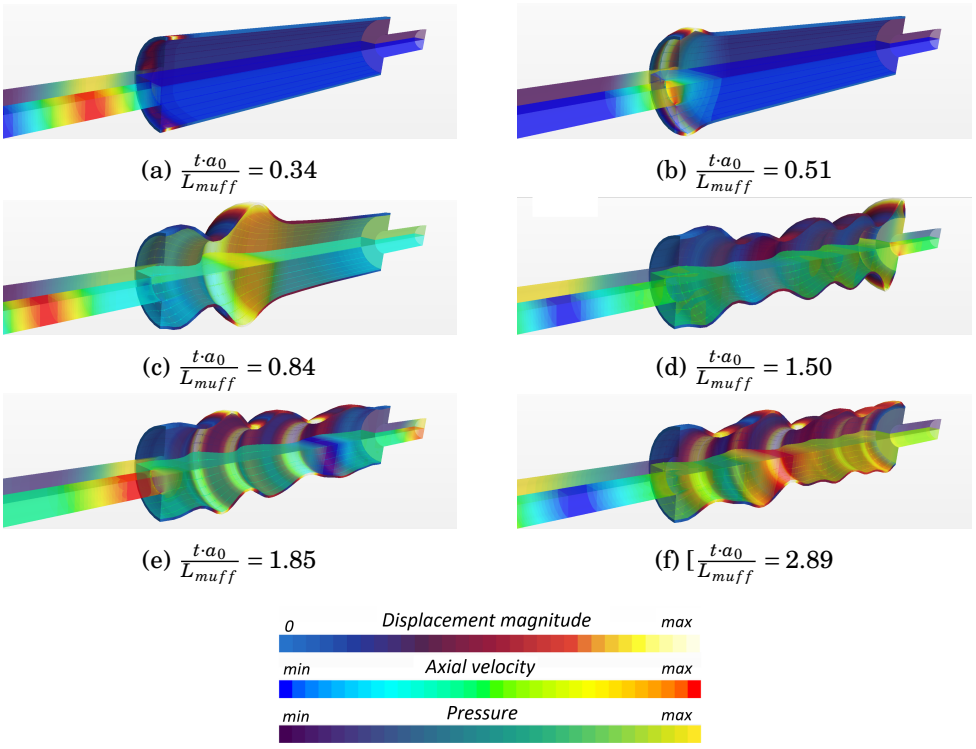

(a) $\frac{t \cdot a_0}{L_{muff}} = 0.34$

(b) $\frac{t \cdot a_0}{L_{muff}} = 0.51$

(c) $\frac{t \cdot a_0}{L_{muff}} = 0.84$

(d) $\frac{t \cdot a_0}{L_{muff}} = 1.50$

(e) $\frac{t \cdot a_0}{L_{muff}} = 1.85$

(f) [$\frac{t \cdot a_0}{L_{muff}} = 2.89$

(g) Qualitative color map

Figure 4.14: Time evolution of the pressure and velocity pulse for different time instants and $E = 1$ GPa

Another important result, where differences between the rigid and the flexible cases are found, is the time response of pressure and velocity at the inlet and the outlet. This time response is shown in Fig. 4.15 and, as it can be observed, no differences are noticed between the rigid case and the flexible case with $E = 30$ GPa. For cases of Young modulus $E < 1$ GPa the time response shows significant deviations from the rigid case, specially after some reflections. It can be seen how, as a general trend, pressure peaks of reflections are lower as the value of rigidity decreases.

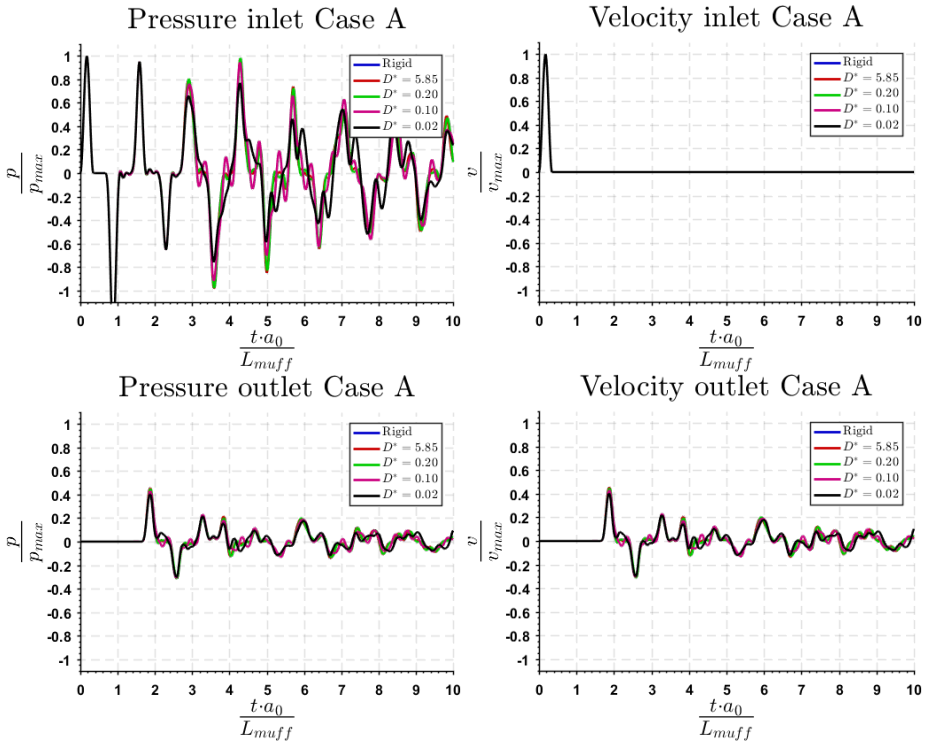

Figure 4.15: Time evolution of the pressure and velocity at domain boundaries for Case A. Different material rigidity

Fig. 4.16 shows the time evolution of deformation at a point located in the mid section of the expansion chamber, at a location ($L_{muff}/2$,R) for different wall rigidities. High differences in the displacement can be observed for the different materials. Fig. 4.16 also shows that the natural modes of the structure remain unattenuated. This is due to absence of damping in the model.

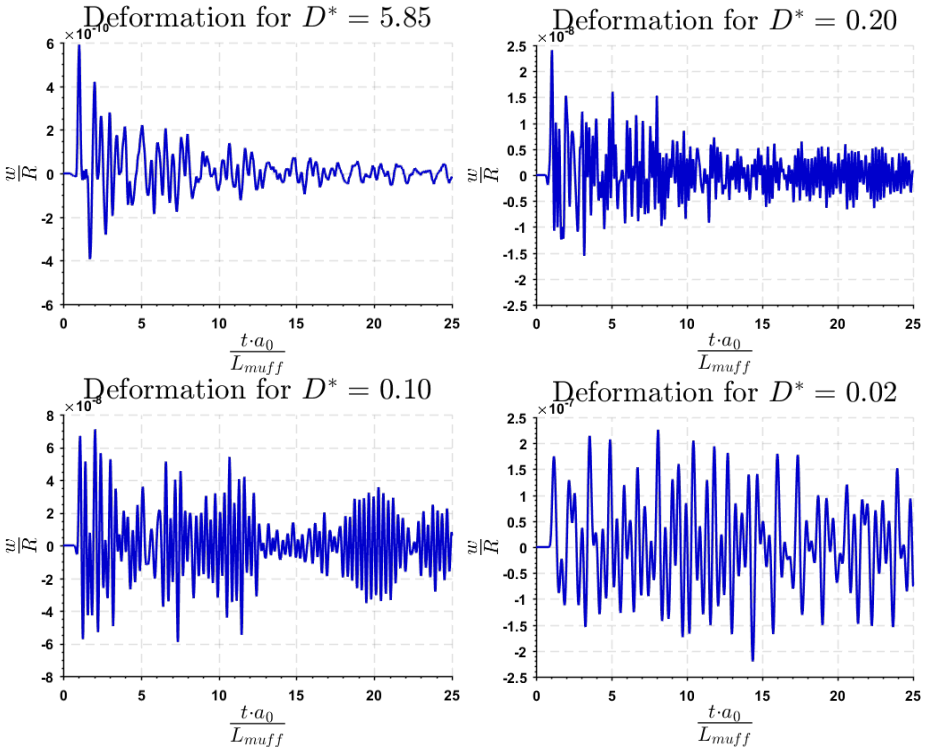

Figure 4.16: Time evolution of the wall displacement for Case A. Different material rigidity

Fig. 4.17 shows the frequency content of this radial displacement history. It can be observed that the frequency response is identical (except, obviously, in the absolute value) for the cases with $D^* = 5.85$ ($E = 30$ GPa), $D^* = 0.20$ ($E = 1$ GPa) and $D^* = 0.10$ ($E = 0.5$ GPa). For these values of rigidity, two well-differentiated peaks are found at $\frac{f\, L_{muffler}}{a_0} = 0.75$ and $\frac{f\, L_{muffler}}{a_0} = 1.00$, which correspond with the chamber resonance frequencies. However, for the case with $D^* = 0.02$ ($E = 0.1$ GPa) a completely different response is obtained. A new, more important peak, appears at $\frac{f\, L_{muffler}}{a_0} = 0.87$, which corresponds to the excitation of the first axisymmetric natural mode of the structure.

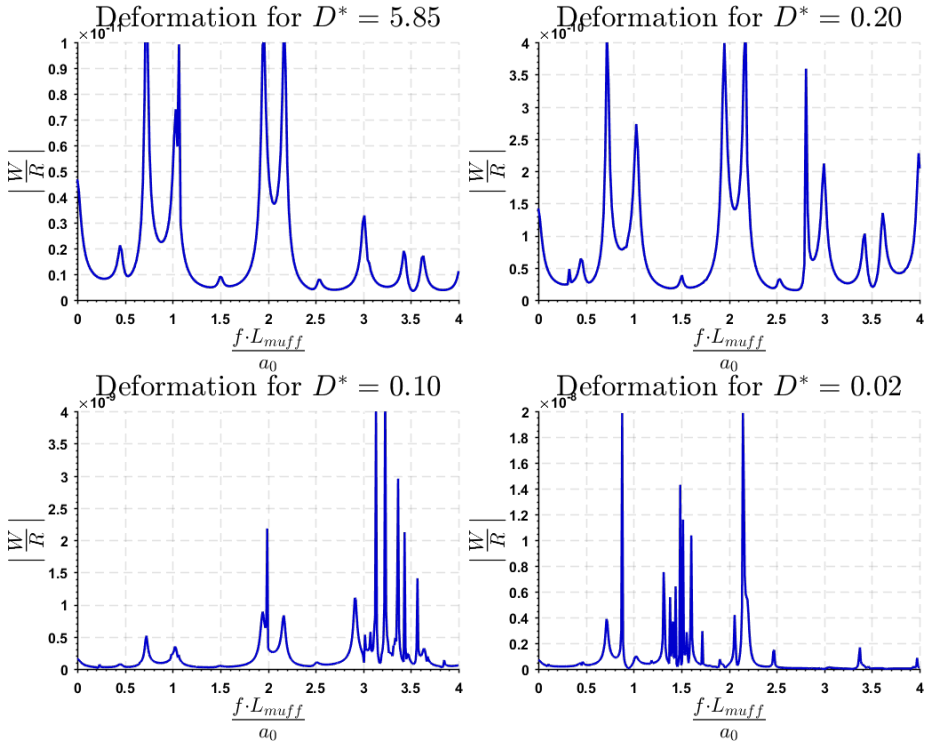

Figure 4.17: Frequency response of the radial wall displacement for Case A. Different material rigidity

4.2.7 FEM frequency domain results and characterization of the flexible muffler

Fig. 4.18 shows the Transmission Loss, calculated using Equation (4.21), for the flexible case with low Young modulus, $E = 0.1$ GPa. The two traces correspond to a calculation using time-domain CFD and a calculation using frequency-domain FEM.

Fig. 4.18 allows to demonstrate that, as well as for the rigid case (see Fig. 4.11), frequency domain FEM and time domain CFD provide similar results, with little discrepancies between both methods.

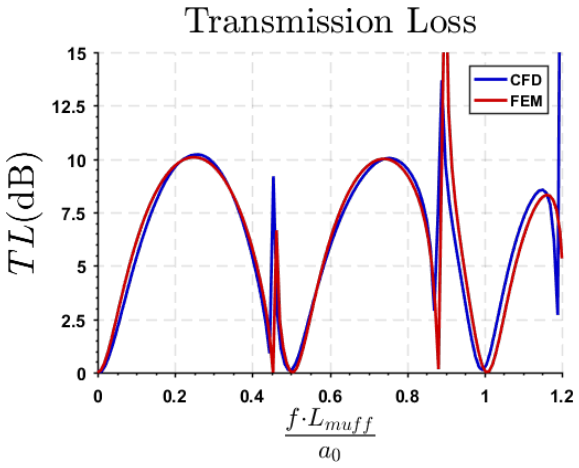

Figure 4.18: Transmission Loss as a function of frequency for $E = 0.1$ GPa. Comparison between time domain CFD model and frequency domain FEM model

In order to examine the dependence of the acoustic response on rigidity, Fig. 4.19 shows the evolution of the Transmission Loss response as the Young modulus is decreased. In order to improve the interpretation of the results, they all are compared with the perfectly rigid result.

It can be observed that, for the two first cases ($E = 1$ GPa and $E = 0.5$ GPa) non-noticeable differences are encountered between the rigid and the flexible cases. Nevertheless, for $E \leq 0.2$ GPa ($D^* \leq 0.04$) important differences appear. This coincides with the excitation of the first and second axisymmetric modes of the structure (see the location of these modes in Table 4.3). Figure 4.20 shows the modal shape corresponding to the first four eigenfrequencies.

Under these circumstances it can be found that, just before the axisymmetric mode is excited, the fluid-structure coupling leads to an important change in behavior. Around this frequency a high attenuation point is found immediately followed or preceded by a sharp pass band of abrupt attenuation drop. This sharp behavior is due to the strong fluid-structure coupling derived from the excitation of the natural axisymmetric modes of the structure. Similar behavior was found in the transfer function studied by Herrmann et al. [211] for the case of thin hydraulic pipes.

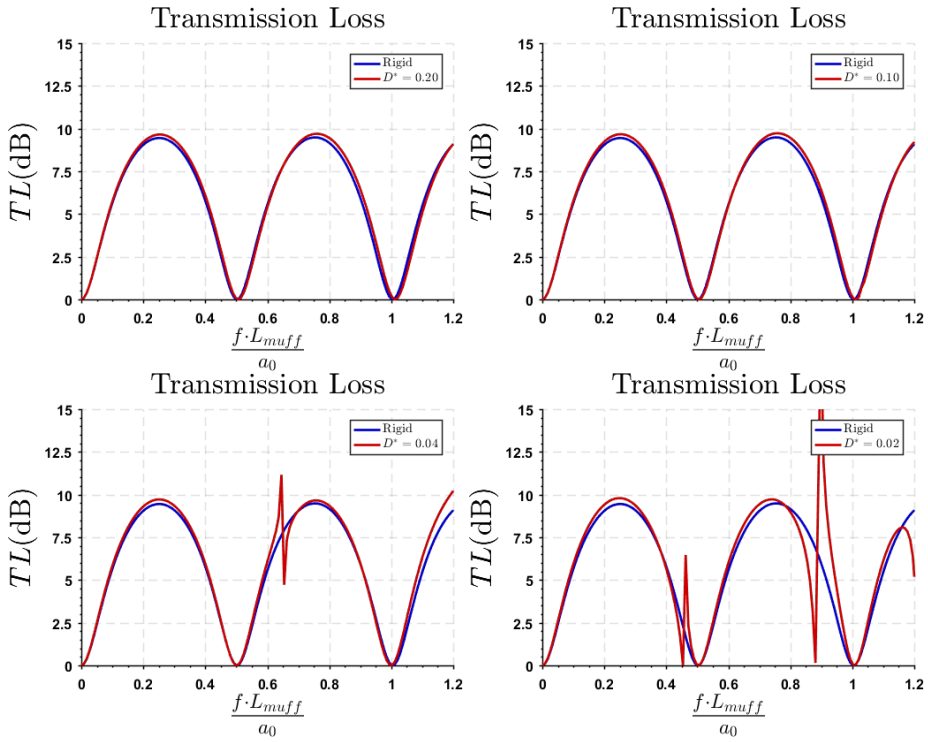

Figure 4.19: Transmission Loss as a function of stiffness for mass parameter $m_l^* = 57$

Table 4.3: Axisymmetric modes for different non-dimensional stiffness parameter, D^*

	$f\ L_{muff}/a_0$			
Mode	$D^* = 0.02$	$D^* = 0.04$	$D^* = 0.10$	$D^* = 0.20$
1	0.45	0.64	1.01	1.43
2	0.89	1.25	1.98	2.80
3	1.21	1.71	2.71	3.83
4	1.33	1.89	2.98	4.22
5	1.37	1.94	3.06	4.33
6	1.39	1.96	3.10	4.38

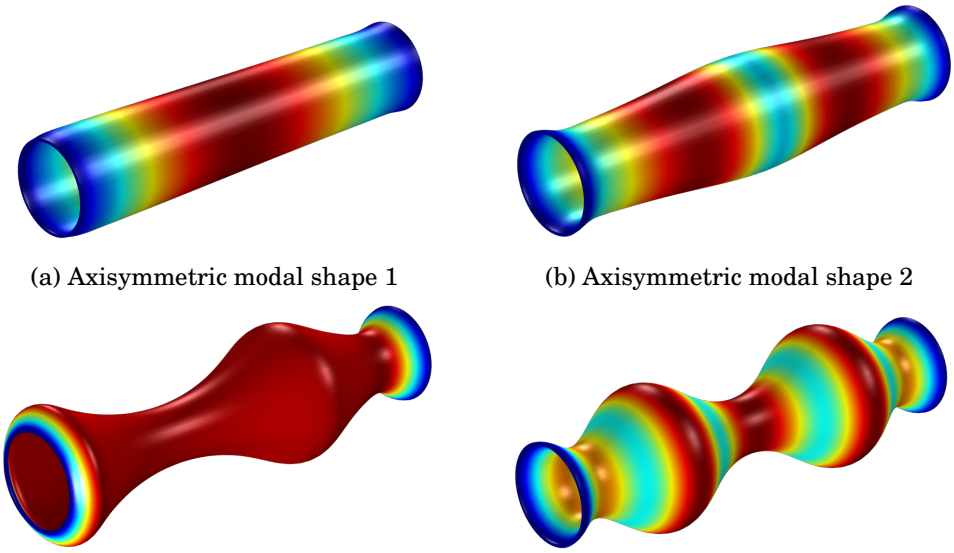

(a) Axisymmetric modal shape 1

(b) Axisymmetric modal shape 2

(c) Axisymmetric modal shape 3

(d) Axisymmetric modal shape 4

Figure 4.20: Axisymmetric structural mode shapes

Fig. 4.21 and Fig. 4.22 show the frequency response field of the Sound Pressure Level and displacement, respectively, for the case A with $E = 0.1$ GPa. It can be observed that, as previously predicted, the cases of minimum acoustic losses $SLP_{out} \approx SPL_{in}$ correspond with the excitation of a structural axisymmetric mode.

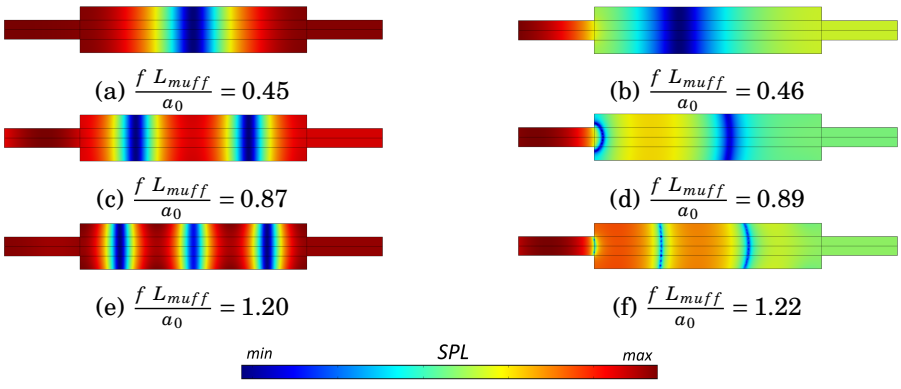

(a) $\frac{f\ L_{muff}}{a_0} = 0.45$

(b) $\frac{f\ L_{muff}}{a_0} = 0.46$

(c) $\frac{f\ L_{muff}}{a_0} = 0.87$

(d) $\frac{f\ L_{muff}}{a_0} = 0.89$

(e) $\frac{f\ L_{muff}}{a_0} = 1.20$

(f) $\frac{f\ L_{muff}}{a_0} = 1.22$

(g) Qualitative color map

Figure 4.21: SPL under different excitation frequencies for the flexible case

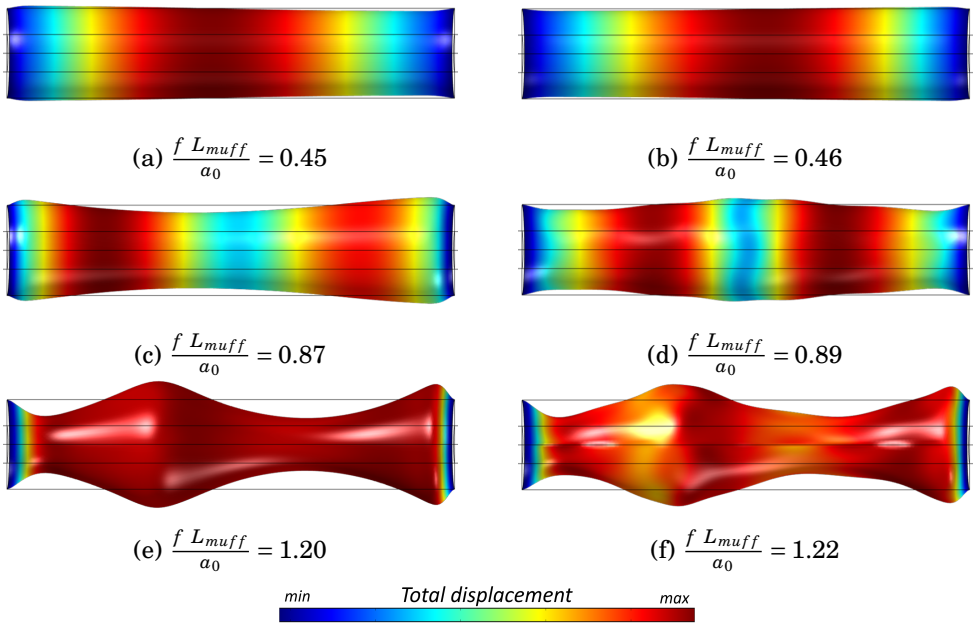

(a) $\frac{f\,L_{muff}}{a_0} = 0.45$

(b) $\frac{f\,L_{muff}}{a_0} = 0.46$

(c) $\frac{f\,L_{muff}}{a_0} = 0.87$

(d) $\frac{f\,L_{muff}}{a_0} = 0.89$

(e) $\frac{f\,L_{muff}}{a_0} = 1.20$

(f) $\frac{f\,L_{muff}}{a_0} = 1.22$

(g) Qualitative color map

Figure 4.22: Displacement under different excitation frequencies for the flexible case

Fig. 4.23 shows the evolution of the strain and kinetic energy stored in the solid. Notice how the maximum peak values of both energies correspond to the excitation of the axisymmetric natural modes.

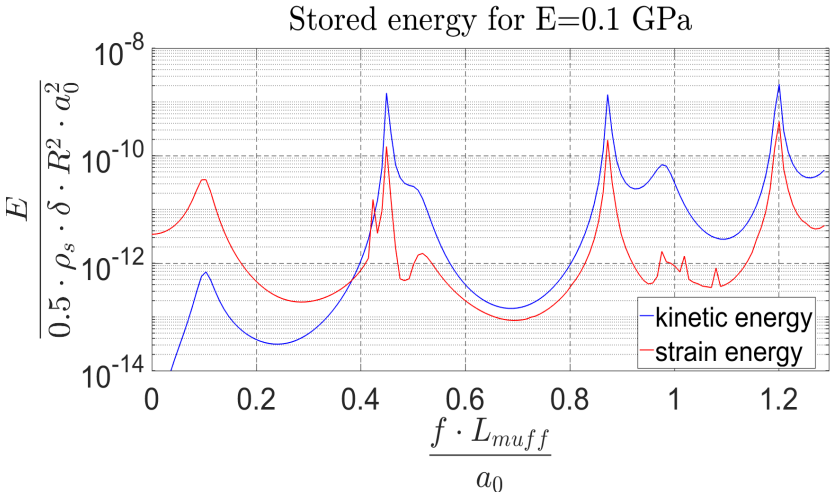

Figure 4.23: Stored energy as a function of the frequency for $E = 0.1$ GPa

4.2.8 Partial conclusions

A methodology based on CFD-FEM method has been presented for the Transmission Loss calculation of vibro-acoustic domains both in time and frequency domain.

A review of the main different techniques used for the characterization of vibro-acoustic problems has been performed.

To fine-tune the methodology under consideration, different simulations are performed using both CFD and FEM in order to predict the acoustic performance of a perfectly rigid expansion chamber. Results show fair agreement between CFD, FEM and analytic cases.

Similar methods are for the case of an expansion chamber with flexible walls. Again, the presented models show good agreement for the frequency range under consideration.

Nevertheless, it is observed that computational requirements of the time-domain CFD method are various orders of magnitude higher than the requirements for the same geometry using a frequency-domain FEM approach.

General trends of the vibroacoustic response were calculated for a rigid and a flexible expansion chamber. Results show that, for the current geometry, the influence of rigidity for a heavy structure is important only for very low Young modulus. The effect of the structural vibrations becomes important when excitation of the first and second axisymmetric natural modes of the structure takes place.

It is demonstrated that, when the inner flow excites the structure at the resonance frequency, the problem becomes strongly coupled and the influence of the flexible walls should be taken into account.

Finally, it is illustrated that, for a geometry of the shapes and sizes like the simplified cylindrical expansion chamber presented during the current work, the mentioned complete coupling only appears for very low values of the Young modulus at the frequencies of interests. As this phenomena is mainly due to the excitation of the natural modes of the structure, mufflers with higher modal density should experience this phenomena even for higher values of the Young Modulus.

4.3 Prediction of Flow Induced Vibration of a flat plate located after a wall mounted obstacle. Aerovibroacoustics

4.3.1 Description of the test case

In this section, a simplified under-body flow is modeled which, nevertheless, can be considered as representative for most of the relevant physical phenomena. The configuration consists of (1) a channel which walls are considered to be rigid; (2) a rigid square step which forces a turbulent flow downstream of it, dominated by large scales, and (3) a thin flexible wall where the magnitude of the displacement is sufficiently high to allow appreciable deformations (and noise radiation), but low enough to not noticeably influence the fluid field.

Figure 4.24 shows a sketch of the fluid domain geometry. $L_{ref} = 1.5$ cm is the edge length of the step, which is confined in a channel of $5L_{ref}$ in height and $10L_{ref}$ in width. A flow of air, with density $\rho_\infty = 1.225\ \mathrm{kg\,m^{-3}}$, viscosity $\mu = 1.78\ \times 10^{-5}\ \mathrm{Pa\,s}$ and average velocity $V_\infty = 22\ \mathrm{m\,s^{-1}}$, which corresponds to a Reynolds number of Re = 22710 and a Mach number, Ma = 0.06, enters the domain from the left. From a fluid dynamic perspective, the obstacle, the plate wall and the bottom walls are treated with a non-slip boundary condition. The inlet and the outlet are located sufficiently far such that the frequency response of the variables of interest is not affected by their location.

It is expected that the boundary layer at the upper wall is sufficiently thin such that its effects on the vibrational response of the plate can be neglected. Therefore, in order to keep the computational cost affordable, a slip boundary condition was used for this wall. For the lateral walls, a similar reasoning could be given, and a periodicity condition can be stated, in a similar way as in the work of Schafer et al. [198] or David et al. [212].

The plate is mounted just after the step and covers the whole width of the channel, with a length of $40/3L_{ref}$. The edges parallel to the flow direction are clamped, while the contours perpendicular to the flow are mounted in a simply supported manner. The plate is made of steel, with Young's Modulus of $E = 200$ GPa; density of $\rho_s = 7745\ \mathrm{kg\,m^{-3}}$; Poisson's ratio equaling $\nu = 0.35$ and a thickness of $h = 0.5$ mm.

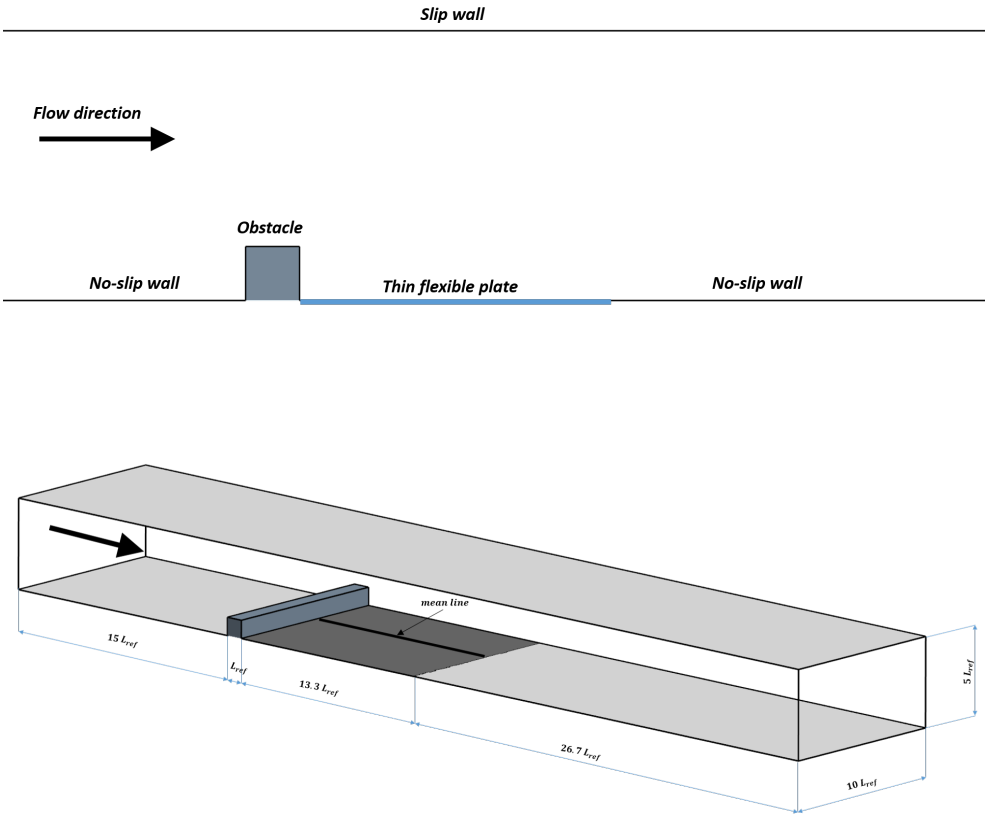

Figure 4.24: Fluid domain geometry sketch

4.3.2 Numerical methodology

Thin plate structural model

As stated, all walls except the plate are considered infinitely rigid and their displacements can thus be neglected. In order to predict the deformations at the plate induced by the fluid flow, the equations for an elastic solid are applied to this body. However, it is well known that, if the plate is sufficiently thin, those equations reduce to the equation of a Kirchoff-Love plate, [213], [214], which is shown in Equation 4.29. In this section, this equation will be used to describe the structural part, since $h/L_{ref} = 1/30$.

$$\frac{E\ h^3}{12\ (1-\nu^2)}\left(\frac{\partial^4 u}{\partial x^4} + 2\ \frac{\partial^4 u}{\partial x^2 \partial z^2} + \frac{\partial^4 u}{\partial z^4}\right) + \rho_s h \frac{\partial^2 u}{\partial t^2} = p \tag{4.29}$$

Here, x and z are, respectively, the directions parallel and perpendicular to the flow; u is the normal displacement of the plate (in the y direction) and p is the pressure acting on the structure. Note that, regardless the strength of the coupling, the plate will be influenced by the flow forces by means of this last term, as indicated, among others, by Bathe et al. [215]. In order to investigate the relative importance of the different parameters on the response of the plate, Equation 4.29 can be non-dimensionalized and transformed into the frequency domain, as expressed in Equation 4.30:

$$\left(\frac{\partial^4 u^*}{\partial {x^*}^4} + 2\ \frac{\partial^4 u^*}{\partial {x^*}^2 \partial {z^*}^2} + \frac{\partial^4 u^*}{\partial {z^*}^4}\right) - \frac{m^*}{k^*}\ St^2\ u^* = \frac{C_p}{k^*} \tag{4.30}$$

Here, $k^* = \frac{E}{6\rho_\infty V_\infty^2 (1-\nu^2)}\left(\frac{h}{L_{ref}}\right)^3 = 2254$ is the non-dimensional stiffness parameter, representing the relative importance of the elastic and pressure forces acting on the plate; $m^* = 8\pi^2 \frac{h}{L_{ref}} \frac{\rho_0}{\rho_\infty} = 16640$ is the non-dimensional mass, which represents the relationship between the solid and fluid inertia; $C_p = \frac{p}{\frac{1}{2}\rho_\infty V_\infty^2}$ is the pressure coefficient, and $\mathrm{St} = \frac{f\ L_{ref}}{V_\infty}$ is the Strouhal number. Both the displacements and the coordinates have been non-dimensionalized with the length of the obstacle leading to $u^* = \frac{u}{L_{ref}}$ and $(x^*, y^*, z^*) = \left(\frac{x}{L_{ref}}, \frac{y}{L_{ref}}, \frac{z}{L_{ref}}\right)$.

It should be pointed out that, when $\mathrm{St} = 0$, Equation (4.30) can be used to predict the stationary time-averaged deformation of the plate.

When the plate is not excited by a fluid flow (e.g. the fluid velocity is zero), Equation (4.30) reduces to an eigenvalue problem, as indicated in Equation 4.31.

As expected, in that case the response becomes completely independent from the flow velocity:

$$\left(\frac{\partial^4 u^*}{\partial {x^*}^4} + 2\,\frac{\partial^4 u^*}{\partial {x^*}^2 \partial {z^*}^2} + \frac{\partial^4 u^*}{\partial {z^*}^4}\right) - \frac{m^*}{k^*}\,St^2\,u^* = 0 \tag{4.31}$$

An inspection of Equation 4.30 allows to distinguish which level of FSI coupling may be expected depending on these non-dimensional numbers. It should be noted that the order of magnitude at which each kind of interaction appears depends also on the frequency content of the excitation. When the structure is excited at its resonance frequency, it will tend to experience higher deformations. The different coupling levels are characterized as follows:

- When $k^* >> 1$, equation 4.30 leads to a solution with very low displacements, which will not appreciably modify the fluid domain geometry and response.
- When $k^* << 1$ the pressure forces are several orders of magnitude higher than the elastic forces, so that the structure experiences deformations which are comparable to its main dimensions. Thus, the fluid domain geometry experiences changes and the interaction must be calculated in a fully coupled way.

A one-way structural excitation can be assumed for the current value of both the stiffness and mass parameters, as it will be shown later, even for frequencies near the resonance. Thus, Equation 4.30 is discretized and solved by the Finite Element Method, making use of the commercial code Virtual.Lab. The pressure field, obtained making use of the methodologies explained in the following sections, is mapped onto the structure mesh and used as a load boundary condition. The plate is discretized by using 50 elements in each direction.

Large Eddy Simulation

In order to obtain the unsteady pressure fluctuations over the wall downstream of the step, Large Eddy Simulations have been shown to provide very good agreement with experiments at low and moderate Reynolds numbers, as can be checked, for instance, in the works of Yang et al. [216] or Zhengtong et al. [217]. For Large Eddy Simulations, the Navier-Stokes equations are solved over

a filtered domain, as shown in Equation 4.32. Note how, due to the low Mach number of the flow, it is considered to be incompressible:

$$\begin{cases} \dfrac{\partial V_i}{\partial x_i} = 0 \\ \dfrac{\partial V_i}{\partial t} + V_j \dfrac{\partial V_i}{\partial x_j} = -\dfrac{1}{\rho}\dfrac{\partial p}{\partial x_i} + \dfrac{\partial}{\partial x_j}\left(\tau_{ij}\right) \end{cases} \tag{4.32}$$

Here, V_i and p_i are the resolved-scale velocity and pressure, respectively; τ_{ij} is the ij component of the subgrid-scale (SGS) Reynolds stress; ρ_0 is the fluid density, and μ is the dynamic viscosity of the fluid. In the computation performed here, an implicit filter was used, so that the grid size itself can be considered to be the filter width.

The subgrid stress tensor results from the interaction between the larger, resolved eddies and the smaller, unresolved eddies, and is modeled using the Boussineq approximation, as indicated by Equation 4.33:

$$\boldsymbol{\tau_t} = 2\mu_t \mathbf{S} - \frac{2}{3}\left(\mu_t \nabla \cdot \vec{V} + \rho k\right)\mathbf{I} \tag{4.33}$$

where $\mathbf{S}$ is the strain rate tensor and k is the subgrid kinetic energy. In this work, the subgrid scale turbulent viscosity, μ_t, was modeled using WALE (Wall Adapting Local Eddy Viscosity), which has been shown to be less dependent on the value of the model coefficient, C_w, than the classical Smagorinsky Subgrid Scale Model (see the works of Nicoud et al. [38] and Smagorinsky [35] for more information about this topic). The WALE model assumes a mixing-length type equation for the subgrid scale viscosity, as follows:

$$\mu_t = \rho \Delta^2 S_w \tag{4.34}$$

being $\Delta = C_w \, \mathcal{V}^{1/3}$ a length scale parameter dependent of the cell volume $\mathcal{V}$, and $\mathbf{S_w}$ is a deformation parameter, dependent of the strain rate tensor. Here, the model constant was set to $C_w = 0.544$, given that this value has been shown to provide acceptable results both for homogeneous isotropic decaying turbulence and for channel flows (see, for example, [218] or Malloupas et al. [219]).

The equations are discretized and solved by means of the commercial software *STAR-CCM+*. RANS and LES computations are performed over two different meshes, with approximately 4×10^6 and 20×10^6 volume cells. In order to ensure reproducibility of the results, Table 4.4 shows the mesh size

at different parts of the fluid domain. For the coarser mesh, the no-slip walls were meshed using a prism layer with total thickness of $0.012\ L_{ref}$ and 8 layers, in order to ensure that the wall y^+ lies within the viscous sublayer, as will be verified later. A time step of $\frac{\Delta t\ V_\infty}{L_{ref}} = 0.050$ for the first mesh and $\frac{\Delta t\ V_\infty}{L_{ref}} = 0.025$ for the second, ensure a Courant-Friedrichs-Lewy (CFL) lower than 1 for the most part of the domain, as can be illustrated by the distribution of CFL, shown in Figure 4.25. A general qualitative sketch of the computational fluid mesh can be seen in Figure 4.26.

Table 4.4: Orientative dimensions of the fluid flow meshes

Mesh Parameter	Mesh 01	Mesh 02
Farfield mesh size	$0.680\ L_{ref}$	$0.400\ L_{ref}$
Down walls mesh size	$0.050\ L_{ref}$	$0.030\ L_{ref}$
Step walls mesh size	$0.010\ L_{ref}$	$0.006\ L_{ref}$
Near field mesh size	$0.050\ L_{ref}$	$0.030\ L_{ref}$
Wake mesh size	$0.100\ L_{ref}$	$0.060\ L_{ref}$
Number of elements	4×10^6	20×10^6

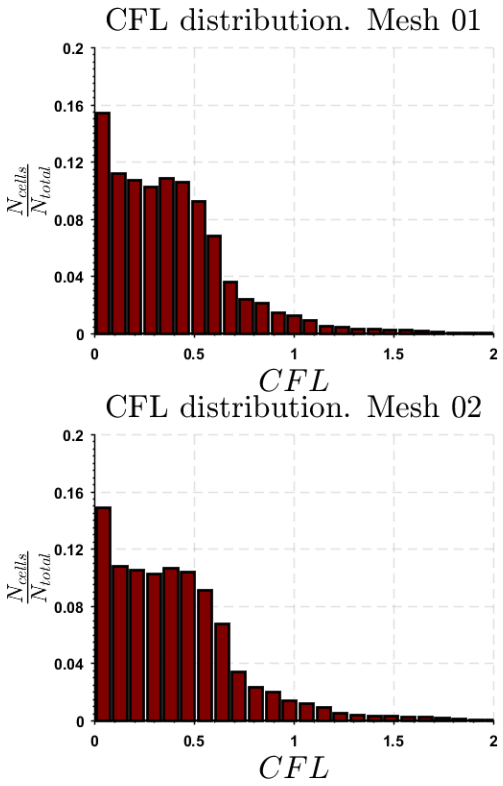

Figure 4.25: Ratio of CFL distribution over the entire fluid domain for the meshes of $N_{elements} \approx 4 \times 10^6$ (up) and $N_{elements} \approx 20 \times 10^6$ (bottom)

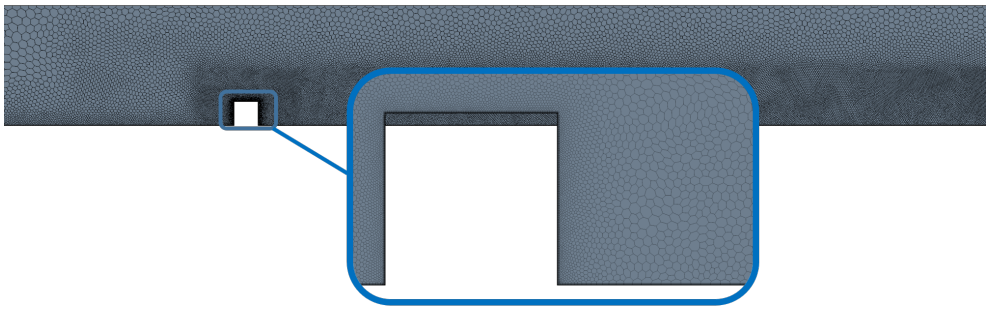

Figure 4.26: Sketch of the computational fluid mesh

With the mesh resolution used, it is not possible to properly model the turbulence of the inlet boundary condition and, consequently, laminar-constant velocity inflow will be considered, similarly as Schafer et al. [198]. The assumption of neglecting the free stream turbulence in the computation can be justified

as follows: as the vibration response at low-to-medium frequencies is dominated by the large turbulent structures downstream of the obstacle, this effect is expected to be of second order importance, as can be verified by the works of Bearman et al. [220] or Nakamura et al. [221]. For instance, at [220] it can be observed how, for free stream turbulence values below 6.1% the wall pressure distribution behind a hard-corners reward facing step and the reattachment length are only slightly affected by the variation of the turbulence intensity.

Reynolds Averaged Navier Stokes

The Reynolds Averaged Navier Stokes equations allows to obtain a mean flow solution, which can be used in order to compute parameters as the reatachment length or the plate static defformations. These equations can be derived from the complete set of mass, momentum and energy conservation equations, and are shown next for an incompressible flow [14].

$$\begin{cases} \dfrac{\partial \langle V_i \rangle}{\partial x_i} = 0 \\ \dfrac{\partial \langle V_i \rangle}{\partial t} + \langle V_j \rangle \dfrac{\partial \langle V_i \rangle}{\partial x_j} = \dfrac{\mu}{\rho} \dfrac{\partial^2 \langle V_i \rangle}{\partial x_j \partial x_i} - \dfrac{\partial \langle v_i \, v_j \rangle}{\partial x_j} - \dfrac{1}{\rho} \dfrac{\partial \langle p \rangle}{\partial x_i} \end{cases} \tag{4.35}$$

where $\langle V_i \rangle$ represents the component in the i^{th} direction of the mean velocity field, $\langle \vec{V} \rangle$ and $\langle p \rangle$ represents the ensemble average pressure field.

Closure of the equations (4.35) can only be achieved by modeling the terms $\langle u_i \, u_j \rangle$ which are commonly referred to as the Reynolds stresses. The selection of an appropriate turbulence model is of primal importance for the evaluation of the flow characteristics. The $k-\omega$ model with shear stress transport (SST) was used with this purpose. This turbulence model has been extensively used in the literature for this type of flows, and has been shown to provide good results for the pressure coefficient near the step [222]-[223], but over predicting the length of the reattachment zone in comparison with experiments or Direct Numerical Simulation [224].

The $k-\omega$ SST model was proposed by Menter [32] and is a transitional model in which the formulation considered varies from the $k-\omega$ turbulence model proposed by Wilcox [225] in the vicinity of the walls, to the $k-\varepsilon$ model away from the walls, thus solving the main inconveniences of both models. In addition to a transport equation for the turbulent kinetic energy, k, the $k-\varepsilon$ and the $k-\omega$ turbulent models solve a transport equation for the turbulent dissipation rate, ϵ, and the specific turbulent dissipation rate, ω, respectively. These variables

are related by $\omega \propto \varepsilon/k$ and allow obtaining the turbulent viscosity $\nu_t = C_\mu\, k^2/\varepsilon$ ($C_\mu = 0.09$ being a modeling constant). This turbulent viscosity is used to model the value of the Reynolds stress tensor as:

$$\langle v_i\, v_j \rangle = \frac{2}{3}\delta_{ij} - \nu_T \left(\frac{\partial \langle V_i \rangle}{\partial x_j} + \frac{\partial \langle V_j \rangle}{\partial x_i} \right) \tag{4.36}$$

Mapping of the fluid field pressure

As stated, the structural model of Equation 4.30 will be solved assuming one way coupling model. This means that the vibrational behavior of the plate is governed by the pressure field generated by the turbulent flow, as can be observed at the right term of Equation 4.30. However, due to the high value of the non dimensional stiffness parameter, $k^* = 2254$, it is supposed that the resulting displacements are small enough as they do not affect the behaviour of the fluid flow. Note that, at this stage, this is only a reasonable hypothesis which will only be confirmed by the comparison of the computational results with measurements.

In order to consider the influence of the pressure contribution onto the plate displacement, note that the finer-volume-mesh CFD solution has to be mapped onto the coearser FEM grid. In order to do so, while preserving the value of the nodal forces, a conservative distance mapping scheme is used, with a second order interpolation, in a similar way as explained by Ullrich et al. [226], [227] or Jones [228].

Figure 4.27 shows an example on how the mapping process works. Figure 4.27 (up) represents the pressure coefficient of the computed LES fluid flow at an arbitrary time step while Figure 4.27 (bottom) shows the resulting mapped pressure field which will be used for the computation of the displacements in accordance with Equation 4.30. Note how the results are essentially equal, even though the smallest resolved scales are filtered on the mapped mesh. However, as the small structures are the less energy containing ones [14] and, in accordance with Taylor's hypotheses they will be related with the energy contained at high frequencies [229] the mapped pressure can be considered to be accurate enough for low-medium frequencies.

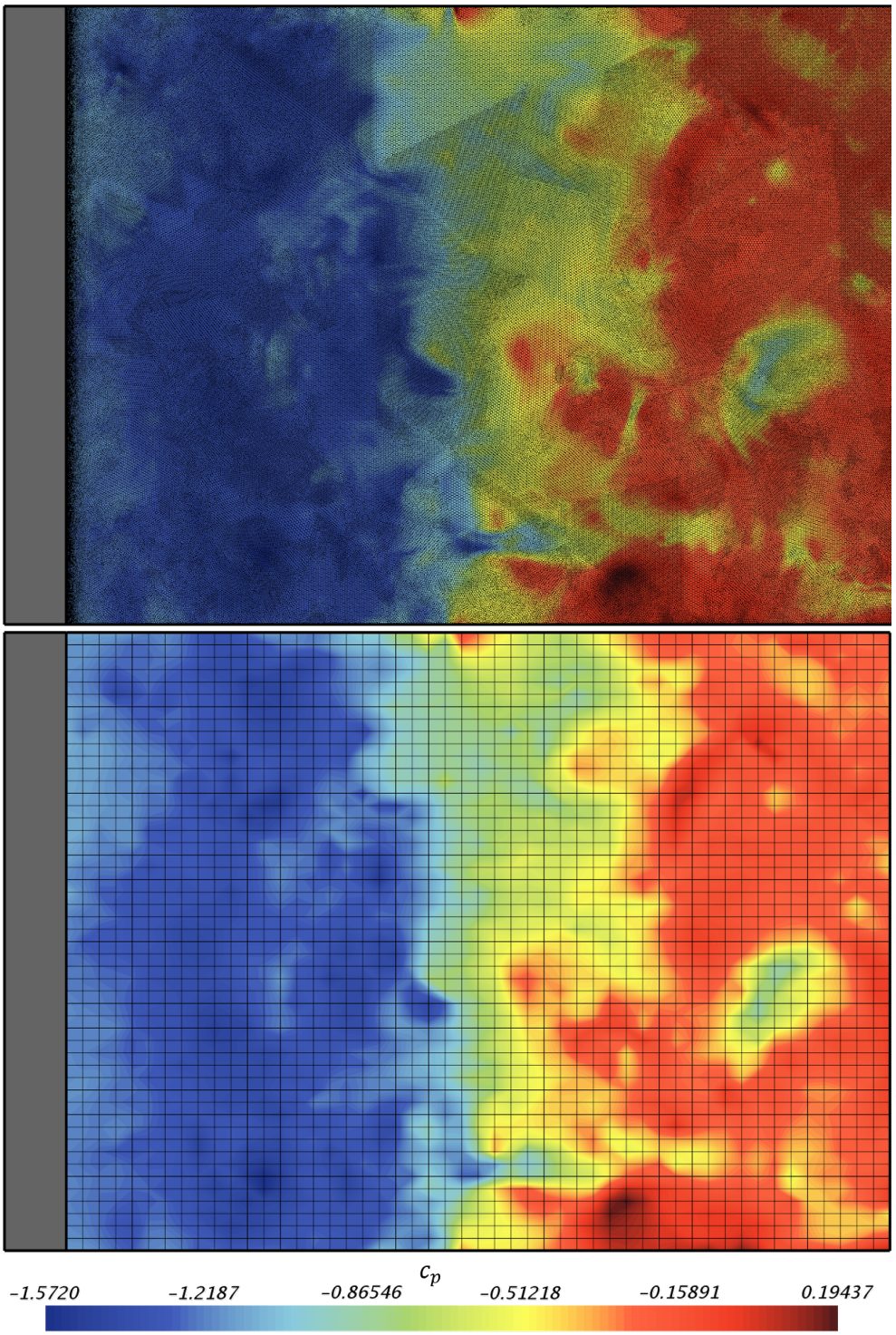

Figure 4.27: Pressure coefficient distribution at the back plate for: fluid finite volume mesh (up) and structural finite element mesh (bottom) at an arbitrary time step of the Large Eddy Simulation solution

4.3.3 Experimental methodology

In order to validate the numerical model, several experimental analyses have been performed in the KU Leuven silent wind tunnel. The tunnel is generally used for identification of aeroacoustic sources and acoustic propagation mechanism in flow confined environment for the subsonic flow region. A detailed description can be found in De Roeck et al. [230].

A roots blower is used to generate a time-uniform flow field. In order to guarantee identical inlet conditions for different measurement campaigns, a frequency regulator with PID controller, coupled with downstream pressure and flow rate sensors, is attached to the roots blower. After the roots blower, a heat exchanger is installed. The presence of the aftercooler is made necessary by the significant increase of the temperature generated by the roots blower. The high temperature generates an increase in the speed of sound which alters the acoustic propagation phenomena. Using the heat exchanger, the temperature increase is reduced with temperature fluctuations of less than 5 % between different measurements.

A similar configuration as the one described in section 4.3.1 is used. The tunnel has a rectangular cross section of $10L_{ref}$ width and $5L_{ref}$ height. A steel plate is flush mounted right behind a step with a square cross section of $5L_{ref}$. The step extends over the width of the tunnel cross section. The plate is 20cm long and 15cm wide with a thickness of 0.5mm. In order to obtain a flush mounted configuration, an external frame is used. The edges of the plate parallel to the flow direction are clamped between the frame and the duct side walls. The two sides perpendicular to the flow direction are simply fixed to the frame using double-sided tape to obtain an approximately simply supported configuration. The averaged air velocity at the inlet is maintained at $V_\infty = 22\mathrm{m\,s^{-}}1$, with free stream turbulence intensity lower than 2%. The temperature of the air is controlled in order to set a Reynolds number of approximately $Re = 22710$. At first, in order to validate the plate boundary condition and to identify the modal behavior of the plate, a modal analysis on the plate for no flow condition has been performed using hammer test, as explained in Ren et al. [231].

The vibration of the plate under operating condition is measured with a Polytec scanning vibrometer with a configuration similar to which used by Roozen et al. [232]. The acquisition is performed on 165 measurement points regularly spaced over the plate and for each of them 100 averages are performed. Finally using the Solo PIV laser (for more information, refer to the work of Butscher et al. [233]) and a high speed camera the flow characteristics are measured along the tunnel middle plane, normal to the z component, at different stations along the flow propagation direction, which will allow to accurately

measure the location of the end of the recirculation bubble, by the inspection of the velocity field, as will be shown later.

4.3.4 Results and discussion

Analysis of the fluid flow

One of the main objectives of the current work is to provide a good understanding of the mechanisms governing the flow-induced vibration, and to validate methodologies currently in use. With these purposes, in this section the main characteristics of the flow field are analyzed in detail by comparing LES and RANS results with the experimental measurements.

In order to ensure that the data are independent on the grid resolution it is recommendable to make a comparison to check that they are almost constant between each study. Thus, both time averaged and frequency content will be analyzed. First of all, the predicted forces exerted over the step were computed and analyzed. These forces are nondimensionlized in accordance with Equation 4.37, where F_y and F_x are the forces perpendicular and parallel to the main flow, respectively. Their time averaged value, $(< C_D >, < C_L >)$ and standard deviation, $\left((< C_D'^2 >)^{1/2}, (< C_L'^2 >)^{1/2}\right)$ are shown in Table 4.5 for the different turbulence modeling (when possible) and grid resolution.

$$C_L = \frac{F_y}{1/2\rho_\infty V_\infty^2 L_{ref} b} \quad C_D = \frac{F_x}{1/2\rho_\infty V_\infty^2 L_{ref} b} \tag{4.37}$$

Table 4.5: Comparison of the force coefficients between RANS and LES computations for the different mesh resolutions

	$< C_D >$	$(< C_D'^2 >)^{1/2}$	$< C_L >$	$(< C_L'^2 >)^{1/2}$
LES. Mesh 01	2.173	0.023	1.344	0.033
RANS. Mesh 01	2.062	–	1.214	–
LES. Mesh 02	2.170	0.028	1.435	0.037
RANS. Mesh 02	2.103	–	1.238	–

Note how, for the prediction of the time averaged force coefficients, the RANS computations can provide with results with a difference of a 5 % and 14% for the prediction of the average horizontal and vertical force coefficients, respectively. Moreover, the LES computation predicts small variations of these coefficients around the average value, letting deduce that RANS can provide acceptable results for those coefficients both quantitatively and qualitatively. Both the mesh of $N_{element} \approx 4 \times 10^6$ and $N_{element} \approx 20 \times 10^6$ provide similar results for the same turbulence modeling. Note how the temporal standard

deviation of the variables for the finer mesh tends to higher values, suggesting a higher energy content at medium-high frequencies.

This can be confirmed by Figure 4.28, that shows the time domain response (up) and the frequency content (bottom) of these forces. This last curve was calculated applying the fast Fourier transform to the temporal history of the variables. The sampling length was taken in a way that the terms of the Fourier series were not substantially changed when adding new samples. It can be observed that no dominant frequencies exist, and that the spectral content quickly decays for St > 0.35 . Additionally, note how the frequency content obtained by the finer mesh is higher, especially at the range of medium high frequencies.

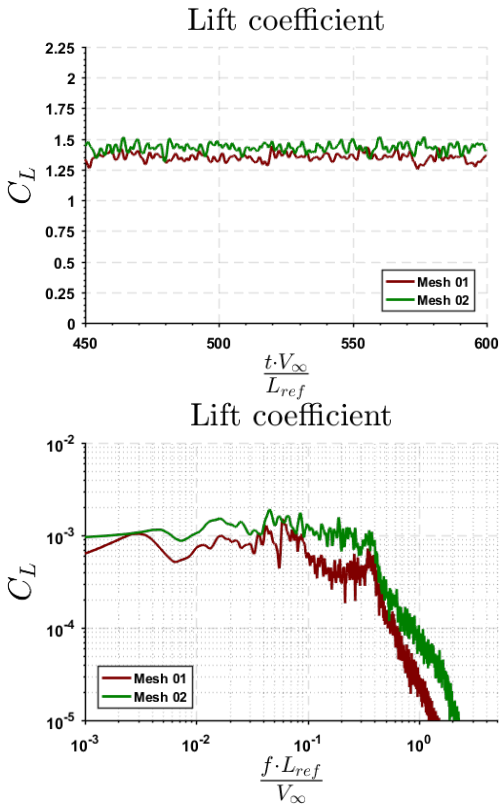

Figure 4.28: Force time history (up) and frequency content (bottom). Computation for the mesh with $N_{elements} \approx 20 \times 10^6$

Another result which is considered to be important in order to evaluate the predictive capabilities of RANS and LES for the different meshes is the

reattachment length. The reattachment length is measured using PIV, which allows to obtain the vectors of the velocity field at a zone near to the location where the reattachment is expected to lie in, as shown in Figure 4.29 where an example of the time-averaged field is sketched. The location of the reattachment length was defined as the place at which the velocity vectors near the down wall tend to be parallel to the ground (with an angle of less than 0.5 deg), with the same direction as the incoming fluid flow. This zone is represented by the vertical line of the Figure 4.29 and it was found to be at $\left(x_{reattach}/L_{ref}\right)_{exp} \approx 10 \pm 0.7$, measured from the end of the step.

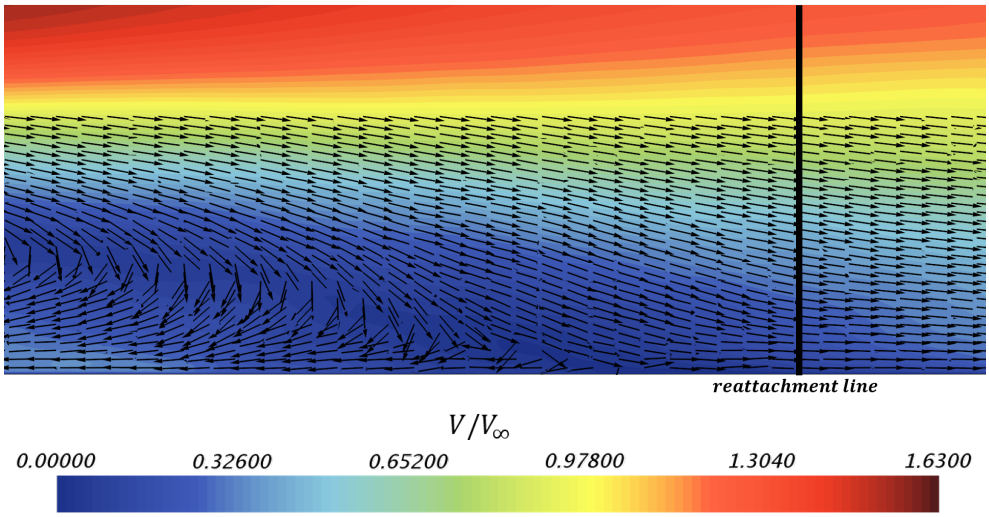

Figure 4.29: Vectors of time averaged velocity for the identification of the experimetnal reattachment length

Figure 4.30 shows the contours of the non-dimensionalized time-averaged velocity obtained with the LES and the RANS methodologies. In both cases, a small recirculation bubble is found in front of the step, followed by a larger bubble downstream of the obstacle. Right after this, the flow reattaches again to the wall at the point highlighted in the figure. Note how, in accordance with the Figure, the length of the reattachment zone predicted by RANS is noticeably higher than the same LES prediction.

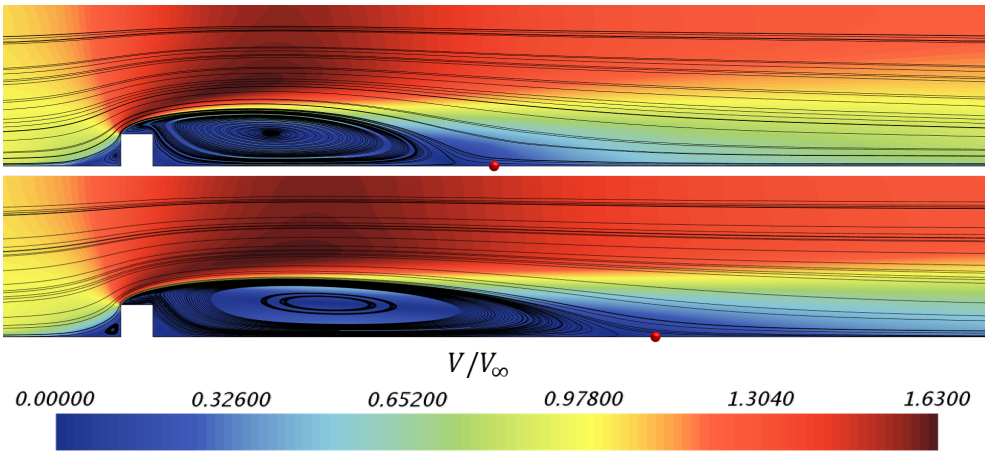

Figure 4.30: Time averaged velocity using LES (top) and RANS (bottom) for the mesh with $N_{elements} \approx 20 \times 10^6$

From the computational calculations, the reattachment location can be identified as the point where the time averaged wall shear stress is in the same direction as the main flow. This criteria is similar to the one stated for the PIV measurements when the velocity is measured close enough to the wall. This fact can be easily observed in Figure 4.31, where the non dimensional x component of the wall shear stress $\left(\frac{\tau_x}{\frac{1}{2}\rho_\infty V_\infty^2}\right)$ is shown for RANS and LES computations. While the LES results are shown for both the finer and coarser meshes, the RANS is only shown for the fine one in order to ease the interpretation of the Figure. Notice that, downstream of the step, both RANS and LES calculations predict the same value for the wall shear stress for non-dimensional distances below $x/L_{ref} \approx 5$. Nevertheless, the LES scheme predicts that the wall shear stress reaches zero at a shorter distance, thus leading to a smaller recirculation bubble. The value of the location of the reattachment length is shown at Table 4.6 for the different grids for LES and RANS. Note how the coarser and finer LES resolutions allows to obtain a similar value for this parameter.

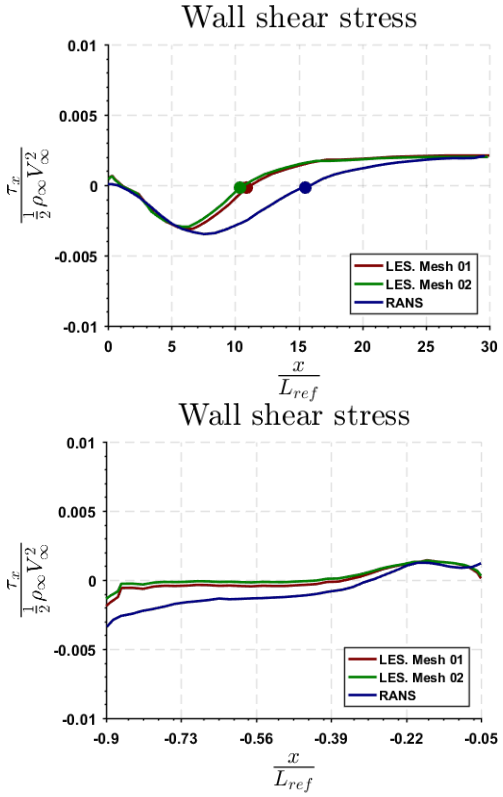

Figure 4.31: Average non dimensional wall shear stress after the step (up) and over the step (bottom) $N_{elements} \approx 20 \times 10^6$ and identification of the reatahcment location

Table 4.6: Value of the reatachment mesh for each of the studied computational calculations. Comparison with the experimental value

Methodology	$(x_{reattach}/L_{ref})$
LES. Mesh 01	10.9
RANS. Mesh 01	16.8
LES. Mesh 02	10.7
RANS. Mesh 02	15.7
exp.	10.0

It can be stated then that the agreement between LES and the experiments

is good for this parameter, for both meshes, whereas the RANS computation fails in predicting the reattachment length. A reasonable explanation of why RANS methodology overpredicts the extension of the recirculation zone can be given as follows: as it can be observed in Figure 4.32, in order to calculate the high values of turbulent kinetic energy existing in the last part of the shear layer, a zone with a very high turbulent viscosity ratio (up to $\mu_t/\mu > 900$) is needed. Such high value of the turbulent viscosity leads to an effective Reynolds number much lower than the real one. It is well known that, for the case of a medium-high Reynolds backstep the reattachment length tends to increase when decreasing the Reynolds number, as it can be found, for instance, in the works of Armaly et al. [234] or Kostas et al. [235]. Similar results were found by Tropea et al. [236] or Durst et al. [237] for the case of a wall-mounted 2D obstacle, explaining why the RANS solution tends to overpredict this parameter.

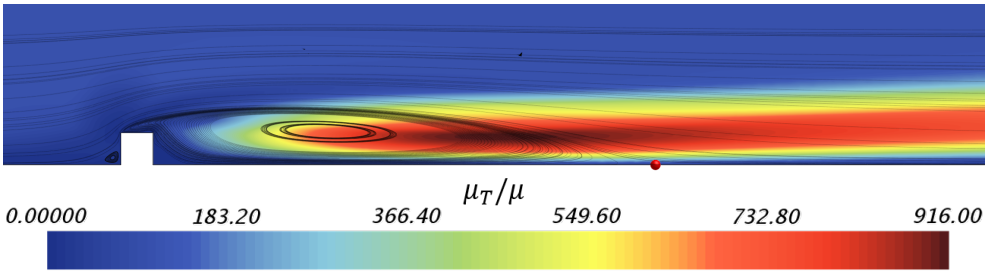

Figure 4.32: Turbulent viscosity ratio for the RANS computation with the mesh of $N_{elements} \approx 20 \times 10^6$

In order to check the resolution of a LES scheme, Celik et al. [238] proposed an index of quality that has been successfully tested on the works of Lucius et al. [239], Konnigk et al. [240] or Dastbelaraki et al. [241]. Another useful indicator derived from these works, which can be used for almost any complex flow, relates the ratio of the turbulent kinetic energy of the calculated non-filtered structures (k_c) and the kinetic energy introduced by the subgrid-scale (k_{SGS}), as defined in Equation 4.38 ([38],[14]):

$$\eta = \frac{k_c}{k_{TOTAL}} = \frac{k_c}{k_c + k_{SGS}} \tag{4.38}$$

When $\eta > 0.7-0.8$ the energy content of the turbulent structures is correctly resolved ($\eta = 1$ means DNS resolution). Both the resolved and the modeled turbulent kinetic energy can be calculated as defined in Equations 4.39 and

4.40:

$$k_c = \frac{1}{2}\left(< v_x'^2 > + < v_y'^2 > + < v_z'^2 >\right) \tag{4.39}$$

$$k_{SGS} = C_t \frac{\mu_t}{\rho} \boldsymbol{S} \tag{4.40}$$

Here, $v_i' = v_i - < v_i >$ represents the deviation of the resolved i^{th} component of the velocity with respect to its time averaged value; $C_t = 3.5$ is a constant of the subgrid model; μ_t represents the turbulent viscosity and $\boldsymbol{S}$ is the strain tensor computed with the resolved velocity field.

The level of resolution of the LES computation will be analyzed for the case of the coarser computational grid, with $N_{elements} \approx 4 \cdot 10^6$, as the finer one will provide a higher level of resolution. In Figure 4.33 the resolved (top), the modeled (middle) and the total (bottom) turbulent kinetic energy are shown at the mid plane. It should be noticed that the computed and total kinetic energy are quite similar over the whole domain. The most important source of modeled subgrid kinetic energy can be found at the shear layer just over the step, where a significant flow velocity gradient exists.

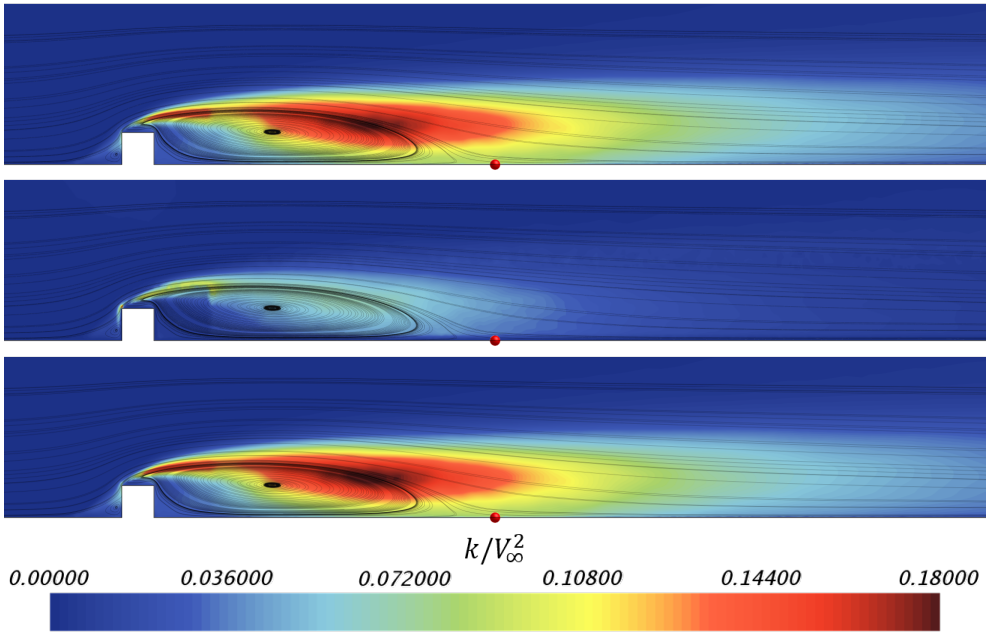

Figure 4.33: Resolved (top), subgrid scale (middle) and total turbulent kinetic energy at the midplane. Computation for the mesh with $N_{elements} \approx 4 \times 10^6$

In order to check the level of resolution of the current simulation, Figure 4.34 shows the ratio of resolved to total turbulent kinetic energy. Observe that, downstream of the step, it is possible to find a value of $\eta \geq 0.7$ for the whole domain. Upstream, where the mesh is coarser, a very low resolution zone is found. Nevertheless, as, in agreement with Figure 4.33, the turbulence kinetic energy is quite low, and the flow just downstream of the step is highly dominated by the detached flow, the resolution was considered sufficient for the present study. Moreover, it should be noted that refining the upstream zone would lead to a significant increase in the computational cost with small added value. Figure 4.35 shows the percentile distribution of the ratio of turbulent kinetic energy (up) and wall y^+ for the whole domain. Notice that $y^+ \leq 1$ for 98% of near-wall cells and $\eta \geq 0.80$ for 92% of the cells.

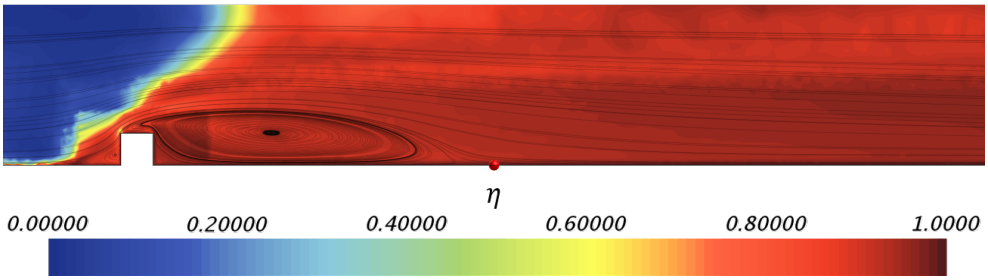

Figure 4.34: Ratio of resolved over total turbulent kinetic energy at the midplane. Computation for the mesh with $N_{elements} \approx 4 \times 10^6$

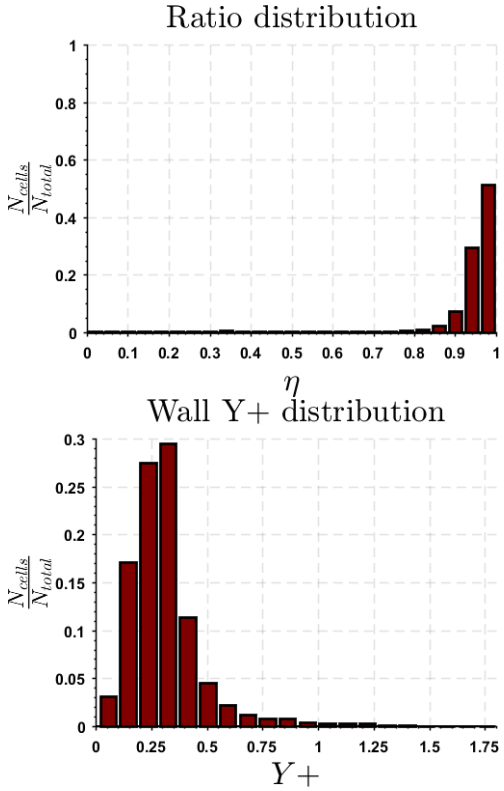

Figure 4.35: Distribution of the ratio of resolved over total turbulent kinetic energy and wall y^+. Computation for the mesh with $N_{elements} \approx 4 \times 10^6$

The unsteady velocity field was constantly recorded in some points of interest. As an example, Figure 4.36 shows the analysis of the deviation of the velocity components from their mean value at a point located over the shear layer, at a point P_1, located at the centerline, and defined by $x/L_{ref} = 20/3$ and $y/L_{ref} = 4/3$, for the mesh with $N_{elements} \approx 20 \times 10^6$. The left plot shows the time history of the velocity while the right one shows its frequency content. Again the absence of any kind of dominant frequency can be observed.

This is corroborated by the instantaneous velocity field shown in Figure 4.37 for an arbitrary time step at the mean plane and at the wake. In this Figure, it can be observed how the largest turbulent structures in the field are approximately of the same size as the obstacle. Also it should be noted how it is not possible to identify any kind of coherent vortex shedding, which is in agreement with the non-existence of dominant frequencies.

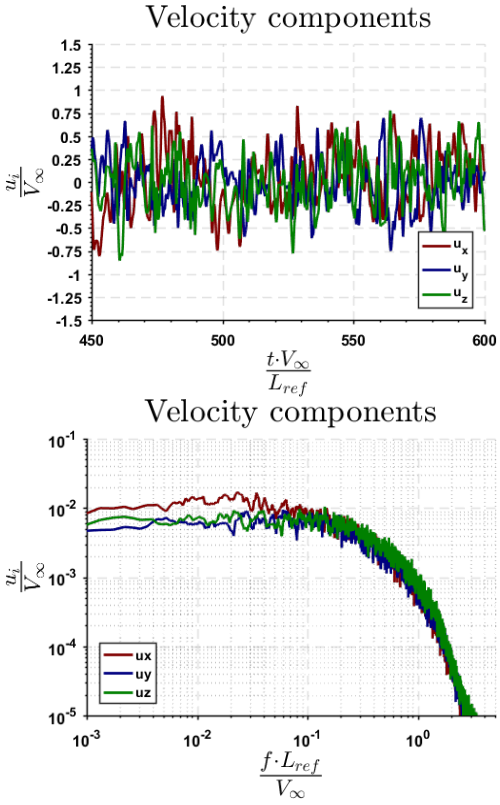

Figure 4.36: Velocity time history (up) and frequency content (bottom) at a point $P1$, located near to the main shear layer. Computations for the mesh with $N_{elements} \approx 20 \times 10^6$

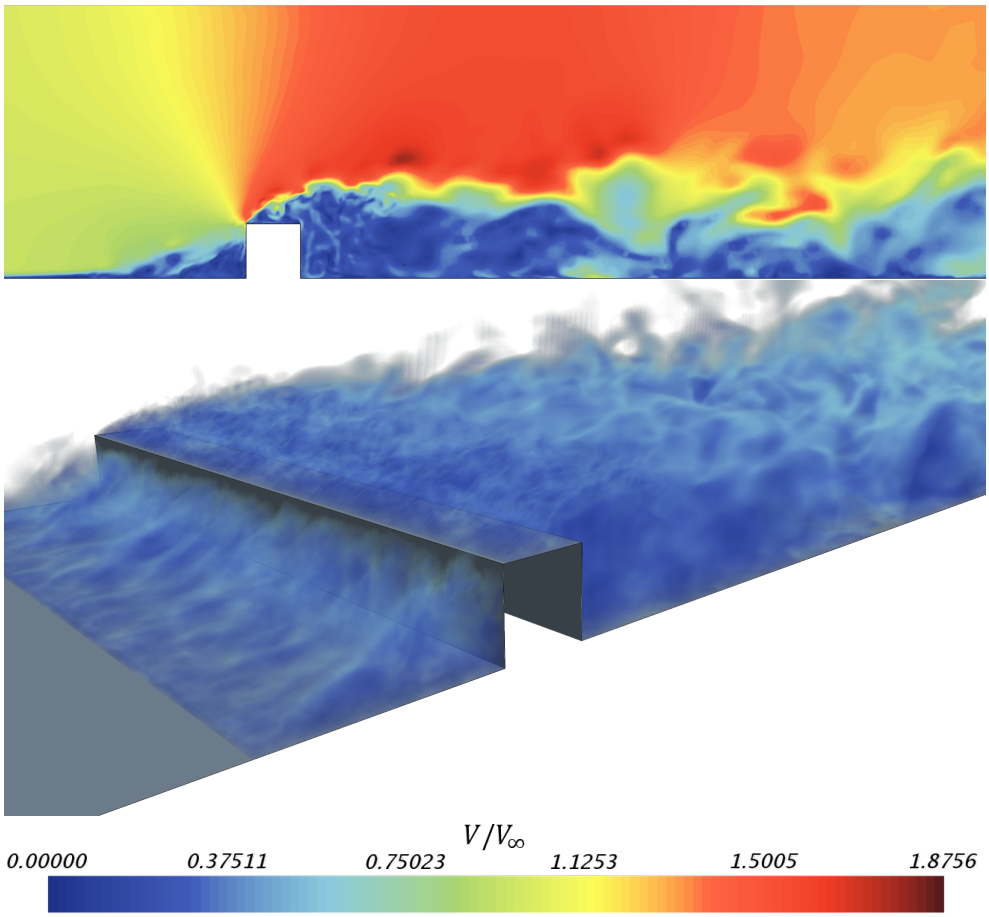

Figure 4.37: Visualization of turbulent strucures at an arbitrary instant for the computation with $N_{elements} \approx 20 \times 10^6$. Contour of instantaneous velocity field at the midplane (top) and volumetric render of the low velocity at the wake (bottom)

The spectrum of the kinetic energy content at point P1 is shown in Figure 4.38 (up) for the two different meshes, it should be noted how the refined mesh allows one to obtain a meaningful higher level of energy. The direct effect of this will be later explained when examining the prediction of the flexible plate vibration. Note how the inertial subrange can be identified by the -5/3 slope, ranging from $St = 0.35$ up to $St = 1.681$. For the large scale energy-containing subrange, the energy spectrum is quite flat, which agrees with the absence of any kind of dominant frequency. A similar tend can be observed in Figure 4.38 (bottom), where the frequency content of the pressure coefficient at a the point G5, located at the plate, is shown. Note, how, in a similar way as for the energy

spectra, higher values of the frequency content are observed for the finer mesh.

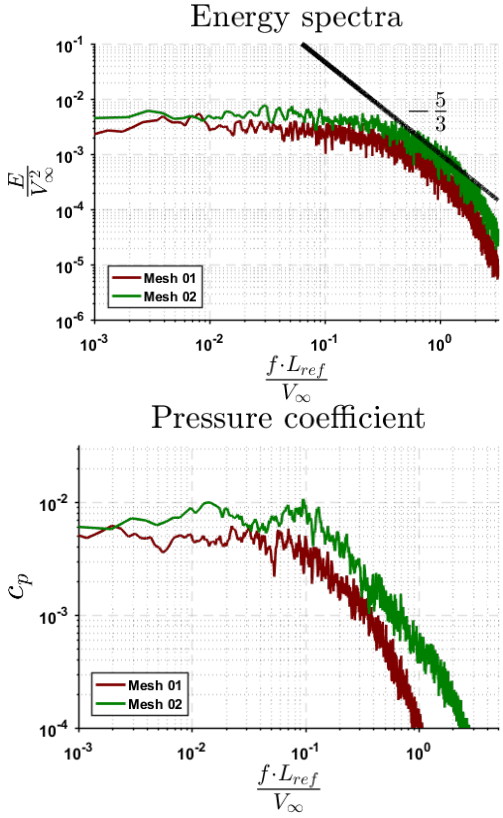

Figure 4.38: Energy spectra at the point located near to the shear layer, $P1$ (up) and frequency content of the pressure coefficient at a point located over the plate, at point $G5$. Comparison between different meshes

Structural model validation

As it could be expected, the prediction of the flow-induced vibration is strongly influenced by the quality of the structural model. Moreover, when the plate is excited by a turbulent unsteady pressure, with a significant spectral content in a wide frequency range, a correct estimation of the natural frequencies of the system becomes vital.

Although it could be argued that, due both to the pre-load state and the added mass effect, the structural eigenfrequencies will not be the same as those corresponding to the structure response under the action of a moving fluid, in fact significant differences should not be expected, due to the low values of the mean pressure, fluid density and Mach number. Therefore the isolated structure

model is a good approximation, as verified by the study of Frampton [242].

In Table 4.7 the numerical values of the first 10 eigenfrequencies are shown. Notice that, although they correspond to the vibration of the plate *in vacuo*, they have been non-dimensionalized by using the fluid flow inlet velocity ($f^* = f \cdot L_{ref}/V_\infty$). The parameters for non-dimensionalization were chosen in order to maintain the coherence on the presentation of the results of the current work. From Table 4.7 it can be seen how, despite the simple set of boundary conditions which was supposed for the current study, the agreement between prediction and measurement is good.

Table 4.7: Structural eigenfrequencies of the flat plate

	f_1^*	f_2^*	f_3^*	f_4^*	f_5^*	f_6^*	f_7^*	f_8^*
Num	0.104	0.143	0.237	0.243	0.292	0.376	0.382	0.461
Exp	0.112	0.140	0.227	0.249	0.295	0.359	0.389	0.425
ε	0.036	0.024	0.043	-0.025	-0.009	0.071	0.020	0.078

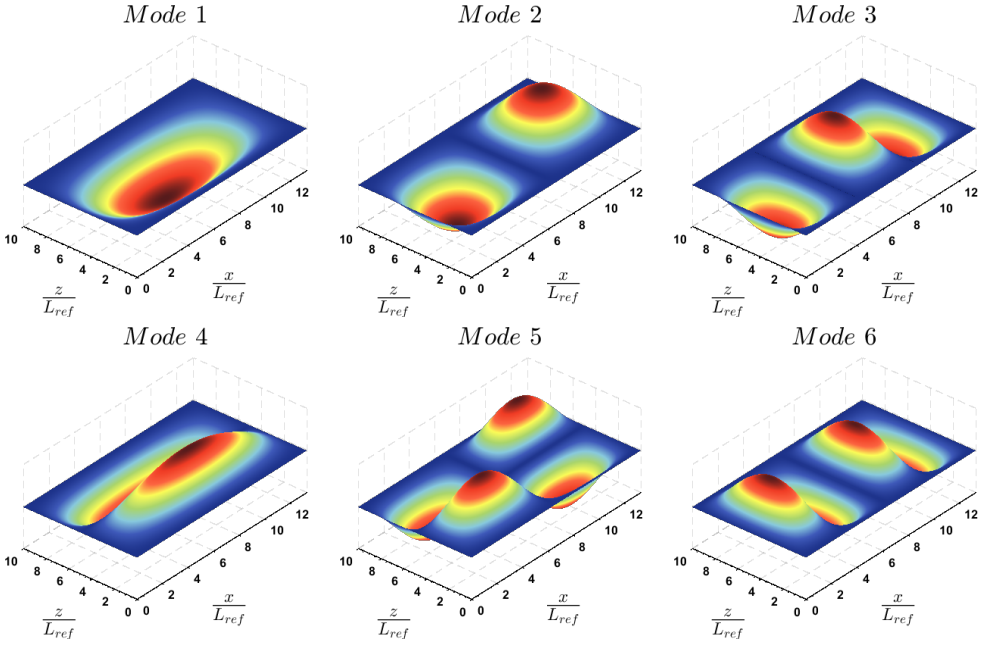

Figure 4.39: Calculated modal displacements

To validate the prediction of the modal shapes, the numerical (ϕ_i^{num}) and experimental (ϕ_i^{exp}) eigenvectors are compared by means of the Modal Assur-

ance Criteria (MAC) [243] which allows to define a MAC matrix, as stated by Equation 4.41:

$$MAC_{ij} = \left(\frac{\phi_i^{num^T} \cdot \phi_j^{exp}}{||\phi_i^{num}|| \, ||\phi_i^{exp}||} \right)^2 \tag{4.41}$$

where, $MAC_{ii} = 1$ means perfect agreement between the numerical and experimental mode shape and $MAC_{ij} = 0$ means perfect orthogonality between the numerical i^{th} and the experimental j^{th} eigenfunctions. Figure 4.40 shows a visual representation of this matrix, where a good agreement between the experimental and numerical data can be observed. MAC coefficients are always above 0.70 at the diagonal and below 0.20 for the terms out of the diagonal. However, it can be noted how modes 4^{th} and 3^{rd} are slightly superimposed. This difference can be attributed to the closeness of the frequencies of these modes (there exist a difference of less than a 3% both in measurements and computations).

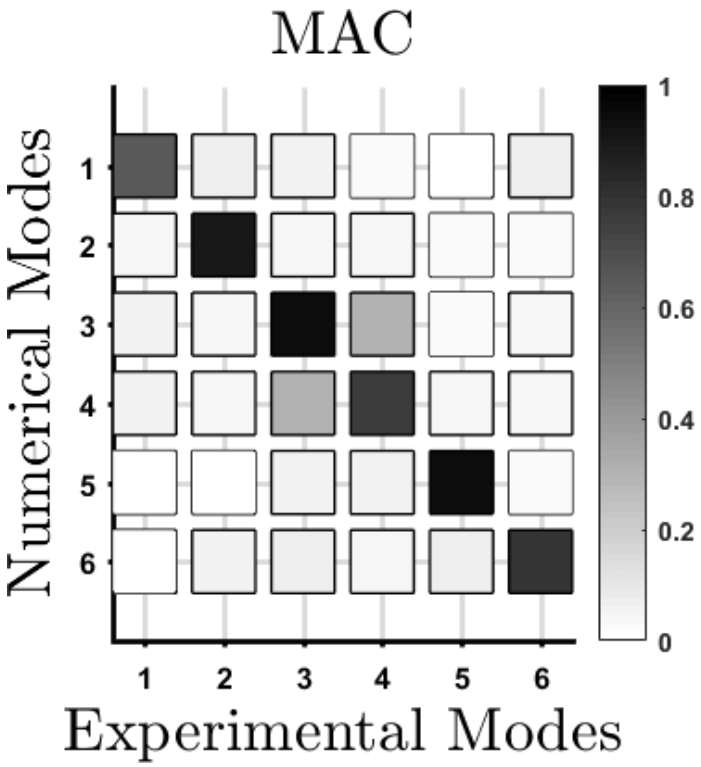

Figure 4.40: Modal Assurance Criterion matrix

Flow induced vibrations

The detached flow downstream of the step generates a turbulent fluctuating pressure, which excites the back plate. As a consequence, this structure experiences a time averaged mean displacement due to the action of the time average pressure and a fluctuating displacement due to pressure fluctuations. Therefore, the correct estimation of the pressure acting over the plate becomes of crucial importance for the correct estimation of the displacement. Figure 4.41 (up) shows the evolution of the time-averaged pressure coefficient downstream, comparing the RANS and LES results, computed at the mean line which was shown at Figure 4.24. Figure 4.41 (bottom) shows the mean displacement appearing in response to such mean pressure.

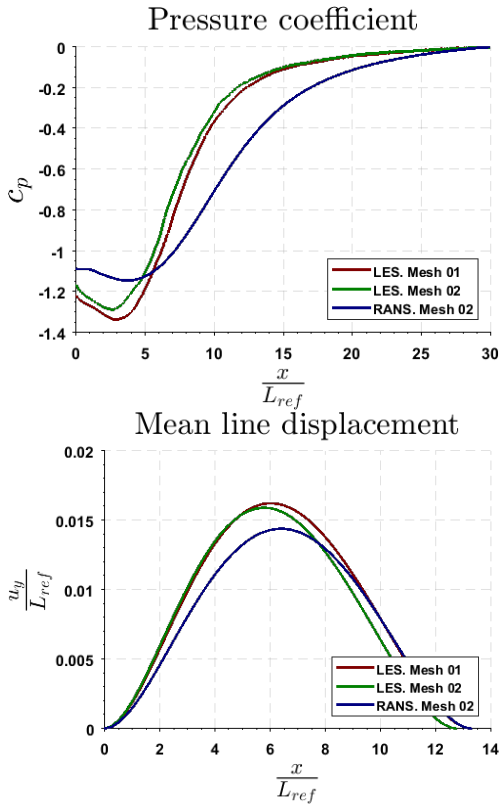

Figure 4.41: Time averaged pressure coefficient (up) and mean line plate displacement (bottom) after the step. Comparison between LES and RANS computations using different meshes

As it can be observed, the LES calculation predicts a lower value of the pressure in the recirculation bubble. Also, the extension of the low pressure zone

is less pronounced and the minimum value is located a 30% closer to the obstacle position. These results are highly in agreement with the best capacity of the LES computation to accurately predict the extension of the recirculation zone, as could be deduced from literature comparing the works of Yang et al. [216] or Werner et al. [244], where the flow over a similar configuration is analyzed using LES and the works of Schmidt et al. [245] or Ariff et al. [246], who used RANS in order to characterize the flow. Note how, As the location of the lowest value of the pressure is not in the center of the plate, the deformation which it experiences is not symmetric.

Table 4.8 shows a comparison of the main values extracted from Figure 4.41 which are: (i) the location of the point of minimum pressure coefficient, $\left(\frac{x}{L_{ref}}\right)_{c_{p_{min}}}$; (ii) the value of the minimum pressure coefficient, $c_{p_{min}}$; (iii) the location of the maximum plate displacement $\left(\frac{x}{L_{ref}}\right)_{u_{ymax}}$ and (iv) the value of the maximum plate displacement $\frac{u_{ymax}}{L_{ref}}$. Note how, despite the location of the minimum pressure coefficient point is highly overpredicted by the RANS calculation by a 30% in comparison with LES this translates at a difference of only 11% on the prediction of the location of the point of maximum amplitude.

Table 4.8: Time averaged displacement predictions using different turbulence modelling and computational grids

	$\left(\frac{x}{L_{ref}}\right)_{c_{p_{min}}}$	$c_{p_{min}}$	$\left(\frac{x}{L_{ref}}\right)_{u_{ymax}}$	$\frac{u_{ymax}}{L_{ref}}$
LES. Mesh 01	2.91	-1.34	5.99	0.0162
RANS. Mesh 01	4.07	-1.47	6.67	0.0149
LES. Mesh 02	2.75	-1.30	5.75	0.0159
RANS. Mesh 02	3.99	-1.44	6.53	0.0144

Figure 4.42 shows the spatial distribution of the time-averaged non-dimensional displacement of the plate for the LES (top) and RANS (bottom) models. The point of maximum time-averaged displacement is highlighted in both figures. It can be observed that, as expected, the displacement field is symmetric with respect to z axis and the maximum displacement point is displaced towards the step. This fact is more clearly noticeable for the LES calculation.

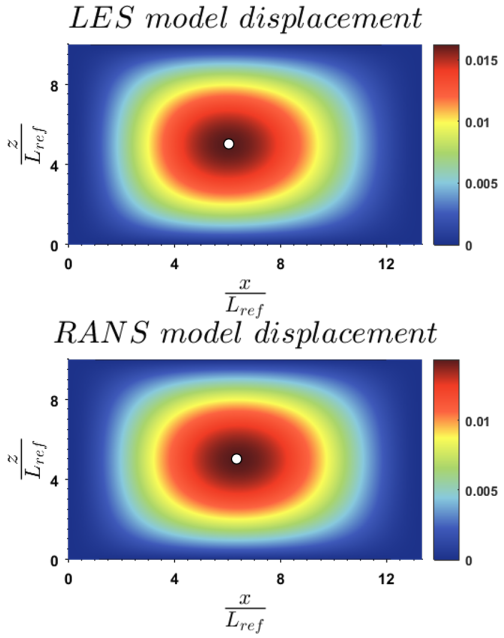

Figure 4.42: Time averaged displacement field with LES (top) and RANS (bottom) computations. Computation with the mesh of $N_{elements} \approx 20 \times 10^6$

The transient flow field which features have been analyzed so far, induces a fluctuating pressure field over the plate located at the rear part of the step. This fluctuating pressure excites the plate, which acquires a vibrational motion superimposed onto the mean displacement analyzed in Figure 4.41.

Figure 4.43 shows the behavior of the fluctuating pressure at four points on the plate: point G1, located at $x/L_{ref} = 1$; G3 at $x/L_{ref} = 3$; G5 at $x/L_{ref} = 5$ and G8 at $x/L_{ref} = 8$. All the points were located at the middle plane ($z/L_{ref} = 5$). The frequency content at low frequencies is in agreement with the averaged pressures shown in Figure 4.41, tending to lower values (closer to atmospheric pressure) as the point is located farther from the obstacle. Also, from $St > 0.15$ the frequency content of the pressure for all the shown points tends to rapidly decay.

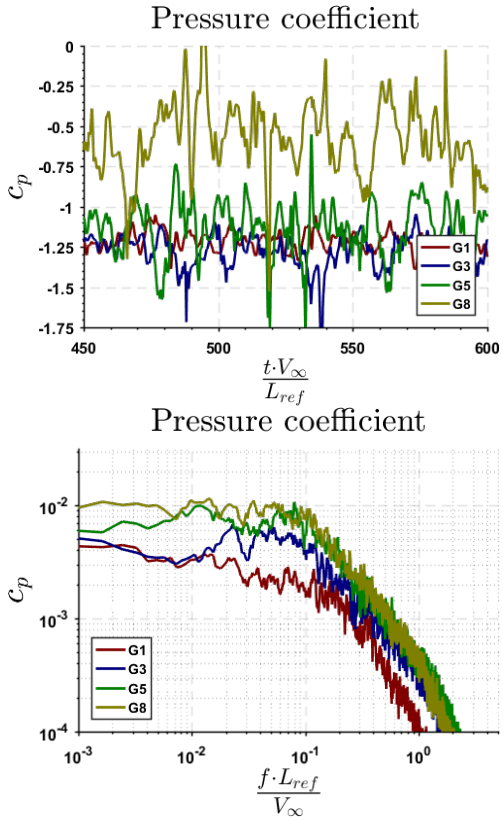

Figure 4.43: Time history (up) and frequency content (bottom) of the unsteady pressure coefficient at points located over the plate for the mesh of $N_{elements} \approx 20 \times 10^6$

The fluctuating pressure history was used as an excitation for the flat plate, whose deformations were computed and compared with experimental measurements. Figure 4.44 shows the displacement field for six different frequencies close to the eigenfrequencies of the structural system. A visual comparison with Figure 4.39 suggest all the modes participate in the deformation of the plate at the evaluated frequency range. The modal participation of the first modes was quantitatively calculated for these frequencies in a similar way as proposed by Chopra [247]: the response of the structure to a vibratory loading can be expressed in accordance with Equation 4.42, assuming a system with N participating modal forms:

$$u(x,z,f) = \sum_{i=1}^{N} \eta_i(f)\phi_i(x,z) \tag{4.42}$$

where ϕ_i denotes the i^{th} eigenfunction, which was previously calculated and shown at Figure 4.39 and η_i represents contribution of the i^{th} mode to the response of the plate at frequency f. Figure 4.45 shows these values in order to specify the contribution of the first seven modes to the total response. For an easier interpretation, they have been scaled so that a value of 1 correspond to the maximum modal contribution of the first mode for the first frequency.

Note how the frequencies of the 3rd and 4th modes are very close (less than 3% of separation). Also, it can be easily observed that, at the frequency of the fourth mode (St ≈ 0.243), the contributions of the 3rd and the 4th modes are comparable, thus supporting the explanation given of why the 4th mode cannot be clearly observed in the frequency response of the averaged surface displacement, as will be stated later.

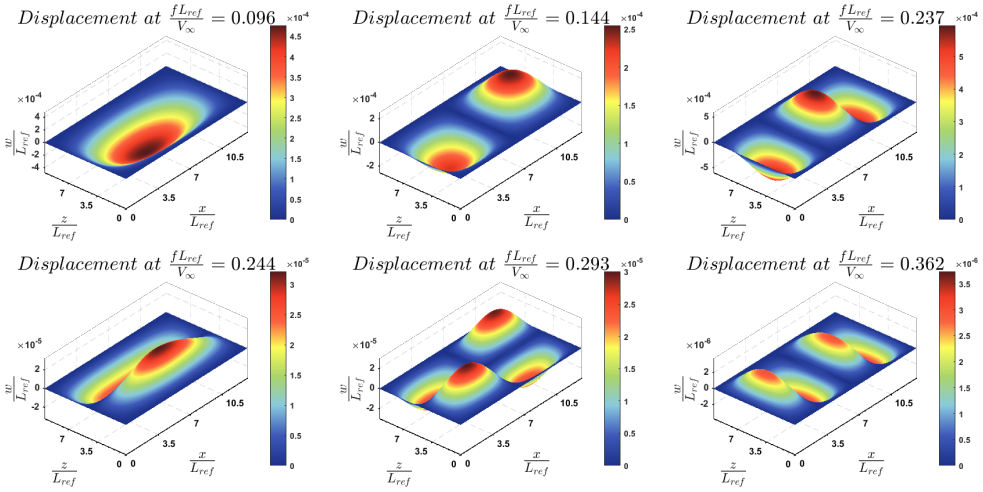

Figure 4.44: Frequency response of the plate displacement under the action of the turbulent pressure field at different frequencies

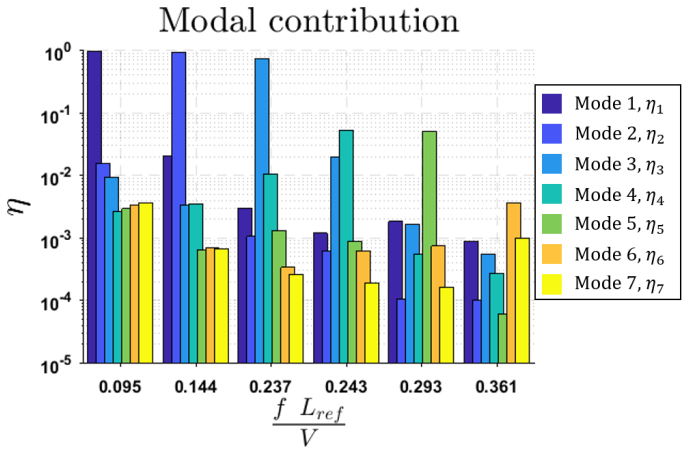

Figure 4.45: Modal contribution of each eigenvector to the total displacement of the plate under the action of the turbulent pressure field at different frequencies. Only the first 7 modes are shown

Additionally, Figure 4.46 (up) shows the spatial-average frequency response of the displacements over the plate, which are calculated as stated in Equation 4.43.

$$\bar{u}_y(f) = \sqrt{\frac{\iint_{plate} u_y^2(f) dA}{A_{plate}}} \tag{4.43}$$

Figure 4.46 (up) shows a comparison between the experimental and computed spatial-averaged vibration of the plate for a range of frequencies ranging from $f \cdot L_{ref}/V_\infty \approx 0$ to $f \cdot L_{ref}/V_\infty \approx 1.300$ ($f = 1900Hz$). Note how, for frequencies below $f \cdot L_{ref}/V_\infty \approx 0.800$, both the coarse and the fine mesh provide results which are excellent in agreement with those deduced from the experiments. For frequencies above this value it is shown that the computations with the coarse mesh tend to underpredict the level of the displacement although, as expected, exhibiting the peaks at the same frequencies than the other computation.

As opposed to the pressure spectrum, some peaks can be observed in the displacement spectrum. The plate resonates at all its eigenfrequencies, which can be visually identified from Figure 4.46 and compared with the eigenvectors shown in Figure 4.39. Only the 4th structural mode is hardly observed in the figure, but as it is very close to that of the third mode it may be masked in the frequency response. The discrepancy between computations for medium values

of the frequency can be explained due to the filtering effect which the gross mesh exhibits over the energy content.

In order to compare with previous works, Figure 4.46 (bottom) shows the results which were obtained by Schafer et al. [198]. Note how, as the plate characteristics are different, current results can only be qualitatively compared with this. Nevertheless, it is important to note how the current computation provides more accurate results both in excitation level and peaks location.

There are, however, some discrepancies between the current calculation and the experiments. For example, a discrepancy of an 8 % was found on the prediction of the first eigenfrequency. This can mainly due to the approximations made on the boundary conditions. Using non-infinitely stiff boundary conditions could provide a better prediction, but it is out of the scope of this contribution. The same reasoning could be argued in order to explain why there are some discrepancies at the peaks location at high frequencies.

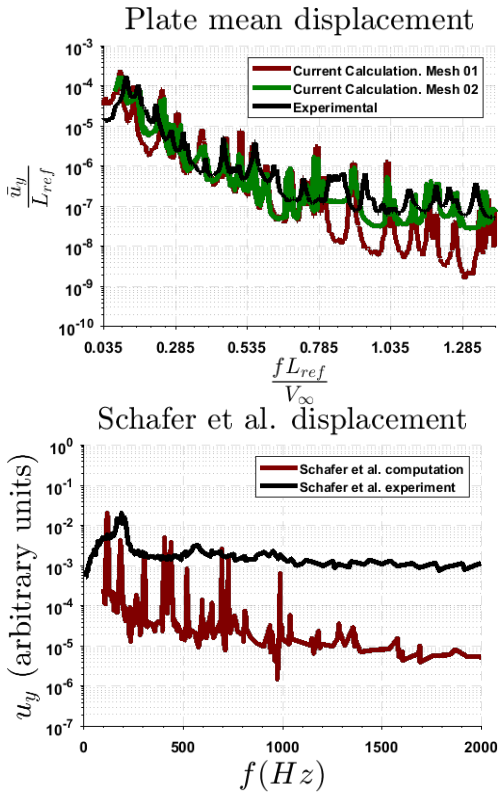

Figure 4.46: Mean displacement spectra for the current calculation (up) and collection of the displacements results taken from *Schafer et al.* for a plate of thickness $h = 40$ μm (bottom)

Extension of the case and computation of the radiated noise

Once the vibration response has been computed and validated against experiments, it is possible to extend it in order to deduce the influence of the different structural parameters, or even the own fluid parameters on the response. In fact, if it is assumed that the dependence with Reynolds number is approximately negligible and that the geometry is fixed to the already mentioned flat plate, it was observed how the system will only depend on the relationship between elastic and fluid forces, $\frac{E}{6(1-\nu^2)V_\infty^2}\left(\frac{h}{L_{ref}}\right)^3$ and on the relationship between the solid and fluid mass, $8\pi^2\frac{h}{L_{ref}}\frac{\rho_0}{\rho_\infty}$.

In this sense, one interesting analysis can be found on the dependence over the vibration response of the selection of the wall thickness. Note that, when this parameter is changed, both k^* and m^* experiment variation. For instance, Figure 4.47 shows the evolution of the maximum computed normal displacement when the thickness of the plate is $h/h_{ref} = 1$, $h/h_{ref} = 2$ and $h/h_{ref} = 5$, being $h_{ref} = 0.5$ mm the reference thickness of the previous paragraphs.

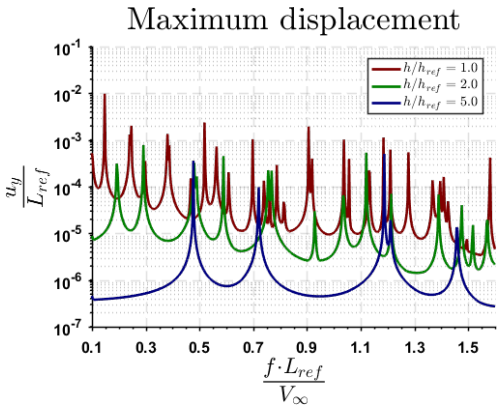

Figure 4.47: Maximum displacement spectra for the calculation with the mesh with $N = 20 \cdot 10^6$ elements for different values of the plate thickness

In Figure 4.47 it can be observed how, as it could be expected, the value of the computed displacement is significantly decreased when increasing the thickness of the plate. Moreover, due to the cubic dependence of the stiffness parameter with h and the linear dependence with this parameter of the mass ratio, a linear dependence of the eigenfrequencies is observed with h. Note how, additional studies could be performed changing the value of other parameters, although, for reasons of brevity it will be not carried out during this work.

Finally, once the vibrational response is computed on the wall, it can be used as a boundary condition in order to predict the radiated aerovibroacoustic noise. In order to do this, a rigid chamber is of height $L_{chamber} = 13.3 L_{ref}$ is mounted below the flexible plate, as sketched in Figure 4.48. Here, the acoustic mesh is also shown, which is constructured by second order hexahedral elements with constant size of $\Delta x = L_{ref}/3$, which was found to be an accurate size for the computed lengthwaves.

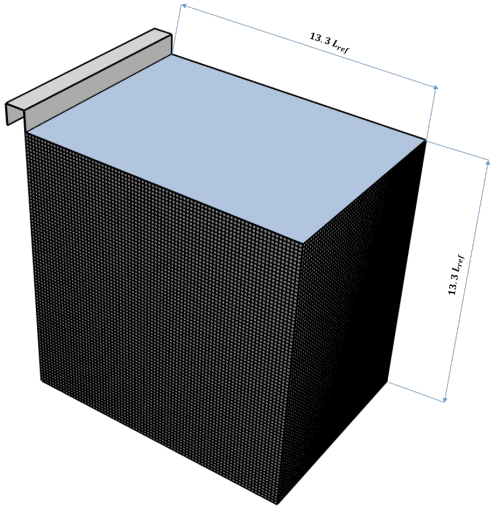

Figure 4.48: Sketch of the acoustic domain for the computation of vibration-radiated noise

The chamber is supposed to be filled with air, initially at rest, with density $\rho_c = 1.225$ kg m^{-3} and a sound velocity of $a_c = 340$ m s^{-1}. Therefore, the Helmholtz equations, 4.16 are complied inside this volume, and they can be resolved using the methodology explained in the previous section.

After performing such calculation, Figure 4.49 can be obtained. Here, the maximum magnitude of the acoustic pressure level inside the chamber is shown. Note that, instead of non-dimensionalizing by using the usual $p_{ref} = 20\mu$ Pa, the dynamic pressure is used as a reference, in order to make this Figure more independent from the boundary conditions.

Some interesting conclusions can be extracted from the observation of Figure 4.49: first, as a general trend, it is found how the sound pressure level inside the chamber for low frequencies is decreased by orders of magnitude when increasing the plate thickness. Additionally, it can be observed how, again, each structural eigenfrequency can be observed as a peak on the frequency

response. However, some additional peaks can be observed in this calculation, corresponding with the excitation of the rigid chamber eigenfrequency.

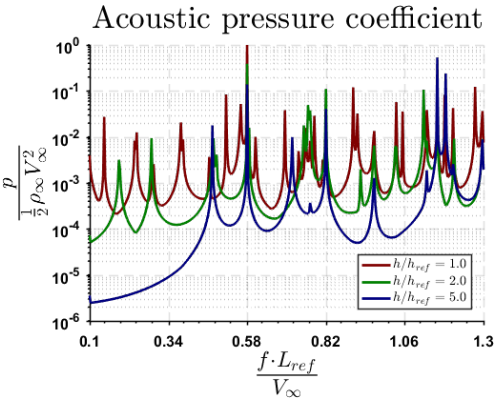

Figure 4.49: Maximum value of the non dimensional acoustic pressure inside the chamber for different values of the plate thickness

The acoustic pressure field can also be interpreted from the observation of Figure 4.50. Here, isosurfaces of the absolute value of the non dimensional acoustic pressure are shown for $h/h_{ref} = 1$ (first row), $h/h_{ref} = 2$ (second row) and $h/h_{ref} = 5$ (third row). Note that the Figure ii^{th} represents the frequency at which the structural eigenfrequency of the corresponding thickness is excited. Due to the important magnitude differences between the cases, the colormap is shown in a qualitative way (despite the maximum and minimum values are shown at each corresponding subfigure).

Note how, before each mode is excited, the qualitative sound pressure field is very similar regardless with the value of the plate thickness: A very uniform distribution is observed (see maximum at minimum values at each case) and a flat wave-like pattern is found relatively near to the deforming plate.

For higher values of the frequency, in all the cases it can be observed an important difference between the maximum and minimum computed sound pressure and more complex patterns on the isosurfaces.

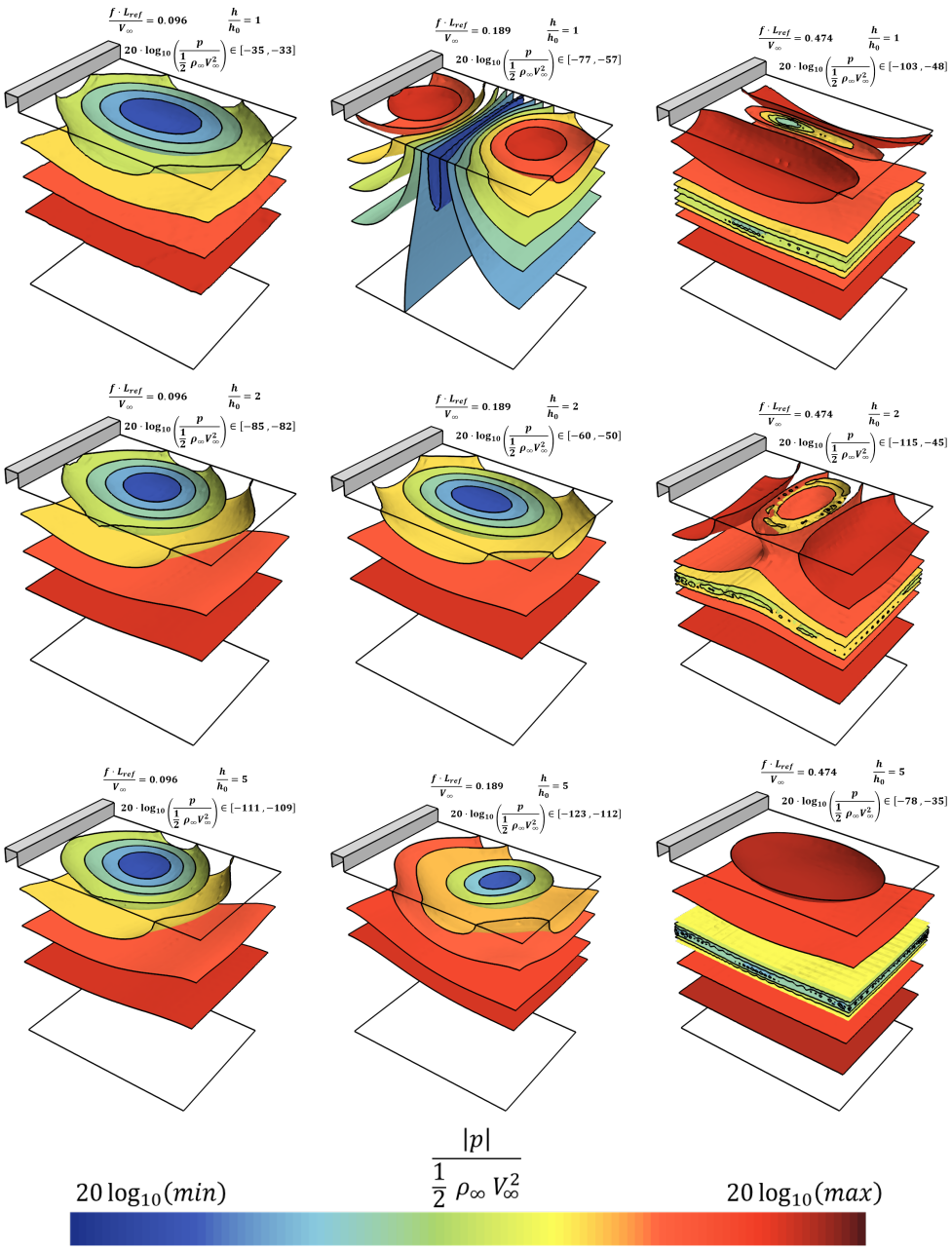

Figure 4.50: Frequency response of the plate displacement under the action of the turbulent pressure field at different frequencies

4.3.5 Partial conclusions

Numerical and Experimental investigations on the flow-induced vibration of a flat plate have been presented. The plate was excited by the turbulent fluid flow downstream of a wall-mounted obstacle.

The numerical model was validated using dedicated experiments, both for the structural eigenfrequencies and the coupled fluid-structure response.

A one-way interaction scheme has been proved to provide good results for a relatively thin plate (0.5mm) due to the low amplitude of the vibrations and allows a fully characterization of all the phenomena intervening in the Flow induced vibrations. For lower values of the thickness of the plate, as is the case of Schafer et al. [198] one way cannot be assumed anymore, as plate displacements can highly affect to the behavior of the own flow. However, for normal working conditions this will not be the case and the current methodology allows to obtain accurate results with a lower computational cost.

Numerical simulations were performed using RANS and LES, and two different mesh resolutions, with $N \approx 4 \times 10^6$ and $N \approx 20 \times 10^6$ elements. It was shown how, although the RANS computations tends to overpredict the location of the reattachment length it allows to obtain a good representation of the time averaged plate displacement, considering the low computational requirements of this methodology, compared with LES computations. Additionally, it was shown how both grids resolutions allow to obtain similar results when using LES for the current configuration. However, as a general tend, the high frequency content of the variables was shown to be more meaningful for the finer mesh.

Both numerical computation and experiments show that almost all the vibration modes can be identified from the induced vibration field for the studied frequency range. Fourth vibration mode is less clear due to being close to the third one. Numerical data and experiments agree well for low frequencies for the LES .

It was shown how, for low values of the frequency $\left(\frac{fL_{ref}}{V_\infty}\right)$, both grid resolutions allows to obtain a correct prediction of the plate mean displacement, compared with the experiments, both qualitatively and quantitatively. For higher frequencies, the coarse mesh tends to underpredict the value of the displacement, due to the lower mesh resolution, which tends to filter the high frequency energy of small eddies. Nevertheless, under these conditions, the results of the coarse mesh allows to qualitatively predict the behavior of the plate.

As the simulation results agrees well with empirical observations, it has been shown how the vibration pattern for a plate located after a wall mounted bluff body is mainly governed by the turbulence generated by the own body, being the influence of the inflow turbulence of second order.

It has been shown how the vibrational response can be used as a boundary condition in order to predict the radiated vibration noise for arbitrary chamber geometries. The capabilities of the one way methodology have been illustrated by presenting a parametric analysis of the influence of the plate thickness.

4.4 Summary and conclusions

During this chapter, the applicability of the fluid structure interaction concepts has been illustrated by means of presenting two different engineering like applications. It has been deduced how a wide number of the industrial fluid structure interaction cases can be supposed to be coupled in only one direction. Moreover, during the presentation of the first case it was shown how, by choosing the proper numerical methodology by means of a previous order of magnitude dimensional analysis not only a less computationally demanding process can be followed, but it even allows one to obtain more valuable (and interpretable) results due to the elimination of some of the important FSI tool possible choices (see Figure 4.46).

The same methodology was applied to the case of the motion of pressure waves inside a flexible muffler. Here, it was shown how the most proper reference velocity for the non dimensionalization could be the pressure wave speed. It was made a comparison between the results of a monolithic approach using the Helmholtz equations (using the commercial software *COMSOL*) and the results for the same case using a segregated implicit approach to solve the time domain Euler equations (using the commercial software *STAR-CCM+*).Additionally, it was shown how, as expected due to previous work, that important coupling between fluid and solid appear at low frequencies for a very low value of the wall Young's Modulus.

4.5 References

[14] S. Pope. *Turbulent Flows*. Ed. by C. U. Press. Cambridge University Press, 2009 (cit. on pp. 17, 18, 76, 169, 170, 179).

[20] O. Zienkiewicz, R. Taylor, and P. Nithiarasu. "The Finite Element Method for Fluid Dynamics". In: *Butterworth-Heinemann* (2014) (cit. on pp. 17, 130, 131).

[32] F. Menter. "Zonal two-equation $k-\omega$ turbulence model for aerodynamic flows". In: *AIAA, Orlando, Florida* 93 (1986), pp. 93–2906 (cit. on pp. 19, 169).

[35] J. Smagorinsky. "General Circulation Experiments with the Primitive Equations: Part I, The Basic Experiment". In: *Monthly Weather Review* 91 (1963), pp. 99–164 (cit. on pp. 19, 166).

[38] F. Nicoud and F. Ducros. "Subgrid-Scale Stress Modelling Based on the Square of the Velocity Gradient Tensor". In: *Flow, Turbulence and Combustion* 62 (1999), pp. 183–200 (cit. on pp. 19, 166, 179).

[162] P. Bremner and J. Wilby. "Aero-vibro-acoustics: problem statement and methods for simulation-based design solution". In: *8th AIAA/CEAS Aeroacoustics Conference and Exhibit* (2002), p. 2551 (cit. on p. 121).

[163] X. Gloerfelt and J. Berland. "Turbulent boundary-layer noise: direct radiation at Mach number 0.5". In: *Journal of Fluid Mechanics* 723 (2013), pp. 318–351 (cit. on p. 122).

[164] D. Lecoq, C. Pezerat, J. Thomas, and W. Bi. "Extraction of the acoustic component of a turbulent flow exciting a plate by inverting the vibration problem". In: *Journal of Sound and Vibration* 333 (2014), pp. 2505–2519 (cit. on p. 122).

[165] S. Amailland, J. Thomas, C. Pezerat, and R. Boucheron. "Boundary layer noise substraction in hydrodynamic tunnel using robust principal component analysis". In: *The Journal of the Acoustical Society of America* 143 (2018), pp. 2152–2163 (cit. on p. 122).

[166] W. H. O. for the European Union. *Night Noise Guidelines for Europe*. Tech. rep. 2010 (cit. on p. 123).

[167] E. Union. *On the sound level of motor vehicles and of replacement silencing systems. Regulation (EU) No 540/2014 of the european parliament and of the council of 16 April 2014*. Tech. rep. 2014 (cit. on p. 123).

[168] C. H. Hansen. *Understanding active noise cancellation*. Spon Press, 2003 (cit. on p. 123).

[169] Y. L. A. Linus, Y. K. Koh, and H. P. Lee. “The performance of active noise-cancelling headphones in different noise environments”. In: *Applied Acoustics* 122 (2017), pp. 16–22 (cit. on p. 123).

[170] H. D. Hwang, K. Ege, Y. Gerges, and J. L. Guyader. “SmEdA vibro-acoustic modelling in the mid-frequency range including the effect of dissipative treatments”. In: *Journal of Sound and Vibration* 393 (2017), pp. 187–215 (cit. on p. 123).

[171] M. L. Munjal. *Acoustics of Ducts and Mufflers - Second Edition*. Wiley, 2014 (cit. on pp. 123, 124, 133, 137, 138).

[172] B. Aydemir and A. Ebrinç. “Effect of Material Properties and Wall Thickness of Polymer Based Intake Manifold on the Engine Radiated Noise Levels”. In: *SAE International* 2001-01 (2009), p. 1544 (cit. on pp. 123, 124).

[173] R. F. Nunes, C. F. Nogueira, M. A. Argentino, and D. Hackenbroich. “Developement of an Air Intake System Using Vibro-Acoustics Numerical Modeling”. In: *SAE International* 2001-01 (2001), p. 1519 (cit. on p. 124).

[174] K. Hu, C. Lee, E. Homsi, and D. Moenssen. “Acoustic Modeling and Radiated Noise Prediction for Plastic Air-Intake Manifolds”. In: *SAE International* 2003-01 (2003), p. 1448 (cit. on p. 124).

[175] L. Huang. “Modal analysis of a drumlike silencer”. In: *The Journal of the Acoustical Society of America* 112 (2002), pp. 2014–2015 (cit. on p. 124).

[176] H. K. Fan, R. C. Leung, and G. C. Lam. “Numerical analysis of aeroacoustic-structural interaction of a flexible panel in uniform duct flow”. In: *The Journal of the Acoustical Society of America* 137 (2015), pp. 3115–3126 (cit. on p. 124).

[177] J. B. Lawrie. “Analytic mode-matching for acoustic scattering in three dimensional waveguides with flexible walls: Application to a triangular duct”. In: *Wave Motion* 50 (2013), pp. 542–557 (cit. on p. 124).

[178] S. Ramamoorthy, S. Grosh, and J. M. Dodson. “A theoretical study of structural acoustic silencers for hydraulic systems”. In: *The Journal of the Acoustical Society of America* 111 (2012), pp. 2097–2108 (cit. on p. 124).

[179] S. H. Ko. “Sound Wave Propagation In A Two-dimensional Flexible Duct In The Presence Of An Inviscid Flow”. In: *Journal of Sound and Vibration* 175 (1994), pp. 279–287 (cit. on p. 124).

[180] F. Gautier, J. Gilbert, J. P. Dalmont, and R. P. Vila. “Wave Propagation in a Fluid Filled Rubber Tube: Theoretical and Experimental Results for Korteweg’s Wave”. In: *Acta Acustica united with Acustica* 93 (2007), pp. 333–344 (cit. on p. 124).

[181] B. Venkatesham, M. Tiwari, and M. L. Munjal. “Analytical prediction of break-out noise from a reactive rectangular plenum with four flexible walls”. In: *The Journal of the Acoustical Society of America* 128 (2010), pp. 1789–1799 (cit. on p. 124).

[182] G. Wang, W. L. Li, J. Du, and W. Li. “Prediction of break-out sound from a rectangular cavity via an elastically mounted panel”. In: *The Journal of the Acoustical Society of America* 139 (2016), pp. 684–692 (cit. on p. 124).

[183] M. L. Munjal and P. T. Thawani. “Prediction of the vibro-acoustic transmission loss of planar hose-pipe systems”. In: *The Journal of the Acoustical Society of America* 101 (1998), pp. 2524–2535 (cit. on p. 124).

[184] A. Cummings. “The attenuation of sound in unlined ducts with flexible walls”. In: *Journal of Sound and Vibration* 174 (1994), pp. 433–450 (cit. on p. 124).

[185] F. Hilderbrand and E. Reissner. *The influence of the aerodynamic span effect on the magnitude of the torsional-divergence velociy and on the shape of the corresponding deflection mode*. Tech. rep. NACA-TN-926. Massachusetts, Inst of Tech Cambridge: NACA, 1944 (cit. on p. 126).

[186] R. L. Bisplinghoff, H. Ashley, and R. L. Halfman. *Aeroelasticity*. Courier Corporation, 1996 (cit. on p. 126).

[187] U. Jeong and S. Kwon. “Sequential numerical procedures for predicting flutter velocity of bridge sections”. In: *Journal of Wind Engineering and Industrial Aerodynamics* 91 (2003), pp. 291–305 (cit. on p. 126).

[188] G. Schewe and A. Larsen. “Reynolds number effects in the flow around a bluff bridge deck cross section”. In: *Journal of Wind Engineering and Industrial Aerodynamics* 74 (1998), pp. 829–838 (cit. on p. 126).

[189] B. Augier, P. Bot, F. Hauville, and M. Durand. “Experimental validation of unsteady models for fluid structure interaction: Application to yacht sails and rigs”. In: *Journal of Wind Engineering and Industrial Aerodynamics* 101 (2012), pp. 53–66 (cit. on p. 126).

[190] Y. Zhang, W. G. Habashi, and R. Khurram. “Predicting wind-induced vibrations of hight-rise buildings using unsteady CFD and modal analysis”. In: *Journal of Wind Engineering and Industrial Aerodynamics* 136 (2015), pp. 165–179 (cit. on p. 126).

[191] M. Ricci, L. Patruno, I. Kalkman, S. Miranda, and B. Blocken. “Towards LES as a design tool: Wind loads assessment on a high-rise building”. In: *Journal of Wind Engineering and Industrial Aerodynamics* 180 (2018), pp. 1–18 (cit. on p. 126).

[192] H. Davies. “Sound from turbulent boundary layer excited panels”. In: *The Journal of the Acoustical Society of America* 49 (1971), pp. 878–889 (cit. on p. 127).

[193] W. Graham. “Boundary Layer Induced Noise in Aircraft, Part 1: The Flat Plate Model”. In: *The Journal of Sound and Vibration* 192 (1996), pp. 101–120 (cit. on p. 127).

[194] M. Howe. “Influence of Mean Flow on Boundary Layer Generated Interior Noise”. In: *Journal of the Acoustical Society of America* 99 (1996), pp. 3401–3411 (cit. on p. 127).

[195] K. Frampton. “Power Flow in an Aeroelastic PLate Backed by a Reverberant Cavity”. In: *Journal of the Acoustical Society of America* 102 (1997), pp. 1620–1627 (cit. on p. 127).

[196] M. Springer, C. Scheit, and S. Becker. “Fluid-struture-acoustic copling for a flat plate”. In: *International Journal of Heat and Fluid Flow* 66 (2017), pp. 249–257 (cit. on pp. 127, 128).

[197] S. Mueller, S. Becker, T. Biermeier, F. Schaefer, J. Grabinger, M. Kaltenbaher, and D. Blanchet. “Investigation of the Fluid-Structure Interaction and the Radiated Sound of Different Plate Structures Deepending on Various Inflows”. In: *15th AIAA/CEAS Aeroacoustics Conference (30th AIAA Aeroacoustics Conference)* (2009), p. 3390 (cit. on p. 127).

[198] F. Schafer, S. Müller, T. Uffinger, S. Becker, J. Grabinger, M. Kaltenbaher, and D. Blanchet. “Fluid-structure-acoustic interaction of the flow past a thin flexible structure”. In: *AIAA journal* 48 (2010), pp. 738–748 (cit. on pp. 127, 128, 162, 168, 194, 199).

[199] Y. Bazilevs, K. Takizawa, and T. E. Tezduyar. *Computational Fluid-Structure Interaction. Methods and Applications*. Wiley, 2013 (cit. on p. 130).

[200] F. Irgens. *Continuum mechanics*. Springer, 2008 (cit. on p. 130).

[201] F. Anselmet and P. O. Mattei. *Acoustics, Aeroacoustics and Vibrations*. Wiley, 2016 (cit. on p. 132).

[202] Y. Inoue and Y. Gotoh. “Formation of weak shock waves caused by a sphere pulsating at large amplitude and low frequency”. In: *Journal of Sound and Vibration* 145 (1991), pp. 269–280 (cit. on p. 132).

[203] M. J. Lighthill. “Viscosity effect in sound waves of finite amplitude”. In: *Survey in Mechanics* 250 (1956), pp. 337–348 (cit. on p. 132).

[204] E. C. Romão, M. D. Campos, and L. F. M. Moura. “Application of the Galerkin and Least-Squares Finite Element Methods in the solution of 3D Poisson and Helmholtz equations”. In: *Computers and Mathematics with Applications* 62 (2011), pp. 4288–4299 (cit. on p. 134).

[205] *COMSOL Multiphysics 5.2 User’s Guide*. 2016 (cit. on p. 134).

[206] A. Broatch, X. Margot, A. Gil, and F. Denia. “A CFD approach to the computation of the acoustic response of exhaust mufflers”. In: *Journal of Computational Acoustics* 13 (2005), pp. 301–316 (cit. on pp. 134, 137).

[207] G. Liu, X. Zhao, W. Zhang, and S. Li. “Study on plate silencer with general boundary conditions”. In: *Journal of Sound and Vibration* 333 (2014), pp. 4881–4896 (cit. on p. 136).

[208] R. Barbieri and N. Barbieri. “Finite element acoustic simulation based shape optimization of a muffler”. In: *Applied Acoustics* 67 (2006), pp. 346–357 (cit. on p. 137).

[209] *STARCCM+ 12.02.010 User’s Guide*. 2016 (cit. on p. 140).

[210] F. J. Fuenmayor, F. D. Denia, J. Albelda, and E. Giner. “H-adaptive refinement strategy for acoustic problems with a set of natural frequencies”. In: *Journal of Sound and Vibration* 255 (2002), pp. 457–479 (cit. on p. 141).

[211] J. Herrmann, J. Koreck, M. Matthias, L. Gaul, and O. Estorff. “Frequency-dependent damping model for the hydroacoustic finite element analysis of fluid-filled pipes with diameter changes”. In: *Mechanical Systems and Signal Processing* 25 (2011), pp. 981–990 (cit. on p. 156).

[212] A. David, F. Hugyes, N. Dauchez, and E. Perrey-Debain. “Vibrational response of a rectangular duct of finite length excited by a turbulent internal flow”. In: *Journal of Sound and Vibration* 422 (2018), pp. 146–160 (cit. on p. 162).

[213] S. Timoshenko and S. Woinowsky-Krieger. *Theory of plates and shells*. Ed. by McGraw-Hill. 1959 (cit. on p. 164).

[214] G. Warburton. “The vibration of rectangular plates”. In: *Proceedings of the Institution of Mechanical Engineers* 168 (1954), pp. 371–384 (cit. on p. 164).

[215] K. Bathe and H. Zhang. “Finite element developments for general fluid flows with structural interactions”. In: *International Journal for numerical methods in engineering* 60 (2004), pp. 213–232 (cit. on p. 164).

[216] K. Yang and F. J.H. “Large-Eddy Simulation of Turbulent Obstacle Flow Using a Dynamic Subgrid-Scale Model”. In: *AIAA Journal* 31 (1993), pp. 1406–1413 (cit. on pp. 165, 189).

[217] X. Zhengtong and I. Castro. “LES and RANS for turbulent flow over arrays of wall-mounted obstacles”. In: *Flow Turbulence Combust* 76 (2006), pp. 291–312 (cit. on p. 165).

[218] C. Moussaed, M. Salvetti, S. Wornom, B. Koobus, and A. Dervieux. “Simulation of the flow past a circular cylinder in the supercritical regime by blending RANS and variational-multiscale LES models”. In: *Journal of Fluids and Structures* 47 (2014), pp. 114–123 (cit. on p. 166).

[219] G. Malloupas, G. Goldin, Y. Zhang, P. Thakre, N. Krishnamoorthy, R. Rawat, D. Gosman, J. Rogerson, and G. Bulat. “Investigation of an Industrial Gas Turbine Combustor and Pollutant Formation Using LES”. In: *ASME Turbo Expo 2017: Turbomachinery Technical Conference and Exposition* (2017) (cit. on p. 166).

[220] P. Bearman and T. Morel. “Effect of free stream turbulence on the flow around bluff bodies”. In: *Progress in aerospace sciences* 20 (1983), pp. 97–123 (cit. on p. 169).

[221] Y. Nakamura and S. Ozono. “The effects of turbulence on a separated and reattaching flow”. In: *Journal of Fluid Mechanics* 178 (1987), pp. 477–490 (cit. on p. 169).

[222] G. Ratnam and S. Vengadesan. “Performance of two equation turbulence models for prediction of flow and heat transfer over a wall mounted cube”. In: *International Jounral of Heat and Mass Transfer* 51 (2008), pp. 2834–2846 (cit. on p. 169).

[223] S. Archaya, S. Dutta, T. Myrum, and R. Baker. “Turbulent flow past a surface-mounted two-dimensional rib”. In: *Journal of Fluids engineering* 116 (1994), pp. 238–246 (cit. on p. 169).

[224] D. Ding and S. Wu. “Direct numerical simulation of turbulent flow over backward-facing at high Reynolds numbers”. In: *Science China* 55 (2012), pp. 3213–3222 (cit. on p. 169).

[225] D. Wilcox. “Multiscale model for turbulent flows”. In: *Proceedings of the 24th AIAA Aerospace Science Meeting* 24 (1986), pp. 1311–1320 (cit. on p. 169).

[226] P. A. Ullrich and M. Taylor. “Arbitrary-order conservative and consistent remapping and theory of linear maps: Part I”. In: *Monthly Weather Review* 143 (2015), pp. 2419–2440 (cit. on p. 170).

[227] P. A. Ullrich and M. Taylor. “Arbitrary-order conservative and consistent remapping and theory of linear maps: Part II”. In: *Monthly Weather Review* 144 (2016), pp. 1529–1549 (cit. on p. 170).

[228] P. Jones. “First- and second-order conservative remapping schemes for grids in spherical coordinates”. In: *Monthly Weather Review* 127 (1999), pp. 2204–2210 (cit. on p. 170).

[229] G. Taylor. “The spectrum of turbulence”. In: *Proceedings of the Royal Society of London* (1938), pp. 476–490 (cit. on p. 170).

[230] W. De Roeck and W. Desmet. “Experimental acoustic identification of flow noise sources in expansion chambers”. In: *Proceedings of ISMA 2018: International Conference on Noise and Vibration Engineering* 1 (2008), pp. 455–470 (cit. on p. 172).

[231] W. Ren and G. De Roeck. “Structural damage identification using modal data II: test verification”. In: *Journal of Structural Engineering* 128 (2002), pp. 96–104 (cit. on p. 172).

[232] N. Roozen, L. Labelle, M. Rychtarikova, and C. Glorieux. “Determining radiated sound power of building structures by means of laser Doppler vibrometry”. In: *Journal of Sound and Vibration* 346 (2015), pp. 81–99 (cit. on p. 172).

[233] D. Butscher, C. Hutter, C. Kuhn, and P. Rohr. “Particle image velocimetry in a foam-like porous structure using refractive index matching: a method to characterize de hydrodynamic performance of porous structures”. In: *Experiments in fluids* 53 (2012), pp. 1123–1132 (cit. on p. 172).

[234] B. Armaly, F. Durst, J. Pereira, and B. Shonung. “Experimental and theoretical investigation of backward-facing step flow”. In: *Journal of Fluid Mechanics* 127 (1983), pp. 473–496 (cit. on p. 179).

[235] J. Kostas, J. Soria, and M. Chong. “A study of a backward facing step flow at two Reynolds numbers”. In: *14th Australasian Fluid Mechanics Conference* (2001), pp. 609–612 (cit. on p. 179).

[236] C. Tropea and R. Gackstatter. “The flow over two-dimensional surface-mounted obstacles at low Reynolds number”. In: *Journal of Fluids Engineering* 107 (1985), pp. 489–494 (cit. on p. 179).

[237] F. Durst, M. Founti, and S. Obi. “Experimental and computational investigation of the two-dimensional channel flow over two feces in tandem”. In: *Journal of Fluids Engineering* 110 (1988), pp. 48–54 (cit. on p. 179).

[238] I. Celik, Z. Cehreli, and I. Yavuz. “Index of Resolution Quality for Large Eddy Simulations”. In: *Journal of Fluids Engineering* 127 (2005), pp. 949–958 (cit. on p. 179).

[239] A. Lucius and G. Brenner. “Numerical Simulation and Evaluation of Velocity Fluctuations During Rotating Stall of a Centrifugal Pump”. In: *Journal of Fluids Engineering* 133 (2011), pp. 081102-1 - 081102-8 (cit. on p. 179).

[240] L. Konnigk, B. Torner, and F. Wurm. “Application of verification methods on a complex flow field calculated by Large Eddy Simulation: Blood pump flow”. In: *7th European Conference on Computational Fluid Dynamics* (2018), pp. 1–13 (cit. on p. 179).

[241] A. Dastbelaraki, M. Yaghoubi, M. Tavakol, and A. Rahmatmand. “Numerical analysis of convection heat transfer from an array of perforated fins using RANS and LES method”. In: *Applied Mathematical Modelling* (2018) (cit. on p. 179).

[242] K. Frampton. “The effect of flow-induced coupling on sound radiation from convected fluid loaded plates”. In: *The Journal of the Acoustical Society of America* 117 (2005), pp. 1129–1137 (cit. on p. 186).

[243] M. Pastor, M. Binda, and T. Harcarik. “Modal Assurance Criterion”. In: *Procedia Engineering* 48 (2012), pp. 543–548 (cit. on p. 187).

[244] H. Werner and H. Wengle. “Large-eddy simulation of turbulent flow over a square rib in a channel”. In: *Advances in Turbulence* 2 (1989), pp. 418–423 (cit. on p. 189).

[245] S. Schmidt and F. Thiele. “Comparison of numerical methods applied to the flow over wall-mounted cubes”. In: *International Journal of Heat and Fluid Flow* 23 (2002), pp. 330–339 (cit. on p. 189).

[246] M. Ariff, S. Salim, and S. Cheah. “Wall y+ approach for dealing with turbulent flow over a surface mounted cube: Part 2-High Reynolds number”. In: *Proceedings of 7th International Conference on CFD in the Minerals and Process Industries CSIRO, Melbourne, Australia* (2009) (cit. on p. 189).

[247] A. K. Chopra. “Modal analysis of linear dynamic systems: physical interpretation”. In: *Journal of structural engineering* 122 (1996), pp. 517–527 (cit. on p. 191).

CHAPTER 5

Conclusions and Future Works

Contents

Figures

5.1 Conclusions

This section shows, as a whole synthesis of the work, the main conclusions which can be derived from the work done, which has been exposed in the form of PhD Thesis during this document. First of all next general results should be addressed:

- During the development of Chapter 2, a whole bibliographic analysis has been carried out in order to establish the most usual kinds of fluid structure interaction coupling levels, the main laws governing this and some examples of the applications of each one. It was seen how, although the field of fluid structure interaction is on growing development, the synthesis of the main ideas around it has not been extensively done and, thank to this, it could be found how that, although it was suggested before, the dimensional analysis of the coupling had not been properly done in order to establish the most proper tool from first principles.
- This fact, has directly lead to the development of the Chapter 3. Here, a relatively simple example of Vortex Induced Vibrations was presented in its most basic non dimensional form in order to show how, for a given value of the Reynolds number, the coupling only depends on $E/(\frac{1}{2}\rho_\infty V_\infty^2)$ and ρ_s/ρ_∞. Moreover, for high values of the Reynolds number it can be expected that its influence on the coupling level will become of second order.
- Finally, the applicability of the dimensional analysis for the selection of the proper tool has been proven by means of two different state of the art FSI coupling problems: a first one consisting on the prediction of the vibration generated on a flexible plate by a fully turbulent flow field and a second one consisting on the prediction of the virboacustic behavior of a flexible silencer due to the motion of pressure waves in its interior.

Besides, it is worth to be mentioned the particular conclusions arising from each of the studies which were carried out during the development of this work.

- Given a Fluid Structure Interaction system, the value of the stiffness at which transition between one-way and two-way coupling arises, is a function of the relative mass between the fluid and solid. As the parameter ρ_s/ρ_∞ becomes higher, the two-way coupling appears for higher values of stiffness.
- It is possible to deduce a behavior map of the coupling regions in order to infer the capability of one-way, two-way explicit and two-way implicit methodologies to resolve each of these regions. From this map it could be deduced how the applicability explicit methodology, which can be considered to be as the less computationally demanding strategy, is limited by the mass parameter. In fact for very low values of ρ_s/ρ_∞, the range of stiffness at which this methodology can be applied is drastically reduced.
- This methodology can be applied to problems of high Reynolds turbulent flow induced vibrations, where it was shown how, for a case similar to the flow encountered at a car's underbody at normal working conditions, the one way methodology is not only computationally less demanding, but it also allows one to obtain more valuable vibration results in comparison with experiments and with bibliography.
- The methodology has also been proven to be valid for the computation of the viboacoustic phenomena arising in the inner pressure field of a flexible expansion chamber-like silencer. Although in this case Euler equations were used instead of Navier-Stokes viscous equations, it was seen how the same methodology could be applied. Moreover, it was also shown how, if correctly carried out, segregated implicit and monolithic two way methodologies allow one to obtain exactly the same results.

5.2 Future Work

As it has been already said, the most important contribution of the current document is the presentation of a generic methodology which would allow one to select the most proper computational tool in order to face with problems of Fluid Structure Interaction, regardless of the strength of the coupling.

As a consequence, after the work carried out for the development of the current document, a wide number of possible investigation lines could be opened with a direct application of these concepts. As an example, some of them will be listed next. Note that they are plausible lines, as the author of the document has already been involved in some of them:

- Characterization of the radiated sound due to the wall vibration in the case of the admission and exhaust systems on Internal Combustion Engines.
- Characterization of the radiated sound due to the wall vibration in the case of Heating Ventilating and Air Conditioning (HVAC) systems .
- Characterization of the radiated noise due to the action of turbulent flow at the outer walls of a moving car and how this is radiated inside the own cabin.
- Analysis of the structural response of solar plates trackers under high wind conditions, in order to avoid aeroelastic problems, due to the low value of the torsional stiffness of these solutions.
- Application to the vibration of the blades of a compressor system in order to characterize possible aeroelastic critical phenomena under extreme conditions.

Bibliography

[1] **Torregrosa, A., Gil, A., Garcia-Cuevas, L., Quintero, P., and Denia, F.**
"Prediction of the Transmission Loss in a Flexible Chamber"
in: *Journal of Fluids and Structures* 82 (2018), pp. 134–153
(cit. on p. vii)

[2] **Torregrosa, A., Gil, A., Quintero, P., Ammirati, A., Denayer, H., and Desmet, W.**
"Prediction of Flow Induced Vibration of a flat plate located after a bluff wall mounted obstacle"
in: *Journal of Wind Engineering and Industrial Aerodynamics* 190 (2019), pp. 23–39 (cit. on p. vii)

[3] **Torregrosa, A., Gil, A., and Quintero P. Tiseira, A.**
"Enhanced design methodology of a low power stall regulated wind turbine. BEMT and MRF-RANS combination and comparison with existing designs"
in: *Journal of Wind Engineering and Industrial Aerodynamics* 190 (2019), pp. 230–244 (cit. on p. vii)

[4] **Barrholm, G., Larsen, C., and Lie, H.**
"On fatigue damage accumulation from in-line and cross-flow vortex-induced vibrations on risers"
in: *Journal of Fluids and Structures* 22 (2006), pp. 109–127
(cit. on p. 2)

[5] **Blaje, W.**
Mechanics of flow-induced sound and vibration, Volume 2
ed. by press, A. 2017 (cit. on pp. 2, 38)

[6] **Pettigrew, M., Taylor, C., Fisher, N., Yetisir, M., and Smith, B.**
"Flow-induced vibration: recent findings and open questions"
in: *Nuclear Engineering and Desing* 185 (1998), pp. 249–276
(cit. on p. 2)

[7] **Chen, Y.**
"Flow-induced vibration and noise in tube-bank heat exchangers due to von Karman streets"
in: *Journal of Engineering for Industry* 90 (1968), pp. 134–146 (cit. on p. 2)

[8] **Dowell E.H. adn Curtiss, H., Schalan, R., and Sisto, F.**
A modern course in aeroelsaticity
ed. by Dordrecht, T. N. K. a. p. 1989 (cit. on p. 2)

[9] **Guidaoui, M., Zhao, M., McInnis, D., and Axworthy, F.**
"A review of water hammer theory and practice"
in: *Applied Mechanics Reviews* 58 (2005), pp. 49–76 (cit. on p. 3)

[10] **Garrick, I. E. and Wilmer, H.**
"Historical Development of Aircraft Flutter"
in: *Journal of Aircraft* 18 (1981), pp. 897–912 (cit. on p. 15)

[11] **Hill, G.**
"Advances in aircraft structural design"
in: *Third Anglo-American Aeronautical Conference* (1951) (cit. on p. 15)

[12] **Brewer, G.**
"The Collapse of Monoplane Wings"
in: *Flight* 5 (1913), p. 33 (cit. on p. 15)

[13] **Collar, A.**
"The First Fifty Years of Aeroelasticity"
in: *Aerospace* 5 (1978), pp. 12–20 (cit. on p. 15)

[14] **Pope, S.**
Turbulent Flows
ed. by Press, C. U. Cambridge University Press 2009 (cit. on pp. 17, 18, 76, 169, 170, 179)

[15] **Hirsch, H.**
"Numerical computation of internal and external flows. Volume 1, Fundamentals of numerical discretization"
in: *John Wiley and Sons* (1988) (cit. on p. 17)

[16] **Hirsch, H.**
"Numerical computation of internal and external flows. Volume 2, Computational methods for inviscid and viscous flows"
in: *John Wiley and Sons* (1988) (cit. on p. 17)

[17] **V.S., P.**
"Numerical heat transfer and fluid flow"
in: *Hemisphere Publishing* (1980) (cit. on p. 17)

[18] **Versteeg, H. and Malalasekera, W.**
"An introduction to Computational Fluid Dynamics"
in: *LongMan Scientific and Technical* (1995) (cit. on pp. 17, 19)

[19] **D., K. and Hamamalainen, J.**
"Finite Element Methods for Computational Fluid Dynamics"
in: *Siam Computational Science and Engineering* (2014)
(cit. on p. 17)

[20] **Zienkiewicz, O., Taylor, R., and Nithiarasu, P.**
"The Finite Element Method for Fluid Dynamics"
in: *Butterworth-Heinemann* (2014) (cit. on pp. 17, 130, 131)

[21] **Shu, C.**
"High-order finite difference and finite volume WENO schemes and discontinuous Galerkin methods for CFD"
in: *International Journal of Computational Fluid Dynamics* 17 (2003), pp. 107–118 (cit. on p. 17)

[22] **Boris, J., Fritts, M., Madala, R., McDonald, B., Winsor, N., and Zalesak, S.**
Finite-difference techniques for vectorized fluid dynamics calculations
Springer Science and Business Media 2012 (cit. on p. 17)

[23] **Galache, J.**
"Study of the flow field through the wall of diesel particulate filter using Lattice Boltzmann methods"
in: *Doctoral dissertation. Universitat Politecnica de Valencia* (2017)
(cit. on p. 17)

[24] **Gil, A., Galache, J., Godenschwager, C., and Rude, U.**
"Optimum configuration ofor accurate simulations of chaotic porous media with Lattice Boltzmann Methods considering boundary conditions, lattice spacing and domain size"
in: *Computers and Mathematics with Applications* 73 (2017), pp. 2515–2528 (cit. on p. 17)

[25] **Chen, S. and Doolen, G.**
"Lattice Boltzmann Method for Fluid Flows"
in: *Annual Review of Fluid Mechanics* 30 (1998), pp. 329–364
(cit. on p. 17)

[26] **Das, A. and Mathew, J.**
"Direct numerical simulation of turbulent spots"
in: *Computers and Fluids* 30 (2001), pp. 553–541 (cit. on p. 18)

[27] **Hutl, T. and Friedrich, R.**
"Direct numerical simulation of turbulent flows in curved and helitically coiled pipes"
in: *Computers and Fluids* 30 (2001), pp. 591–605 (cit. on p. 18)

[28] **Friedrich, R., Hutl, T., Manhart, M., and Wagner, C.**
"Direct numerical simulation of incompressible turbulent flows"
in: *Computers and Fluids* 30 (2001), pp. 555–579 (cit. on p. 18)

[29] **Spalart, P. and Allmaras, S.**
"A one-equation turbulence model for aerodynamic flows"
in: *30 th aerospace science meeting and exhibit* (1992), p. 439 (cit. on p. 19)

[30] **Rodi, W.**
"Turbulence models for environmental problems"
in: *Von Karman Inst. for Fluid Dynamics: Prediction Methods for Turbulent Flows* (1979) (cit. on p. 19)

[31] **Menter, F.**
"Influence of freestream values on k-omega turbulence model predictions"
in: *AIAA journal* 30 (1992), pp. 1657–1659 (cit. on p. 19)

[32] **Menter, F.**
"Zonal two-equation $k-\omega$ turbulence model for aerodynamic flows"
in: *AIAA, Orlando, Florida* 93 (1986), pp. 93–2906 (cit. on pp. 19, 169)

[33] **Lien, F. and Leschziner, M.**
"Assessment of turbulence-transport models including non-linear RNG eddy-viscosity formulation and second-moment closure for flow over a backward-facing step"
in: *Computers and Fluids* 23 (1994), pp. 983–1004 (cit. on p. 19)

[34] **Sarkar, F. and Balakrishnan, L.**
"Application of a Reynolds-stress turbulence model to the compressible shear layer"
in: *ICASE Report 90-18, NASA CR 182002* (1990) (cit. on p. 19)

[35] **Smagorinsky, J.**
"General Circulation Experiments with the Primitive Equations: Part I, The Basic Experiment"
in: *Monthly Weather Review* 91 (1963), pp. 99–164 (cit. on pp. 19, 166)

[36] **Germano, M., Piomelli, U., Moin, P., and Cabot, W.**
"A Dynamic Subgrid-Scale Eddy Viscosity Model"
in: *Physics of Fluids* 3 (1991), pp. 1760–1765 (cit. on p. 19)

[37] **Lilly, D.**
"A proposed modification of the Germano subgrid-scale closure method"
in: *Physics of Fluids* 4 (1992), pp. 663–635 (cit. on p. 19)

[38] **Nicoud, F. and Ducros, F.**
"Subgrid-Scale Stress Modelling Based on the Square of the Velocity Gradient Tensor"
in: *Flow, Turbulence and Combustion* 62 (1999), pp. 183–200
(cit. on pp. 19, 166, 179)

[39] **Spalart, P., Jou, W., Strelets, M., and Allmaras, S.**
"Comments on the feasibility of LES for wings, and on a hybrid RANS/LES approach"
in: *1st AFOSR Int. Conf. on DNS/LES Aug, 4-8. In: Advances in DNS/LES* (1997) (cit. on p. 20)

[40] **Shur, M., Spalart, P., Strelets, M., and Travin, A.**
"A hybrid RANS-LES approach with delayed.DES and wall-modelled LES capabilities"
in: *International Journal of Heat and Fluid Flow* 29 (2008), pp. 1638–1649 (cit. on p. 20)

[41] **Spalart, P.**
"Detached-eddy simulation"
in: *Annual Review of fluid mechanics* 41 (2009), pp. 181–202
(cit. on p. 20)

[42] **Zienkiewicz, O. and Taylor, R.**
The Finite Element Method for Solid and Structural Mechanics
ed. by Butterworth-Heinemann, E. Oxford 2006 (cit. on pp. 20, 74)

[43] **Zienkiewicz, O., Taylor, R., and Zhu, J.**
The Finite Element Method: Its Basics and Fundamentals
ed. by Butterworth-Heinemann, E. Oxford 2005 (cit. on pp. 21, 74)

[44] **Michler, C., Hulshoff, S., Brummelen, E. H. van, and Borst, R.**
"A monolithic approach to Fluid-Structure Interaction"
in: *Computers and fluids* 33 (2004), pp. 839–848 (cit. on p. 27)

[45] **Brummelen, E. van, Hulshoff, S., and Borst, R.**
"Energy conservation under incompatibility for fluid-structure interaction problems"
in: *Proceedings of the Fifth World Congress on Computational Mechanics, Vienna University of Technology* (2002) (cit. on p. 27)

[46] **Lozovskiy, A., Olshanskii, M., and Vassilevski, Y.**
"Analysis and assessment of a monolithic FSI finite element method"
in: *Computers and Fluids* (2019) (cit. on p. 27)

[47] **Heil, M., Hazel, A., and Boyle, J.**
"Solvers for large-displacement fluid-structure interaction problems: segregated versus monolithic approaches"
in: *Computational Mechanics* (2008) (cit. on p. 27)

[48] **Krause, E., Shokin, Y., Resch, M., and Shokin, N.**
"Computational Science and High Performance Computing II"
in: *Proceedings of the 2nd Russian-German Advance Workshop, Sttugart, Germany* (2005) (cit. on p. 27)

[49] **Forster, C., Wall, W., and Ramm, E.**
"Artificial mass instabilities in sequential staggered coupling of nonllinear structures and incompressible viscous flows"
in: *Computational Methods Applied to Mechanical Engineering* 196 (2007), pp. 1278–1293 (cit. on p. 27)

[50] **Fernandez, M., Gerbeau, J., and Grandmont, C.**
"A projection semi-implicit scheme for the coupling of an elastic structure with an incompressible fluid"
in: *International Journal of Numerical Methods in Engineering* 69 (2007), pp. 794–821 (cit. on p. 27)

[51] **Takizawa, K., Henicke, B., Puntel, A., Kostov, N., and Tezduyar, T.**
"Computer modeling techniques for flapping-wing aerodynamics of a locust"
in: *Computers and Fluids* 85 (2013), pp. 125–134 (cit. on p. 27)

[52] **Hwang, S., Khayyer, A., Gotoh, H., and Park, J.**
"Development of a fully Lagrangian MPS-based coupled method for simulation of fluid-structure interaction problems"
in: *Journal of Fluids and Structures* 50 (2014), pp. 497–511 (cit. on pp. 27, 29)

[53] **Loon, R.**
"Towards computational modelling of aortic stenosis"
in: *International Jounral for Numerical Methods in Biomedical Engineering* 26 (2010), pp. 405–420 (cit. on p. 27)

[54] **Wu, Y. and Cai, X.**
"A fully implicit domain decomposition based ALE framework for three-dimensional fluid-structure interaction with applicatoin in blood flow computation"
in: *Journal of Computational Physics* 258 (2014), pp. 524–537 (cit. on p. 27)

[55] **Leng, W., Zhang, C., Sun, P., Gao, B., and Xu, J.**
"Numerical simulation of an immersed rotating structure in fluid for hemodynamic applcations"
in: *Journal of Computational Science* 30 (2019), pp. 79–89
(cit. on p. 27)

[56] **Fernandez, M.**
"Coupling schemes for incompresible fluid-structure interaction: implicit, semi-implicit and explicit"
in: *SeMA Journal* 55 (2011), pp. 59–108 (cit. on p. 30)

[57] **Banks, J., Henshaw, W., and Schwendeman, D.**
"An analysis of a new stable partitioned algorithm for FSI problems. Part I: Incompressible flow and elastic solids"
in: *Journal of Computational Physics* 269 (2014), pp. 108–137
(cit. on p. 32)

[58] **Banks, J., Henshaw, W., and Schwendeman, D.**
"An analysis of a new stable partitioned algorithm for FSI problems. Part II: Incompressible flow and structural shells"
in: *Journal of Computational Physics* 268 (2014), pp. 399–416
(cit. on p. 32)

[59] **Causin, P., Gerbeau, J., and Nobile, F.**
"Added-mass effect in the design of partitioned algorithms for fluid-structure problems"
in: *Computational Methods Applied to Mechanical Engineering* 194 (2005), pp. 4506–4527 (cit. on p. 32)

[60] **Mok, D., Wall, W., and Ramm, E.**
"Partitioned analysis approach for the transient, coupled response of viscouse fluids and flexible structures"
in: *Proceedings of the European Conference on Computational Mechanics* (1999) (cit. on p. 32)

[61] **Tallec, P. and Moure, J.**
"Fluid Structure Interaction with large structural displacements"
in: *Computational Methods applied to Mechanical Engineering* 190 (2001), pp. 3039–3067 (cit. on pp. 32, 34, 79)

[62] **Rugngy, S. and Bathe, K.**
"On finite element analysis of fluid flows coupled with structural interaction"
in: *Computational Modeling Engineering Science* 2 (2001), pp. 195–212
(cit. on p. 32)

[63] **Gerbeau, J. and Vidrascu, M.**
"A quasi-Newton algorithm based on a reduced model for fluid-structure interactions problems in blood flows"
in: *Mathematical Modeling Numerical Analysis* 37 (2003), pp. 631–648 (cit. on pp. 32, 34)

[64] **Figueroa, C., Vignon-Clementel, I., Jansen, K., Highes, T., and Taylor, C.**
"A coupled momentum method for modeling blood flow in three-dimesnional deformable arteries"
in: *Computational Methods Applied to Mechanical Engineering* 195 (2006), pp. 5685–5706 (cit. on p. 32)

[65] **Guidoboni, G., Glowinski, R., Cavallini, N., and Canic, S.**
"Stable loosely-coupled-type algorithm for fluid-structure interaction in blood flow"
in: *Journal of Computational Physics* 228 (2009), pp. 6916–6937 (cit. on p. 33)

[66] **Piperno, S. and Bournet, P.**
"Numerical simulations of wind effects on flexible civil engineering structures"
in: *Revue Europeenne des Elements Finis* 8 (1999), pp. 659–687 (cit. on p. 33)

[67] **Fourestey, G. and Piperno, S.**
"A second-order time-accurate ALE Lagrange-Galerkin method applied to wind engineering and control of brige profiles"
in: *Computer methods in applied mechanics and engineering* 193 (2004), pp. 4117–4137 (cit. on p. 33)

[68] **Piperno, S. and Farhat, C.**
"Design of efficient partitioned procedures for the transient solution of aeroelastic problems"
in: *Revue Europeenne des Elements Finis* 9 (2000), pp. 655–680 (cit. on p. 33)

[69] **Farhat, C., Zee, K. van der, and Geuzaine, P.**
"Provably second-order time-accurate loosely-coupled solution algorithms for transient nonlinear computational aeroelasticity"
in: *Computer Methods in Applied Mechanics and Engineering* 195 (2006), pp. 1973–2001. DOI: 10.1016/j.cma.2004.11.031 (cit. on pp. 33, 69)

[70] **Degroote, J., Bathe, K., and Vierendeels, J.**
"Performance of a new partitioned procedure versus a monolithic procedure in fluid-structure interaction"
in: *Computational Structures* 87 (2009), pp. 793–801 (cit. on p. 34)

[71] **Kuttler, U., Gee, M., Forster, C., and Comeford, W.**
"Coupling strategies for biomedical fluid-structure interaction problems"
in: *International Journal of Numerical Methods in Biomedical Engineering* 26 (2010), pp. 305–321 (cit. on p. 34)

[72] **Dettmer, W. and Peric, D.**
"A computational framework for fluid-structure interaction: finite element formulation and applications"
in: *Computational methods applied to mechanical engineering* 195 (2006), pp. 5754–5779 (cit. on p. 34)

[73] **Tezduyar, T. and Sathe, S.**
"Modelling of fluid-structure interaction with the space-time finite elements: solution techniques"
in: *International Journal of Numerical Methods in Fluids* 54 (2007), pp. 855–900 (cit. on p. 34)

[74] **Wall, W., Genkinger, S., and Ramm, E.**
"A strong coupling partitioned approach for fluid-structure interaction with free surfaces"
in: *Computational Fluids* 36 (2007), pp. 169–183 (cit. on p. 34)

[75] **Kuttler, U. and Wall, W.**
"Fixed-point fluid-structure interaction solvers with dynamic relaxation"
in: *Computational Mechanics* 43 (2008), pp. 61–72 (cit. on p. 34)

[76] **Kloppel, T., Popp, A., Kuttler, U., and Wall, W.**
"Fluid-structure interaction for non-conforming interfaces based on a dual mortar formulation"
in: *Computational Nethods for applied mechanical engineering* 200 (2011), pp. 3111–3126 (cit. on p. 34)

[77] **Sternel, D., Schafer, M., Heck, M., and Yigit, S.**
"Efficiency and accuracy of fluid-structure interaction simulations using an implicit partitioned approach"
in: *Computational Mechanics* 43 (2008), pp. 103–113 (cit. on p. 34)

[78] **Bazilevs, Y., Takizawa, K., and Tezduyar, T.**
"Computational Fluid-Structure Interactions Mehtods and Applications"
in: *Wiley* (2013) (cit. on pp. 34, 41)

[79] **Tallec, P. L. and Hauret, P.**
"Energy conservation in fluid structure interactions"
in: *Computational Mehtods for scientific computing. Variational problems and applications* (2003) (cit. on p. 34)

[80] **Fernandez, M., Gerbeau, J., and Grandmont, C.**
"A proyection algorithm for fluid-structure interaction problems with strong added-mass effect"
in: *Comptes Rendus Mathematique* 342 (2006), pp. 279–284 (cit. on p. 34)

[81] **Matthies, H. and Steindorf, J.**
"Partitioned but strongly coupled iteration schemes for nonlinear fluid-structure interaction"
in: *Computers and Structures* 80 (2002), pp. 1991–1999 (cit. on p. 34)

[82] **Matthies, H., Niekamp, R., and Steindorf, J.**
"Algorithms for strong coupling procedures"
in: *Computational Methods Applied to Mechanical Engineering* 195 (2006), pp. 2028–2049 (cit. on p. 34)

[83] **Formaggia, L., Gerbeau, J., Nobile, F., and Quarteroni, A.**
"On the coupling of 3D and 1D Navier-Stokes equations for flow problems in compliant vessels"
in: *Computational Methods Applied to Mechanical Engineering* 191 (2001), pp. 561–582 (cit. on p. 34)

[84] **Habchi, C., Russeil, S., Bougeard, D., Harion, J., Lemenand, T., Ghanem, A., Valle, D., and Peerhossaini, H.**
"Partitioned solver for strongly coupled fluid-structure interaction"
in: *Computers and Fluids* 71 (2013), pp. 306–319 (cit. on p. 34)

[85] **Tezduyar, T., Sathe, S., Shcwaab, M., Pausewank, J., Cristopher, J., and Crabtree, J.**
"Fluid-Structure Interaction modeling of a ringsail parachutes"
in: *Computational Mechanics* 43 (2008), pp. 133–142 (cit. on p. 34)

[86] **Takizawa, K., Wright, S., Moorman, C., and Tezduyar, E.**
"Fluid-Structure Interaction modeling of parachite clusters"
in: *International Journal for Numerical Methods in Fluids* 65 (2011), pp. 286–307 (cit. on p. 34)

[87] **Rebouillat, S. and Liksonov, D.**
"Fluid-Structure Interaction in partially filled liquid containers: A comparative review of numerical approaches"
in: *Computers and Fluids* 39 (2010), pp. 739–746 (cit. on p. 34)

[88] **Bazilevs, Y., Hsu, M., Kiendl, J., Wuchner, R., and Bletzinger, K.**
"3D Simulation of wind turbine rotors at full scale. Part II: Fluid-Structure interaction modeling with composite blades"
in: *International Journal for numerical methods in fluids* 65 (2011), pp. 236–253 (cit. on p. 34)

[89] **Bazilevs, Y., Hsu, M., Akkerman, I., Wright, S., Takizawa, K., Henicke, B., Spelman, T., and Tezduyar, T.**
"3D Simulation of wind turbine rotors at full scale. Part I: Geometry modeling and aerodynamics"
in: *International Journal for numerical methods in fluids* 65 (2011), pp. 207–235 (cit. on p. 34)

[90] **Hsu, M. and Bazilevs, Y.**
"Fluid-structure interaction modeling of wind turbines: simulating the full machine"
in: *Computational Mechanics* 50 (2012), pp. 821–833 (cit. on pp. 34, 35)

[91] **Guner, H., Thomas, D., Dimitriadis, G., and Terrapon, V.**
"Unsteady aerodynamic modeling methodology based on dynamic mode interpolation for transonic flutter calculations"
in: *Journal of Fluids and Structures* 84 (2019), pp. 218–232 (cit. on p. 34)

[92] **Jonsson, E., Mader, C., Kennedy, G., and Martins, J.**
"Computational Modeling of Flutter Constraint for High-Fidelity Aeroestructural Optimization"
in: *AIAA Scitech 2019 Forum* (2019), p. 2354 (cit. on p. 34)

[93] **Shyang, L., Ning, C., Peng, Y., Dazhuan, W., and Jerome, A.**
"Cyclostationary approach to detect flow-induced effects on vibration signals from centrifugal pumps"
in: *Mechanical Systems and Signal Processing* 114 (2019), pp. 275–289 (cit. on p. 37)

[94] **Jiang, Y., Yoshimura, S., Imai, R., Katsura, H., Yoshida, T., and Kato, C.**
"Quantitative evaluation of flow-induced structural vibration and noise in turbomachinery by full-scale wakly coupled simulation"
in: *Journal of Fluids and Structures* 23 (2007), pp. 531–544 (cit. on p. 37)

[95] **Hayashi, I. and Kaneko, S.**
"Pressure pulations in piping system excited by a centrifugal turbomachinery taking the damping characteristics into consideration"

in: *Journal of Fluids and Structures* 45 (2014), pp. 216–234 (cit. on p. 37)

[96] **Finnveden, S., Birgesson, F., Ross, U., and Kremer, T.**
"A model of wall pressure correlation for prediction of turbulence-induced vibration"
in: *Journal of Fluids and Structures* 70 (2005), pp. 1127–1143 (cit. on p. 37)

[97] **Chase, D.**
"Modelling the wavevector-frequency spectrum of turbulent boundary layer wall-pressure"
in: *Journal of Sound and Vibration* 70 (1980), pp. 125–147 (cit. on p. 37)

[98] **Liu, B.**
"Noise radiation of aircraft panels subjected to boundary layer pressure fluctuations"
in: *Journal of Sound and Vibration* 314 (2008), pp. 693–711 (cit. on p. 37)

[99] **Broatch, A., Olmeda, P., Margot, X., and Gomez-Soriano, J.**
"Numerical simulations for evaluating the impact of advanced coatings on H2 additivated gasoline lean combustion in a turbocharged spark-ignited engine"
in: *Applied Thermal Engineering* 148 (2019), pp. 674–683 (cit. on p. 39)

[100] **Robert, A., Richard, S., Colin, O., Martinez, I., and Francqueville, I.**
"LES prediction and analysis of knocking combustion in a spark ignition engine"
in: *Combustion Flame* 162 (2015), pp. 2788–2807 (cit. on p. 39)

[101] **Burg, C.**
"A robust unstructured grid movement strategy using three-dimensional torsional springs"
in: *34th AIAA Fluid Dynamics Conference and Exhibit* 84 (2004), p. 2529 (cit. on p. 39)

[102] **Farhat, C., Degand, C., Koobus, B., and Losoinne, M.**
"Torsional springs for two dimensional dynamics unstructured fluid meshes"
in: *Computational Methods Applied to Mechanica Engineering* (1998), pp. 231–245 (cit. on p. 39)

[103] **Liu, X., Qin, N., and Xia, H.**
"Fast dynamic grid deformation based on Delaunay graph mapping"
in: *Journal of Computational Physics* 211 (2006), pp. 405–423
(cit. on p. 40)

[104] **Boer A. Schoot, M. and Bikil, H.**
"Mesh deformation based on radial basis function interpolation"
in: *Computers and Structures* 85 (2007), pp. 784–795 (cit. on p. 40)

[105] **Gagliardi, F. and Giannakoglou, K.**
"A two-step radial basis function-based CFD mesh displacement tool"
in: *Advances in Engineering Software* 128 (2019), pp. 86–97
(cit. on p. 40)

[106] **Jakobsson, S. and Amoignon, O.**
"Mesh deformation using radial basis functions for gradient-based aerodynamic shape optimization"
in: *Computers and Fluids* 36 (2007), pp. 1119–1136 (cit. on p. 40)

[107] **Lee, S., Wolberg, G., and Shin, S.**
"Scattered Data Interpolation with Multilevel B-Splines"
in: *IEEE Transactions on Visualization and Computer Graphics* 3 (1997), pp. 228–244 (cit. on pp. 41, 79)

[108] **Tezduyar, T., Behr, M., Mittal, S., and Johnson, A.**
"Computation of unsteady incompressible flows with the finite element methods space time formulations, iterative strategies and massively parallel implementations"
in: *New Methods in Transient Analysis* 246 (1992), pp. 7–24
(cit. on p. 41)

[109] **Tezduyar, T., Behr, M., Mittal, S., and Johnson, A.**
"Parallel finite-element computation of 3D flows"
in: *Computer* 26 (1993), pp. 27–36 (cit. on p. 41)

[110] **Johnson, A. and Tezduyar, T.**
"Mesh update strategies in parallel finite element computations of flow problems with moving boundaries and interfaces"
in: *Computer Merhods in Applied Mechanics and Engineering* 119 (1994), pp. 73–94 (cit. on p. 41)

[111] **Vollmer, J., Mencl, R., and Mueller, H.**
"Improved Laplacian smoothing of noisy surface meshes"
in: *Computer graphics forum* 18 (1999), pp. 131–138 (cit. on p. 41)

[112] **Nealen, A., Igarashi, T., and Sorkine, O.**
"Laplacian mesh optimization"
in: *Proceedings of the 4th international conference on Computer graphics and interactive techniques in Australasia and Southeast Asia* (2006), pp. 381–389 (cit. on p. 41)

[113] **Zhou, K., Huang, J., Snyder, J., Liu, X., Bao, H., Guo, B., and Shum, H.**
"Large mesh deformation using the volumetric graph laplacian"
in: *ACM transactions on graphics* 24 (2005), pp. 496–503
(cit. on p. 41)

[114] **Hessenthaler, A., Gaddum, N., Holub, O., Sinkus, R., Rohrle, O., and Nordsletten, D.**
"Experiment for validation of fluid-structure interaction models and algorithms"
in: *International journal for numerical methods in biomedical engineering* 33 (2017), e2848 (cit. on p. 42)

[115] **Xie, Q. and Zhi, X.**
"Wind tunnel test of an aeroelastic model of a catenary system for high-speed railway in China"
in: *Journal of Wind Engineering and Industrial Aerodynamics* 184 (2019), pp. 23–33 (cit. on p. 44)

[116] **Bdeiwi, H., Ciarella, A., Peace, A., and Hahn, M.**
"Model structure effect on static aeroelastic deformation of the NASA CRM"
in: *International Jounral of Numerical Methods for Heat and Fluid Flo* 184 (2019), pp. 23–33 (cit. on p. 44)

[117] **Panciroli, R. and Porfiri, M.**
"Analysis of hydroelastic slamming through particle image velocimetry"
in: *Journal of Sound and Vibration* 347 (2015), pp. 63–78
(cit. on p. 45)

[118] **Dey, A., Modarres-Sadeghi, Y., and Rothstein, J.**
"Viscoelastic fluid-structure interactions between a flexible cylinder and wormlike micelle solution"
in: *Physical Review Fluids* 3 (2018), p. 063301 (cit. on pp. 45, 46)

[119] **Zhang, P., Peterson, S., and Porfiri, M.**
"Combined particle image velocimetry/digital image correlation for load estimation"
in: *Experimental Thermal and Fluid Science* 100 (2019), pp. 207–221
(cit. on p. 45)

[120] **Palacz, M.**
"Spectral Methods for Modelling of Wave Propagation in Structures in Terms of Damage Detection. A review"
in: *Applied Sciences* 8 (2018), p. 1124 (cit. on p. 47)

[121] **Zhang, X., Fatemi, M., Kinnick, R., and Greenleaf, J.**
"Noncontact ultrasound stimulated optical vibrometry study of coupled vibration of arterial tubes in fluids"
in: *Journal of the Acoustic Society of America* 118 (2003), pp. 1249–1257 (cit. on p. 47)

[122] **Garafolo, N. and McHugh, G.**
"Mitigation of flutter vibration using embedded shape memory alloys"
in: *Journal of Fluids and Structures* 76 (2018), pp. 495–605 (cit. on p. 47)

[123] **D.R., O., Rice, B., Peltier, S., Staines, J., Claucherty, S., and Combs, C.**
"Simultaneous Stereo Digital Image Correlation and Pressure-Sensitive Paint Measurements of a Compliant Panel in a Mach 2 Wind Tunnel"
in: *AIAA Fluid Dynamics Conference* (2018), p. 3869 (cit. on p. 49)

[124] **Wood, J., Breuer, M., and De Nayer, G.**
"Experimental studies on the instantaneous fluid-structure interaction of an air-inflated flexible membrane in turbulent flow"
in: *Journal of Fluids and Structures* 80 (2018), pp. 405–440 (cit. on p. 49)

[125] **Sousa, P., Barros, J., Tavares, O., and Moreira, P.**
"Digital image correlation diplacement measurement of a rotating RC helicopter blade"
in: *Engineering Failure Analysis* 90 (2018), pp. 371–379 (cit. on p. 49)

[126] **Subhash, S. and Bhattacharyya, S. K.**
"Finite Element analysis of fluid-structure interaction effect on liquid retaining structures due to sloshing"
in: *Computers and Structures* 6 (1996), pp. 1165–1176. DOI: 10.1016/0045-7949(95)00271-5 (cit. on p. 69)

[127] **Eisinger, F., Rao, M., Steininger, D., and Haslinger, K.**
"Numerical Simulation of Cross-Flow-Induced Fluidelastic Vibration of Tube Arrays and Comparison with experimental Results"
in: *Journal of Pressure Vessel Technology* 117 (1995), pp. 31–39. DOI: 10.1115/1.2842087 (cit. on p. 69)

[128] **Young, Y.**
"Fluid-structure interaction analysis of flexible composite marine propellers"
in: *Journal of Fluids and Structures* 24 (2008), pp. 799–818. DOI: 10.1016/j.jfluidstructs.2007.12.010 (cit. on p. 69)

[129] **Gramola, M.**
"Experimental FSI study of adaptative shock control bumps"
in: *Journal of Fluids and Structures* 81 (2018), pp. 361–377. DOI: 10.1016/j.jfluidstructs.2018.05.005 (cit. on p. 69)

[130] **Hubner, B., walhorn, E., and Dinkler, D.**
"A monolithic approach to fluid-structure interaction using space-time finite elements"
in: *Computer methods in applied mechanics and engineering* 193 (2004), pp. 23–26. DOI: 10.1016/j.cma.2004.01.024 (cit. on p. 69)

[131] **Hron, J. and Turek, S.**
"A monolithic FEM/multigrid solver for an ALE formulation of fluid-structure interaction with application in biomechanics"
in: *Fluid-Structure Interaction* 53 (2006), pp. 146–170 (cit. on p. 69)

[132] **Hermann, G. and Steindorf, J.**
"Partitioned strong coupling algorithms for fluid-structure interaction"
in: *Computers and Structures* 81 (2003), pp. 805–812. DOI: 10.1016/S0045-7949(02)00409-1 (cit. on p. 69)

[133] **Wenyong, M., Qingkuan, L., and Matsumoto, M.**
"Excitation of the large-amplitude vibrations of a circular cylinder under normal wind conditions in the critical Reynolds number range"
in: *Journal of Fluids and Structures* 84 (2019), pp. 318–328 (cit. on p. 70)

[134] **Turek, S. and Hron, J.**
"Proposal for Numerical Benchmarking of Fluid-Structure Interaction between an Elastic Object and Laminar Incompressible Flow"
in: *Fluid-Structure Interaction. Lecture Notes in Computational Science and Engineering*. Ed. by Springer Berlin, H. Vol. 53 2006, pp. 371–385 (cit. on pp. 70–72, 82)

[135] **Nassar, A., Rogers, B., Revell, A., and Stansby, P.**
"Flexible slender body fluid interaction: Vector-based discrete element method with Eulerian smoothed particle hydrodynamics"
in: *Computers and Fluids* 179 (2019), pp. 563–578 (cit. on p. 70)

[136] **Tang, L., Paidoussis, M., and Jiang, J.**
"Cantilivered flexible plates in axial flow: Energy transfer and the concept of flutter-mull"
in: *Journal of Sound and Vibration* 326 (2009), pp. 263–276. DOI: 10.1016/j.jsv.2009.04.041 (cit. on pp. 70, 108)

[137] **Purohit, A., Darpe, A., and Singh, S.**
"Influence of flow velocity and flexural rigidity on the flow induced vibration and acoustic characteristics of a flexible plate"
in: *Journal of Vibration and Control* 24 (2016), pp. 2284–2300. DOI: 10.1177/1077546316685227 (cit. on pp. 70, 108)

[138] **Wang, H., Zhai, Q., and Zhang, J.**
"Numerical study of flow-induced vibration of a flexible plate behind a circular cylinder"
in: *Ocean Engineering* 163 (2018), pp. 419–430. DOI: 10.1016/j.oceaneng.2018.06.004 (cit. on pp. 70, 89, 108)

[139] **Abdi, R., Rezazadeh, N., and Abdi, M.**
"Investigation of passive oscillations of flexible splitter plates attached to a circular cylinder"
in: *Journal of Fluids and Structures* 84 (2019), pp. 302–317 (cit. on p. 71)

[140] **Kiyoung, K. and Haecheon, C.**
"Control of laminar vortex shedding behind a circular cylinder using splitter plates"
in: *Physics of Fluids* 8 (1996), pp. 479–486. DOI: 10.1063/1.868801 (cit. on p. 73)

[141] **Unal, M. and Rockwell, D.**
"On vortex formation from a cylinder. Part 1. The initial instability"
in: *Journal of Fluid Mechanics* 190 (1988), pp. 491–512. DOI: 10.1017/S0022112088001429 (cit. on p. 73)

[142] **Unal, M. and Rockwell, D.**
"On vortex formation from a cylinder. Part 2. Control by splitter-plate interference"
in: *Journal of Fluid Mechanics* 190 (1987), pp. 513–529. DOI: 10.1017/S0022112088001430 (cit. on p. 73)

[143] **Hwang, J., Yang, K., and Sun, S.**
"Reduction of flow-induced forces on a circular cylinder using a detached splitter plate"
in: *Physics of Fluids* 15 (2003), pp. 2433–2436. DOI: 10.1063/1.1583733 (cit. on p. 73)

[144] **Galdi, G. P. and Rannacher, R.**
Fundamental Trends in Fluid-Structure Interaction
ed. by Galdi, G. P. World Scientific 2010. DOI: 10.1142/7675
(cit. on p. 73)

[145] **Haisler, W., Stricklin, J., and Key, J.**
"Displacement incrementation in non-linear structural analysis by the self-correcting method"
in: *International Journal for Numerical Methods in Engineering* 11 (1977), pp. 3–10 (cit. on p. 75)

[146] **Wood, R. D. and Zienkiewicz, O. C.**
"Geometrically nonlinear finite element analysis of beams, frames, arches and axisymmetric shells"
in: *Computers and Structures* 7 (1977), pp. 725–735 (cit. on p. 75)

[147] **Humphrey, A. C., Schuler, C. A., and Webster, D.**
"Unsteady laminar flow between a pair of disks corotating in a fixed cylindrical enclosure"
in: *Physics of Fluids* 7 (1995), pp. 1225–1240 (cit. on p. 76)

[148] **Sahu, A. K., Chhabra, P., R., and Eswaran, V.**
"Two-dimensional unsteady laminar flow of a power law fluid across a square cylinder"
in: *Journal of Non-Newtonian Fluid Mechanics* 160 (2009), pp. 157–167
(cit. on p. 76)

[149] **Smith, R. and Shyy, W.**
"Computation of unsteady laminar flow over a flexible two-dimensional membrane wing"
in: *Physics of Fluids* 7 (1995), pp. 2175–2184 (cit. on p. 76)

[150] **Yu, Y. and Li, Y.**
"Reynolds-Averaged Navier-Stokes simulation of the heave performance of a two-body floating-point absorber wave energy system"
in: *Computers and Fluids* 73 (2013), pp. 104–114 (cit. on p. 77)

[151] **Gao, X., Chen, P., and Tang, L.**
"Deforming mesh for computational aeroelasticity using a nonlinear elastic boundary element method"
in: *AIAA Journal* 40 (2002), pp. 1512–1517 (cit. on p. 77)

[152] **Demirdzic, I. and Peric, M.**
"Space conservation law in finite volume calculations of fluid flow"
in: *International Journal for numerical methods in fluids* 8 (1988), pp. 1037–1050 (cit. on p. 77)

[153] **Souli, M., Ouahsine, A., and Lewin, L.**
"ALE formulation for fluid-structure interaction problems"
in: *Computer methods in applied mechanics and engineering* 190 (2000), pp. 659–675 (cit. on pp. 77, 79)

[154] **Heil, M.**
"An efficient solver for the fully coupled solution of large-displacement fluid-structure interaction problems"
in: *Computer methods in applied mechanics and engineering* 193 (2004), pp. 1–23 (cit. on p. 79)

[155] **Bhardwaj, R. and Mittal, R.**
"Benchmarking a coupled immersed-boundary-finite-element solver for large-scale flow-induced deformation"
in: *AIAA Journal* 50 (2012), pp. 1638–1642 (cit. on p. 89)

[156] **Nayer, G., Kalmbach, A., Breuer, M., Sicklinger, S., and Wuchner, R.**
"Flow past a cylinder with a flexible splitter plate: A Complementary experimental-numerical investigation and a new FSI test case (FSI-PfS-1a)"
in: *Computers and Fluids* 99 (2014), pp. 18–43 (cit. on p. 89)

[157] **Gedikli, E., Chelidze, D., and Dahl, J. M.**
"Observed mode shape effects on the vortex-induced vibration of bending dominated flexible cylinders simply supported at both ends"
in: *Journal of Fluids and Structures* 81 (2018), pp. 399–417 (cit. on p. 89)

[158] **Sarpkaya, T.**
"A critical review of the intrinsic nature of vortex-induced vibrations"
in: *Journal of Fluids and Structures* 19 (2004), pp. 389–447 (cit. on p. 89)

[159] **Huang, L.**
"Flutter of cantilevered plates in axial flow"
in: *Journal of Fluids and Structures* 9 (1995), pp. 127–147 (cit. on p. 91)

[160] **Tang, L. and Paidoussis, M.**
"On the instability and the post-critical behaivour of two-dimensional cantilevered plates in axial flow"
in: *Journal of Sound and Vibration* 305 (2007), pp. 97–115 (cit. on p. 91)

[161] **Tang, L. and Paidoussiss, M.**
"The coupled dynamics of two cantilevered flexible plates in axial flow"
in: *Journal of Sound and Vibration* 323 (2009), pp. 790–801
(cit. on p. 91)

[162] **Bremner, P. and Wilby, J.**
"Aero-vibro-acoustics: problem statement and methods for simulation-based design solution"
in: *8th AIAA/CEAS Aeroacoustics Conference and Exhibit* (2002), p. 2551
(cit. on p. 121)

[163] **Gloerfelt, X. and Berland, J.**
"Turbulent boundary-layer noise: direct radiation at Mach number 0.5"
in: *Journal of Fluid Mechanics* 723 (2013), pp. 318–351
(cit. on p. 122)

[164] **Lecoq, D., Pezerat, C., Thomas, J., and Bi, W.**
"Extraction of the acoustic component of a turbulent flow exciting a plate by inverting the vibration problem"
in: *Journal of Sound and Vibration* 333 (2014), pp. 2505–2519
(cit. on p. 122)

[165] **Amailland, S., Thomas, J., Pezerat, C., and Boucheron, R.**
"Boundary layer noise substraction in hydrodynamic tunnel using robust principal component analysis"
in: *The Journal of the Acoustical Society of America* 143 (2018), pp. 2152–2163
(cit. on p. 122)

[166] **European Union, W. H. O. for the**
Night Noise Guidelines for Europe
tech. rep. 2010
(cit. on p. 123)

[167] **Union, E.**
On the sound level of motor vehicles and of replacement silencing systems. Regulation (EU) No 540/2014 of the european parliament and of the council of 16 April 2014
tech. rep. 2014
(cit. on p. 123)

[168] **Hansen, C. H.**
Understanding active noise cancellation
Spon Press 2003
(cit. on p. 123)

[169] **Linus, Y. L. A., Koh, Y. K., and Lee, H. P.**
"The performance of active noise-cancelling headphones in different noise environments"
in: *Applied Acoustics* 122 (2017), pp. 16–22
(cit. on p. 123)

[170] **Hwang, H. D., Ege, K., Gerges, Y., and Guyader, J. L.**
"SmEdA vibro-acoustic modelling in the mid-frequency range including the effect of dissipative treatments"
in: *Journal of Sound and Vibration* 393 (2017), pp. 187–215 (cit. on p. 123)

[171] **Munjal, M. L.**
Acoustics of Ducts and Mufflers - Second Edition
Wiley 2014 (cit. on pp. 123, 124, 133, 137, 138)

[172] **Aydemir, B. and Ebrinç, A.**
"Effect of Material Properties and Wall Thickness of Polymer Based Intake Manifold on the Engine Radiated Noise Levels"
in: *SAE International* 2001-01 (2009), p. 1544 (cit. on pp. 123, 124)

[173] **Nunes, R. F., Nogueira, C. F., Argentino, M. A., and Hackenbroich, D.**
"Developement of an Air Intake System Using Vibro-Acoustics Numerical Modeling"
in: *SAE International* 2001-01 (2001), p. 1519 (cit. on p. 124)

[174] **Hu, K., Lee, C., Homsi, E., and Moenssen, D.**
"Acoustic Modeling and Radiated Noise Prediction for Plastic Air-Intake Manifolds"
in: *SAE International* 2003-01 (2003), p. 1448 (cit. on p. 124)

[175] **Huang, L.**
"Modal analysis of a drumlike silencer"
in: *The Journal of the Acoustical Society of America* 112 (2002), pp. 2014–2015 (cit. on p. 124)

[176] **Fan, H. K., Leung, R. C., and Lam, G. C.**
"Numerical analysis of aeroacoustic-structural interaction of a flexible panel in uniform duct flow"
in: *The Journal of the Acoustical Society of America* 137 (2015), pp. 3115–3126 (cit. on p. 124)

[177] **Lawrie, J. B.**
"Analytic mode-matching for acoustic scattering in three dimensional waveguides with flexible walls: Application to a triangular duct"
in: *Wave Motion* 50 (2013), pp. 542–557 (cit. on p. 124)

[178] **Ramamoorthy, S., Grosh, S., and Dodson, J. M.**
"A theoretical study of structural acoustic silencers for hydraulic systems"
in: *The Journal of the Acoustical Society of America* 111 (2012), pp. 2097–2108 (cit. on p. 124)

[179] **Ko, S. H.**
"Sound Wave Propagation In A Two-dimensional Flexible Duct In The Presence Of An Inviscid Flow"
in: *Journal of Sound and Vibration* 175 (1994), pp. 279–287
(cit. on p. 124)

[180] **Gautier, F., Gilbert, J., Dalmont, J. P., and Vila, R. P.**
"Wave Propagation in a Fluid Filled Rubber Tube: Theoretical and Experimental Results for Korteweg's Wave"
in: *Acta Acustica united with Acustica* 93 (2007), pp. 333–344
(cit. on p. 124)

[181] **Venkatesham, B., Tiwari, M., and Munjal, M. L.**
"Analytical prediction of break-out noise from a reactive rectangular plenum with four flexible walls"
in: *The Journal of the Acoustical Society of America* 128 (2010), pp. 1789–1799
(cit. on p. 124)

[182] **Wang, G., Li, W. L., Du, J., and Li, W.**
"Prediction of break-out sound from a rectangular cavity via an elastically mounted panel"
in: *The Journal of the Acoustical Society of America* 139 (2016), pp. 684–692
(cit. on p. 124)

[183] **Munjal, M. L. and Thawani, P. T.**
"Prediction of the vibro-acoustic transmission loss of planar hose-pipe systems"
in: *The Journal of the Acoustical Society of America* 101 (1998), pp. 2524–2535
(cit. on p. 124)

[184] **Cummings, A.**
"The attenuation of sound in unlined ducts with flexible walls"
in: *Journal of Sound and Vibration* 174 (1994), pp. 433–450
(cit. on p. 124)

[185] **Hilderbrand, F. and Reissner, E.**
The influence of the aerodynamic span effect on the magnitude of the torsional-divergence velociy and on the shape of the corresponding deflection mode
tech. rep. NACA-TN-926. Massachusetts, Inst of Tech Cambridge: NACA 1944
(cit. on p. 126)

[186] **Bisplinghoff, R. L., Ashley, H., and Halfman, R. L.**
Aeroelasticity
Courier Corporation 1996
(cit. on p. 126)

[187] **Jeong, U. and Kwon, S.**
"Sequential numerical procedures for predicting flutter velocity of bridge sections"
in: *Journal of Wind Engineering and Industrial Aerodynamics* 91 (2003), pp. 291–305 (cit. on p. 126)

[188] **Schewe, G. and Larsen, A.**
"Reynolds number effects in the flow around a bluff bridge deck cross section"
in: *Journal of Wind Engineering and Industrial Aerodynamics* 74 (1998), pp. 829–838 (cit. on p. 126)

[189] **Augier, B., Bot, P., Hauville, F., and Durand, M.**
"Experimental validation of unsteady models for fluid structure interaction: Application to yacht sails and rigs"
in: *Journal of Wind Engineering and Industrial Aerodynamics* 101 (2012), pp. 53–66 (cit. on p. 126)

[190] **Zhang, Y., Habashi, W. G., and Khurram, R.**
"Predicting wind-induced vibrations of hight-rise buildings using unsteady CFD and modal analysis"
in: *Journal of Wind Engineering and Industrial Aerodynamics* 136 (2015), pp. 165–179 (cit. on p. 126)

[191] **Ricci, M., Patruno, L., Kalkman, I., Miranda, S., and Blocken, B.**
"Towards LES as a design tool: Wind loads assessment on a high-rise building"
in: *Journal of Wind Engineering and Industrial Aerodynamics* 180 (2018), pp. 1–18 (cit. on p. 126)

[192] **Davies, H.**
"Sound from turbulent boundary layer excited panels"
in: *The Journal of the Acoustical Society of America* 49 (1971), pp. 878–889 (cit. on p. 127)

[193] **Graham, W.**
"Boundary Layer Induced Noise in Aircraft, Part 1: The Flat Plate Model"
in: *The Journal of Sound and Vibration* 192 (1996), pp. 101–120 (cit. on p. 127)

[194] **Howe, M.**
"Influence of Mean Flow on Boundary Layer Generated Interior Noise"
in: *Journal of the Acoustical Society of America* 99 (1996), pp. 3401–3411 (cit. on p. 127)

[195] **Frampton, K.**
"Power Flow in an Aeroelastic PLate Backed by a Revererant Cavity"
in: *Journal of the Acoustical Society of America* 102 (1997), pp. 1620–1627 (cit. on p. 127)

[196] **Springer, M., Scheit, C., and Becker, S.**
"Fluid-struture-acoustic copling for a flat plate"
in: *International Journal of Heat and Fluid Flow* 66 (2017), pp. 249–257 (cit. on pp. 127, 128)

[197] **Mueller, S., Becker, S., Biermeier, T., Schaefer, F., Grabinger, J., Kaltenbaher, M., and Blanchet, D.**
"Investigation of the Fluid-Structure Interaction and the Radiated Sound of Different Plate Structures Deepending on Various Inflows"
in: *15th AIAA/CEAS Aeroacoustics Conference (30th AIAA Aeroacoustics Conference)* (2009), p. 3390 (cit. on p. 127)

[198] **Schafer, F., Müller, S., Uffinger, T., Becker, S., Grabinger, J., Kaltenbaher, M., and Blanchet, D.**
"Fluid-structure-acoustic interaction of the flow past a thin flexible structure"
in: *AIAA journal* 48 (2010), pp. 738–748 (cit. on pp. 127, 128, 162, 168, 194, 199)

[199] **Bazilevs, Y., Takizawa, K., and Tezduyar, T. E.**
Computational Fluid-Structure Interaction. Methods and Applications
Wiley 2013 (cit. on p. 130)

[200] **Irgens, F.**
Continuum mechanics
Springer 2008 (cit. on p. 130)

[201] **Anselmet, F. and Mattei, P. O.**
Acoustics, Aeroacoustics and Vibrations
Wiley 2016 (cit. on p. 132)

[202] **Inoue, Y. and Gotoh, Y.**
"Formation of weak shock waves caused by a sphere pulsating at large amplitude and low frequency"
in: *Journal of Sound and Vibration* 145 (1991), pp. 269–280 (cit. on p. 132)

[203] **Lighthill, M. J.**
"Viscosity effect in sound waves of finite amplitude"
in: *Survey in Mechanics* 250 (1956), pp. 337–348 (cit. on p. 132)

[204] **Romão, E. C., Campos, M. D., and Moura, L. F. M.**
"Application of the Galerkin and Least-Squares Finite Element Methods in the solution of 3D Poisson and Helmholtz equations"
in: *Computers and Mathematics with Applications* 62 (2011), pp. 4288–4299 (cit. on p. 134)

[205] *COMSOL Multiphysics 5.2 User's Guide*
2016 (cit. on p. 134)

[206] **Broatch, A., Margot, X., Gil, A., and Denia, F.**
"A CFD approach to the computation of the acoustic response of exhaust mufflers"
in: *Journal of Computational Acoustics* 13 (2005), pp. 301–316 (cit. on pp. 134, 137)

[207] **Liu, G., Zhao, X., Zhang, W., and Li, S.**
"Study on plate silencer with general boundary conditions"
in: *Journal of Sound and Vibration* 333 (2014), pp. 4881–4896 (cit. on p. 136)

[208] **Barbieri, R. and Barbieri, N.**
"Finite element acoustic simulation based shape optimization of a muffler"
in: *Applied Acoustics* 67 (2006), pp. 346–357 (cit. on p. 137)

[209] *STARCCM+ 12.02.010 User's Guide*
2016 (cit. on p. 140)

[210] **Fuenmayor, F. J., Denia, F. D., Albelda, J., and Giner, E.**
"H-adaptive refinement strategy for acoustic problems with a set of natural frequencies"
in: *Journal of Sound and Vibration* 255 (2002), pp. 457–479 (cit. on p. 141)

[211] **Herrmann, J., Koreck, J., Matthias, M., Gaul, L., and Estorff, O.**
"Frequency-dependent damping model for the hydroacoustic finite element analysis of fluid-filled pipes with diameter changes"
in: *Mechanical Systems and Signal Processing* 25 (2011), pp. 981–990 (cit. on p. 156)

[212] **David, A., Hugyes, F., Dauchez, N., and Perrey-Debain, E.**
"Vibrational response of a rectangular duct of finite length excited by a turbulent internal flow"
in: *Journal of Sound and Vibration* 422 (2018), pp. 146–160 (cit. on p. 162)

[213] **Timoshenko, S. and Woinowsky-Krieger, S.**
Theory of plates and shells
ed. by McGraw-Hill 1959 (cit. on p. 164)

[214] **Warburton, G.**
"The vibration of rectangular plates"
in: *Proceedings of the Institution of Mechanical Engineers* 168 (1954), pp. 371–384 (cit. on p. 164)

[215] **Bathe, K. and Zhang, H.**
"Finite element developments for general fluid flows with structural interactions"
in: *International Journal for numerical methods in engineering* 60 (2004), pp. 213–232 (cit. on p. 164)

[216] **Yang, K. and J.H., F.**
"Large-Eddy Simulation of Turbulent Obstacle Flow Using a Dynamic Subgrid-Scale Model"
in: *AIAA Journal* 31 (1993), pp. 1406–1413 (cit. on pp. 165, 189)

[217] **Zhengtong, X. and Castro, I.**
"LES and RANS for turbulent flow over arrays of wall-mounted obstacles"
in: *Flow Turbulence Combust* 76 (2006), pp. 291–312 (cit. on p. 165)

[218] **Moussaed, C., Salvetti, M., Wornom, S., Koobus, B., and Dervieux, A.**
"Simulation of the flow past a circular cylinder in the supercritical regime by blending RANS and variational-multiscale LES models"
in: *Journal of Fluids and Structures* 47 (2014), pp. 114–123 (cit. on p. 166)

[219] **Malloupas, G., Goldin, G., Zhang, Y., Thakre, P., Krishnamoorthy, N., Rawat, R., Gosman, D., Rogerson, J., and Bulat, G.**
"Investigation of an Industrial Gas Turbine Combustor and Pollutant Formation Using LES"
in: *ASME Turbo Expo 2017: Turbomachinery Technical Conference and Exposition* (2017) (cit. on p. 166)

[220] **Bearman, P. and Morel, T.**
"Effect of free stream turbulence on the flow around bluff bodies"
in: *Progress in aerospace sciences* 20 (1983), pp. 97–123 (cit. on p. 169)

[221] **Nakamura, Y. and Ozono, S.**
"The effects of turbulence on a separated and reattaching flow"
in: *Journal of Fluid Mechanics* 178 (1987), pp. 477–490 (cit. on p. 169)

[222] **Ratnam, G. and Vengadesan, S.**
"Performance of two equation turbulence models for prediction of flow and heat transfer over a wall mounted cube"
in: *International Jounral of Heat and Mass Transfer* 51 (2008), pp. 2834–2846 (cit. on p. 169)

[223] **Archaya, S., Dutta, S., Myrum, T., and Baker, R.**
"Turbulent flow past a surface-mounted two-dimensional rib"
in: *Journal of Fluids engineering* 116 (1994), pp. 238–246 (cit. on p. 169)

[224] **Ding, D. and Wu, S.**
"Direct numerical simulation of turbulent flow over backward-facing at high Reynolds numbers"
in: *Science China* 55 (2012), pp. 3213–3222 (cit. on p. 169)

[225] **Wilcox, D.**
"Multiscale model for turbulent flows"
in: *Proceedings of the 24th AIAA Aerospace Science Meeting* 24 (1986), pp. 1311–1320 (cit. on p. 169)

[226] **Ullrich, P. A. and Taylor, M.**
"Arbitrary-order conservative and consistent remapping and theory of linear maps: Part I"
in: *Monthly Weather Review* 143 (2015), pp. 2419–2440 (cit. on p. 170)

[227] **Ullrich, P. A. and Taylor, M.**
"Arbitrary-order conservative and consistent remapping and theory of linear maps: Part II"
in: *Monthly Weather Review* 144 (2016), pp. 1529–1549 (cit. on p. 170)

[228] **Jones, P.**
"First- and second-order conservative remapping schemes for grids in spherical coordinates"
in: *Monthly Weather Review* 127 (1999), pp. 2204–2210 (cit. on p. 170)

[229] **Taylor, G.**
"The spectrum of turbulence"
in: *Proceedings of the Royal Society of London* (1938), pp. 476–490 (cit. on p. 170)

[230] **De Roeck, W. and Desmet, W.**
"Experimental acoustic identification of flow noise sources in expansion chambers"
in: *Proceedings of ISMA 2018: International Conference on Noise and Vibration Engineering* 1 (2008), pp. 455–470 (cit. on p. 172)

[231] **Ren, W. and De Roeck, G.**
"Structural damage identification using modal data II: test verification"
in: *Journal of Structural Engineering* 128 (2002), pp. 96–104
(cit. on p. 172)

[232] **Roozen, N., Labelle, L., Rychtarikova, M., and Glorieux, C.**
"Determining radiated sound power of building structures by means of laser Doppler vibrometry"
in: *Journal of Sound and Vibration* 346 (2015), pp. 81–99
(cit. on p. 172)

[233] **Butscher, D., Hutter, C., Kuhn, C., and Rohr, P.**
"Particle image velocimetry in a foam-like porous structure using refractive index matching: a method to characterize de hydrodynamic performance of porous structures"
in: *Experiments in fluids* 53 (2012), pp. 1123–1132 (cit. on p. 172)

[234] **Armaly, B., Durst, F., Pereira, J., and Shonung, B.**
"Experimental and theoretical investigation of backward-facing step flow"
in: *Journal of Fluid Mechanics* 127 (1983), pp. 473–496
(cit. on p. 179)

[235] **Kostas, J., Soria, J., and Chong, M.**
"A study of a backward facing step flow at two Reynolds numbers"
in: *14th Australasian Fluid Mechanics Conference* (2001), pp. 609–612
(cit. on p. 179)

[236] **Tropea, C. and Gackstatter, R.**
"The flow over two-dimensional surface-mounted obstacles at low Reynolds number"
in: *Journal of Fluids Engineering* 107 (1985), pp. 489–494
(cit. on p. 179)

[237] **Durst, F., Founti, M., and Obi, S.**
"Experimental and computational investigation of the two-dimensional channel flow over two feces in tandem"
in: *Journal of Fluids Engineering* 110 (1988), pp. 48–54
(cit. on p. 179)

[238] **Celik, I., Cehreli, Z., and Yavuz, I.**
"Index of Resolution Quality for Large Eddy Simulations"
in: *Journal of Fluids Engineering* 127 (2005), pp. 949–958
(cit. on p. 179)

[239] **Lucius, A. and Brenner, G.**
"Numerical Simulation and Evaluation of Velocity Fluctuations During Rotating Stall of a Centrifugal Pump"
in: *Journal of Fluids Engineering* 133 (2011), pp. 081102-1 - 081102-8
(cit. on p. 179)

[240] **Konnigk, L., Torner, B., and Wurm, F.**
"Application of verification methods on a complex flow field calculated by Large Eddy Simulation: Blood pump flow"
in: *7th European Conference on Computational Fluid Dynamics* (2018), pp. 1–13 (cit. on p. 179)

[241] **Dastbelaraki, A., Yaghoubi, M., Tavakol, M., and Rahmatmand, A.**
"Numerical analysis of convection heat transfer from an array of perforated fins using RANS and LES method"
in: *Applied Mathematical Modelling* (2018) (cit. on p. 179)

[242] **Frampton, K.**
"The effect of flow-induced coupling on sound radiation from convected fluid loaded plates"
in: *The Journal of the Acoustical Society of America* 117 (2005), pp. 1129–1137 (cit. on p. 186)

[243] **Pastor, M., Binda, M., and Harcarik, T.**
"Modal Assurance Criterion"
in: *Procedia Engineering* 48 (2012), pp. 543–548 (cit. on p. 187)

[244] **Werner, H. and Wengle, H.**
"Large-eddy simulation of turbulent flow over a square rib in a channel"
in: *Advances in Turbulence* 2 (1989), pp. 418–423 (cit. on p. 189)

[245] **Schmidt, S. and Thiele, F.**
"Comparison of numerical methods applied to the flow over wall-mounted cubes"
in: *International Journal of Heat and Fluid Flow* 23 (2002), pp. 330–339
(cit. on p. 189)

[246] **Ariff, M., Salim, S., and Cheah, S.**
"Wall y+ approach for dealing with turbulent flow over a surface mounted cube: Part 2-High Reynolds number"
in: *Proceedings of 7th International Conference on CFD in the Minerals*

and Process Industries CSIRO, Melbourne, Australia (2009)
(cit. on p. 189)

[247] **Chopra, A. K.**
"Modal analysis of linear dynamic systems: physical interpretation"
in: *Journal of structural engineering* 122 (1996), pp. 517–527
(cit. on p. 191)